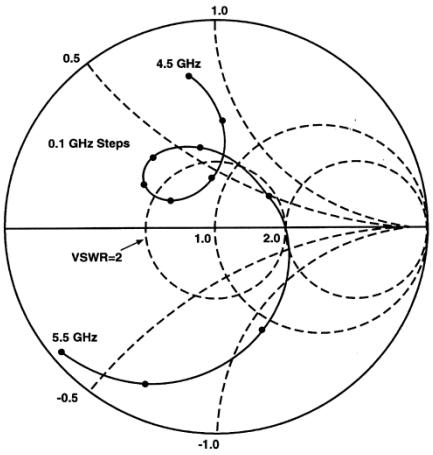

Applied Computational Electromagnetics Society Journal

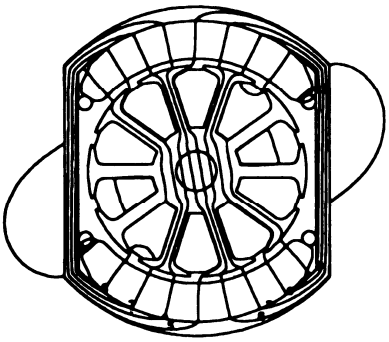

Special Issue on
ACES 2010 Conference

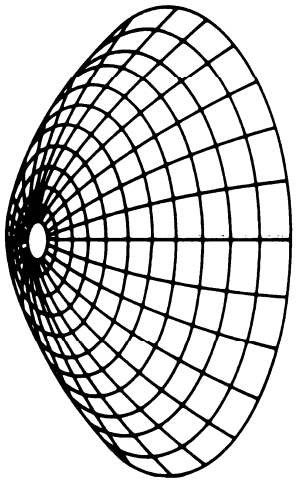

Editor-in-Chief
Atef Z. Elsherbeni

December 2010
Vol. 25 No. 12
ISSN 1054-4887

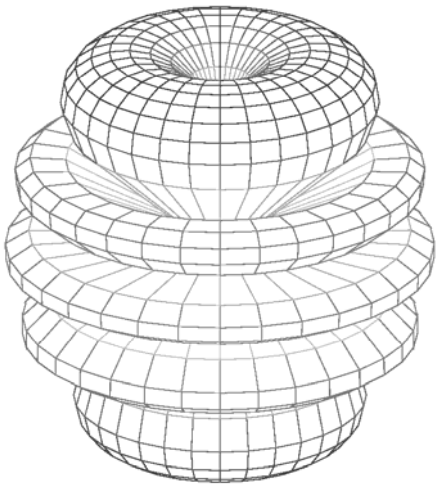

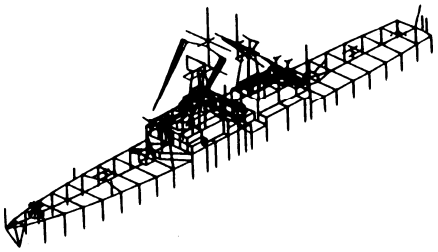

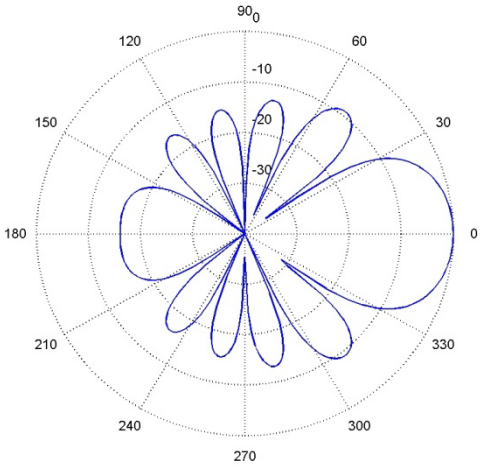

GENERAL PURPOSE AND SCOPE: The Applied Computational Electromagnetics Society ***(ACES)*** Journal hereinafter known as the ***ACES Journal*** is devoted to the exchange of information in computational electromagnetics, to the advancement of the state-of-the art, and the promotion of related technical activities. A primary objective of the information exchange is the elimination of the need to "re-invent the wheel" to solve a previously-solved computational problem in electrical engineering, physics, or related fields of study. The technical activities promoted by this publication include code validation, performance analysis, and input/output standardization; code or technique optimization and error minimization; innovations in solution technique or in data input/output; identification of new applications for electromagnetics modeling codes and techniques; integration of computational electromagnetics techniques with new computer architectures; and correlation of computational parameters with physical mechanisms.

SUBMISSIONS: The ***ACES Journal*** welcomes original, previously unpublished papers, relating to applied computational electromagnetics. Typical papers will represent the computational electromagnetics aspects of research in electrical engineering, physics, or related disciplines. However, papers which represent research in applied computational electromagnetics itself are equally acceptable.

Manuscripts are to be submitted through the upload system of ***ACES*** web site http://aces.ee.olemiss.edu See "Information for Authors" on inside of back cover and at ***ACES*** web site. For additional information contact the Editor-in-Chief:

Dr. Atef Elsherbeni
Department of Electrical Engineering
The University of Mississippi
University, MS 386377 USA
Phone: 662-915-5382 Fax: 662-915-7231
Email: atef@olemiss.edu

SUBSCRIPTIONS: All members of the Applied Computational Electromagnetics Society who have paid their subscription fees are entitled to receive the ***ACES Journal*** with a minimum of three issues per calendar year and are entitled to download any published journal article available at http://aces.ee.olemiss.edu.

Back issues, when available, are $15 each. Subscriptions to ***ACES*** is through the web site. Orders for back issues of the ***ACES Journal*** and changes of addresses should be sent directly to ***ACES***:

Dr. Allen W. Glisson
302 Anderson Hall
Dept. of Electrical Engineering
Fax: 662-915-7231
Email: aglisson@olemiss.edu

Allow four week's advance notice for change of address. Claims for missing issues will not be honored because of insufficient notice or address change or loss in mail unless the Executive Officer is notified within 60 days for USA and Canadian subscribers or 90 days for subscribers in other countries, from the last day of the month of publication. For information regarding reprints of individual papers or other materials, see "Information for Authors".

LIABILITY. Neither ***ACES***, nor the ***ACES Journal*** editors, are responsible for any consequence of misinformation or claims, express or implied, in any published material in an ***ACES Journal*** issue. This also applies to advertising, for which only camera-ready copies are accepted. Authors are responsible for information contained in their papers. If any material submitted for publication includes material which has already been published elsewhere, it is the author's responsibility to obtain written permission to reproduce such material.

APPLIED COMPUTATIONAL ELECTROMAGNETICS SOCIETY JOURNAL

Special Issue on
ACES 2010 Conference

Editor-in-Chief
Atef Z. Elsherbeni

December 2010
Vol. 25 No.12
ISSN 1054-4887

The ACES Journal is abstracted in INSPEC, in Engineering Index, DTIC, Science Citation Index Expanded, the Research Alert, and to Current Contents/Engineering, Computing & Technology.

The first, fourth, and sixth illustrations on the front cover have been obtained from the Department of Electrical Engineering at the University of Mississippi.

The third and fifth illustrations on the front cover have been obtained from Lawrence Livermore National Laboratory.

The second illustration on the front cover has been obtained from FLUX2D software, CEDRAT S.S. France, MAGSOFT Corporation, New York.

THE APPLIED COMPUTATIONAL ELECTROMAGNETICS SOCIETY

JOURNAL

Vol. 25 No. 12 December 2010

TABLE OF CONTENTS

Twenty Three Years: The Acceptance of Maxwell's Equations

James C. Rautio

Sonnet Software, Inc.
North Syracuse, NY 13212, USA
rautio@sonnetsoftware.com

Abstract ─ Maxwell first published what came to be called "Maxwell's equations" in 1865. However, it was not until 1888, and Heinrich Hertz's experimental validation, that Maxwell's equations were widely accepted as correct. The story of the intervening 23 years is little known. Maxwell, who died in 1879, was exceptionally modest and did not promote his own results at any time. The survival of Maxwell's equations was up to the only three researchers in the entire world who paid serious attention to Maxwell's paper in 1865, and his seminal *Treatise* in 1873: Oliver Heaviside, Oliver Lodge, and George Francis FitzGerald. Later, Hertz joined the group forming "The Four Maxwellians". In this paper, we describe the torturous 23 year path Maxwell's equations took from their creation to their initial acceptance.

Index Terms ─ Fitzgerald, Heaviside, Hertz, history, Lodge, Maxwell's equations.

I. PROLOGUE

Flying splinters of wood from cannon balls exploding through the sides of the ships wreak the most carnage in the battle of Trafalgar, Fig. 1. One hundred fifty five years ago on October 21, 1805, the final and the greatest sailing ship battle of all time is fought to its gory end. Lord Nelson's 27 British battle ships and 2,150 cannons face 33 French and Spanish ships of Napoleon's navy carrying 2,640 cannons. Lord Nelson's flag ship, the HMS Victory becomes locked, rigging entangled, side-by-side with the French ship Redoubtable. The British reduce the gun powder in each charge, so the cannon balls penetrate only the near side of the Redoubtable and then bounce around inside, wreaking even more carnage. The crew of the Redoubtable valiantly return fire…

Every man does his duty and Britain wins the battle, however Lord Nelson does not survive. All

Fig. 1. The death of Lord Nelson on his flagship, the HMS Victory, in the battle of Trafalgar, image from a philatelic souvenir sheet issued by the Island of Jersey.

ships receive extensive damage and soon a major storm scatters survivors. Today, you can view a statue of Nelson on a hundred foot column in the exact center of London in Trafalgar Square. Little known, the radical battle-winning strategy Nelson used (which is detailed in any book on the battle) was first suggested by John Clerk of Eldin, great-great uncle of James Clerk Maxwell [1].

Britain's victory assures British dominance of the oceans for the remainder of the 19th century. As part of this dominance, Britain secures a monopoly on the production of "gutta percha", a natural plastic made from the sap of a tropical tree. Gutta percha will become the perfect, and for many years, the only practical insulator for the undersea cables linking far-flung dominions of the Empire. Dominance on the ocean and in undersea cables, these two factors are critical in Britain's leading role in science and technology for the 19th century…all tracing back to a naval strategy suggested by Maxwell's great-great uncle.

Flash forward 60 years to 1865. The American Civil War is ending. Maxwell, Fig. 2, [2], working at home [3], Fig. 3, publishes, "A Dynamical Theory of the Electromagnetic Field," in the Royal

Fig. 2. Unveiling of a statue in honor of Maxwell in Edinburgh [2]. Sandy Stoddart, the sculptor, watches to the left.

Society Transactions, Vol. CLV (he actually presented the paper orally in December 1864). Comparing several measurements of the speed of light to that calculated by his new electromagnetic theory, he notes, "The agreement of the results seems to shew[1] that light and magnetism are affections of the same substance, and that light is an electromagnetic disturbance propagated through the field according to electromagnetic laws."

The directly measured values for the speed of light that Maxwell quotes are 314,858,000 m/s (M. Fizeau), 298,000,000 m/s (M. Foucault), and 308,000,000 m/s (by stellar aberration). Measurements of a capacitor discharge applied to Maxwell's theory yields 310,740,000 m/s (MM. Weber, and Kohlrausch). Given the modern knowledge of the speed of light, we know which results are presented to appropriate precision and with minimum error (Foucault eventually refined his result to within 4 km/s of the correct answer),

Fig. 3. Maxwell's home in Scotland [3], recently and partially restored, where Maxwell wrote his *Treatise* and the field of electromagnetic theory began.

and even with that knowledge, Maxwell's conclusion is strong.

Thus, one of the greatest problems of physics is now solved! Break out the champagne, wild celebration, Maxwell is our hero! Hold on, not quite yet. We must patiently wait 23 years. One problem, Maxwell offers no mechanical model for the "luminiferous ether", the medium in which this supposed wave travels. Maxwell and friends all know that light is a transverse wave (assuming that it is actually a wave, not a particle as Newton had insisted). So whatever medium you propose, it must not allow a longitudinal wave. Further, the earth plows through this medium without spiraling into the sun, so either it has no mechanical effect on matter or it has no shear strength. But without shear strength, it cannot support a transverse wave. And if there is no interaction with matter, how could any wave ever get started? Maxwell's theory is just a bunch of equations, no model what-so-ever.

[1] Modern spelling is "show".

And what a bunch of equations. There are 20 of them, simultaneous differential equations, not the four equations we know today. Maxwell has the concepts of divergence (he uses the opposite sign and calls it convergence), and curl. But vector calculus is not yet formalized, so he just writes out all 20 equations. Sometimes he uses "quaternions", encouraged by quaternion champion and very good lifelong friend P. G. Tait. Quaternions are a combination of a scalar and a vector, which have the not so nice requirement of a squared magnitude of -1, and of complicating situations better dealt with by vectors.

Wait, there's more. Those twenty equations are not easily recognized today. Maxwell places as primary something he calls "electromagnetic momentum" (because its time derivative is force). Electric and magnetic fields are secondary. His friend, Michael Faraday, who originated the field concept as an alternative to the then popular "action at a distance", called it the "electrotonic state". It is, Faraday said, changes in the electrotonic state surrounding magnets that cause magnetic induction. Maxwell formalized Faraday's field concept. The electrotonic state is today called the magnetic vector potential, usually introduced only in graduate level EM courses as a side-effect of a cute little vector identity. (Primacy of the vector potential is returning to popularity in physics.)

Maxwell viewed magnetic vector potential as primary (presumably why he gave it the symbol A) and magnetic field as secondary (presumably why he gave it the symbol B). However, by making the vector (and scalar) potentials primary, Maxwell's equations become complicated. Very few take the time to learn them.

Finally, unlike Newton, Maxwell was not a self-promoter. For example, while president of Section A of the British Association, he gave a presidential address (published in Vol. 2 of the new British journal Nature) at the 1870 annual meeting with high praise for a vortex theory of molecules due to his good friend William Thomson (later Lord Kelvin). Rather than wave the flag to the scientific world about his own electromagnetic theory, he only briefly mentions at the end, "Another theory of electricity which I prefer…," not even taking credit for his own work [4].

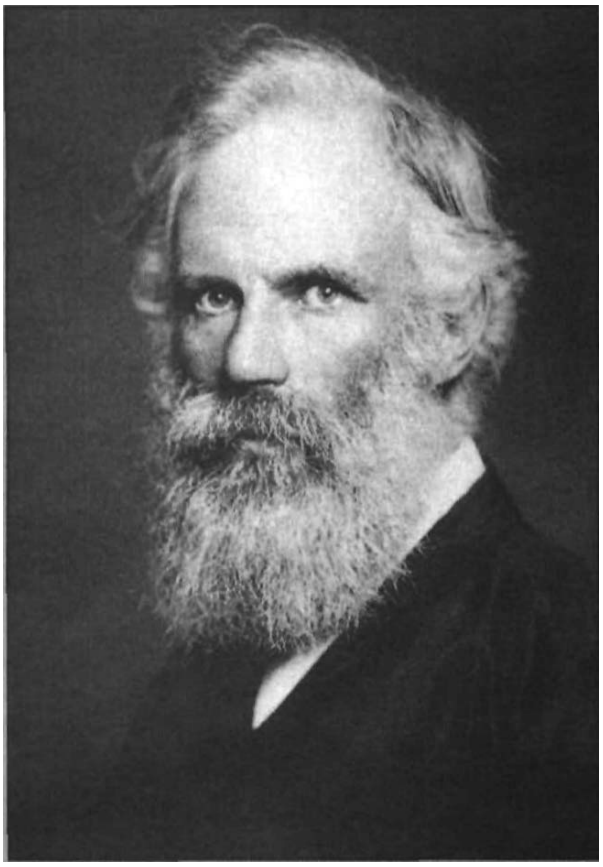

Fig. 4. George Francis FitzGerald found a connection to an earlier theory of the ether, and thus, introduced reflection, refraction, and diffraction to Maxwell's work, image from [7].

Those with further interest in Maxwell's life with respect to the origin of electromagnetics will find more information in [2-5].

II. MAXWELLIAN FITZGERALD

Maxwell dies in 1879. There is no one, no students, no colleagues, to carry on his work in electromagnetics. Well, almost no one. Two days after Maxwell's death, the Royal Society mails a paper review written by Maxwell some months earlier back to George Francis FitzGerald, Fig. 4, Fellow and soon to be professor of Trinity College Dublin [6-7]. The future of electromagnetics now lies in FitzGerald's hands.

FitzGerald is a brilliant idea man. However, he describes himself as "lazy" when it comes to follow up experimental work. More typically, he does the initial work, and then hopes others (usually friends or students) will be inspired to continue. In the paper that Maxwell reviewed,

FitzGerald links Maxwell's electrodynamic theory to an earlier theory of Prof. James MacCullagh, also, of Trinity College. This theory models the luminiferous ether required by Fresnel's wave theory of light and requires a purely rotational elasticity, i.e., no translational stress can be allowed to form. MacCullagh had shown that given this form for the ether, one can model refraction, reflection, and polarization perfectly. Quite the coincidence! However, there are a couple of problems. First, MacCullagh does not suggest a physical form for this mysterious ether; it is certainly unknown in normal matter. Second, in 1862, G. G. Stokes, in reviewing a number of proposed ethereal models, points out that MacCullagh's ether violates conservation of angular momentum. Nice idea, while it lasted.

Maxwell published his *Treatise* on electromagnetics (the founding document of our field) in 1873. However, in this, and in all of Maxwell's EM theory publications, there is no electromagnetic treatment of reflection or refraction. FitzGerald is one of the very few people who read and learn the *Treatise* in detail. FitzGerald also extensively studied MacCullagh's ether model while preparing for his fellowship exam. His well annotated copy of Maxwell's *Treatise* includes a long note dated 7 September 1878 where he first mentions that it might be possible to connect Maxwell's theory to MacCullagh's. Over-simplifying just a bit, FitzGerald found a mapping of variables from Maxwell's theory to MacCullagh's. In his paper, he describes the mapping and points out that MacCullagh's work now brings reflection and refraction to Maxwell's theory.

However, Stokes' objections still hold; MacCullagh's ether does not conserve angular momentum. If MacCullagh's ether is the same as Maxwell's, then Maxwell cannot be correct either. FitzGerald, a lifelong believer in some kind of ether, optimistically announces that perhaps we should "emancipate our minds from the thraldom of a material ether."

III. MAXWELLIAN LODGE

Oliver Lodge [6], Fig. 5, is a son of a pottery clay merchant. He takes a higher road when he wins a scholarship and completes a University of London external degree. He completes a doctorate at University College in London, later becoming

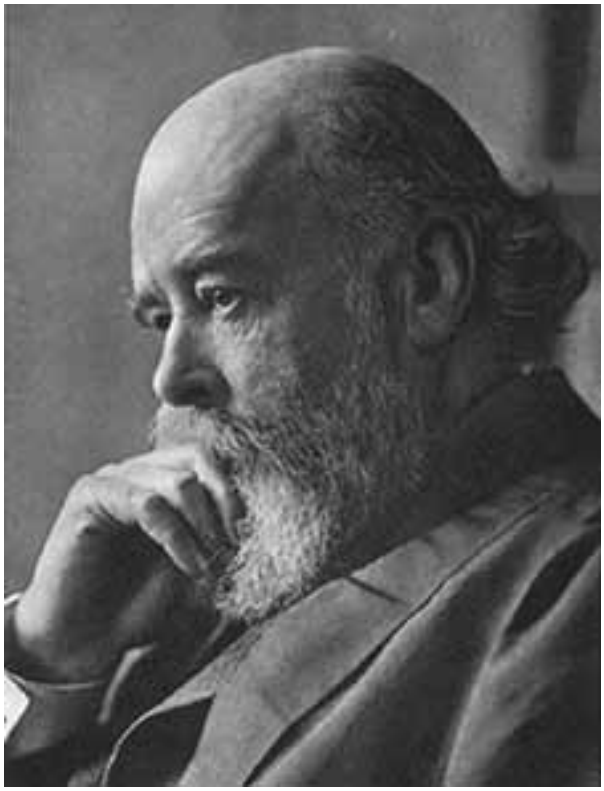

Fig. 5. Oliver Lodge worked extensively with mechanical models of the ether inspired by Maxwell's *Treatise* and his association with Fitzgerald.

the first professor of physics at the new University College in Liverpool in 1881. Lodge had acquired a copy of Maxwell's *Treatise* in 1873, right after it was published. The bookseller grumbled that it was, "a product of the over educated." He started studying it in 1876. He first meets FitzGerald at the August 1878 Dublin meeting of the British Association. Sharing a strong interest in Maxwell's *Treatise*, they quickly become good friends.

A great unsolved mystery is why Maxwell never tried to produce electromagnetic waves. Historians suggest that it is most likely Maxwell simply missed that implication of his theory. The possibility that changing currents could make light just did not occur to Maxwell and that radiation could be generated by electricity is not obvious from Maxwell's equations, especially in the form Maxwell used. Maxwell appears to have believed that light was made by mechanically vibrating molecules somehow coupling to and vibrating the ether. And EM waves of long wavelength? At that

time, such "dark light" was outside human experience.

Lodge is more comfortable working with mechanical models, rather than directly with equations. In 1879, one of his models suggests that it might be possible to create light electrically. But how? He suggests applying a voltage source through a switch that switches ("breaks") 400 times a second. The square wave is applied to a coil which somehow doubles the frequency. A cascade of 40 such coils should yield light. FitzGerald gently points out that the square wave would be smoothed into a sine wave after only several coils and thus would not work.

Lodge, not one to give up easily, suggests that a discharging condenser (i.e., capacitor, in the form of a Leyden jar) is oscillatory. FitzGerald's response is not preserved, but he likely told Lodge that the frequency would be too low for light. So close…they missed the idea that it would be just fine to generate long wavelengths, "dark light", if only they could find a way to "see" such wavelengths.

FitzGerald then pursues the problem mathematically, using Maxwell's *Treatise*. He makes several errors. First, he reads Maxwell too literally, as though the *Treatise* is an electromagnetic bible. For example, Maxwell states repeatedly that his theory gives results equivalent to the old "action at a distance" concept. In this case, there can be no radiation. However, it appears that Maxwell's comment was limited to the non-time varying situation, something FitzGerald did not realize. A second very serious error concerns what is now called the gauge condition. Maxwell selected what we call the Coulomb gauge (divergence of A is zero) and then incorrectly specified the scalar potential to be independent of time, yielding a static solution. Eventually FitzGerald realizes the problem, in part by toying with mechanical models of the ether that he had built. Then likely inspired by Lord Rayleigh's Theory of Sound, and by electromagnetic research published by Lorenz, he introduces retarded potentials to Maxwell's theory.

FitzGerald, with considerable effort, does find a solution to Maxwell's equations for a time varying current, but it is a non-radiating solution, "like the nodes and loops in an organ pipe". He, thus, concludes that generating EM waves electrically is impossible. What FitzGerald did not realize is he had unwittingly found the solution assuming a conducting wall boundary condition. This illustrates a problem of the vector potential; boundary conditions are difficult to see. Years later, FitzGerald realizes that an alternative solution (assuming a different boundary condition) takes the form of the sought after traveling waves. Regardless, the damage is done. FitzGerald and Lodge continue enthusiastically working with Maxwell's theory, but the search for an EM wave generation is terminated…until 1888.

IV. MAXWELLIAN HEAVISIDE

"The following story is true. There was a little boy, and his father said, 'Do try to be like the other people. Don't frown.' And he tried and tried, but could not. So his father beat him with a strap; and then he was eaten up by lions."

This is the first paragraph in Vol. III of Oliver Heaviside's *Electromagnetic Theory*. Heaviside is a "first rate oddity" as described by a friend [8]. He is, also, an exceptionally prolific writer, difficult to read, and an absolute mathematical genius, Fig. 6. He was raised in Dickensian poverty in Camden Town, London, in fact just around the corner from where Dickens himself had lived and worked as a boy in a blacking factory. In addition to the harsh treatment, he was often ill. A bout with scarlet fever left him deaf until young manhood and unable to interact normally with other children. He never attended a university. Beyond a reasonable early education (partially provided by his mother), he was self taught in science and mathematics. He learned by reading books from the library. It appears he passionately avoided books on theology and metaphysics (unlike Maxwell), but he adored books dealing with Newton, and Laplace, to name a few.

He started his first and only job in 1867 as a telegraph clerk. His uncle by marriage, Charles Whetstone (of bridge fame), helped him obtain the position. The first undersea cable (Dover to Calais) was laid in 1851. By 1885, there are nearly 100,000 miles of cable under the ocean, mostly laid by Britain due to their dominance on the ocean and monopoly of the only viable undersea cable insulator, gutta percha. Because of its importance to the Empire, much of British science is now focused on problems relating to undersea cables.

Heaviside obtained a copy of Maxwell's *Treatise* in 1873. "I browsed through it and I was astonished! I read the preface and the last chapter, and several bits here and there; I saw that it was great, greater, and greatest…I was determined to master the book and set to work." Heaviside left his job the next year and moved in with his parents to pursue the mathematics of Maxwell, especially with regard to telegraphic (and soon, telephonic) cable problems.

Heaviside has no patience with stupidity. One person in particular, William Henry Preece, later the Engineer-in-Chief of the British General Post Office (which controls all British telegraph and telephone lines), considers himself to be an especially intelligent "Practical Man" who has no need for theoretical mathematicians. In reality, Preece's high self-esteem is undeserved, as Heaviside often bluntly points out. Preece takes offense.

In one case, Heaviside discovers the transmission line "telegraphers" equation, deriving it from Maxwell's theory. William Thomson (Lord Kelvin) had successfully analyzed undersea cables based on the diffusion equation, i.e., just resistance and capacitance, no inductance. In this case, a pulse effectively diffuses into the cable. This actually provides reasonable results for most undersea cables but fails miserably for overhead lines.

When Heaviside derives the full telegrapher's equation, he determines that if the ratio of L/R is equal to C/G, distortion (i.e., pulse spreading) is eliminated. G is very small, thanks to gutta percha. R is expensive to decrease. So, simply increase L. His work is effectively suppressed over a long period by Preece. Preece is vehement that the inductance of a transmission line is zero and increasing it only leads to disaster. As a "practical man", he cannot be convinced otherwise by these silly mathematicians. Later, engineers in the United States successfully make, apply, and patent the same discovery. Heaviside receives no credit.

In the summer of 1884, Heaviside starts working on energy flow in the electromagnetic field. The derivation is complicated, but the result is simple, $S = E \times H$. Heaviside, being reclusive and not well connected with the rest of the scientific community, is later only a little disappointed to find that Prof. Poynting of the new Mason College of Science in Birmingham had published the same result a few months earlier.

Fig. 6. Oliver Heaviside was the first to put Maxwell's equations in their modern form, image from IEE archives.

As an example of energy flow, take the field around a straight copper wire at DC. $E \times H$ points radially into the wire. Energy does not flow along the wire as had been thought. It flows from the field surrounding the wire and dissipates as heat as it enters the wire. This is the big clue. In sharp contrast to action at a distance, where energy is viewed as flowing along the wire with the current like water in a pipe; Maxwell's equations suggest that energy is in the field and flows from the field into the resistance of the conductor.

In fact, the Maxwellian view at this time is that charge and current are not physical. Rather, they are changes in the stresses and strains of the ether. The conductor of the wire relieves the stress of the field and dissipates the energy as heat. This view fades with the advent of a new discovery a few years later, the electron. As for the modern view, electromagnetic energy is calculated in terms of either the field or the current. It's hard to say precisely "where" it is.

Heaviside went further than Poynting. As Heaviside was working with his energy concept, he came upon a new form for Maxwell's equations, the "duplex" form, the four equations with which we are familiar today. These differential curl equations involve *E*, *H*, *D*, and *B*. The potentials are gleefully "murdered" according to Heaviside, "I never made any progress until I threw all the potentials overboard," he later wrote to FitzGerald. With the duplex form, the symmetries in Maxwell's equations are beautifully seen, but something is missing. Heaviside adds the fictitious magnetic current to complete the symmetry.

If Heaviside modified Maxwell's equations to this degree, why don't we call them Heaviside's equations? Heaviside answered this question in the preface to Vol. 1 of his over 1500 page, three volume, lifetime culminating work, *Electromagnetic Theory* stating that if we have good reason, "to believe that he [Maxwell] would have admitted the necessity of change when pointed out to him, then I think the resulting modified theory may well be called Maxwell's."

In 1888, Lodge is requested to give two lectures on lightning protection and he conducts experiments by discharging condensers in the vicinity of models of various structures. The lectures stimulate major controversy with Preece as Lodge's results contradict standard practice (in this case, Preece actually turned out to be correct). But all that is minor. In the course of his experiments, Lodge notices arcs being induced in nearby circuits. In one experiment, he sees an arc at the end of two parallel wires. In the dark, he can even see a distinct standing wave glowing in the air around the wires. Lodge has generated and detected electromagnetic waves! The British Association is meeting in Bath in September. Lodge plans to report his astounding results at that meeting, right after he returns from vacation in the Alps.

On the train out of Liverpool, he picks up the July issue of *Annalen der Physik*. He immediately notices an article, "Ueber elektrodynamische Wellen in Luftraume und deren Reflexion" ("On Electromagnetic Waves in Air and Their Reflection").

Fig. 7. Heinrich Hertz independently put Maxwell's equations into their modern form and went on to achieve experimental validation.

IV. MAXWELLIAN HERTZ

Six years of Heinrich Hertz's education was in Berlin under Hermann von Helmholtz. Helmholtz had incorporated the electromagnetic theories of Maxwell, Weber, and Neumann into a single theory with a parameter (k), whose value selected the theory to be used. It was not realized until later that Maxwell's theory was not fully correctly incorporated, but Hertz, Fig. 7, was able to study much of Maxwell's theory under Helmoholtz's guidance in this manner.

Helmholtz had encouraged Hertz to perform experiments to test and differentiate the theories. Hertz at first declined, having determined that the experiments would be difficult to perform. However, he kept the possibility in mind. A few years later, while teaching at Technische Hochschule in Karlsruhe, he notices while discharging a condenser through a loop, that an identical loop some distance away develops arcs.

He instantly recognizes a resonance condition and suspects electromagnetic waves. The experiments he subsequently conducts verify reflection, refraction, diffraction, and polarization for both free space waves and wire guided waves. It is Hertz's experimental results that Lodge is reading in *Annalen der Physik* as he leaves for vacation.

As Lodge reads the paper, he realizes that his own results are now superfluous. However, his disappointment is more than compensated by the beauty and completeness of Hertz's work. Fitzgerald (who had actually heard about one of Hertz's papers a month before Lodge, and had requested a copy from Hertz) presents Hertz's results at the September 1888 British Association meeting in Bath and is Hertz is hailed as a hero. His results provide full confirmation of Maxwell's electromagnetic theory. The British Maxwellians, after 15 years of careful theoretical investigation of Maxwell's theory, are catapulted to the top of British science thanks to Hertz's timely experimental validation. Hertz is warmly welcomed into the small Maxwellian group and takes an active role, but, unfortunately, for far too short a time.

In Germany, because of the continental pre-disposition toward action at a distance, the importance of Hertz's results is not at first fully recognized. In fact some say, only partly in jest, that word of Hertz's experiments reached Germany by way of England. Once recognized, German researchers likewise embrace Maxwell's theory as well.

Hertz had, independently of Heaviside, discarded Maxwell's potentials and developed the modern duplex form of Maxwell's equations. When Hertz becomes aware of Heaviside's work, he graciously yields priority to Heaviside and likewise chooses to call them Maxwell's equations. As a tribute to Hertz, they are for a few years also sometimes called the Hertz-Maxwell equations.

IV. EPILOGUE

Hertz, always refusing travel to conferences, finally agrees to visit England to receive the prestigious Rumford Medal from the Royal Society in November 1890. The year before, Hertz had received a major promotion and moved to the chair of physics at the University of Bonn. However, the move deprived him of experimental facilities. Hertz still makes significant theoretical contributions in close collaboration with the British Maxwellians. Work becomes difficult when he starts suffering from an infection (perhaps autoimmune disease) that spreads to his jaw and sinuses. He writes to his parents in August 1892, "At present my nose is my universe." He dies tragically and painfully at the age of 36 in January 1894, on New Year's Day, from blood poisoning after an operation.

As researchers adopt and study Maxwell's theory, Joseph Larmor of Cambridge proposes the existence of the electron. Larmor and Heaviside don't get along especially well, but Heaviside evaluates the field around a moving electron. The field includes the square root of $1 - (v/c)^2$ in the denominator, hinting of things to come. Heaviside adamantly insists that there is no reason why electrons cannot move faster than the speed of light. Of course, by modern physics, we know he was only partially correct. Electrons cannot move faster than the speed of light in free space.

Michelson and Morley perform their interferometer experiment in 1887, the year before the Bath meeting, casting doubt on the existence of ether. However, FitzGerald later points out that atomic structure might depend in some way on electromagnetic fields. Heaviside had found that the fields of a moving electron contract in the direction of movement; perhaps matter contracts likewise. This concept was also independently developed by Lorentz. A quick calculation shows that the Michelson-Morley interferometer would contract just enough in the direction of the earth's movement to make it appear that the ether is not moving no matter how fast the earth is moving. British researchers continue searching for mechanical models of the ether well into the 20th century before the effort is gradually dropped as pointless.

FitzGerald periodically experienced long bouts of "indigestion". He passes away after an operation on February 22, 1901. He is 49. To Heaviside and Lodge his death is a great shock.

Lodge did not contribute further to Maxwell's theory after 1900. He did spend considerable effort researching communication with the dead. He died on August 22, 1940, promising to make public appearances after his death. No such appearances have been recorded.

In 1896, Heaviside's father dies, leaving Heaviside on his own for the first time in his life. FitzGerald and John Perry arrange a Civil List pension for him of 120 pounds per year. In a more difficult task, they convince Heaviside to accept it, offering it as recognition of service to his country.

Heaviside becomes senile in his old age, "I am as stupid as an owl." He dies on February 3, 1925 after falling off a ladder and landing on his back. He is 74. His ride to the hospital is his first and final ride in an automobile.

I close with a paragraph written on January 30, 1891, in Heaviside's *Electromagnetic Theory*:

"Lastly, from millions of vibrations per second, proceed to billions, and we come to light (and heat) radiation, which are, in Maxwell's theory, identified with electromagnetic disturbances. The great gap between Hertzian waves and waves of light has not yet been bridged, but I do not doubt that it will be done by the discovery of improved methods of generating and observing very short waves."

We truly do stand on the shoulders of giants.

ACKNOWLEDGMENT

This paper is a revised and supplemented version of [5], reprinted with permission.

REFERENCES

[1] L. Campbell and W. Garnett, *The Life of James Clerk Maxwell*, London, Macmillan and Co., 1882, 2nd edition 1884.

[2] J. C. Rautio, "MTT Society news: Toby's statue," *IEEE Microwave Magazine*, vol. 10, no. 4, pp 48-60, June 2009.

[3] J. C. Rautio, "In search of Maxwell," *IEEE Microwave Magazine*, vol. 6, no. 2, pp 44-53, June 2005.

[4] F. Dyson, "Why is Maxwell's theory so hard to understand?" *James Clerk Maxwell Commemorative Booklet,* 4th International Congress on Industrial and Applied Mathematics, Edinburgh, Scotland, July 1999.

[5] J. C. Rautio, "Twenty three years: The acceptance of Maxwell's equations," *Microwave Journal,* vol. 51, no. 7, pp. 104 - 116, July 2008.

[6] B. Hunt, *The Maxwellians*, Ithaca, Cornell University Press, 1991.

[7] J. Bell, and D. Weaire, "George Francis FitzGerald," *Physics World*, pp. 31-35, Sept. 1992.

[8] P. J. Nahin, *Oliver Heaviside: Sage in Solitude*, New York, IEEE Press, 1987.

James C. Rautio received a BSEE from Cornell in 1978, a MS Systems Engineering from University of Pennsylvania in 1982, and a Ph. D. in Electrical Engineering from Syracuse University in 1986. From 1978 to 1986, he worked for General Electric, first at the Valley Forge Space Division, then at the Syracuse Electronics Laboratory. At this time, he developed microwave design and measurement software, and designed microwave circuits on Alumina and on GaAs. From 1986 to 1988, he was a visiting professor at Syracuse University and at Cornell. In 1988, he went full time with Sonnet Software, a company he had founded in 1983. In 1995, Sonnet was listed on the Inc. 500 list of the fastest growing privately held US companies, the first microwave software company ever to be so listed. Dr. Rautio was elected a fellow of the IEEE in 2000 and received the IEEE MTT Microwave Application Award in 2001. He has lectured on the life of James Clerk Maxwell over 100 times.

Material Realizations of Perfect Electric Conductor Objects

Ari Sihvola, Ismo V. Lindell, Henrik Wallén, and Pasi Ylä-Oijala

Department of Radio Science and Engineering
Aalto University School of Science and Technology
P.O. Box 13000, FI–00076 AALTO, Finland
ari.sihvola@tkk.fi, ismo.lindell@tkk.fi henrik.wallen@tkk.fi, pasi.yla-oijala@tkk.fi

Abstract – This article discusses the distinction between interfaces and boundaries in electromagnetics. Boundary conditions can be used to narrow down the computation domain of complex problems. However, terminating the space by a boundary condition is an approximation in real-world situations where fields penetrate across interfaces. To make this approximation accurate, the material parameters need to have a very strong contrast between the materials on the adjacent sides of the interface. In this article, the question is addressed how extreme the permittivity and permeability have to be in order to reasonably model a surface as a perfect electric conductor (PEC) boundary. It is argued that in addition to the large value of the permittivity, also a very small magnitude of the permeability is necessary in order to speed up the convergence of a material response towards the ideal PEC case.

Index Terms – Boundary conditions, extinction, extreme-parameter materials, metamaterials, PEC, scattering.

I. INTRODUCTION

In electromagnetics, the objective is often to solve electric and magnetic fields in a given region of space. Fields, due to a source, radiate and penetrate into the near and far surroundings, reacting to the environment, its structure, and boundaries. Sometimes, for reasons of decreasing the computational complexity and cost, the problems are formulated in a form that the domain of interest is bounded in which the fields need to be calculated. On the boundary of this domain, certain sufficient conditions for the fields have to be forced in order that the solutions are correct and non-ambiguous.

Boundary conditions simplify the solution process because one does not need to bother what happens on the other side of the boundary. On the other hand, when applied to model real-world situations, boundary conditions only approximate the electromagnetic effect of the material behind the surface. It is well known that replacing a dielectric boundary by an impedance condition is not exact or even accurate for an arbitrary field setting. This happens especially when the discontinuity of the material parameter contrasts over the interface is not very large.

It is essential to emphasize this fundamental difference between the interface problem and boundary problem (Figure 1). In the interface problem, the materials everywhere, on both sides of the interface, affect the fields in both domains. On the other hand, if the region 1 is terminated by a boundary condition, nothing behind this boundary can have any effect on the fields. In fact, it is senseless to talk about the region behind this boundary because it does not exist in the electromagnetic problem.

Despite this distinction, a connection exists between the two situations. Indeed, either of them can be approximated with the other one in certain cases. When such an approximation is taken, it is important to keep in mind which one of the pictures is primary. The first choice is that one treats the interface picture as a true model of the real world. Then it is possible to solve the electromagnetic problem in the interesting region by replacing the interface with a boundary and cutting away everything on the other side. This procedure can be termed as the *analytic* approach.

However, the complementary view is very important and useful: the boundary condition itself is primary. A great variety of different electromagnetic boundary conditions exist, and it is a legitimate

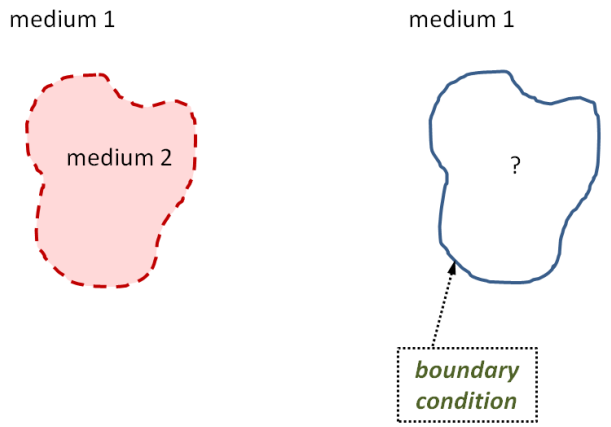

Fig. 1. The distinction between interface (left) and boundary (right) problems. In the latter case, there is nothing beyond the boundary.

project to study their properties in a systematic manner. Some of such ideal boundary conditions may turn out to display potential for interesting applications. For example, using such a concept, a desired antenna structure can be theoretically designed, and if the result is worth realizing, the next step is to synthesize it using composites or metamaterials. This procedure of starting from the boundary condition and proceeding to materials is called the *synthetic* approach.

Materials with extreme parameters are hence a natural choice for creating ideal boundaries. The term "extreme parameters" often refer to cases where one or more of the material parameters (permittivity, permeability, refractive index, and wave impedance) have either very small or very large values [1, 2]. Also anisotropic materials with certain components of the parameter tensors being extreme fall into this class. In the following, the effect of boundary conditions (in particular, the perfect electric boundary, PEC) is approximated by materials with isotropic extreme parameters, and the accuracy of the approximation is being estimated in quantitative terms.

II. EXAMPLES OF BOUNDARY CONDITIONS

Well-known boundary conditions are perfect electric conductor (PEC) and perfect magnetic boundary (PMC) conditions. In the former, the electric field component tangential to the surface vanishes ($\mathbf{n} \times \mathbf{E} = 0$), and the latter condition requires that the tangential magnetic field becomes zero ($\mathbf{n} \times \mathbf{H} = 0$). Here $\mathbf{n}$ is the unit normal pointing away from the boundary.

A generalization of PEC and PEC conditions is the impedance boundary condition [3] which defines the ratio between the tangential electric and magnetic fields on the surface. Another generalization is the so-called PEMC condition [4, 5] with one parameter M which states that the fields satisfy $\mathbf{n} \times (\mathbf{H} + M\mathbf{E}) = 0$. Furthermore, the so-called soft-and-hard surface [6] is characterized by another interesting pair of boundary conditions $\mathbf{v} \cdot \mathbf{E} = 0,\ \mathbf{v} \cdot \mathbf{H} = 0$, for a vector $\mathbf{v}$ along the boundary.

Also, field components normal to the boundary have been of interest in terms of surfaces [7]. The so-called DB boundary condition [8] requires that the normal components of the electric and magnetic flux densities vanish on the surface, which in connection with isotropic media means that the fields themselves do not have normal components: $\mathbf{n} \cdot \mathbf{E} = 0$ and $\mathbf{n} \cdot \mathbf{H} = 0$. Recent generalizations to the DB boundary condition include the so-called D'B' boundary [9, 10].

In the following, we will focus the analysis on the PEC boundary condition, and look for ways to simulate it by material structures.

III. ISOTROPIC EXTREME-PARAMETER MATERIALS

Let us limit the discussion to isotropic materials whose electromagnetic response can be characterized by two (complex) parameters, the relative permittivity ϵ_r and relative permeability μ_r.[1] Using these parameters, two other quantities can be written, the refractive index $m = \sqrt{\mu_r \epsilon_r}$ and the relative wave impedance $\eta_r = \sqrt{\mu_r / \epsilon_r}$. Then, depending on whether the magnitudes of any of these four parameters are very large (VL) or very small (NZ, "near-zero"), we can distinguish the eight classes of extreme-parameter electromagnetic media that are listed in Table 1.

Plotted in the plane where the axes give the logarithm of the permittivity and the permeability, the extreme-parameter materials are located away from the origin, as shown in Figure 2. The logarithm implies here that the parameters are assumed to have only positive values.

[1] The relative permittivity of the material is defined by normalizing the absolute permittivity ϵ by the free-space permittivity ϵ_0, likewise for the permeability: $\mu = \mu_r \mu_0$. The speed of light is $c = 1/\sqrt{\mu_0 \epsilon_0}$.

Table 1: Classes of extreme-parameter media

	very large	very small
ϵ_r	EVL	ENZ
μ_r	MVL	MNZ
m	IVL	INZ
η_r	ZVL	ZNZ

IV. ARTIFICIAL PEC MATERIAL

Intuitively, the concept of a perfect electric conductor is close to medium with a very large permittivity value. Indeed, a high permittivity means that the electric field inside the medium is forced to vanish in order not to run into an infinite energy density (which is proportional to $\epsilon_r|\mathbf{E}|^2$). Consequently, due to the continuity of the tangential electric field over the boundary, the tangential field has to vanish on both sides of the boundary. Hence, the PEC condition is satisfied on the surface of a material with $\epsilon_r = \infty$.

In addition, also from the point of electrostatics, a similar argument can be made. The image of a point charge from a dielectric half space of permittivity ϵ_r has the amplitude $-(\epsilon_r - 1)/(\epsilon_r + 1)$ compared to the original source [11, p. 111]. This image clearly approaches, when $\epsilon_r \to \infty$, the mirror image of a point charge from a PEC plane, which is of the same magnitude as the original charge but of opposite sign.

However, the situation is not as simple in electrodynamics. From Faraday's law in the electromagnetic time-harmonic case ($\nabla \times \mathbf{E} = -\mathrm{j}\omega\mathbf{B}$), one can infer that also the magnetic flux density $\mathbf{B}$ has to vanish inside a medium where the electric field is identically zero. Furthermore, the magnetic constitutive relation reads

$$\mathbf{B} = \mu\mathbf{H}. \tag{1}$$

While $\mathbf{B}$ is identically zero, no condition is set to the magnetic field strength. If finite values are allowed for the $\mathbf{H}$ field, the inevitable conclusion is that the permeability has to vanish: $\mu_r = 0$. Furthermore, due to the continuity of the normal-directed flux densities over interfaces, a corollary of the PEC condition would be that the normal component of the magnetic flux density is zero on this boundary: $\mathbf{n} \cdot \mathbf{B} = 0$.

This line of argument raises the question whether it is possible to replace a situation involving the mathematically idealized PEC condition by a homogeneous high-permittivity structure, or does one need to require an additional condition that the permeability is small. In the following, we examine the validity of the previous argumentation which calls for extreme values for both permittivity and permeability by solving electromagnetic scattering problems from such structures.

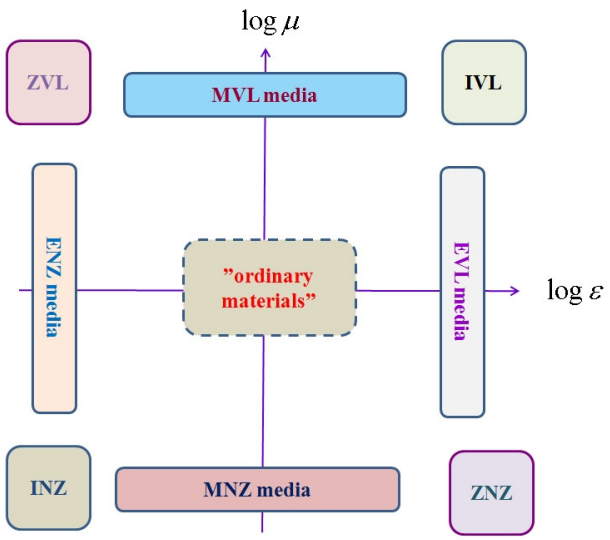

Fig. 2. Plotted in the plane where the axes are the logarithms of the (positive and isotropic) permittivity ϵ_r and permeability μ_r, the various classes of extreme materials fall away from the center. Depending on whether the permittivity (E), permeability (M), the refractive index (I), or the impedance (Z) is very small or very large, the different extreme-material parameters occupy a certain place in the plane.

V. SCATTERING BY EXTREME-PARAMETER OBJECTS

For small objects, the scattering by an electromagnetic plane wave can be explained by dipole scattering. For example, the Rayleigh scattering from a dielectric particle is due to an electric dipole whose amplitude can be calculated from the electrostatic excitation. It is, however, known in the Rayleigh-scattering regime [12, Section 8.25] that to replace a PEC object by an equivalent penetrable object, one needs to account for the magnetic dipole (calculated with $\mu_r = 0$), in addition to the electric dipole (with $1/\epsilon_r = 0$). For example, the scattering pattern of a purely dielectric (small) sphere has the same amplitude in both forward and backward directions, whereas a PEC sphere

has a dominating backscattering: the back-to-front ratio is close to 10 dB in the Rayleigh scattering regime [13].

In this section, we examine the scattering problem from extreme-parameter objects in more detail.

A. Mie scattering by a sphere

The scattering situation is of course more complicated when the scatterer is no longer small compared with the wavelength. For a homogeneous sphere, the problem can be solved using Mie theory [14, 15]. The scattered fields of a dielectric sphere with relative permittivity ϵ_r, relative permittivity μ_r, refractive index $m = \sqrt{\mu_r \epsilon_r}$, radius r, and size parameter $x = \omega r/c$, are expanded using the Mie coefficients a_n and b_n:

$$a_n = \frac{\epsilon_r \mathrm{j}_n(mx)[x\mathrm{j}_n(x)]' - \mathrm{j}_n(x)[mx\mathrm{j}_n(mx)]'}{\epsilon_r \mathrm{j}_n(mx)[x\mathrm{h}_n^{(2)}(x)]' - \mathrm{h}_n^{(2)}(x)[mx\mathrm{j}_n(mx)]'} \tag{2}$$

$$b_n = \frac{\mu_r \mathrm{j}_n(mx)[x\mathrm{j}_n(x)]' - \mathrm{j}_n(x)[mx\mathrm{j}_n(mx)]'}{\mu_r \mathrm{j}_n(mx)[x\mathrm{h}_n^{(2)}(x)]' - \mathrm{h}_n^{(2)}(x)[mx\mathrm{j}_n(mx)]'} \tag{3}$$

that involve spherical Bessel j_n and Hankel $\mathrm{h}_n^{(2)}$ functions and where the prime indicates differentiation with respect to the argument in parenthesis.

For a spherical domain, on the surface of which the PEC condition is forced, the corresponding coefficients can be derived:

$$a_n = \frac{[x\mathrm{j}_n(x)]'}{[x\mathrm{h}_n^{(2)}(x)]'} = \frac{x\mathrm{j}_{n-1}(x) - n\mathrm{j}_n(x)}{x\mathrm{h}_{n-1}^{(2)}(x) - n\mathrm{h}_n^{(2)}(x)} \tag{4}$$

$$b_n = \frac{\mathrm{j}_n(x)}{\mathrm{h}_n^{(2)}(x)}. \tag{5}$$

It is worth noting that Equations (4) and (5) also follow from the coefficients (2) and (3) in case $\epsilon_r \to \infty$, $\mu_r \to 0$, for a finite m.

Let us compare the Mie coefficients of the PEC sphere and same-sized spheres with extreme material parameters. Figure 3 shows the behavior of the first Mie scattering coefficient a_1 for a PEC sphere and two material realizations to approximate it. In the first of the cases, the relative permittivity is $\epsilon_r = 10^6$ and there is no magnetic response. The other one is less extreme in permittivity $\epsilon_r = 10^3$, but it has the relative permeability value of $\mu_r = 10^{-3}$.

The figure shows clearly that the most effective way to simulate the smooth PEC behavior by a penetrable sphere is using a medium with high-permittivity along with low-permeability, instead of a non-magnetic, solely extreme-permittivity response. In the case where the sphere is purely dielectric, there are numerous narrow resonances in the frequency dependence of the Mie coefficient which contaminate the curve (that in average follows the PEC function). In contrast, if the penetrable sphere becomes diamagnetic

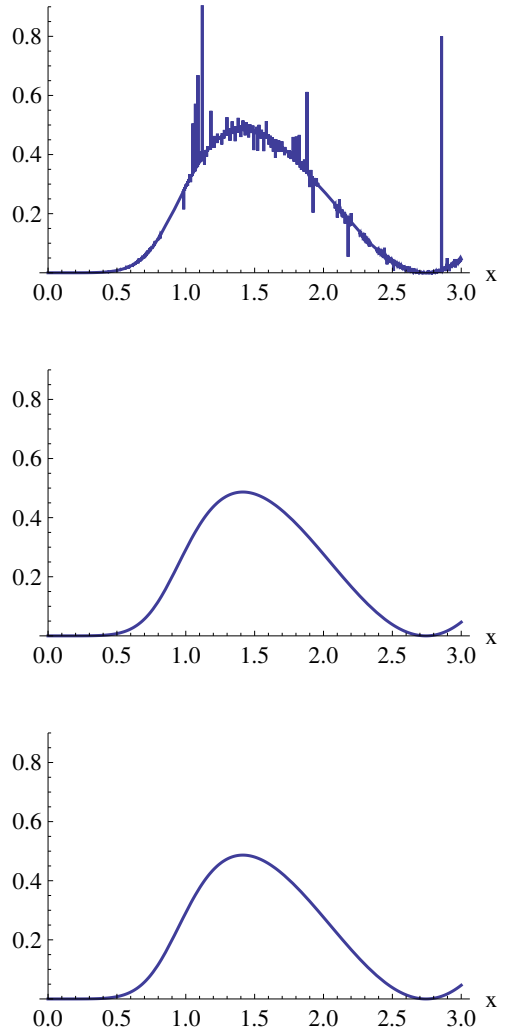

Fig. 3. Real part of the Mie coefficient a_1 as function of size parameter $0 < kr < 3$ for a non-magnetic dielectric sphere with $\epsilon_r = 10^6$ (top), a dielectric–magnetic sphere with $\epsilon_r = 10^3$ and $\mu_r = 10^{-3}$ (middle), and for a sphere on the surface of which the PEC condition is forced (bottom). The resolution of the picture is not able to display all the resonances in the topmost curve. However, it is anyway sufficient to show that the curve in the center figure is clearly a better approximation to the PEC than the topmost one.

($\mu_r < 1$), the PEC behavior is captured even if the permittivity and permeability parameters are not very extreme.

In other words, at least for this case of a sphere, the ZNZ model ($\eta_r = \sqrt{\mu_r/\epsilon_r}$ near zero) approximates PEC better than the EVL model (ϵ_r very large).

B. Scattering by a cube

A similar comparison can be made for the case when the scatterer is a cube. Figures 4 and 5 display the forward and backward scattering cross sections of various type of cubes: a PEC cube, and two penetrable cubes for which the permittivity increases. One of these cubes is purely dielectric, whereas the other's permeability decreases along with increasing permittivity. The size of the cube is comparable with the wavelength ($ka = 3$, with a being the side length), and the plane wave is incident head-on to one of the faces of the cube.

The scattering results have been calculated using the surface integral equation formulation where the scatterer is modeled either as a non-penetrable object with the PEC boundary condition or as a penetrable object. In the first case, the PEC condition, $\mathbf{n}\times\mathbf{E} = 0$, is enforced to the surface integral representation of the electric field and the solution is found with the electric field integral equation formulation [16, 17]. In this case, the fields inside the object are not modeled.

In the latter case, the scatterer is penetrable and the fields are modeled also inside the object. On the surface, the interface conditions, i.e., the continuity of the tangential electric and magnetic fields, are required and the solution is found with the Poggio–Miller–Chang–Harrington–Wu–Tsai (PMCHWT) formulation [18]. In both cases, the surface current densities are approximated with the triangular Rao–Wilton–Glisson (RWG) [16] basis functions, the equations are converted into matrix equations with Galerkin's testing procedure, and the matrix equations are solved with a direct method.

The message of the curves in the figures is clear. As the permittivity of the penetrable spheres increases, the scattering cross section approaches that of the PEC cube, both in the backward and forward scattering directions. However, the convergence for the purely dielectric cube is slow due to the jumps and resonances in the curve as the permittivity increases towards the EVL case. On the other hand, if the permeability decreases at the same time as the permittivity increases,

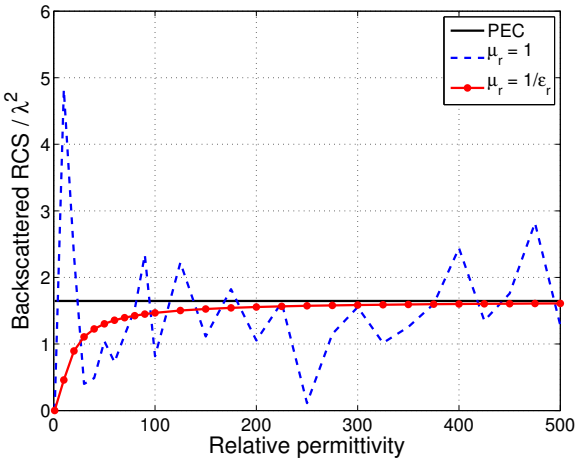

Fig. 4. The normalized backscattering cross section of a PEC cube ($ka = 3$), compared with penetrable cubes of the same size but of varying permittivity. One of the cubes is purely dielectric and the other has also diamagnetic response. The cross section is normalized by wavelength squared.

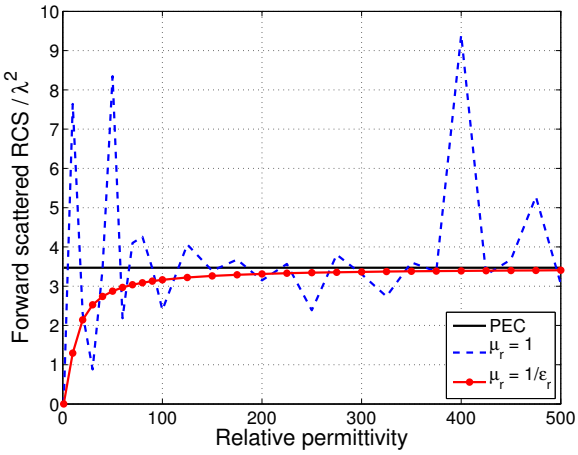

Fig. 5. The same as in Figure 4, the forward scattering cross section.

the scattering coefficients approach very soon those of the PEC cube. For instance, when $\epsilon_r = 1/\mu_r = 500$, the relative difference in the cross section is a couple of percents.

The EVL case ($\epsilon_r \to \infty$, $\mu_r = 1$) is numerically challenging, because the wave number inside the object becomes very large and the Green's function highly oscillating. This may partially explain the jumps in the curves in Figures 4 and 5. In the other case, (ZNZ, $\epsilon_r \to \infty$ and $\mu_r = 1/\epsilon_r$), the refractive index $m = \sqrt{\epsilon_r\mu_r}$ is unity and the problem is much easier to solve with numerical methods.

C. Effect of losses

In microwave and radio engineering, a common practice is to assume that good conductors, for example copper or some other metals, behave reasonably as approximations for PEC. In the frequency domain, the effect of conductivity σ comes through the imaginary part of the permittivity ($\mathrm{Im}\,\epsilon = -\sigma/\omega$). This raises the question whether the ideal PEC behavior can be synthetized more effectively when the imaginary part—instead of the real part—of the permittivity becomes very large.

In Figure 6, we compare the scattering efficiencies of various spheres (with size parameter $kr = 1$) against the ideal PEC sphere. The scattering efficiency is a dimensionless parameter, defined as the integrated total scattering cross section divided by the geometrical cross section of the scatterer. We plot the absolute difference of the efficiency of the PEC sphere and that of the material sphere when the material parameters grow to very large values. Three different cases are treated: purely dielectric ($\epsilon_r \to \infty$), dielectric–magnetic ($\epsilon_r \to \infty, \mu_r \to 0$), and electrically dissipative ($\sigma \to \infty$).

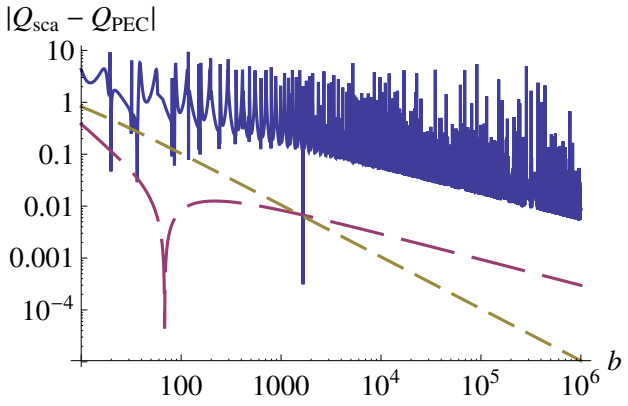

Fig. 6. The absolute value of the difference between the scattering efficiency of a PEC sphere and three material realizations: dielectric sphere ($\epsilon_r = b, \mu_r = 1$, solid line), dielectric–magnetic sphere ($\epsilon_r = 1/\mu_r = b$, short-dashed line), and dielectrically lossy sphere ($\epsilon_r = 1 - \mathrm{j}\,b, \mu_r = 1$, long-dashed line). The size of the sphere is $kr = 1$.

The curves show that when the parameter b grows to very large values, all material realizations approach the PEC case in terms of the scattering efficiency. As was seen also earlier (Figure 3), the purely dielectric sphere exhibits narrow resonances which destroy its possibilities of being a very good PEC approximation. Furthermore, even if the resonances were filtered away from this curve, the error would still decrease rather slowly. The ZNZ curve (large permittivity along with small permeability) approaches much faster the PEC state than the baseline of the EVL curve.

In the case of the conducting sphere in which the imaginary part of the permittivity grows, no resonances are seen, which is also expected. Also, the error in approximating PEC scattering becomes smaller for increasing conductivity. However, the speed at which the error becomes smaller is clearly lower that of the EVL curve. Numerically it can be shown that the asymptotic behavior of the latter (ZNZ) one is b^{-1} whereas the curve showing the error of the conducting sphere decreases as $b^{-1/2}$.

A further disadvantage of the model of the PEC object as an extreme conductor is that for a conducting scatterer, the extinction is larger than the scattering cross section. This is due to the dissipation of the fields that penetrate within the skin depth of the object which means that absorption adds up to scattering with the result that extinction increases. Hence the comparisons of the scattering cross section and the extinction cross section against the PEC case yield different results. In this respect, the ZNZ object is much closer to the PEC object; both ZNZ and PEC lack absorption and therefore have unit albedo.

Figure 7 displays the albedo (defined as the ratio of the scattering cross section to the extinction cross section [19, p. 183]) of a dielectric, lossy sphere (size parameter $kr = 1$) as a function of the imaginary part of the permittivity. The figure shows that the scattering and extinction can be clearly different, even if it is true that for low losses on one hand and high losses on the other, the albedo approaches unity.

D. Single and double negative permittivity

For metals at microwave frequencies, the approximation of a very large imaginary part of the permittivity is well-founded. However, far higher in the frequency range, the imaginary part of metal permittivity decreases according to the Drude dispersion model, and the dominating character of the dispersion is the negative real part of the permittivity [20]. This fact suggests one further possibility to mimic PEC objects: with negative-permittivity scatterers.

Figure 8 displays the scattering efficiencies of various spheres with size parameter $kr = 3$ as a function

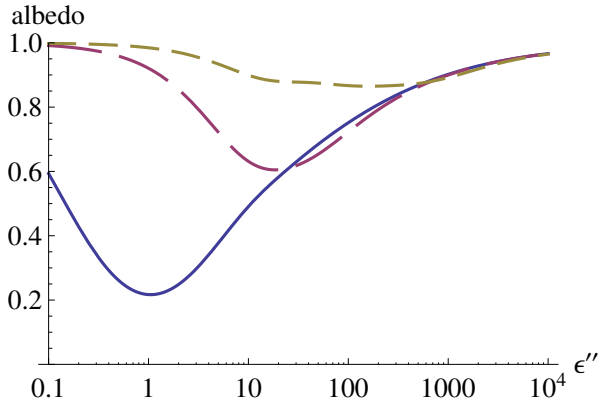

Fig. 7. The albedo (scattering efficiency divided by extinction efficiency) of a lossy dielectric sphere as a function of the (negative) imaginary part of the permittivity. Solid line: $\epsilon = 2 - \mathrm{j}\epsilon''$, long-dashed line: $\epsilon = 50 - \mathrm{j}\epsilon''$, short-dashed line: $\epsilon = 1000 - \mathrm{j}\epsilon''$. The sphere size is $kr = 1$.

of increasing medium parameter values. In addition to the dielectric–magnetic and lossy objects, also single and double-negative permittivity scatterers are shown.

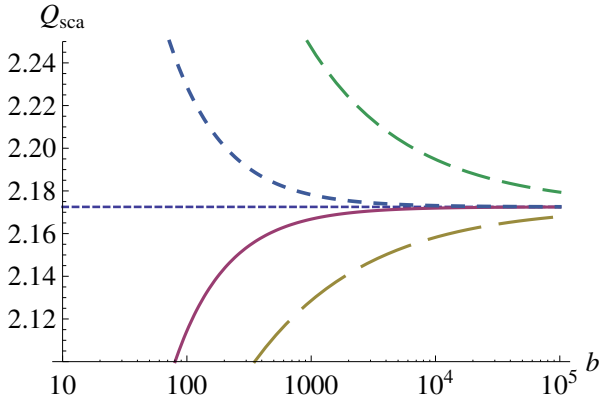

Fig. 8. The scattering efficiencies of four spheres: dielectric–magnetic sphere ($\epsilon_r = b, \mu_r = 1/b$, solid line), dielectrically lossy sphere ($\epsilon_r = 1 - \mathrm{j}\,b, \mu_r = 1$, long-dashed), single-negative sphere ($\epsilon_r = -b, \mu_r = 1$, medium-dashed), and double-negative sphere ($\epsilon_r = -b, \mu_r = -1/b$, short-dashed). The size of the sphere is $kr = 3$. The dotted line shows the PEC value.

We can observe from the curves that a negative-permittivity scatterer does not perform better in approximating the PEC response than the lossy scatterer (with large imaginary permittivity). However, if also the permeability is negative and small, in addition to the large and negative permittivity, the scattering efficiency approaches more effectively that of the PEC sphere, and the convergence speed is the same as for the positive dielectric–magnetic (ZNZ) sphere.

VI. DISCUSSION

The previous analysis has focused on the difference between the boundary problem and the interface problem. One needs to make a clear distinction between ideal boundaries on one hand and material interfaces on the other. Boundary conditions can serve as approximations to inhomogeneous real world structures (analytic approach) and vice versa: one can try to mimic boundary conditions using electromagnetic materials (synthetic approach). To be able to approximate boundary conditions, extreme-parameter materials were needed.

The clear message of the analysis is that to simulate a PEC object by a homogeneous isotropic material object, it is most efficient to use a material with simultaneously large permittivity *and* small permeability, instead of a pure dielectric medium with either high permittivity or high conductivity. In other words, a ZNZ ("near-zero impedance") medium is better than an EVL ("epsilon-very-large") medium.

It is important to note that in addition to the requirement of small value for the relative impedance in the ZNZ picture, there is an additional degree of freedom in the extreme-medium desciption: the refractive index m. In the calculations of this study, m was taken as unity. This is not compulsory. In fact, the errors in scattering magnitudes of ZNZ objects compared against PEC are functions of m. However, it seems that the best value of m of a ZNZ scattering in simulating PEC behavior is always quite close to unity, even if not exactly. The optimum depends on the shape and size of the object.

This result about the PEC–ZNZ connection can be generalized to perfectly magnetic conductors. Even if the analysis did not treat PMC boundary conditions, we can make use of the duality between electric and magnetic quantities in Maxwell equations and conclude that a material realization for a PMC boundary is a "very large impedance" (ZVL) material rather than a "mu-very-large" (MVL) medium.

One important question in trying to simulate boundary conditions with electromagnetic materials is uniqueness. The synthesis of a given boundary condition does not necessarily lead to unique recipes. The fabrication of a DB boundary (the normal components

of the electric and magnetic flux densities are forced zero) is an example showing the degrees of freedom in this respect. To create the effect of a DB surface, one possibility is to take uniaxial material in which the permittivity and permeability eigenvalues vanish in the axial direction. If such a material is cut so that the interface is perpendicular to the optical axis, the normal components of both the electric and magnetic flux densities are forced to vanish on the surface.

However, as shown in [21], another choice to create a DB boundary is by use of the so-called IB material. The IB medium, also termed as skewon–axion medium [22], is characterized by a four-dimensional material tensor dominated by the antisymmetric part with the additional PEMC parameter. The number of medium parameters in the general IB medium is 16, meaning that there are several degrees of freedom in the construction of a materials to give rise to a DB boundary.

The uniqueness question can, also, be raised in connection of the PEC synthesis. The condition on the PEC boundary is that the *tangential* electric field vanish. On the other hand, due to the continuity of the tangential electric field across an interface, it suffices to force the tangential electric field within the synthetized medium to vanish. Allowing for an anisotropic medium, this can be done by letting the tangential component of the permittivity dyadic grow to infinity (and, at the same time, the normal component of the permeability dyadic decreases to zero). Such an anisotropic medium would be another choice, in addition to the isotropic ZNZ medium, to simulate the PEC behavior.

Another aspect of the question of uniqueness of the PEC realization concerns the realization of infinite material parameters. The numerical calculations in this article have indicated that there are several different material realizations (for example, EVL, ZNZ, well-conducting, double-negative, etc.) of media which all in the extreme limit approach the PEC behavior. In this sense, the PEC realization can be considered non-unique. However, the message is that for pragmatic and numerical purposes, the ZNZ method to mimic PEC behavior is computationally most effective.

ACKNOWLEDGMENT

This study has been supported by the Academy of Finland, through grants 108801 and 124204.

REFERENCES

[1] A. Sihvola, S. Tretyakov, and A. de Baas, "Metamaterials with extreme material parameters," *Journal of Communications Technology and Electronics*, vol. 52, no. 9, pp. 986–990, 2007. Also published (in Russian): Metamaterialy s ekstremal'nymi material'nymi parametrami, *Radiotekhnika i elektronika*, vol. 52, no. 9, pp. 1066–1071, 2007.

[2] M. G. Silveirinha, A. Alù, B. Edwards, and N. Engheta, "Overview of theory and applications of Epsilon-Near-Zero materials," in *Proceedings of URSI XXIX General Assembly*, International Union of Radio Science, Chicago, USA, August 2008. Paper *B01p6*.

[3] G. Pelosi and P. Ufimtsev, "The impedance-boundary condition," *Antennas and Propagation Magazine, IEEE*, vol. 38, pp. 31–35, Feb 1996.

[4] I. V. Lindell and A. H. Sihvola, "Perfect electromagnetic conductor," *Journal of Electromagnetic Waves and Applications*, vol. 19, no. 7, pp. 861–869, 2005.

[5] A. Sihvola and I. V. Lindell, "Perfect electromagnetic conductor medium," *Annalen der Physik (Berlin)*, vol. 17, no. 9-10, pp. 787–802, 2008.

[6] P.-S. Kildal, "Definition of artificially soft and hard surfaces for electromagnetic waves," *Electronics Letters*, vol. 24, pp. 168–170, Feb 1988.

[7] V. Rumsey, "Some new forms of Huygens' principle," *Antennas and Propagation, IRE Transactions on*, vol. 7, pp. 103–116, December 1959.

[8] I. V. Lindell and A. H. Sihvola, "Electromagnetic boundary and its realization with anisotropic metamaterial," *Physical Review E (Statistical, Nonlinear, and Soft Matter Physics)*, vol. 79, no. 2, p. 026604, 2009.

[9] I. V. Lindell and A. H. Sihvola, "Electromagnetic boundary conditions defined in terms of normal field components," *Antennas and Propagation, IEEE Transactions on*, vol. 58, pp. 1128–1135, april 2010.

[10] I. V. Lindell, H. Wallén, and A. Sihvola, "General electromagnetic boundary conditions involving normal field components," *Antennas and Wireless Propagation Letters, IEEE*, vol. 8, pp. 877 –880, 2009.

[11] J. G. V. Bladel, *Electromagnetic Fields*. Hoboken, New Jersey: Wiley-Interscience, sec-

ond ed., 2007.

[12] D. S. Jones, *The theory of electromagnetism*. Oxford: Pergamon Press, 1964.

[13] A. Sihvola, P. Ylä-Oijala, and I. V. Lindell, "Scattering from a PEMC (perfect electromagnetic conductor) spheres using surface integral equation approach," *Applied Computational Electromagnetics Society Journal*, vol. 22, pp. 236–249, July 2007.

[14] G. Mie, "Beiträge zur Optik trüber Medien, speziell kolloidaler Metallösungen," *Annalen der Physik*, vol. 25, pp. 377–445, 1908.

[15] C. F. Bohren and D. R. Huffman, *Absorption and Scattering of Light by Small Particles*. New York: Wiley, 1983.

[16] S. Rao, D. Wilton, and A. Glisson, "Electromagnetic scattering by surfaces of arbitrary shape," *Antennas and Propagation, IEEE Transactions on*, vol. 30, pp. 409–418, May 1982.

[17] V. Jandhyala and S. Chakraborty, "Surface-based integral equation formulations for multiple material and conducting objects," *Applied Computational Electromagnetics Society Newsletter*, vol. 20, pp. 25–47, November 2005.

[18] K. Umashankar, A. Taflove, and S. Rao, "Electromagnetic scattering by arbitrary shaped three-dimensional homogeneous lossy dielectric objects," *Antennas and Propagation, IEEE Transactions on*, vol. 34, pp. 758–766, June 1986.

[19] H. C. van de Hulst, *Light scattering by small particles*. New York: Dover, 1981.

[20] S. A. Maier, *Plasmonics: Fundamentals and applications*. New York: Springer, 2007.

[21] I. V. Lindell and A. H. Sihvola, "Uniaxial IB-medium interface and novel boundary conditions," *Antennas and Propagation, IEEE Transactions on*, vol. 57, pp. 694–700, March 2009.

[22] F. W. Hehl and Y. N. Obukhov, *Foundations of Classical Electrodynamics*. Boston: Birkhäuser, 2003.

Ari Sihvola was born on October 6th, 1957, in Valkeala, Finland. He received the degrees of Diploma Engineer in 1981, Licentiate of Technology in 1984, and Doctor of Technology in 1987, all in Electrical Engineering, from the Helsinki University of Technology (TKK), Finland. Besides working for TKK and the Academy of Finland, he was visiting engineer in the Research Laboratory of Electronics of the Massachusetts Institute of Technology, Cambridge, in 1985–1986, and in 1990–1991, he worked as a visiting scientist at the Pennsylvania State University, State College. In 1996, he was visiting scientist at the Lund University, Sweden, and for the academic year 2000–01 he was visiting professor at the Electromagnetics and Acoustics Laboratory of the Swiss Federal Institute of Technology, Lausanne. In the Summer of 2008, he was visiting professor at the University of Paris XI, France. Ari Sihvola is professor of electromagnetics in Aalto University School of Science and Technology (before 2010, Helsinki University of Technology) with interest in electromagnetic theory, complex media, materials modelling, remote sensing, and radar applications. He is Chairman of the Finnish National Committee of URSI (International Union of Radio Science) and Fellow of IEEE. He also served as the Secretary of the 22nd European Microwave Conference, held in August 1992, in Espoo, Finland. He was awarded the five-year Finnish Academy Professor position starting August 2005.

Ismo Lindell was born in 1939 in Viipuri, Finland. He received his degrees of Electrical Engineer (1963), Licentiate of Technology (1967), and Doctor of Technology (1971), at the Helsinki University of Technology (HUT), Espoo, Finland. In 1962, Dr. Lindell joined the Electrical Engineering Department of HUT, since 1975 as Associate Professor of Radio Engineering and, since 1989, as Professor of Electromagnetic Theory at the Electromagnetics Laboratory which he founded in 1984. During a sabbattical leave in 1996-2001, he held the position of Professor of the Academy of Finland. Currently, he is Professor Emeritus at the Department of Radio Science and Engineering within the Faculty of Electronics, Telecommunications and Automation of the School of Science and Technology in Aalto University. Dr. Lindell enjoyed the Fulbright scholarship as a visiting scientist at the University of Illinois, Champaign-Urbana in 1972-1973 and the Senior Scientist scholarship of Academy of Finland at the M.I.T., Cambridge, in 1986-1987. Dr Lindell has authored and coauthored 265 scientific papers and 12 books, for example, *Methods for Electromagnetic Field Analysis* (IEEE Press, New York 3rd printing 2002), *Electromagnetic Waves in Chiral and Bi-Isotropic Media* (Artech House, Norwood MA, 1994), *Differential Forms in Electromagnetics* (Wiley and IEEE Press, New York 2004), and *Long History of Electricity* (Gaudeamus, Helsinki, Finland 2009, in Finnish). Dr. Lindell has received the IEEE S.A. Schelkunoff award (1987), the IEE Maxwell Premium (1997 and 1998) and the URSI van der Pol gold medal in 2005 as well as the State Award for Public Information (2010).

Henrik Wallén was born in 1975 in Helsinki, Finland. He received the M.Sc. (Tech.) and D.Sc. (Tech.) degrees in Electrical Engineering in 2000 and 2006 from the Helsinki University of Technology (which is now part of the Aalto University).

He is currently working as a Postdoctoral Researcher at the Aalto University School of Science and Technology, Department of Radio Science and Engineering in Espoo, Finland. He is Secretary of the Finnish National Committee of URSI (International Union of Radio Science). His research interests include electromagnetic theory, modeling of complex materials, and computational electromagnetics.

Pasi Ylä-Oijala received the M.Sc. and Ph.D. degrees in applied mathematics from the University of Helsinki, Helsinki, Finland, in 1992 and 1999, respectively. Currently, he is a Finnish Academy Research Fellow with the Aalto University, School of Science and Technology, Department of Radio Science and Engineering, Finland. His field of interest includes integral equation and fast methods in computational electromagnetics.

Domain Decomposition Methods Combining Surface Equivalence Principle and Macro Basis Functions

Pasi Ylä-Oijala[1], Vito Lancellotti[2], Bastiaan P. de Hon[2], and Seppo Järvenpää[1]

[1]Aalto University, Department of Radio Science and Engineering
P.O. Box 13000, FI-00076 AALTO, Finland, pasi.yla-oijala@tkk.fi

[2]Department of Electrical Engineering, Eindhoven University of Technology
P.O. Box 513, 5600 MB Eindhoven, The Netherlands, V.Lancellotti@tue.nl

Abstract – The basics of two domain decomposition methods based on the surface equivalence principle and the method of moments, namely, the surface tangential equivalence principle (TEPA) and the linear embedding via Green's operators (LEGO), are outlined to solve electromagnetic scattering problems. In order to efficiently solve large problems, the methods are combined with the characteristic basis function method and the eigencurrent expansion method. Numerical examples demonstrate that the developed hybrid techniques lead to a significant reduction on the number of degrees of freedom and the size of the matrix equation to be solved.

Index Terms – Domain decomposition methods, electromagnetic scattering, method of moments, multiscale problems, surface integral equations.

I. INTRODUCTION

Electromagnetic (EM) scattering by large and complex structures, such as EM band gaps, frequency selective surfaces, metamaterials, antenna arrays, etc. have received a lot of interest lately. In the conventional integral equation and finite element approaches, the structure is first divided into simple elements and then the unknown quantities, currents or fields, are expanded with basis functions defined on these elements. As the size of the structure gets large, the number of elements required to sufficiently model the unknown and the structure details increases, eventually leading to the problem of solving huge, possibly very ill-conditioned, linear systems. This may be a very challenging task even with the most powerful computers and efficient fast algorithms.

Domain decomposition methods (DDM) have been successfully used to solve many complex multi-scale EM problems, in particular, in the context of the finite element method, see e.g. [1] and [2]. The basic idea in a DDM is to divide a large and complex problem into smaller and simpler subproblems that can be solved independently. This essentially isolates the solution of one region from another and in many cases significantly improves the matrix conditioning. The other benefits of DDMs include, for example, the inherent aptitude for parallelization and for usage in combination with hybrid methods.

In this paper, we discuss two DDM approaches based on the surface equivalence (Huygens) principle and the method of moments (MoM) to solve large and complex EM problems. The algorithms are the surface tangential equivalence principle algorithm (TEPA) [3] and the linear embedding via Green's operators (LEGO) [4]. TEPA is a modification of the equivalence principle algorithm [5–7] and LEGO is the full 3-D extension of the procedure presented in [8].

In many cases, these algorithms can lead to savings on the number of unknowns and improvements on the condition number of the matrix compared to the traditional MoM formulations. However, the methods still produce dense matrix equations and the computational cost increases with the same rate as in the conventional formulations. Hence, the methods can become too expensive for large scale problems. In order to further reduce the number of unknowns and the solution time, TEPA and LEGO are combined with the characteristic basis function method (CBFM) [9–13] and the eigencurrent expansion method (EEM) [4], respectively.

II. INTEGRAL EQUATIONS

Let us consider time-harmonic electromagnetic (EM) scattering by a large number of arbitrarily shaped objects D_p, $p = 1, \ldots, P$, in a homogeneous background D_0. The objects can be either perfect electric conductors (PEC) or homogeneous dielectric, as well as their combinations. For simplicity, assume that the objects are disjoint.

Let S_p denote the surface of D_p. The scattered EM fields $\boldsymbol{E}_p^s$ and $\boldsymbol{H}_p^s$ due to D_p can be expressed at point $\boldsymbol{r}$ in D_0 as

$$\begin{bmatrix} \boldsymbol{E}_{0p}^s \\ \boldsymbol{H}_{0p}^s \end{bmatrix} = \begin{bmatrix} \eta_0 \, \boldsymbol{\mathcal{L}}_{0p}^{(0)} & -\boldsymbol{\mathcal{K}}_{0p}^{(0)} \\ \boldsymbol{\mathcal{K}}_{0p}^{(0)} & \dfrac{1}{\eta_0} \boldsymbol{\mathcal{L}}_{0p}^{(0)} \end{bmatrix} \begin{bmatrix} \boldsymbol{J}_p \\ \boldsymbol{M}_p \end{bmatrix}. \quad (1)$$

Here $\eta_0 = \sqrt{\mu_0/\varepsilon_0}$ is the wave impedance of D_0, $\boldsymbol{J}_p = \boldsymbol{n}_p \times \boldsymbol{H}_p$ and $\boldsymbol{M}_p = -\boldsymbol{n}_p \times \boldsymbol{E}_p$ are the equivalent electric and magnetic current densities on S_p with the unit normal vector $\boldsymbol{n}_p$ pointing into D_0. The surface integral operators $\boldsymbol{\mathcal{L}}_{qp}^{(d)}$ and $\boldsymbol{\mathcal{K}}_{qp}^{(d)}$ are defined as

$$\begin{aligned} \boldsymbol{\mathcal{L}}_{qp}^{(d)}(\boldsymbol{F})(\boldsymbol{r}) &= \frac{-1}{ik_q} \nabla \int_{S_p} G_d(\boldsymbol{r}, \boldsymbol{r}') \, \nabla_s' \cdot \boldsymbol{F}(\boldsymbol{r}') \, dS' \\ &\quad + ik_q \int_{S_p} G_d(\boldsymbol{r}, \boldsymbol{r}') \, \boldsymbol{F}(\boldsymbol{r}') \, dS' \\ &\quad + \frac{\delta_{S_p} \boldsymbol{n}(\boldsymbol{r})}{2ik_q} \nabla_s \cdot \boldsymbol{F}(\boldsymbol{r}), \quad (2) \\ \boldsymbol{\mathcal{K}}_{qp}^{(d)}(\boldsymbol{F})(\boldsymbol{r}) &= \nabla \times \int_{S_p} G_d(\boldsymbol{r}, \boldsymbol{r}') \, \boldsymbol{F}(\boldsymbol{r}') \, dS' \\ &\quad - \frac{\delta_{S_p}}{2} \boldsymbol{n}(\boldsymbol{r}) \times \boldsymbol{F}(\boldsymbol{r}), \quad (3) \end{aligned}$$

where $k_q = \omega\sqrt{\varepsilon_q \mu_q}$ is the wavenumber of D_q, $\boldsymbol{r}' \in S_p, \boldsymbol{r} \in D_q$ and

$$G_d(\boldsymbol{r}, \boldsymbol{r}') = \frac{e^{ik_d|\boldsymbol{r}-\boldsymbol{r}'|}}{4\pi|\boldsymbol{r}-\boldsymbol{r}'|}, \quad (4)$$

is the homogeneous space Green's function of D_d with the wavenumber of D_d. In addition, $\boldsymbol{F}$ is either $\boldsymbol{M}_p$ or $\boldsymbol{J}_p$, and

$$\delta_{S_p} = \begin{cases} 1 & \text{if } \boldsymbol{r} \in S_p, \\ 0 & \text{otherwise.} \end{cases} \quad (5)$$

By expressing the fields separately in each non-PEC domain with (1) and by applying the EM boundary conditions on the interfaces and surfaces gives a set of surface integral equations that can be solved numerically with the MoM. The problem is that if the number of the objects is large and/or the structures are complicated, this traditional surface integral equation formulation leads to a large and ill-conditioned dense matrix equation which is difficult to solve. In the following sections the scattering problem is reformulated using domain decomposition methods.

III. DOMAIN DECOMPOSITION

The basic idea of the formulation applied in this paper is to reformulate the original scattering problem as a new equivalent problem with generalized scattering and translation operators. First, the objects (scatterers) are divided into groups. The groups may consist of one or more objects and are enclosed by virtual equivalence surfaces R_l, $l = 1, \ldots, L$. The domains enclosed by surfaces R_l are called bricks. Next, we define the scattering and translation operators of the bricks. The grouping, bricks, and the scattering and translation operators are illustrated in Figure 1.

A. Scattering operators

Let us first consider the EM problem consisting of a single brick only. The brick embeds a structure which, being illuminated by an incident field $\boldsymbol{F}^{\mathrm{i}} = [\boldsymbol{E}^{\mathrm{i}}, \boldsymbol{H}^{\mathrm{i}}]^T$, develops induced (secondary) sources that radiate the scattered field $\boldsymbol{F}^{\mathrm{s}} = [\boldsymbol{E}^{\mathrm{s}}, \boldsymbol{H}^{\mathrm{s}}]^T$. That scattered field remains the same if we replace the actual sources on the structure inside the brick with equivalent (secondary) sources $\boldsymbol{J}_l^s$ and $\boldsymbol{M}_l^s$ on the surface of the brick. Formally, this can be expressed via a generalized scattering operator $\boldsymbol{\mathcal{S}}_{ll}$ of the brick l as a mapping from the incident currents $\boldsymbol{U}_l^i$ onto the secondary currents $\boldsymbol{U}_l^s$

$$\boldsymbol{U}_l^s = \boldsymbol{\mathcal{S}}_{ll} \, \boldsymbol{U}_l^i, \qquad \boldsymbol{U}_l^{s/i} = \left[\boldsymbol{J}_l^{s/i}, \boldsymbol{M}_l^{s/i}\right]^T. \quad (6)$$

The scattering operator is defined via the use of the surface equivalence principle (1) as a product of four surface integral operators, as follows

$$\boldsymbol{\mathcal{S}}_{ll} = \left(\boldsymbol{\mathcal{P}}_{ll}^{(0)}\right)^{-1} \boldsymbol{\mathcal{P}}_{lp}^{(0)} \left(\boldsymbol{\mathcal{P}}_{pp}\right)^{-1} \boldsymbol{\mathcal{P}}_{pl}^{(0)}, \quad (7)$$

where the operators $(\boldsymbol{\mathcal{P}}_{ll}^{(0)})^{-1}$, $\boldsymbol{\mathcal{P}}_{lp}^{(0)}$, $\boldsymbol{\mathcal{P}}_{pl}^{(0)}$ and $\boldsymbol{\mathcal{P}}_{pp}^{-1}$ are called the self-propagator, inside-out propagator, and outside-in propagator and the current solver, respectively. Here, the first lower index indicates

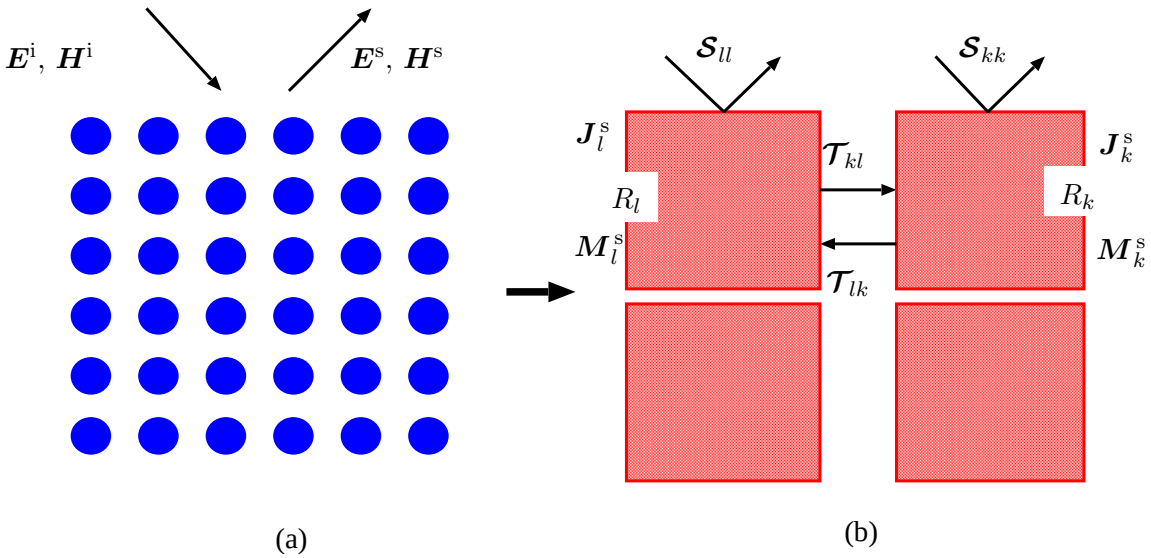

Fig. 1. Reformulation of a scattering problem. Left: original scattering problem. Right: reformulated problem with the scattering and translation operators and new unknowns.

the surface of the observation point, the second one indicates the surface of the source point, and the upper index indicates the domain whose Green's function is used in (1). The actual form of the operators depends on both the nature of the object and the adopted formulation [3, 4]. For example, in the case of homogeneous penetrable objects modeled with the PMCHWT (Poggio-Miller-Chang-Harrington-Wu-Tsai) formulation the propagators have the following expressions

$$\boldsymbol{\mathcal{P}}_{ij}^{(d)} = \begin{bmatrix} \eta^{(d)}\boldsymbol{\mathcal{L}}_{ij}^{(d)} & -\boldsymbol{\mathcal{K}}_{ij}^{(d)} \\ \boldsymbol{\mathcal{K}}_{ij}^{(d)} & \dfrac{1}{\eta^{(d)}}\boldsymbol{\mathcal{L}}_{ij}^{(d)} \end{bmatrix}_{\tan}, \tag{8}$$

where $i, j = l, k,$ or p and tan denotes the tangential component. Also the current solver, $\boldsymbol{\mathcal{P}}_{pp}$, can be expressed with the same propagation operators as

$$\boldsymbol{\mathcal{P}}_{pp} = \boldsymbol{\mathcal{P}}_{pp}^{(0)} + \boldsymbol{\mathcal{P}}_{pp}^{(p)}, \tag{9}$$

where 0 stands for the background and p for the object. For the PEC objects modeled with the EFIE (electric field integral equation), the inside-out and outside-in propagators have to be modified as

$$\boldsymbol{\mathcal{P}}_{lp}^{(0)} = \begin{bmatrix} \eta_0\boldsymbol{\mathcal{L}}_{lp}^{(0)} & \boldsymbol{\mathcal{K}}_{lp}^{(0)} \end{bmatrix}_{\tan}^{T}, \tag{10}$$

$$\boldsymbol{\mathcal{P}}_{pl}^{(0)} = \begin{bmatrix} \eta_0\boldsymbol{\mathcal{L}}_{pl}^{(0)} & -\boldsymbol{\mathcal{K}}_{pl}^{(0)} \end{bmatrix}_{\tan}, \tag{11}$$

and $\boldsymbol{\mathcal{P}}_{pp} = \eta_0(\boldsymbol{\mathcal{L}}_{pp}^{(0)})_{\tan}$ is the EFIE operator on S_p.

B. Translation operators

Let us next consider the EM problem consisting of two separate bricks l and k with surfaces R_l and R_k. The direct scattering from the bricks is described with the scattering operators $\boldsymbol{\mathcal{S}}_{ll}$ and $\boldsymbol{\mathcal{S}}_{kk}$ as in (6). The scattering operators, however, do not model the interactions (multiple scattering) between the bricks. The multiple scattering between the bricks are particularly important if the bricks are close to each other.

The field scattered by brick k, i.e., the field due to secondary current $\boldsymbol{U}_k^s = \boldsymbol{\mathcal{S}}_{kk}\boldsymbol{U}_k^i$, produces new fields to R_l. These fields can be interpreted as incident currents on R_l and can be expressed via a translation operator $\boldsymbol{\mathcal{T}}_{lk}$, $l \neq k$, as

$$\boldsymbol{U}_{lk}^i = \boldsymbol{\mathcal{T}}_{lk}\boldsymbol{\mathcal{S}}_{kk}\boldsymbol{U}_k^i. \tag{12}$$

The translation operator can be defined using the same self and outside-in propagators as the scattering operator

$$\boldsymbol{\mathcal{T}}_{lk} = \left(\boldsymbol{\mathcal{P}}_{ll}^{(0)}\right)^{-1}\boldsymbol{\mathcal{P}}_{lk}^{(0)}, \tag{13}$$

Note that the form of the translation operators do not depend on the nature of the scatterers nor the applied integral equation formulation. The secondary current on R_l is now given by

$$\begin{aligned} \boldsymbol{U}_l^s &= \boldsymbol{\mathcal{S}}_{ll}\boldsymbol{U}_l^i + \boldsymbol{\mathcal{S}}_{ll}\boldsymbol{\mathcal{T}}_{lk}\boldsymbol{\mathcal{S}}_{kk}\boldsymbol{U}_k^i \\ &= \boldsymbol{\mathcal{S}}_{ll}\left(\boldsymbol{U}_l^i + \boldsymbol{\mathcal{T}}_{lk}\boldsymbol{U}_k^s\right). \end{aligned} \tag{14}$$

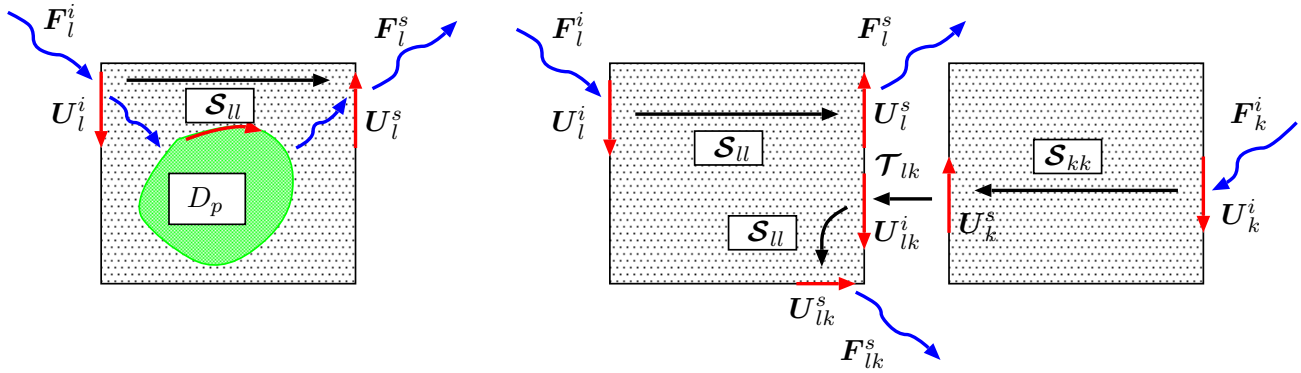

Fig. 2. Scattering and translation operators seen by the brick l: (a) single brick, (b) two bricks.

The procedure can be generalized for L bricks as

$$\boldsymbol{U}_l^s = \boldsymbol{\mathcal{S}}_{ll}\left(\boldsymbol{U}_l^i + \sum_{k=1,k\neq l}^{L} \boldsymbol{\mathcal{T}}_{lk}\,\boldsymbol{U}_k^s\right), \qquad (15)$$

$l = 1, \ldots, L$. This can be expressed by a matrix

$$\begin{bmatrix} \boldsymbol{\mathcal{I}} & -\boldsymbol{\mathcal{S}}_{11}\boldsymbol{\mathcal{T}}_{12} & \ldots & -\boldsymbol{\mathcal{S}}_{11}\boldsymbol{\mathcal{T}}_{1L} \\ -\boldsymbol{\mathcal{S}}_{22}\boldsymbol{\mathcal{T}}_{21} & \boldsymbol{\mathcal{I}} & \ldots & -\boldsymbol{\mathcal{S}}_{22}\boldsymbol{\mathcal{T}}_{2L} \\ \vdots & & \ddots & \vdots \\ -\boldsymbol{\mathcal{S}}_{LL}\boldsymbol{\mathcal{T}}_{L1} & \ldots & & \boldsymbol{\mathcal{I}} \end{bmatrix} \begin{bmatrix} \boldsymbol{U}_1^s \\ \boldsymbol{U}_2^s \\ \vdots \\ \boldsymbol{U}_L^s \end{bmatrix} = \begin{bmatrix} \boldsymbol{\mathcal{S}}_{11}\boldsymbol{U}_1^i \\ \boldsymbol{\mathcal{S}}_{22}\boldsymbol{U}_2^i \\ \vdots \\ \boldsymbol{\mathcal{S}}_{LL}\boldsymbol{U}_L^i \end{bmatrix}, \qquad (16)$$

where $\boldsymbol{\mathcal{I}}$ is the identity operator. Next, we reformulate matrix (16) by solving equations (15) with respect to $\boldsymbol{U}_l^i$

$$\boldsymbol{U}_l^i = \boldsymbol{\mathcal{S}}_{ll}^{-1}\,\boldsymbol{U}_l^s - \sum_{k=1,k\neq l}^{L} \boldsymbol{\mathcal{T}}_{lk}\,\boldsymbol{U}_k^s, \qquad (17)$$

giving

$$\begin{bmatrix} \boldsymbol{\mathcal{S}}_{11}^{-1} & -\boldsymbol{\mathcal{T}}_{12} & \ldots & -\boldsymbol{\mathcal{T}}_{1L} \\ -\boldsymbol{\mathcal{T}}_{21} & \boldsymbol{\mathcal{S}}_{22}^{-1} & \ldots & -\boldsymbol{\mathcal{T}}_{2L} \\ \vdots & & \ddots & \vdots \\ -\boldsymbol{\mathcal{T}}_{L1} & \ldots & & \boldsymbol{\mathcal{S}}_{LL}^{-1} \end{bmatrix} \begin{bmatrix} \boldsymbol{U}_1^s \\ \boldsymbol{U}_2^s \\ \vdots \\ \boldsymbol{U}_L^s \end{bmatrix} = \begin{bmatrix} \boldsymbol{U}_1^i \\ \boldsymbol{U}_2^i \\ \vdots \\ \boldsymbol{U}_L^i \end{bmatrix}. \qquad (18)$$

The matrix on the left hand side of (18) can be interpreted as a total inverse scattering operator [4].

The benefit of (18) over (16) is that only the diagonal entries, $\boldsymbol{\mathcal{S}}_{ll}^{-1}$, convey information about the objects comprising the structure. In contrast, the off-diagonal entries, $-\boldsymbol{\mathcal{T}}_{lk}$, which tell how the bricks interact, do not depend on the bricks content, but solely on their relative position in the structure. This means that if, we allow for a change either in the EM properties or in the shape of the objects within each brick, only the diagonal terms $\boldsymbol{\mathcal{S}}_{ll}^{-1}$ have to be re-computed.

The tangential equivalence principle algorithm (TEPA) [3] is based on (16) and the linear embedding with Green's operators (LEGO) [4] uses (18). For more details we refer to [3] and [4].

IV. NUMERICAL DISCRETIZATION

In the previous section, the original scattering problem was reformulated as a new problem by utilizing the generalized scattering and translation operators and the unknowns are the secondary equivalent surface current densities on the surfaces of the bricks. The next step is to convert the operator equations into discretized matrix equations. We will apply standard MoM with Galerkin's method and Rao-Wilton-Glisson (RWG) functions defined on planar triangular elements.

First, the unknown secondary currents on the surfaces of the bricks are expanded with the RWG functions $\boldsymbol{f}_l$ as

$$\boldsymbol{J}_l^s \approx \sum_{n=1}^{N^l} \alpha_n^{(l)}\,\boldsymbol{f}_l, \quad \text{and} \quad \boldsymbol{M}_l^s \approx \sum_{n=1}^{N^l} \beta_n^{(l)}\,\boldsymbol{f}_l. \qquad (19)$$

Then these approximations are substituted into the equations, i.e., either to (16) or to (18). Next, we discretize the scattering and translation operators, $\boldsymbol{\mathcal{S}}_{ll}$ and $\boldsymbol{\mathcal{T}}_{lk}$. Since these operators are defined by the standard surface integral operators $\boldsymbol{\mathcal{L}}$ and $\boldsymbol{\mathcal{K}}$, they are discretized similarly as the traditional surface integral formulations. As a result, we may write (6) and (13) as

$$[S_{ll}] = [P_{ll}^{(0)}]^{-1}\,[P_{lp}^{(0)}]\,[P_{pp}]^{-1}\,[P_{pl}^{(0)}], \tag{20}$$

and

$$[T_{lk}] = [P_{ll}^{(0)}]^{-1}\,[P_{lk}^{(0)}], \quad k \neq l, \tag{21}$$

where the matrices on the right hand sides denote the matrices due to the propagators and the current solver.

The right hand side of equation (16) is considered as follows. Let b_l^E and b_l^H denote the usual excitation vectors due to the incident electric and magnetic fields on R_l tested with the RWG functions. Then, the incident currents on R_l are replaced with

$$[U_l^i] = [P_{ll}^{(0)}]^{-1}\,[b_l^E, b_l^H]^T. \tag{22}$$

Once all operators are discretized and the continuous operator equations are converted into a matrix equation, the matrix equation can be solved either with a direct or an iterative method. This gives us the coefficients of the secondary currents on the surfaces of the bricks. Thereafter, the scattered fields can be calculated outside the bricks using the surface integral representations (1).

V. MACRO BASIS FUNCTIONS

In many cases, the procedure introduced above can lead to savings on the number of unknowns and improvements on the condition number of the matrix compared to the traditional MoM formulations. However, the method still produces dense matrix equation and the computational cost increases with the same rate as in the conventional MoM formulation. To efficiently solve large scale problems, next we discuss two macro basis function methods, to further reduce the number of degrees of freedom (DoF).

A. Characteristic basis functions

Consider first, the characteristic basis function method (CBFM) [9–13]. CBFM is a generic technique to reduce the size of the discretized matrix equation. In CBFM, the object (or objects) are divided into groups (blocks). The matrix equation for L groups can be expressed as

$$\begin{bmatrix} \boldsymbol{A}_{11} & \dots & \boldsymbol{A}_{1L} \\ \vdots & \ddots & \vdots \\ \boldsymbol{A}_{L1} & \dots & \boldsymbol{A}_{LL} \end{bmatrix} \begin{bmatrix} \boldsymbol{U}_1 \\ \vdots \\ \boldsymbol{U}_L \end{bmatrix} = \begin{bmatrix} \boldsymbol{b}_1 \\ \vdots \\ \boldsymbol{b}_L \end{bmatrix}, \tag{23}$$

where $\boldsymbol{A}_{lk}$ denotes a matrix block due to the interaction of the lth and kth group, $\boldsymbol{U}_l$ are the unknowns of the lth group and $\boldsymbol{b}_l$ is the excitation vector due to the lth group. Assume next that the bricks and the CBFM groups coincide.

The CBFs of the groups can be determined with alternative ways. In [9], so called primary and secondary CBFs of the blocks, $\boldsymbol{f}_l^{(l)}$ and $\boldsymbol{f}_k^{(l)}$, are defined as follows

$$\boldsymbol{f}_l^{(l)} = \boldsymbol{A}_{ll}^{(-1)}\,\boldsymbol{b}_l, \tag{24}$$

$$\boldsymbol{f}_k^{(l)} = \boldsymbol{A}_{ll}^{(-1)}\left(-\boldsymbol{A}_{lk}\,\boldsymbol{f}_k^{(k)}\right), \quad l \neq k, \tag{25}$$

for all $l, k = 1, \dots, L$. By applying this to (16) gives

$$\boldsymbol{f}_l^{(l)} = \boldsymbol{\mathcal{S}}_{ll}\,\boldsymbol{U}_l^{\mathrm{inc}}, \tag{26}$$

$$\boldsymbol{f}_k^{(l)} = -\boldsymbol{\mathcal{S}}_{ll}\,\boldsymbol{\mathcal{T}}_{lk}\,\boldsymbol{f}_k^{(k)}, \quad l \neq k. \tag{27}$$

Hence, the CBFs for system (16) can be obtained without need to invert any matrix.

Later in [10], an alternative method to find the CBFs was presented. In this approach each group is illuminated with a sufficiently large number of planewaves incident from different angles. The most significant planewave based CBFs

$$\boldsymbol{f}_k^{(l)},\ l = 1, \dots, L,\ k = 1, \dots, \tilde{N}^{PW}, \tag{28}$$

are found via the use of SVD [10] and used as CBFs of the groups, i.e., the bricks.

In both approaches, the unknowns of each brick are expanded with these new basis functions, CBFs, as

$$\boldsymbol{U}_l^s = \sum_k \alpha_k^{(l)}\,\boldsymbol{f}_k^{(l)}, \quad \text{for all } l = 1, \dots, L. \tag{29}$$

Once the coefficients of the CBFs are found, the coefficients of the original subdomain basis functions can be obtained from (29). These methods are denoted by TEPA-CBFM and TEPA-CBFM-pw, respectively, since they are based on the TEPA formulation of [3] and equation (16).

Table 1: Geometrical data and the numbers triangles and edges for a single dipole and brick: the second column gives the data for the first example (single cross dipole), and the last two for the second one (double cross dipole)

	Single dipole	Double dipole (first case)	Double dipole (second case)
Dipole arm width	2 mm	2 mm	2 mm
Dipole arm length	12 mm	12 mm	12 mm
Vertical distance between dipoles	–	2 mm	2mm
Triangles on dipole	88	420	420
Edges on dipole	108	552	552
Brick shorter edge	5 mm	4 mm	4 mm
Brick longer edge	16 mm	16 mm	20 mm
Distance between brick centers	32 mm	22.5 mm	22.5 mm
Triangles on brick	256	256	360
Edges on brick	384	384	540

B. Eigencurrent expansions

Next, we consider another technique to find the macro basis functions of the bricks. The method is called the eigencurrent expansion method (EEM) and used with the LEGO in [4]. The EEM uses the eigenfunctions of $\boldsymbol{\mathcal{S}}_{ll}$, called eigencurrents, to expand the unknowns on the surfaces of the bricks. The resulting method is denoted by LEGO-EEM.

We form a basis out of the eigenvectors of $[S_{ll}]$ and we practically implement the EEM as a basis change from the set of RWG functions [4]. We separate the eigencurrents into two groups: coupled and uncoupled. The coupled eigencurrents, associated with the larger, lower-order eigenvalues of $[S_{ll}]$, substantially depart from the true eigencurrents of $[S]$, the total scattering matrix, and contribute to the multiple scattering occurring among the bricks. By contrast, the uncoupled eigencurrents, associated with the smaller, higher-order eigenvalues of $[S_{ll}]$, represent better and better approximations to the true eigencurrents of $[S]$, and do not interact with one another.

These observations enabled us to reduce the system matrix $[S]^{-1}$ (in the basis of the eigencurrents) to block-diagonal form with just two blocks. In particular, the block arising from the interaction of the coupled eigencurrents is usually far smaller than the whole system matrix, so it can be easily stored and inverted with direct methods. The other block, possibly huge, is just diagonal, hence it can effortlessly be stored and (formally) inverted. The order reduction we have just described is actually a consequence of two concurring, though independent, facts: i) the eigenvalues of $[S_{ll}]$ decrease; ii) the entries of $[T_{lk}]$ become smaller and smaller when the distance between bricks l and k increases [14].

VI. NUMERICAL RESULTS

Next, the developed methods are verified with numerical examples and their properties are investigated.

As a first numerical example, we consider the scattering by a 5×5 array of thin PEC cross dipoles arranged in a regular lattice parallel to the xy plane. The dipoles are embedded into rectangular bricks, so that each brick contains only a single dipole. Figure 3 (a) shows the dipoles and Figure 3 (b) shows the bricks. Incident wave is a linearly polarized planewave propagating toward the negative z direction. The derivation of the methods does not set any requirements for the incident fields and, e.g., oblique incidence can be considered without any modifications to the algorithms. The detailed geometrical data is given in the second column of Table 1.

The scattering problem is formulated using the methods described in the previous sections and with the EFIE. The bricks are divided to $4 \times 4 \times 2$ small rectangles and each rectangle is divided into four triangles. The numbers of triangles and (interior) edges on the dipoles and brick's surface are shown in the second column of Table 1. The results are verified by solving the same problem with the conventional MoM using EFIE and 2700 RWGs. Figure 4 shows the monostatic RCS as a function of frequency. In the TEPA-CBFM, we consider the primary CBFs of the

bricks and all secondary ones, hence, the total number of CBFs for all frequencies is $25^2 = 625$. In the TEPA-CBFM-pw method, the planewave based CBFs are found by first using 360 initial planewave excitations from different directions. Then, SVD with the tolerance 10^{-3} is used to determine the most important directions that are used to generate the CBFs of the bricks. The total DoF in CBF-pw depends on the frequency and varies from 275 at 7 GHz (11 CBFs for each brick) to 425 at 17 GHz (17 CBFs for each brick).

In LEGO-EEM, the tolerance for defining the last coupled eigenvalue is set to 10^{-5}. Accordingly (see [14]), the expected accuracy of computed currents (over bricks) is no larger 10^{-2} (as the bricks are not adjacent). With this criterion, the number of coupled eigencurrents is 30 for each brick and the same for all frequencies. The total number of DoF in LEGO-EEM is thus 750.

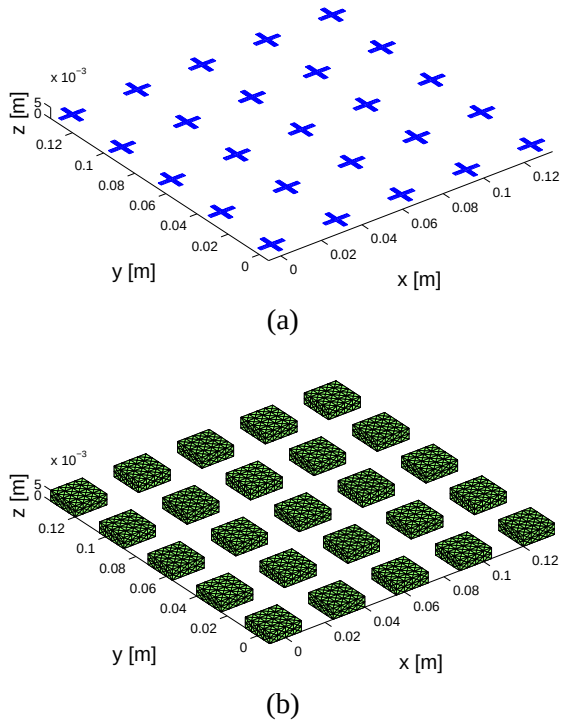

(a)

(b)

Fig. 3. An array of cross dipoles: (a) original structure (dipoles), (b) bricks.

As a second example, a larger problem is considered. We, also, study the effect of changing the size of the bricks. Consider a 5×5 array of double cross dipoles by putting two similar dipoles as used in the first example on the top of each other. The dipoles

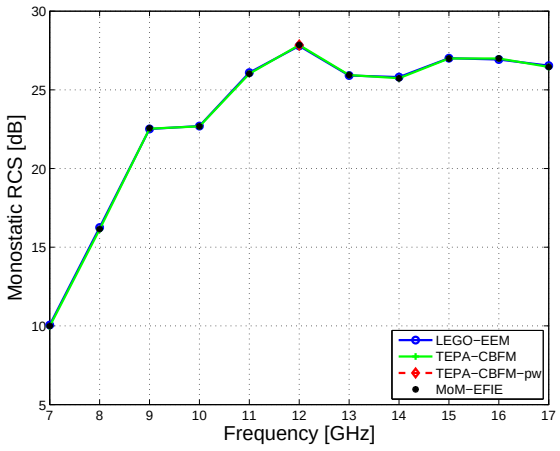

Fig. 4. Monostatic RCS in dB for the geometry of Figure 3 as a function of frequency.

are arranged in a similar regular lattice parallel to the xy plane as in the previous example. Figure 5 shows the geometry and discretization of a single element and Figure 6 shows the full geometry.

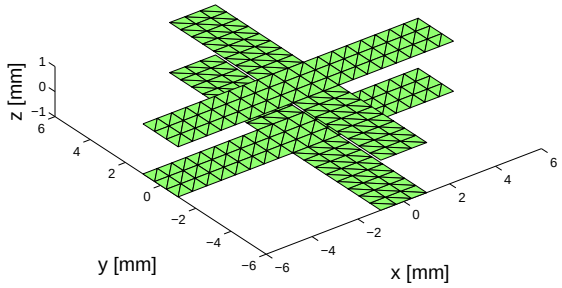

Fig. 5. A double cross dipole.

Figure 7 shows the monostatic RCS as a function of frequency. We have used two different brick sizes. The detailed geometrical data is given in the last two columns of table 1. The bricks are discretized so that first each face of a brick is divided into $4 \times 4 \times 2$ (first case) or $5 \times 5 \times 2$ (second case) planar rectangles and then each rectangle is divided into four triangles. A direct discretization of (16) with MoM (without CBFM and EEM) would lead to 19200 (first case) and 27000 (second case) unknowns, respectively.

Figure 8 shows the required DoF of the TEPA-CBFM-pw method. The CBFs are found using a similar procedure as in the first example. As the frequency or the brick size is increased, the number of required

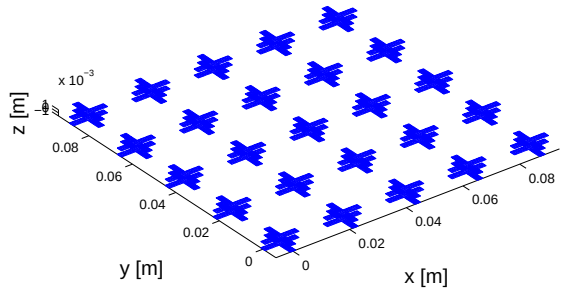

Fig. 6. An array of double cross dipoles.

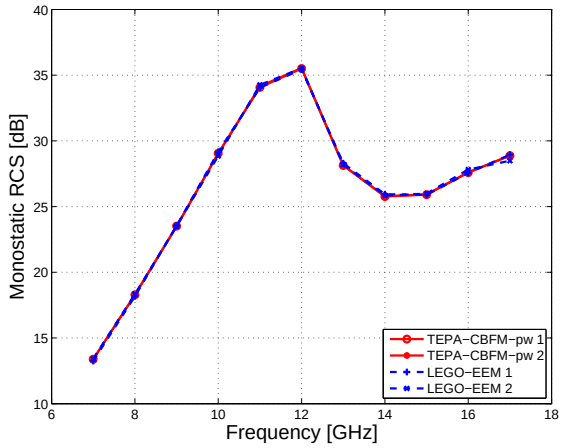

Fig. 7. Monostatic RCS in dB for the geometry of Figure 6 as a function of frequency for two brick sizes. 1 = brick size $16 \times 16 \times 4$mm and 2 = brick size $20 \times 20 \times 4$mm.

planewave based CBFs increases too. This can be explained by the facts that for higher frequencies, the current distribution on the bricks' surfaces become more complicated, and that as the bricks' distance becomes smaller, the coupling between the bricks becomes stronger. In this example, the CBFM based on the primary and secondary basis functions was not applied.

In LEGO-EEM, the DoF were set to $70 \times 25 = 1750$ and $100 \times 25 = 2500$ for the cases 1 and 2, respectively, 70 and 100 being the number of coupled eigencurrents contributed by each brick [4]. The tolerances for the coupled eigencurrents are 10^{-4} for the first case and 10^{-5} for the second one. As the spectrum of $\mathcal{S}_{ll}$ is insensitive to frequency to a large extent [14], the required number of DoF does not change with frequency either. On the other hand, the number of coupled eigencurrents is affected by both a brick's size and the relative distance among the bricks modeling the structure. In case 2, the spectrum of $\mathcal{S}_{ll}$ decays faster than in case 1, because the brick's boundary is set farther away from the crosses. Nonetheless, since in case 2 the bricks are closer than in case 1, a stronger coupling is expected and, accordingly, more coupled eigencurrents are necessary. In the limiting case, when the bricks touch one another – which is the worst case scenario – a criterion has been developed to relate the error on the computed scattered currents (i.e., the near fields) to the number of coupled eigencurrents [14, 15]. Such a criterion can be used to control the error a priori. In situations when the bricks are separated (as discussed here), given that the coupling decreases with increasing bricks' distance, the aforesaid criterion most certainly yields a convenient upper bound to the error.

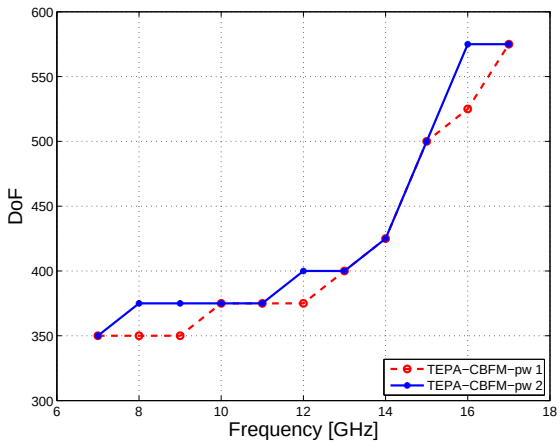

Fig. 8. The number of DoF of the TEPA-CBFM-pw as a function of frequency for two brick sizes.

VII. CONCLUSIONS

In this paper, two algorithms, the tangential equivalence principle algorithm (TEPA) [3] and the linear embedding via Green's operators (LEGO) [4], are reviewed for solving EM scattering problems. A general framework of the methods is presented and the methods are shown to be based on the same principles and operators. The major difference is on the form of the matrix equation to be solved. In addition, two macro basis function methods, the characteristic basis function method (CBFM) and the eigencurrent expansion method (EEM), are applied to reduce the number of unknowns. The developed hybrid methods, TEPA-CBFM and LEGO-EEM, are shown to lead to

dramatic reduction on the size of the matrix equation and hence, allow efficient solutions of large problems with reduced computer resources.

The numerical results show that the planewave based CBFM may be the most efficient method to reduce the number of degrees of freedom. However, the number of the required CBFs depends on the frequency, and the bricks' size and distance. In EEM, on the other hand, the number of degrees of freedom can be controlled a priori.

ACKNOWLEDGMENT

The first author would like to thank the Academy of Finland for financial support, grant number 108801.

REFERENCES

[1] K. Zhao, V. Rawat, and J.-F. Lee, "A domain decomposition method for electromagnetic radiation and scattering analysis of multi-target problems," *IEEE Trans. Antennas Propag.*, vol. 56, no. 8, pp. 2211-2221, Aug. 2008.

[2] J.-M. Jin, Z. Lou, Y. J. Li, N. W. Riley, and D. J. Riley, "Finite element analysis of complex antennas and arrays," *IEEE Trans. Antennas Propag.*, vol. 56, no. 8, pp. 2211-2221, Aug. 2008.

[3] P. Ylä-Oijala and M. Taskinen, "Electromagnetic scattering by large and complex structures with surface equivalence principle algorithm," *Waves in Random and Complex Media*, vol. 19, no. 1, pp. 105-125, Feb. 2009.

[4] V. Lancellotti, B. P. de Hon, and A. G. Tijhuis, "An eigencurrent approach to the analysis of electrically large 3-D structures using linear embedding via Green's operators," *IEEE Trans. Antennas Propag.*, vol. 57, no. 11, Nov. 2009.

[5] M-K. Li and W. C. Chew, "Wave-field interaction with complex structures using equivalence principle algorithm," *IEEE Trans. Antennas Propag.*, vol. 55, no. 1, pp. 130-138, Jan. 2007.

[6] M.-K. Li, W. C. Chew, and L. J. Jiang, "A domain decomposition scheme based on equivalence theorem," *Microw. Optical Techn. Letters*, vol. 48, no. 9, pp. 1853-1857, Sep. 2006.

[7] M-K. Li and W. C. Chew, "Multiscale simulation of complex structures using equivalence principle algorithm with high-order field point sampling scheme," *IEEE Trans. Antennas Propag.*, vol. 56, no. 8, pp. 2389-2397, 2008.

[8] A. M. van de Water, B. P. de Hon, M. C. van Beurden, A. G. Tijhuis, and P. de Maagt, "Linear embedding via Green's operators: A modeling technique for finite electromagnetic band-gap structures," *Phys. Rev. E*, vol. 72, pp. 1-11, 2005.

[9] V. V. S. Prakash and R. Mittra, "Characteristic basis function method: A new technique for efficient solution of method of moments matrix equations," *Microw. Optical Techn. Letters*, vol. 36, no. 2, pp. 95-100, Jan. 2002.

[10] E. Lucente, A. Monorchio and R. Mittra, "An iteration-free MoM approach based on excitation independent characteristic basis functions for solving large multiscale electromagnetic problems," *IEEE Trans. Antennas Propag.*, vol. 56, no. 4, pp. 999-1007, April 2008.

[11] J. Laviada, M. R. Pino, and F. Las-Heras, "Characteristic spherical wave expansion with application to scattering and radiation problems," *IEEE Antennas and Wireless Propagation Letters*, vol.8, pp. 599-602, 2009.

[12] J. Laviada, F. Las-Heras, M. R. Pino, and R. Mittra, "Solution of electrically large problems with multilevel characteristic basis functions," *IEEE Trans. Antennas Propag.*, vol. 57, no. 10, pp. 3189-3198, Oct., 2009.

[13] R. Mittra, "Characteristic basis function method (CBFM) – An iterative-free domain decomposition approach in computationally electromagnetics," *ACES Journal*, vol. 24, no. 2, pp. 204-223, April 2009.

[14] V. Lancellotti, B. P. de Hon, and A. G. Tijhuis, "On the convergence of the eigencurrent expansion method applied to linear embedding via Green's operators (LEGO)," *IEEE Trans. Antennas Propag.*, vol. 58, no. 10, pp. 3231-3238, Oct. 2010.

[15] V. Lancellotti, B. P. de Hon, and A. G. Tijhuis, "A priori error estimate and control in the eigencurrent expansion method applied to linear embedding via Green's operators (LEGO)," *2010 IEEE International Symposium on Antennas and Propagation*, Toronto, Canada, July, 2010.

Validation, Verification and Calibration in Applied Computational Electromagnetics

Gökhan Apaydin [1] and Levent Sevgi [2]

[1] Department of Electrical and Electronics Engineering
Zirve University, Gaziantep, 27260, Turkey
gokhan.apaydin@zirve.edu.tr

[2] Department of Electronics and Communications Engineering
Dogus University, Acibadem, Istanbul, Turkey
lsevgi@dogus.edu.tr

Abstract ─ Model validation, data verification, and code calibration (VV&C) in applied computational electromagnetics is discussed. The step by step VV&C procedure is given systematically through canonical scenarios and examples. Propagation over flat-Earth with linearly decreasing vertical refractivity profile, having an analytical exact solution, is taken into account as the real-life problem. The parabolic wave equation (PWE) is considered as the mathematical model. MatLab-based numerical simulators for both the split step Fourier and finite element implementations of the PWE are developed. The simulators are calibrated against analytical exact and high frequency asymptotic solutions. Problems related to the generation of reference data during accurate numerical computations are presented.

Index Terms ─ Calibration, finite elements method, geometric optics, groundwaves, mode method, narrow angle, parabolic equation method, propagation, split step parabolic equation method, validation, verification, wide angle.

I. INTRODUCTION

Real life engineering and electromagnetic (EM) problems can be handled via measurements or numerical simulations because only a limited number of problems with idealized geometries have mathematical exact solutions. The challenge in solving real-life engineering problems is therefore the reliability of the results. Reliability is achieved after a series of (model) validation, (data) verification, and (code) calibration (VV&C) tests. These issues are discussed in [1] and this paper is the extended version of that presentation.

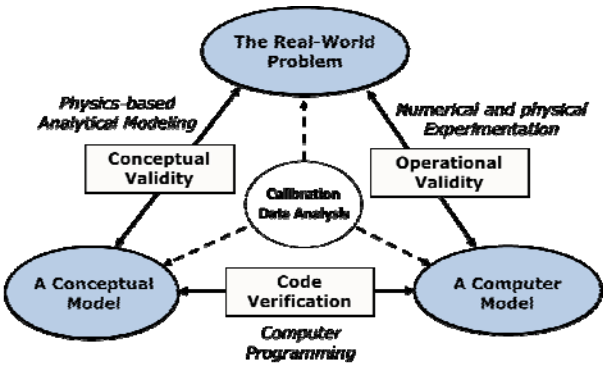

Fig. 1. Fundamental VV&C concepts & procedures.

Three fundamental building blocks of a simulation are the real-world problem entity being simulated, the conceptual model representation of that entity, and the computer implementation model. As illustrated in Fig. 1, engineers start with the definition of the real-life problem at hand. Electromagnetic problems, in general, are modeled with Maxwell's equations and EM theory is well-established by these equations. Maxwell's equations are general and represent all linear EM problems. Once the geometry of the problem at hand (i.e., boundary conditions, BC) is given, they represent a unique solution; the solution found by

using Maxwell's equations plus BC is the solution we are looking for. Unfortunately, there are only a few real-life problems which have mathematically exact solutions therefore many different and approximate conceptual models can be used. It is the process of conceptual validity which shows that chosen conceptual model fits into the real-life problem best under the specified initial and/or operational conditions. The next step is to develop a computer code for the chosen conceptual model. It is only after this that code verification via a computer programming process may be applied to show that the developed code represents the chosen conceptual model under given sets of conditions (accuracy, resolution, uncertainty, etc.). Finally, the solution for the real-life problem is obtained with a confidence after numerical and/or physical experimentation; nothing but the operational validity process [2].

The suitability (validation) of the conceptual model and verification of the software and synthetically generated data are the technical processes that must be addressed to show that a model is *credible*. Credibility is based on two important checks that must be performed in every simulation: validation and verification. Validation is the process of determining that *the right model is built*, whereas verification is designed to see if *the model is built right*. The final step of the verification is the calibration.

The VV&C procedure in applied computational electromagnetics is discussed here. The real-life problem chosen for this purpose is the two-dimensional (2D) propagation over flat-Earth with a perfectly electrical conductor (PEC) surface through a non-homogeneous atmosphere. The linearly decreasing vertical refractivity profile under these circumstances yields an analytical exact solution. There are many conceptual/mathematical models which might fit into these conditions; one of them, the parabolic wave equation (PWE), is chosen as the test model. MatLab-based numerical simulators for both the split step Fourier and finite element implementations of the PWE are developed. The VV&C procedure necessitates quantitatively and qualitatively answering these questions: (i) How precise is the PWE model? (ii) To what extent does the PWE correspond to the real-life problem? (iii) Under what/which conditions do SSPE and FEMPE yield reliable solutions? (iv) What is the accuracy of the numerical calculations? In order to answer these questions and similar ones, one needs to generate a reference data and systematic comparisons. Here, the simulators are calibrated against analytical exact (in terms of modal summation) and high frequency asymptotic (in terms of geometric optic (GO)-ray summation) solutions. Problems related to the generation of reference data during accurate numerical computations are presented. Then, the problems related to model simplifications and inadequacy, model truncation (because of a finite number of modes taken into account), and error introduced from improper discretization are all discussed.

II. PARABOLIC EQUATION MODEL FOR GROUNDWAVE PROPAGATION PROBLEM

The PWE has become a classical tool in modeling groundwave propagation problems. It is derived from the 2D Helmholtz's equation by separating rapidly varying phase term in a medium to obtain an amplitude factor which varies slowly in range when the direction of propagation is predominantly along $+z$ paraxial direction under $\exp(-i\omega t)$ time dependence [3-7]

$$\left\{\frac{\partial^2}{\partial z^2}+\frac{\partial^2}{\partial x^2}+2ik_0\frac{\partial}{\partial z}+k_0^2(n^2-1)\right\}u(z,x)=0, \quad (1)$$

where $u(z,x)$ denotes the wave amplitude either of the electric or magnetic field components for horizontal and vertical polarization respectively; $k_0=2\pi/\lambda$ is the free space wavenumber, n is the refractive index, x and z stand for the transverse and the longitudinal coordinates, respectively (note that, PWE was first introduced in acoustics [3] and since then has been applied to a huge number of propagation problems not only in acoustics but also in electromagnetics and optics and has become classical. None of the lists of references would be complete on the PWE topic; therefore, the reader is referred to in [4] and the references there to initiate a literature search. If the refractive index is range-independent and backward propagation is ignored, (1) reduces to

$$\left\{\frac{\partial}{\partial z}+ik_0(1-\sqrt{1+q})\right\}u(z,x)=0, \quad (2)$$

where $q=k_0^{-2}\,\partial^2/\partial x^2+(n^2-1)$. If the angle of propagation measured from the paraxial direction

is less than 15°, the standard parabolic equation (PE) can be used with the help of square root approximation $\left(\sqrt{1+q} \approx 1+q/2\right)$. If this angle is more than 15°, Claerbout equation can be obtained by using the first order Padé approximation $\left(\sqrt{1+q} \approx (1+0.75q)/(1+0.25q)\right)$ to satisfy the propagation angle up to 35°-40° [4]. Hence, the PE is described as

$$\left\{A_0 \frac{\partial^3}{\partial x^2 \partial z} + A_1 \frac{\partial}{\partial z} + A_2 \frac{\partial^2}{\partial x^2} + A_3\right\} u(z,x) = 0, \quad (3)$$

with coefficients $A_0 = 0$, $A_1 = 2ik_0$, $A_2 = 1$, and $A_3 = k_0^2(n^2-1)$ for narrow angle case or $A_0 = 1$, $A_1 = k_0^2(n^2+3)$, $A_2 = -2ik_0$, $A_3 = -2ik_0^3(n^2-1)$ for wide angle case with one-way forward propagation.

Choosing the appropriate longitudinal BC

$$\left\{\frac{\partial}{\partial z} - ik_0\right\} u(z,x)\Big|_{z\to\pm\infty} \to 0, \quad (4)$$

and transverse BC

$$\left\{\alpha_1(z)\frac{\partial}{\partial x} + \alpha_2(z)\right\} u(z,x)\Big|_{x=0} = 0, \quad (5)$$

with the flat-Earth assumption completes the definition of the conceptual model. Here, $\alpha_1(z)$, $\alpha_2(z)$ become constants for homogeneous path and $\alpha_j(z) = 0$ (j=1,2) results in Dirichlet (horizontal polarization) and Neumann (vertical polarization) boundary conditions (DBC and NBC), respectively for PEC surface.

Since waves propagating upwards either go to infinity or bent down because of the refractivity variations, the open boundary upward in height can be modeled by using artificial lossy layer with the help of Hanning window in order to eliminate reflection effects [4-8]. The PWE and its application under different circumstances are pictured in Fig. 2. As illustrated in the figure, the beauty of the PWE is that all curvature effects including irregular terrain can be modeled via refractivity perturbations. On the other hand, PWE is an initial value problem, therefore boundary conditions must be satisfied artificially [4].

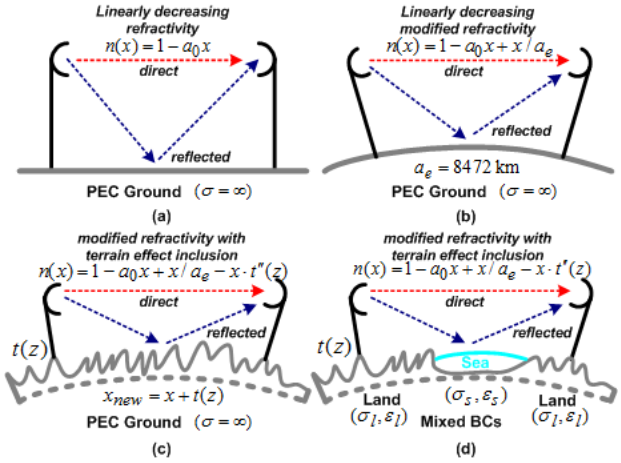

Fig. 2. 2D-PE modeling of groundwave propagation: a) flat Earth, b) Earth's curvature effect, c) irregular terrain effect, d) mixed boundary condition effect.

A. The split step parabolic equation (SSPE) propagator

The standard fast Fourier transform (FFT) based SSPE solution for narrow [4] and wide [5] angle, respectively,

$$u(z+\Delta z, x) = \exp\left[i\frac{k_0}{2}(n^2-1)\Delta z\right] \times F^{-1}\left\{\exp\left[-i\frac{k_x^2 \Delta z}{2k_0}\right] F\{u(z,x)\}\right\}, \quad (6)$$

$$u(z+\Delta z, x) = \exp\left[ik_0(n-1)\Delta z\right] \times F^{-1}\left\{\exp\left[\frac{-ik_x^2\Delta z}{k_0\left(1+\sqrt{1-k_x^2/k_0^2}\right)}\right] F\{u(z,x)\}\right\}, \quad (7)$$

can be used to calculate the vertical field $u(z+\Delta z, x)$ from $u(z,x)$ along z at range steps of Δz. The FFT based PE solution uses a longitudinally marching procedure. First, an antenna pattern representing the initial height profile is injected. Then, this initial field is propagated longitudinally from z_0 to $z_0+\Delta z$ and the transverse field profile at the next range is obtained. This new height profile is then used as the initial profile for the next step and the procedure goes on until the propagator reaches the desired range. SSPE sequentially operates between vertical domain and the transverse domain. SSPE cannot automatically handle the BCs at Earth's surface. It is satisfied by removing the surface and taking a mirror copy of the initial vertical field

profile below (odd and even symmetric for DBC and NBC, respectively).

B. The finite element method based parabolic equation (FEMPE) propagator

The idea of FEM-based formulation of the PE is to divide the transverse domain into sub domains (called elements), use approximated field values at the selected discrete nodes in the vertical domain between ground and selected maximum height, and propagate longitudinally by the application of the Crank-Nicholson approach based on the improved Euler method which yields an unconditionally stable system and accurate method [8-10] starting from the initial field at $z=0$, which is generated from a Gaussian antenna pattern specified by its height (h_s), beamwidth (θ_{bw}), and elevation angle (θ_{tilt}).

Using (3), the matrix representation form of the FEMPE propagator is obtained as $\left[-A_0K^e_{mj}+A_1M^e_{mj}\right]\left\{\partial c^e_j/\partial z\right\}+\left[-A_2K^e_{mj}+A_3M^e_{mj}\right]\left\{c^e_j\right\}=\{0\}$

for $M^e_{mj}=\int_{x_1^e}^{x_2^e}B^e_mB^e_j\,dx$, $K^e_{mj}=\int_{x_1^e}^{x_2^e}\frac{\partial B^e_m}{\partial x}\frac{\partial B^e_j}{\partial x}\,dx$, $e=1,\ldots,n_e$, $m=1,...,d$, $j=1,...,d$ with the help of basis functions (B) of degree d where e stands for the elements, n_e is the number of elements in the vertical domain, and $c^e_j(z)$ denotes the coefficients of unknown functions. The DBC at the surface are satisfied by eliminating the first column and row of matrices since the initial node is always zero [9-10].

C. Typical applications of the SSPE and FEMPE propagators

The SSPE and FEMPE propagators are used to investigate various complex propagation problems [10-13]. Two examples are presented here in order to show the significance and requirement of the VV&C procedure in these problems. First, a typical irregular terrain path is generated and propagation above this irregular terrain through homogeneous atmosphere (including the Earth's curvature) is simulated under both DBC and NBC. Three dimensional (3D) field strength vs. range/height plot at 300MHz is pictured in Fig. 3. Only, the SSPE map is shown but the FEMPE map is also the same; it is almost impossible to distinguish the maps of both propagators. The source is a down-tilted Gaussian beam. As observed, down propagation of the beam, reflection from the terrain, and interference between the direct and terrain-reflected waves are clearly observed. Moreover, the BC effects on the surface seem to be well-modeled [11-12].

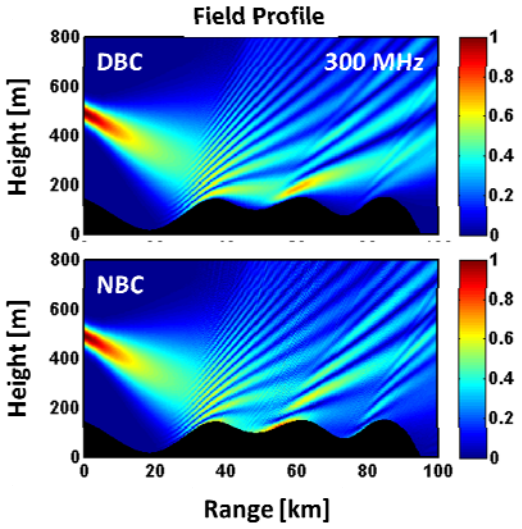

Fig. 3. Irregular terrain effect (PEC ground): 3D field map obtained via SSPE propagator under DBC and NBC (h_s=350m, θ_{bw}=0.5°, θ_{tilt}=-0.5°).

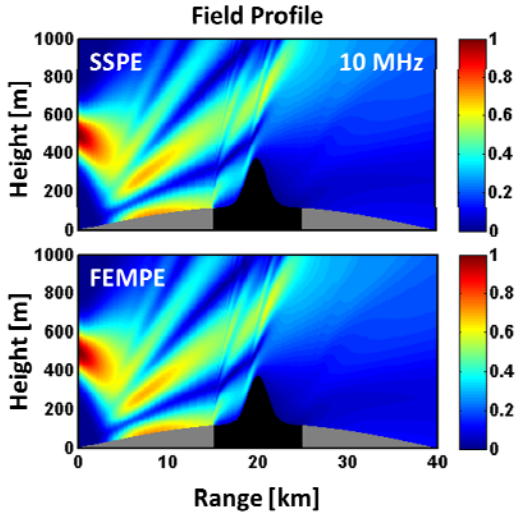

Fig. 4. Surface wave propagation: 3D signal vs. range/height map over a 3-segment 40km mixed path (a 10km long, 250m high Gauss-shaped island is 15km away from the transmitter) (Island: $\sigma=0.002$ S/m, $\varepsilon_r=10$; Sea: $\sigma=5$ S/m, $\varepsilon_r=80$).

The other example belongs to surface wave propagation over a three-section mixed-path (sea-land-sea) with a Gaussian shaped hilly island [12-13]. Surface wave propagation along this path at

10MHz generated via both propagators is shown in Fig. 4. Here, an elevated antenna is used (a Gaussian shaped antenna pattern with 5° vertical beamwidth, tilted 2° downwards, located 500m above the sea surface) is used to excite surface waves. As observed, waves hit the sea surface around 5km; energy couples to the surface and propagates thereafter. Also, observe how surface wave coupling in the near vicinity of the transmitter is important on the signal attenuation and range variations.

III. CANONICAL PROBLEMS AND GENERATING REFERENCE SOLUTIONS

The crucial questions in modeling and simulation as presented in the previous section are (i) Are they correct? (ii) How accurate are they? (iii) How can reliable comparisons be possible? The answer can only be given after a step by step, precise VV&C procedure. This section presents the generation of reference data which necessitates exact and/or asymptotic models as well as precise and accurate generation of reference numerical data.

A. Surface duct problem

Propagation over the PEC flat Earth with a linearly decreasing vertical refractivity profile (i.e. $n^2(x) = 1 - a_0 x$) is a canonical structure with analytical solutions in terms of Airy functions for the range-independent vertical refractive index. Here, a_0 is a positive constant which controls the strength of the duct. The exact modal solution of the Airy type wave equation using N modes is [2]

$$u(z,x) = \sum_{q=1}^{N} c_q Ai\left[(a_0 k_0^2)^{1/3} x - \sigma_q\right] e^{i\beta_q z}, \quad (8)$$

where c_q is the modal excitation coefficients, β_q is the longitudinal propagation constant for the related mode represented by index q as

$$\beta_q = \pm\sqrt{k_0^2 - (a_0 k_0^2)^{2/3}\sigma_q}, \quad (9)$$

Ai is the first kind of Airy function. The BC at the surface is satisfied with $Ai(-\sigma_q) = 0$ and $Ai'(-\sigma_q) = 0$ for the DBC and NBC, respectively. Here, the prime denotes the derivative with respect to the vertical coordinate. The problem is then reduced to find the modal excitation coefficients from a given antenna pattern using orthonormality property from a given source function as:

$$c_q = \int_0^{X_{\max}} g(x)\, Ai\left[(a_0 k_0^2)^{1/3} x - \sigma_q\right] dx,$$
$$\text{where} \quad g(x) = \frac{1}{\sqrt{2\pi\sigma^2}} \exp\left[\frac{(x-h_s)^2}{2\sigma^2}\right]. \quad (10)$$

Here, σ is the spatial width and h_s is the height of the Gaussian source $g(x)$. The Gaussian source pattern is often used in applications since it represents various antenna types (but any other source profile may also be used). The Gaussian antenna pattern can also be defined in the vertical wavenumber domain as

$$g(k_x) = \exp\left[\frac{-k_x^2 \ln 2}{2k_0^2 \sin^2(\theta_{bw}/2)}\right]. \quad (11)$$

The tilt (or elevation) angle (θ_{tilt}) is introduced by shifting the antenna pattern, i.e., $g(k_x) \to g(k_x - k_0 \sin\theta_{tilt})$. The vertical field in the spatial domain is then obtained by taking the inverse Fourier transform of (11).

The fundamental issue here is the construction of the reference data. An antenna radiation pattern may be used for the transmitter modeling which is mathematically achieved by locating a vertical Gaussian pattern, $g(x) = u(z_0, x)$, on a specified height. Then, the modal summation in (8) is used together with the orthonormality condition (10) and the number of modes and their excitation coefficients are derived numerically for a given error boundary. Note that, modal excitation coefficients are real if the antenna pattern has no vertical tilt (i.e., antenna pattern is horizontal, parallel to the flat-Earth). These modal excitation coefficients become complex when upslope or downslope tilt is introduced. Moreover, the modes are confined between the Earth's surface and modal caustics which depend on the mode number; the higher the mode, the higher the location of the caustic. Therefore, the number of modes used in the superposition directly depends on the antenna height.

Finally, vertical boundaries of the numerical integration during the modal excitation coefficient extraction from the orthonormality property increase as the mode number increases. The specification of the number of numerical integration steps for the calculation of modal

excitation coefficients is crucial. The code must adopt the number of integration steps automatically as the mode index increases.

Table 1 lists the number of modes required to establish a given Gaussian antenna pattern for a fixed error and antenna tilt. As seen from this table, the number of modes tremendously increases as the antenna tilt increases. It is quite inefficient to continue the modal summation procedure for the tilts beyond 10°.

Table 1: Number of modes used with respect to maximum initial field error<1e-8 ($f = 300$ MHz $h_s = 250$ m, $bw = 0.35$, $dM/dx = -600$ M/km)

Tilt angle (°)	# of modes (N)	Tilt angle (°)	# of modes (N)
0	19	6	2099
1	69	7	3114
2	191	8	4380
3	418	9	5984
4	795	10	7926
5	1342		

B. Single knife-edge problem and the four ray model

It appears that the surface duct model in Sec. III. A can be used within the paraxial region because the numerical instabilities and insufficiencies meet there during the generation of the reference data. The single-knife-edge problem, the four ray model (4Ray), and Fresnel integral representations [14] can be used as an alternative model from which reliable reference data can be generated. The scenario of this canonical problem is pictured in Fig. 5. Here, h_t, h_r, and h_w are the heights of the transmitter, receiver, and the knife-edge obstacle; d_1 and d_2 are the distances from source to obstacle and from obstacle to receiver, respectively.

Possible four rays are as follows: Ray 1 is the direct path between the transmitter and the receiver. Ray 2 is considered as the ray from the transmitter reflected from the right side of the knife-edge obstacle. This ray reaches the receiver directly or tip-diffraction may occur. Ray 3 is considered as the ray from the transmitter reflected from the left side of the knife-edge obstacle. Same as before, this ray also reaches the receiver directly or tip-diffraction will occur. Ray 4 is considered as the ray from the transmitter reflected

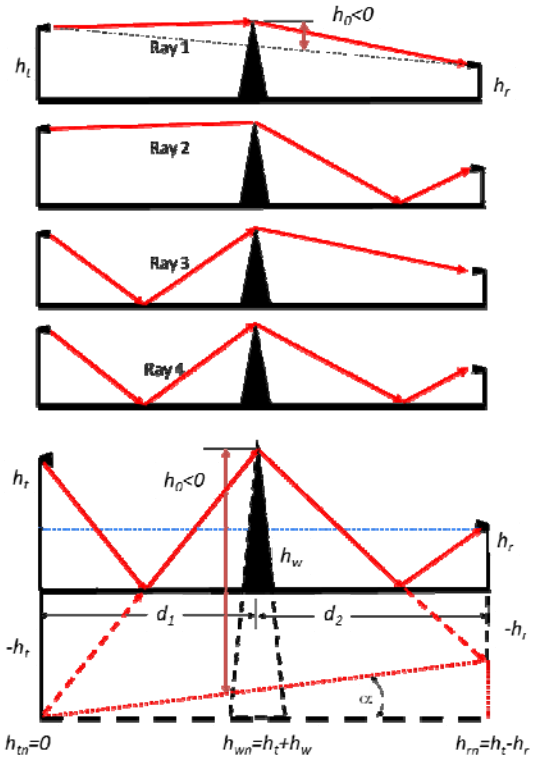

Fig. 5. (Top) The geometry of the flat-Earth and the single knife-edge problem. (Bottom) The construction of Ray 4 from the source/receiver images and h_0.

from both the left side and the right side of the knife-edge obstacle.

The parameters of the Fresnel integrals are derived by using the image source/receiver for the reflected waves. The Fresnel clearance, the height of the knife-edge above the line-of-sight may be positive or negative [14]. When the direct ray between the transmitter and receiver intersects obstacle, h_0 is taken negative. The Fresnel integrals $C(v)$ and $S(v)$ are evaluated, where $v = h_0\sqrt{2}$ with h_0 equal to the *ray clearance* over the knife-edge. The pattern propagation factor (PF) is equal to:

$$F = \frac{E}{E_0} = \sum_{q=1}^{4} E_q \exp(i\psi_q), \qquad (12)$$

where $E_q = A(v_q)\Gamma_q$, $\Gamma_1 = 1$, $\Gamma_2 = \Gamma_R$, $\Gamma_3 = \Gamma_L$, $\Gamma_4 = \Gamma_L\Gamma_R$, and $\psi_q = \beta_q + (R_q - R_1)k_0$. Here,

$$A(v_q)=\sqrt{\frac{\left(C(v_q)+0.5\right)^2+\left(S(v_q)+0.5\right)^2}{2}}, \quad (13)$$

for $C(v_q)=\int_0^v \cos(v_q^2)dv$, $S(v_q)=\int_0^v \sin(v_q^2)dv$; the distances of four rays are

$$R_q=\begin{Bmatrix}\sqrt{d^2+(h_t-h_r)^2} & \text{for} \quad q=1,q=3\\ \sqrt{d^2+(h_t+h_r)^2} & \text{for} \quad q=2,q=4\end{Bmatrix}, \quad (14)$$

$$\beta_q=\begin{Bmatrix}\arctan\left(\frac{S(v_q)+0.5}{C(v_q)+0.5}\right)-\frac{\pi}{4} & \text{if} \quad C(v_q)\ge -0.5\\ \arctan\left(\frac{S(v_q)+0.5}{C(v_q)+0.5}\right)+\frac{3\pi}{4} & \text{if} \quad C(v_q)<-0.5\end{Bmatrix}, \quad (15)$$

and the complex reflection coefficients, for the horizontal and vertical polarizations, respectively, are:

$$\Gamma=\frac{\sin(\theta)-\sqrt{\varepsilon-\cos^2(\theta)}}{\sin(\theta)+\sqrt{\varepsilon-\cos^2(\theta)}}, \Gamma=\frac{\varepsilon\sin(\theta)-\sqrt{\varepsilon-\cos^2(\theta)}}{\varepsilon\sin(\theta)+\sqrt{\varepsilon-\cos^2(\theta)}}, \quad (16)$$

where $\varepsilon=\varepsilon_r-i60\sigma_g\lambda$, σ_g is the conductivity and ε_r is the relative permittivity of ground, θ is the angle of incidence in radians. The ray clearances for the four rays are:

$$h_{01}=\sqrt{\frac{2d}{\lambda d_1 d_2}}\left(-h_t+\frac{(h_r-h_t)d_1}{d}-h_w\right), \quad (17a)$$

$$h_{02}=\sqrt{\frac{2d}{\lambda d_1 d_2}}\left(-h_t+\frac{(h_r+h_t)d_1}{d}-h_w\right), \quad (17b)$$

$$h_{03}=\sqrt{\frac{2d}{\lambda d_1 d_2}}\left(h_t+\frac{(-h_r-h_t)d_1}{d}-h_w\right), \quad (17c)$$

$$h_{04}=\sqrt{\frac{2d}{\lambda d_1 d_2}}\left(-h_t+\frac{(h_t-h_r)d_1}{d}-h_w\right). \quad (17d)$$

IV. VALIDATION, VERIFICATION AND CALIBRATION (VV&C)

VV&C starts with the model validation. The SSPE and FEMPE codes are based on one-way, forward propagation PE model which neglects back-scattered waves. This is not a serious limitation as long as one is interested in path losses between a transmitter and a receiver. Another limitation of the PE model is that, both narrow and wide angle PE models are valid within paraxial region. This should be taken into account for waves propagating upwards/downwards with some tilts and/or for propagation paths having longitudinally irregular terrain profiles with certain terrain slopes. Proper discretization (i.e., range and height step sizes, Δz and Δx, respectively) is essential in numerical simulations. These are important issues that should be tested during the VV&C procedure.

The first VV&C example is presented in Fig. 6. Here, 3D visualization of both analytical and numerical solutions is presented where the transmitter contains two Gaussian patterns (i.e., two antennas) at 200m and 400m, with -0.5° and 0.5° tilts, respectively. In Fig. 6b, vertical field profiles at two different ranges obtained with all three (analytical, SSPE, and FEMPE) codes, are shown. Excellent agreement illustrates the success and completeness of the VV&C procedure.

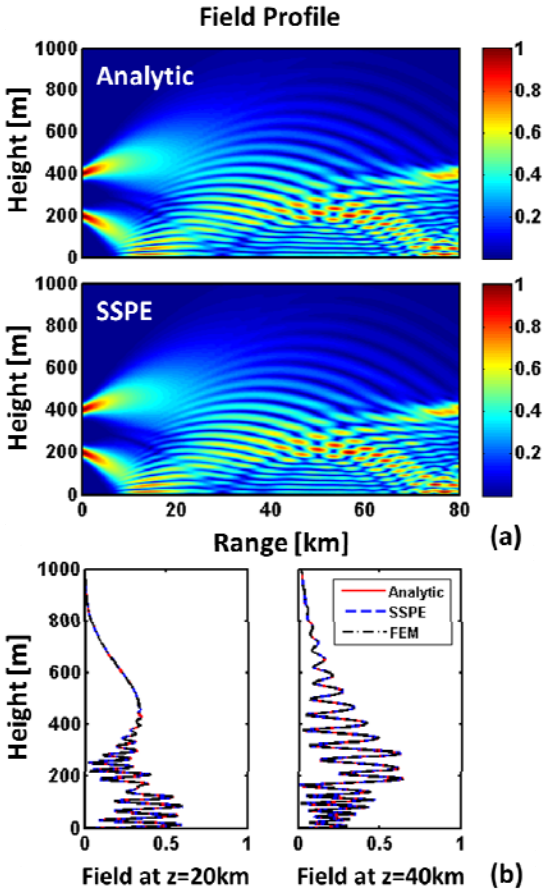

Fig. 6. (a) SSPE and analytic propagators with tilted waves at 200m and 400m with -0.5°, 0.5° tilts, respectively, (b) vertical field profiles at two different ranges ($dM/dx=-600$ M/km).

Obviously, the PE codes can be tested and calibrated against the numerically generated reference data obtained from analytical exact model for tilts up to 10° at most. Beyond that, SSPE and FEMPE can only be tested against some

other methods or using some physical electromagnetic reality. One way of testing narrow angle (6) and wide angle (7) PE representations is to tilt up or down the antenna pattern up to 40°-45°. The modal summation procedure for this example shows that, although an exact mathematical solution is at hand, it might be extremely difficult to produce numerical reference data for the VV&C tests. An example for this case is given in Fig. 7. Since the SSPE result is exactly the same with the FEMPE result, it is not included here.

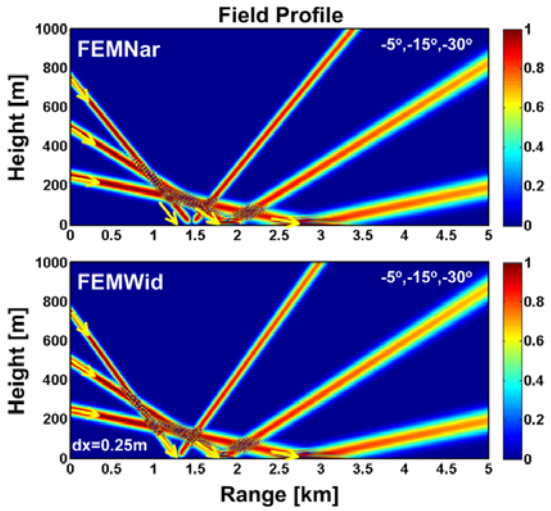

Fig. 7. Narrow and wide angle FEMPE propagators for -5°, -15°, -30° tilted waves at 250m, 500m, 700m, respectively.

Here, a three antenna transmit system is used. The antennas are located at 250m, 500m, and 750m heights with -5°, -15°, -30° tilts, respectively. The frequency is 300MHz. The tilt down waves hit the ground at 2.85km, 1.86km, 1.29km for -5°, -15°, -30°, respectively (the effects of refractivity variations at these ranges are almost negligible and waves propagate almost as in free space with straight lines). Note that vertical step should satisfy $\Delta x \le \lambda/(2\sin(2\alpha_{\max}))$ where $\alpha_{\max}$ is the maximum tilt (or terrain slope if irregular terrain is present). At 300MHz (i.e., $\lambda = 1\,\mathrm{m}$) $\Delta x \le 1\,\mathrm{m}$ for -15° tilt, but $\Delta x \le 0.5\,\mathrm{m}$ for -45° tilt. The 3D plots in this figure are produced with $\Delta x = 0.25\mathrm{m}$ for SSPE and FEMPE; therefore, the discretization satisfies the tilt requirements. It is clearly observed from these plots that both narrow and wide angle PE models can handle tilts up to ±15°, but only wide angle PE can handle tilts beyond these values. Note that the computation times for this example for the selected list of parameters with the narrow and wide angle SSPE are 48s and 51s, and with the narrow and wide angle FEMPE are 2844s and 3350s, respectively.

The VV&C of the PE tools out of the paraxial region is conducted on the single knife-edge model given in Sec. III. B. The last three figures belong to this VV&C procedure. In Fig. 8, 3D field maps generated via the SSPE tool and the 4Ray model. The scenario belongs to one-way propagation for horizontal polarization over PEC ground with 75m height-wall at 15km range. The line source is at 15m height at *z=0*. The FEMPE result is exactly the same with the SSPE map, therefore it is not included in this figure.

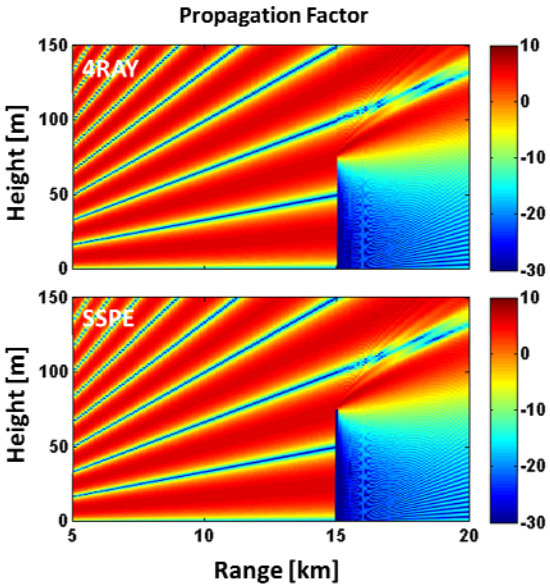

Fig. 8. One-way propagation for horizontal polarization over PEC ground with 75m height-wall at 15km range. The propagation factor vs. range/height for a given source (at 20m height, 0km range): *f*=3GHz, *Δx*=0.1m, *Δz*=50m.

The PFs vs. height in front of and beyond the wedge-type obstacle are plotted in Fig. 9. Here, four vertical field profiles obtained with both SSPE and four ray model are plotted. The first plot on the left belongs to the interference region (before the obstacle); the other three are in the diffraction region (beyond the obstacle). As observed, excellent agreement is obtained in all of the plots. Note that the height of the edge of the obstacle is 75m and the distances of these three profiles from the obstacle are 100m, 1km, and

3km, respectively. The maximum diffraction angles of these three are around 36.9°, 4.3°, and 1.5°, respectively. It is expected that the PE models are not effective and accurate for the angles beyond 30°-35°. As observed, the PE models are insufficient in modeling the diffracted fields in the deep shadow regions.

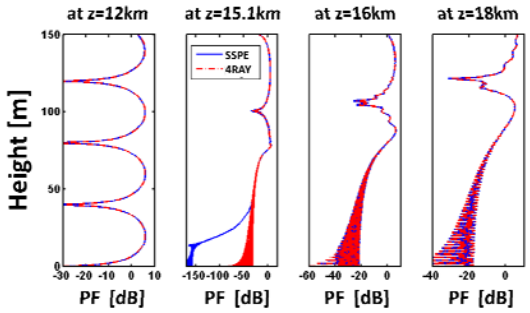

Fig. 9. The PF vs. height at four ranges; 12km, 15.1km, 16km, and 18km (f=3GHz, solid: 4Ray, dashed: SSPE, Δx=0.1m, Δz=50m).

V. CONCLUSIONS

Model validation, data verification, and code calibration (VV&C) is an important engineering task. Engineers deal with real-life problems; they design, test, measure, simulate, etc. The first step is the definition of the problem; the solution cannot be found without clear definition of the problem. In electromagnetics, Maxwell's equations plus BCs well-define the problem at hand. Mathematically speaking, the existence and uniqueness of the solution is already there once Maxwell's equations are stated with the right BCs. Therefore, the conceptual (mathematical) model is already at hand in electromagnetics. The challenge is the numerical computation. Unfortunately, only a few problems with idealized conditions have mathematical exact solutions; therefore one needs to introduce approximations, assumptions, simplifications, etc., which yield a variety of different conceptual models. The VV&C procedure starts with the choice of the right model and necessitates the validation procedure. Then, the computer coding and verification procedure come. The final stage is the calibration.

The VV&C procedure is discussed systematically over a 2D groundwave propagation problem. The flat-Earth above PEC surface with vertically decreasing refractivity profile (without and with a single knife-edge obstacle) is taken into account for this purpose. The well-known PWE model is chosen as the conceptual model. Both split-step and finite-element based PWE codes are developed. Numerical data generated via these models are compared against analytical exact results. Difficulties in producing numerical data for the analytical exact solutions and in calibration are presented.

Note that the VV&C procedure discussed in Sec. IV automatically answers the crucial questions asked at the beginning of Sec. III. The terrain profiles used in Figs. 3 and 4 are synthetically generated; measurements along these paths are not possible. Furthermore, a mathematical/ analytical model is not available because of the complexity of the boundary conditions there. Therefore, reference data (which can only be obtained either from a reliable analytical model or measurements) cannot be generated. All that can be done is to do comparisons among different numerical models/packages. For these kinds of problems (where no reference data could be generated) results should be presented with caution. The results of different numerical models/packages might show a perfect agreement but still be totally erroneous [11-13].

REFERENCES

[1] G. Apaydin and L. Sevgi, "Validation, verification, and calibration in applied computational electromagnetics," *26th International Review of Progress in Applied Computational Electromagnetics*, Tampere, Finland, pp. 679-684, Apr. 2010.

[2] L. Sevgi, *Complex Electromagnetic Problems and Numerical Simulation Approaches*, IEEE Press/Wiley, Piscataway, NJ, Jun. 2003.

[3] M. A. Leontovich and V. A. Fock, "Solution of propagation of electromagnetic waves along the Earth's surface by the method of parabolic equation," *Journal of Physics of the USSR*, vol. 10, pp. 13-23, 1946.

[4] M. F. Levy, *Parabolic Equation Methods for Electromagnetic Wave Propagation*, The Institution of Electrical Engineers, London, U.K., 2000.

[5] D. J. Thomson and N. R. Chapman, "A wide-angle split-step algorithm for the parabolic equation," *J. Acoust. Soc. Am.,* vol. 74, no. 6, Dec. 1983.

[6] L. Sevgi, "Modeling and simulation strategies for electromagnetic wave propagation in complex environments: Groundwave path loss prediction virtual tools," *IEEE Trans. Antennas Propagat.*, vol. 55, no. 6, pp. 1591-1598, Jun. 2007.

[7] L. Sevgi, C. Uluisik, and F. Akleman, "A Matlab-based two-dimensional parabolic equation radiowave propagation package," *IEEE Antennas and Propag. Mag.*, vol. 47, no. 4, pp. 164-175, Aug. 2005.

[8] D. Huang, "Finite element solution to the parabolic wave equation," *J. Acoust. Soc. Am.* vol. 84, no. 4, pp. 1405-1413, Oct. 1988.

[9] K. Arshad, F. A. Katsriku and A. Lasebae, "An investigation of tropospheric radio wave propagation using finite elements," *WSEAS Trans. Commun.,* vol. 4, no. 11, pp. 1186-1192, Nov. 2005.

[10] G. Apaydin and L. Sevgi, "The split step Fourier and finite element based parabolic equation propagation prediction tools: canonical tests, systematic comparisons, and calibration," *IEEE Antennas and Propag. Mag.*, vol. 52, no. 3, Jun. 2010.

[11] G. Apaydin and L. Sevgi, "A novel split-step parabolic equation package for surface wave propagation prediction along multi-mixed irregular terrain paths," *IEEE Antennas and Propag. Mag.,* vol. 52, no. 3, Aug. 2010.

[12] G. Apaydin and L. Sevgi, "FEM-based surface wave multi-mixed-path propagator and path loss predictions," *IEEE Antennas Wireless Propag. Lett.,* vol. 8, pp. 1010-1013, 2009.

[13] G. Apaydin and L. Sevgi, "Numerical investigations of and path loss predictions for surface wave propagation over sea paths including hilly island transitions," *IEEE Trans. Antennas Propagat.,* vol. 58, pp. 1302-1314, Apr. 2010.

[14] M. L. Meeks, *Radar Propagation at Low Altitudes*, Artech House, 1982.

Gokhan Apaydin received the B.S., M.S., and Ph.D. degrees in Electrical and Electronics Engineering from Bogazici University, Istanbul, Turkey, in 2001, 2003, and 2007, respectively.

He was employed as a Teaching and Research Assistant by Bogazici University from 2001 to 2005, and a Project and Research Engineer by Applied Research and Development, University of Technology, Zurich, Switzerland, from 2005 to 2010. Since 2010, he has been with Zirve University, Turkey. He has been working several research projects on electromagnetic scattering, the development of finite element method for electromagnetic computation, propagation, positioning, digital signal processing, filter design, and related areas. He has (co)authored 14 journals, 26 conference papers, and many technical reports at the University of Applied Science Zurich.

Levent Sevgi received the Ph.D. degree from Istanbul Technical University and Polytechnic Institute of New York, in 1990. Prof. Leo Felsen was his advisor.

He was with Istanbul Technical University (1991–1998), TUBITAK-MRC, Information Technologies Research Institute (1999–2000), Weber Research Institute/Polytechnic University in New York (1988–1990), Scientific Research Group of Raytheon Systems, Canada (1998 – 1999), Center for Defense Studies, ITUV-SAM (1993 –1998, 2000–2002). Since 2001, he has been with Dogus University. He has been involved with complex electromagnetic problems and systems for more than 20 years. His research study has focused on propagation in complex environments, analytical and numerical methods in electromagnetic, EMC/EMI modeling and measurement, radar and integrated surveillance systems, surface wave HF radars, FDTD, TLM, FEM, SSPE, and MoM techniques and their applications, RCS modeling, bio-electromagnetics. He is also interested in novel approaches in engineering education, teaching electromagnetics via virtual tools. He also teaches popular science lectures such as science, technology, and society.

Prof. Sevgi is a Fellow of the IEEE, the writer/editor of the "Testing ourselves" Column in the IEEE Antennas and Propagation Magazine, a member of the IEEE Antennas and Propagation Society Education Committee, and the "Scientific Literacy" column writer of the IEEE Region 8 Newsletter.

Quasi-Dynamic Homogenization of Geometrically Simple Dielectric Composites

Jiaran Qi, Henrik Kettunen, Henrik Wallén, and Ari Sihvola

Aalto University School of Science and Technology
P.O. Box 13000, FI–00076 AALTO, Finland
qi.jiaran@tkk.fi

Abstract ─ The frequency dependence of the effective permittivities of simple dielectric composites is evaluated by different quasi-dynamic homogenization methods. Three retrieval approaches based on the scattering parameters are proposed for dielectric materials. A compensation method for the conventional Nicolson-Ross-Weir (NRW) retrieval is applied to eliminate the Fabry-Pérot (FP) resonances and their distortions of the retrieval results. All these quasi-dynamic homogenization methods are then evaluated by comparing the corresponding retrieval results against one another. Finally, by comparing these retrieval results with the static Lord Rayleigh prediction, the limitation of the quasi-static approximation for such composites is considered.

Index Terms ─ Dispersion diagram, homogenization, Rayleigh mixing rule, S-parameter retrieval.

I. INTRODUCTION

Homogenization is a method whereby the complicated and spatially varying microscopic fields existing in a heterogeneous medium, when it is excited by an electromagnetic (EM) wave with sufficiently large wavelength, are replaced by smoothly varying (or macroscopic) fields. These fields can be used for characterizing the behavior of the medium with effective parameters [1, 2], the permittivity ε and the permeability μ. Indeed, depending on the symmetry, the arrangement and the intrinsic EM properties of the constituents of the composites, the effective bulk medium may exhibit anisotropic, bianisotropic, or chiral characteristics [3]. We, however, confine our focus to mixtures composed of linear, lossless, and passive dielectric materials, which in turn allows us to compress all EM properties approximately into the effective permittivity ε_{eff}.

In electrostatics, the permittivity of the effective bulk medium ε_{eff} can be successfully predicted by various classical mixing formulas. These mixing rules in general determine ε_{eff} in terms of the permittivity of the individual phases and their volume fractions for specific inclusion shapes. The Lord Rayleigh formula is taken due to its sufficient accuracy as the static prediction for the ε_{eff} of the composites of our interest in this paper. For spherical inclusions (ε_{i}) with volume fraction p dispersed in the host medium (ε_{e}), the Rayleigh effective permittivity ε_{Ray} reads [4],

$$\varepsilon_{\text{Ray}} = \varepsilon_{\text{e}} + \frac{3p\varepsilon_{\text{e}}}{\dfrac{\varepsilon_{\text{i}} + 2\varepsilon_{\text{e}}}{\varepsilon_{\text{i}} - \varepsilon_{\text{e}}} - p - \dfrac{1.305 \cdot p^{10/3}\left(\varepsilon_{\text{i}} - \varepsilon_{\text{e}}\right)}{\varepsilon_{\text{i}} + 4\varepsilon_{\text{e}}/3}} . \quad (1)$$

When the scale of the local inhomogeneity is, however, no longer very small compared with the wavelength of the applied fields, the validity of the quasi-static description of heterogeneous media with effective medium parameters becomes a critical issue.

With the recent emergence of metamaterials, many researchers [5, 6] had extended such a homogenization procedure into this sensitive region, where the dimension of unit cell is usually an appreciable fraction of the wavelength [7], to characterize their EM properties with the effective medium parameters ε and μ. On the contrary, in [8] the authors found that the conventional effective material parameters are meaningless for an optical fishnet metamaterial due to the mesoscopic nature and the related spatial

dispersion. Instead of questioning its validity, we discuss in this paper how far upwards in frequency range we can approximately apply the static permittivity. We explore this problem by considering the quasi-dynamic homogenization of two kinds of simple composites — a transversally infinite slab and a simple cubic lattice, and constrain the homogenization of the slab to only one of the principal axes to eliminate the spatial dispersion influences. It is furthermore assumed that the constituents of the composites are dielectric materials and no artificial magnetism is generated by the homogenization. In order to determine the limit of the quasi-static approximation, we present four different S-parameter-based methods and the *ka–βa* dispersion diagram method [9] to retrieve the frequency dependence of the effective permittivity of two composites, and then compare them with the corresponding static Lord Rayleigh prediction to decide up to what extent it still holds the predictive power. It is moreover demonstrated that below such limits the spatial dispersion can be neglected for the simple cubic lattice.

II. GEOMETRY SETUP

Composites are analyzed in this paper using two models. The first one is a slab of thickness *d* which is infinite in the transverse direction (*x* and *y*) and formed from 9 cubic unit cells in *z* direction, while the other one is an infinite simple cubic lattice. Both composites are composed of the same unit cells. The unit cell is constructed by a dielectric spherical inclusion with relative permittivity ε_i centered in a dielectric cube ($\varepsilon_e = 1$) with edge length *a*, and the inclusion volume fraction is *p*. In this paper, we use the 3D EM simulator CST Microwave Studio (CST MWS) [10] to compute the required data for the ε_{eff} retrievals of different mixtures.

A. The slab

We consider the situation when a plane wave with *y*-polarized electric field is normally incident on the transversally infinite slab. Such a scenario can be realized by a finite structure with proper boundary conditions in CST MWS, due to the symmetry of the field distribution. As shown in Fig. 1, a slab of thickness *d* is made of 9 unit cells in a row, and an additional free space is added to prevent higher modes from propagating. PEC boundary conditions are assigned to the slab's upper and lower surfaces in *y* direction, while in *x* directions PMC boundaries are given. The whole geometry is then excited by two waveguide ports, which as well compute the S-parameters for retrievals. Only the electric response in *y* direction is of interest due to the *y*-directionally polarized electric field. Since the whole structure is symmetric with respect to the *xz* and *yz* planes, the computational complexity can be reduced by defining them respectively as electric and magnetic symmetry planes. Therefore, merely one quarter of the structure needs to be computed.

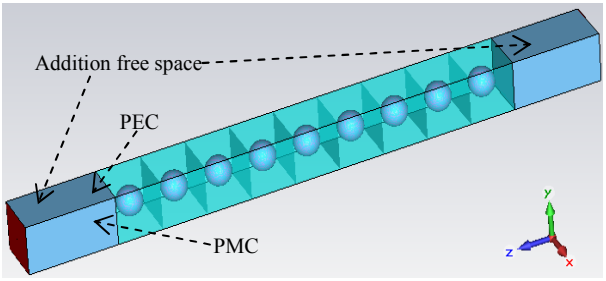

Fig. 1. 3D simulation configuration for the nine layer transversally infinite slab in CST MWS.

B. The simple cubic lattice

The simple cubic lattice can be constructed in CST MWS readily by assigning periodic boundary conditions to all six surfaces of the cubic unit cell. The *ka–βa* dispersion diagrams of the TEM modes for three different propagation directions, along the cube edge, surface diagonal and volume diagonal, are then generated respectively for retrievals.

III. RETRIEVAL METHODS

Many sophisticated techniques have been employed for the practical measurements to estimate the dielectric properties of materials [11]. But the full wave simulator, which eliminates many realistic uncertainties, enables us to retrieve the permittivities of the proposed composites with more straightforward methods. In this section, different retrieval methods will be introduced targeted on different composites. For the slab, four S-parameter-based methods are applied, while the *ka–βa* dispersion diagram approach is presented for the infinite lattice.

A. The slab case — S-parameter-based methods

1. The conventional NRW method

The classical approach of retrieving the effective ε and μ from S-parameters was originally studied by Nicolson, Ross, and Weir [12, 13]. Smith and coauthors improved and extended this method to determine the effective medium parameters of metamaterials [14]. Later, Chen and coauthors presented a more robust method aiming at metamaterials as well [15]. For a plane wave normally incident on a homogeneous slab with thickness d, the simulated S-parameters are related to n and z by [15]:

$$z = \pm\sqrt{\frac{\left(1+\mathrm{S}_{11}\right)^2-\mathrm{S}_{21}^2}{\left(1-\mathrm{S}_{11}\right)^2-\mathrm{S}_{21}^2}}. \tag{2}$$

$$Q = e^{-jnkd} = \frac{\mathrm{S}_{21}}{1-\mathrm{S}_{11}\dfrac{z-1}{z+1}}. \tag{3}$$

$$n = \frac{1}{kd}\left\{\left[-\mathrm{Im}\left[\ln\left(Q\right)\right]+2m\pi\right]+j\cdot\mathrm{Re}\left[\ln\left(Q\right)\right]\right\}, \tag{4}$$

where k denotes the free space wave number. The sign ambiguity in Eq. (2) can be cleared by the requirement $\mathrm{Re}(z) \geq 0$. Once z is determined, the imaginary part of the refractive index n will be solved by Eq. (3) and (4). The branch index m (integer value) of the logarithm function is then decided by the non-magnetic presumption. The effective permittivity and permeability can, hence, be directly calculated from the refractive index n and the impedance z by $\varepsilon_{\mathrm{eff}} = n/z$, $\mu_{\mathrm{eff}} = nz$.

2. Retrieval from either S_{11} *or* S_{21}

It is important to notice that for nonmagnetic materials with the assumption $\mu_{\mathrm{eff}} = 1$, when a plane wave is normally incident on a homogenous slab with thickness d, the gap between S-parameters and medium parameters $\varepsilon_{\mathrm{eff}}$ can also be bridged by the following equations,

$$\mathrm{S}_{11} = \frac{R\left(1-e^{-j2\sqrt{\varepsilon_{\mathrm{eff}}}kd}\right)}{1-R^2e^{-j2\sqrt{\varepsilon_{\mathrm{eff}}}kd}}. \tag{5}$$

$$\mathrm{S}_{21} = \frac{\left(1-R^2\right)e^{-j\sqrt{\varepsilon_{\mathrm{eff}}}kd}}{1-R^2e^{-j2\sqrt{\varepsilon_{\mathrm{eff}}}kd}}, \tag{6}$$

where $R = (z-1)/(z+1) = (1-\varepsilon_{\mathrm{eff}}^{1/2})/(1+\varepsilon_{\mathrm{eff}}^{1/2})$. Both Eq. (5) and (6) then become functions of only one variable $\varepsilon_{\mathrm{eff}}$, meaning either S_{11} or S_{21} contains sufficient information for the retrieval. In other words, this fact enables us to retrieve the effective permittivity from either one of S-parameters by solving the complex roots of Eq. (5) or (6).

3. Effective wavelength retrieval (EWR)

For a lossless slab, the FP resonances will occur when the thickness of the slab d is equivalent to an integer t multiple of one half of the effective wavelength of the field inside the slab. In this occasion, there is no reflection, i.e., $\mathrm{S}_{11} = 0$. From either the above condition or Eq. (5), we have $\exp(-j2nkd) = 1$, which gives the following equation,

$$\varepsilon_{\mathrm{eff}} = \left(\frac{t\lambda_t}{2d}\right)^2, \qquad t = 1,2,3... \tag{7}$$

where λ_t is the free space wavelength at the FP resonance of order t. Although this method is only valid for the retrieval at frequency points corresponding to the FP resonances, it provides a good comparison and validation for the results by other retrieval approaches.

In particular, the FP resonance and its influence on the retrieved results are usually neglected in the previous literature, partially due to the narrow retrieval frequency band. Another major factor is that the test samples are usually lossy materials, such as various kinds of metamaterials.

B. The lattice case ─ *ka–βa* method

The frequency dependence of the $\varepsilon_{\mathrm{eff}}$ of the infinite simple cubic lattice can be addressed as long as the *ka–βa* dispersion diagram is obtained, given that the effective wave number β is related to k by $\beta = k\,\varepsilon_{\mathrm{eff}}^{1/2}$.

For an infinite lattice composed of nonmagnetic materials, the following eigenfunction can be derived from Maxwell equations [16],

$$\nabla\times\left(\frac{1}{\varepsilon(\boldsymbol{r})}\nabla\times\boldsymbol{H}(\boldsymbol{r})\right) = \left(\frac{\omega}{c}\right)^2\boldsymbol{H}(\boldsymbol{r}), \tag{8}$$

where $\boldsymbol{H}(\boldsymbol{r})$ denotes the magnetic field pattern of the harmonic mode, c is the free space light speed and ω represents the eigenfrequency. Only the TEM mode $\boldsymbol{H}(\boldsymbol{r}) = \boldsymbol{H}_0\,e^{-j\beta a}$ needs to be considered here. Then according to Eq. (8), under a certain propagation direction, the eigenfrequencies ω (or k) can be calculated by giving different phase shifts βa. The desired *ka–βa* dispersion diagram can thus be generated. In CST MWS, a certain propagation direction can be specified by

systematically varying the three phase shifts $\beta_x a$, $\beta_y a$, and $\beta_z a$ between the periodic boundary pairs in the x, y, and z directions. Three different propagation directions are considered in this paper for the simple cubic lattice — along the edge, the surface diagonal, and the volume diagonal of the cubic unit cell. The computed field pattern is then utilized to identify the direction of the retrieved ε_{eff}.

IV. RESULTS AND DISCUSSION

For the quasi-dynamic homogenization, an important parameter is the number of unit cells in one effective wavelength λ_{eff} at a certain frequency. We define the effective wavelength by reducing the free-space wavelength according to the static Rayleigh prediction, $\lambda_{\text{eff}} = \lambda/(\varepsilon_{\text{Ray}})^{1/2}$. But since the frequency dependence of ε_{eff} is also of our interest, we normalize the frequency to f_{20}, which denotes the frequency when the reduced wavelength is 20 times the length of the unit cell, $\lambda_{\text{eff}} = 20a$.

A. Compensation method

For the composite with $p = 0.1$, $\varepsilon_i = 10$, and $\varepsilon_e = 1$ shown in Fig. 1, the comparison of the retrieved effective permittivities by four S-parameter-based methods is visualized in Fig. 2. According to Eq. (1), the Rayleigh εeff for such a mixture is roughly 1.2434 (green dotted), and at low frequency all the results are in good agreement with this value. As the frequency increases, the effective permittivities gradually deviate from the static prediction and grow as expected. However, for the NRW (black solid), the FP resonances appear at 2.9851, 5.9617, 8.921, 11.851, and 14.738 GHz, and there is clearly a systematic leap following each FP resonance. For the S_{11} method (blue dot-dashed), the retrieved permittivity presents a small variation around the more stable results by the S_{21} approach (red dashed). As for the EWR (black dots), the results not only coincide as expected with those by S_{11} since the EWR is actually a special case of the S_{11} method, but follow closely those by the S_{21} method. The EWR therefore provides a good confirmation of the validity of the S_{21} method.

As shown in Fig. 2, the presence of the FP resonance prevents us from utilizing the results by the conventional NRW technique. In order to compensate its influence, the μ_{eff} by the NRW is also shown in Fig. 3. It can be seen that although we use the condition that μ_{eff} is closest to unity to settle the branch index m, the retrieved μ_{eff} leaps away from 1 after each FP resonance. A further investigation into the calculated n and z indicates

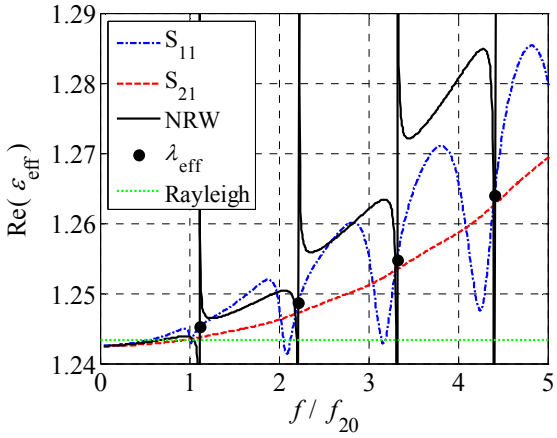

Fig. 2. The retrieved permittivities by four different S-parameter-based retrieval methods.

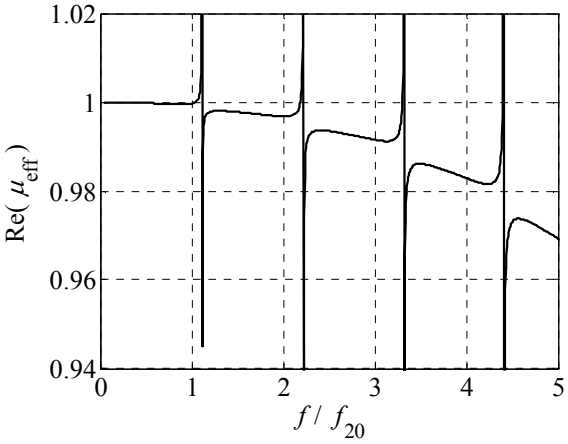

Fig. 3. The retrieved μ_{eff} by the conventional NRW method.

that the ill-retrieved z causes the abnormal leaps of the ε_{eff} and μ_{eff}, while the n displays reasonable frequency dependence. The effective permittivity can hence be calculated by $\varepsilon_{\text{eff}} = n^2$ instead of $\varepsilon_{\text{eff}} = n/z$, provided the nonmagnetic assumption $\mu_{\text{eff}} = 1$.

Figure 4 clearly illustrates that the compensated result has an excellent agreement with that by the S_{21} method. It should be noticed that since the electrical size of the dielectric inclusion (whose permittivity is reasonably low) is so small that the magnetic response can be

neglected, and since no other assumptions are applied, the compensation method does make physical and numerical sense. In addition, the compensated ε_{eff} is not exactly the same as that by the S_{21} method, suggesting that these two methods are independent of each other.

In particular, the unstable retrieval by the S_{11} method in Fig. 2 inspires us to study the imaginary parts of the ε_{eff}, respectively, by the S_{11} and S_{21} methods. Figure 5 illustrates that the S_{21} method is superior to the S_{11} method in that it manages to present clearly smaller values for the imaginary part of the ε_{eff} for this lossless mixture. This point shows that the S_{11} method is not suitable for such small reflection cases.

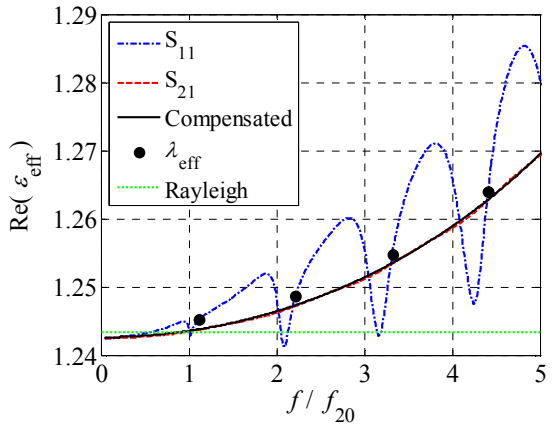

Fig. 4. The compensated result to the NRW method compared with those by the other three S-parameter-based approaches for the composites with $p = 0.1$, $\varepsilon_i = 10$, and $\varepsilon_e = 1$.

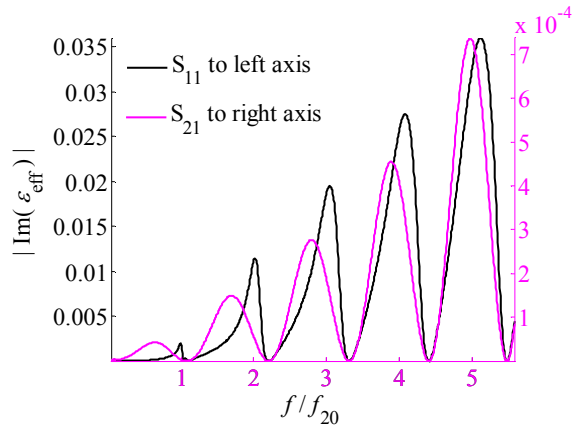

Fig. 5. Comparison between the imaginary part of the retrieved ε_{eff} by only S_{11} and that by only S_{21}.

B. *ka–βa* retrieval and spatial dispersion

Figure 6 visualizes the retrieved ε_{eff} for different wave propagation directions, and its legend provides not only the direction of propagation but also that of the field polarization. The 'SD–VD' (short for surface diagonal–volume diagonal), for instance, denotes the case when a plane wave travels along the surface diagonal of the cubic unit cell with a volume-diagonal-polarized electric field. As can be seen, the retrieved permittivities converge to the static Rayleigh prediction when the frequency decreases. For small values of f/f_{20}, the composite looks very isotropic, and the spatial dispersion becomes more apparent as the value of f/f_{20} increases over 2, i.e., a/λ_{eff} is larger than 1/10. Another interesting observation is that in this 3D scenario, waves propagating in different directions with the electric field in the same direction will result in the same dispersion curve. As shown in Fig.6, the 'Edge–Edge' curve agrees well with the 'SD–Edge' curve. Moreover, the dispersion curve when the electric field is polarised along the edge deviates most from the dotted curve predicted by the Rayleigh mixing rule, while the volume-directed electrical field leads to least deviation. The dispersion curve resulting from a surface-diagonal-directed electrical field lies between these two utmost cases.

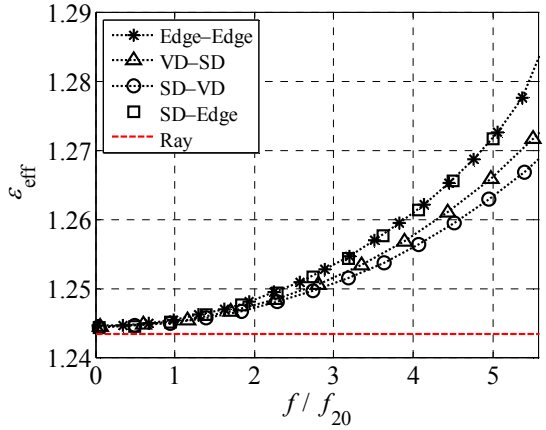

Fig. 6. The retrieval results for different directions of propagation when $p = 0.1$ and $\varepsilon_i = 10$. Note that the relative difference $|\varepsilon_{\text{Edge–Edge}} - \varepsilon_{\text{SD–VD}}| / \varepsilon_{\text{Ray}}$ is less than 1% up to 5 in terms of f/f_{20} (SD and VD stand for surface and volume diagonal).

C. Frequency dependence of ε_{eff} and quasi-static approximation limit

1. Frequency dependence of ε_{eff}

The one-principal-axis homogenization of the 9-layer slab (y direction) and the infinite simple cubic lattice (along the edge) are analyzed and shown in Fig. 7. The result shows that the permittivities of these two composites are in good agreement with one another, which further confirms the validity of all the presented ε_{eff} retrieval methods. In order for further validation, the ε_{eff} of these composites with the similar geometry but larger inclusions (p = 0.3) are considered. As shown in Fig. 8, the ε_{eff} of the slab along y direction and that of the lattice along the cube edge have a good match. Moreover, stronger spatial dispersion is observed, and the relative difference $|\varepsilon_{\text{Edge–Edge}} - \varepsilon_{\text{SD–VD}}| / \varepsilon_{\text{Ray}}$ is less than 1% up to 3.24 in terms of f/f_{20}.

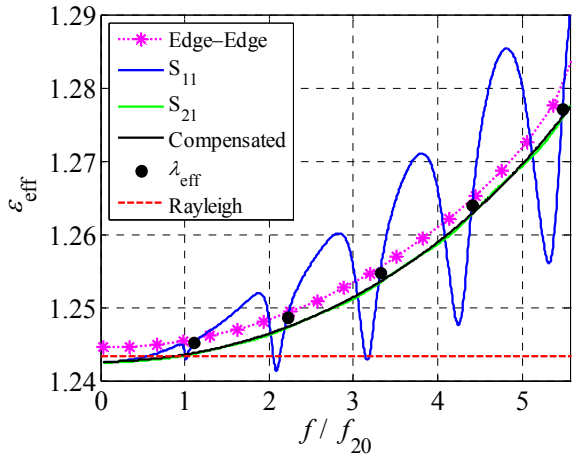

Fig. 7. The comparison among all the retrieved permittivities by different methods for p = 0.1 and ε_i = 10.

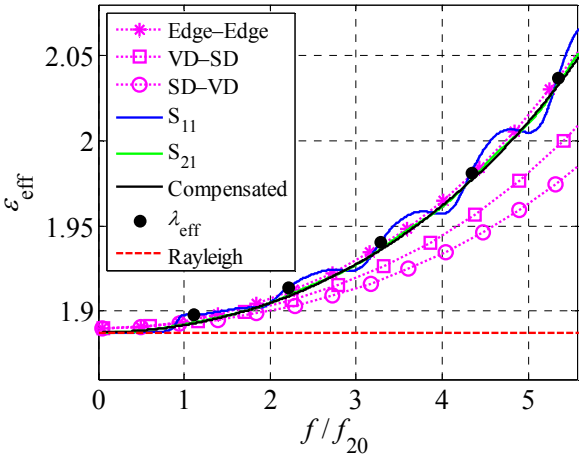

Fig. 8. The comparison among all the retrieved ε_{eff} by different methods for p = 0.3 and ε_i = 10.

It is also noted from Fig. 8 that the S_{11} method still seems unstable but the variation is much smaller than in Fig. 7 due to the increase of the targeted effective permittivity. For smaller p and moderate ε_i = 10, S_{11} is very small in amplitude and close to zero. When p increases, S_{11} becomes larger and thus less sensitive to the errors. So the tolerance of the S_{11} method could be improved as sufficiently large S_{11} is encountered, for instance, when the composites with a larger p or higher permittivity contrast are considered.

2. Quasi-static approximation limit

These results provide us possibilities to address the question regarding the limitations of the quasi-static homogenization principles for these dielectric composites with relatively small permittivity contrasts and volume fractions.

It is true that the homogenization with the effective constitutive parameters is in essence an approximation process, and may become less meaningful in the rigorous sense when the geometry details of the composites are not sufficiently small compared with the free-space or effective wavelength inside [8, 17]. However, it will be still interesting to quantitatively explore the limitation of the quasi-static approximation in a quasi-dynamic range by defining some criterion. In this paper, the relative difference between the retrieved ε_{eff} and the static Lord Rayleigh prediction ε_{Ray} is chosen as a proper target to be investigated, i.e., $|\varepsilon_{\text{eff}} - \varepsilon_{\text{Ray}}| / \varepsilon_{\text{Ray}}$.

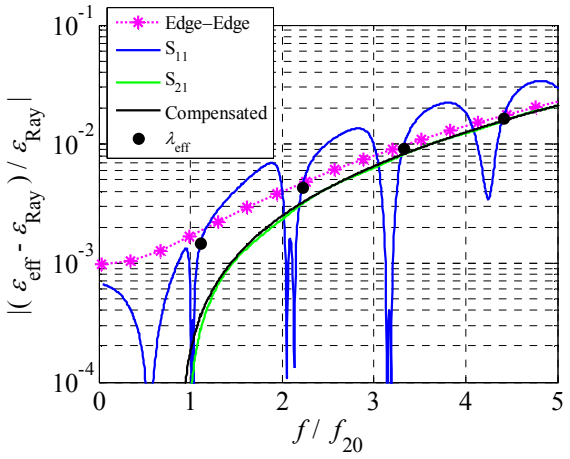

Fig. 9. The relative difference between all the retrieved permittivities and the static Rayleigh prediction for p = 0.1 and ε_i = 10.

Figures 9 and 10 illustrate the relative differences between the retrieved ε_{eff} and the static prediction ε_{Ray} for different p. Let us regard 1% relative difference as a satisfactory tolerance, and define the limit frequency meeting this criterion as f_{L}. Thus, the quasi-static approximation limit is denoted as f_{L}/f_{20}. Then for composites of our interest with different p, the one-principal-axis quasi-static approximation can be considered to be valid up to 3.5 and 2.1 in terms of f/f_{20}, correspondingly $a/\lambda_{\text{eff}} \approx$ 1/5.7 and 1/9.5. Within these limits, the relative difference between the ε_{eff} along the edge and the volume diagonal, i.e., $|\varepsilon_{\text{Edge–Edge}} - \varepsilon_{\text{SD–VD}}| \,/\, \varepsilon_{\text{Ray}}$, is also less than the 1% satisfactory tolerance for the cubic lattice. As a result, the spatial dispersion can be neglected below these quasi-static limits.

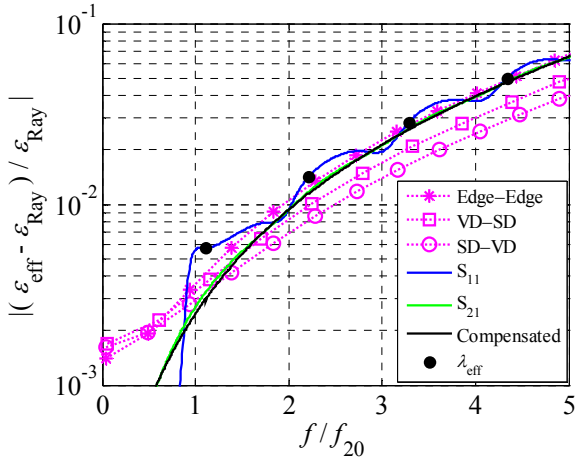

Fig. 10. The relative difference between all the retrieved permittivities and the static Rayleigh prediction for $p = 0.3$ and $\varepsilon_{\text{i}} = 10$.

To grasp the dependence of this limit on the inclusion properties, more composites, similar to that shown in Fig. 1 but with different ε_{i} and p, are considered and the computed limits f_{L}/f_{20} are shown in Table 1. It is shown that this limit decreases with the increase of either the permittivity contrast or the inclusion volume fraction. That is, for increasing frequency, the quasi-static approximation will lose its predictive power more quickly for the composite whose inclusions have stronger interactions.

3. Quasi-static limit for one-dimensional lattice

The computational complexity of the 3D simulation prevents us from any exhaustive analyses for different p and ε_{i}. In order to confirm the results above, a computationally inexpensive 1D periodic lattice in Fig. 11 is considered, whose dispersion equation reads [18],

$$\cos(\beta d_2) = \cos(k_1 d_1)\cos(k_2(d_2 - d_1)) - \frac{\varepsilon_1 + \varepsilon_2}{2\sqrt{\varepsilon_1 \varepsilon_2}} \sin(k_1 d_1)\sin(k_2(d_2 - d_1)), \quad (9)$$

where the wave numbers are $k_1 = k\,(\varepsilon_1)^{1/2}$, $k_2 = k\,(\varepsilon_2)^{1/2}$, the volume fraction of the material with ε_1 and thickness d_1 is $p = d_1/d_2$ and d_2 is the unit cell width. The frequency dependence of the ε_{eff} can therefore be calculated according to $\beta = k\varepsilon_{\text{eff}}^{1/2}$. We can then find out in a similar way the quasi-

Table 1: f_{L}/f_{20} for varying inclusion permittivity ε_{i} and volume fraction p for the 3D composites

p \ ε_{i}	3	10	60
0.1	7	3.5	1.6
0.2	5.2	2.4	1
0.3	4.5	2.1	0.8

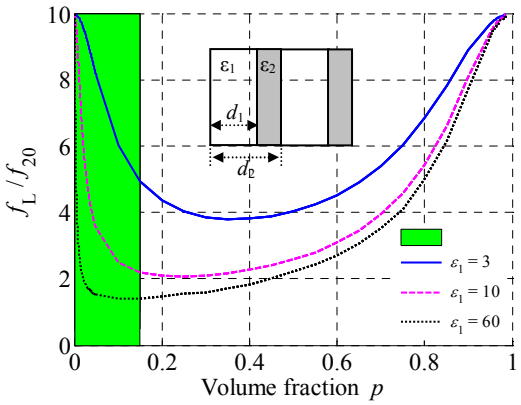

Fig. 11. f_{L}/f_{20} as a function of p and ε_1 for a 1D lattice with $\varepsilon_2 = 1$.

static limit as a function of full sets of p and ε_1. In this case, the satisfactory tolerance is defined as 1% deviation of the quasi-dynamic ε_{eff} from the Maxwell Garnett prediction ($\varepsilon_{\text{MG}} = p\varepsilon_1 + \varepsilon_2 - p\varepsilon_2$), i.e., $|\varepsilon_{\text{eff}} - \varepsilon_{\text{MG}}| \,/\, \varepsilon_{\text{MG}}$. The comparison between Table 1 and Fig. 11 shows that for the same choice of p and ε_{i}, the quasi-static limits f_{L}/f_{20} for the 3D and 1D composites are close to each other despite the obviously geometrical differences. Figure 11, also, supports our remarks in the previous subsection that the increase of the permittivity contrast will reduce the f_{L}/f_{20}, but it does not change monotonously with the volume fraction p for this 1D lattice. The reason we do not observe a similar phenomenon in 3D composites can be explained

as follows. If clusters are not allowed, the maximum p of such composites is about 0.52, with which the ε_i cannot dominate the ε_{eff}. The Rayleigh result, for example at $p = 0.5$, $\varepsilon_e = 1$, and $\varepsilon_i = 60$, is roughly 4.52, which still inclines toward the host permittivity ε_e. Thus, we are in a region similar to the green area in Fig. 11, where f_L/f_{20} decreases monotonously with increasing p.

V. CONCLUSION

The quasi-dynamic approximation of simple composites is studied. By comparing the retrieved quasi-dynamic ε_{eff} with the static Lord Rayleigh prediction, the frequency limit of the quasi-static approximation is then considered.

Moreover, different homogenization methods are developed and validated by a comparison of all the retrieval results. For the slab composite, the conventional NRW method will give rise to FP resonances distorting the result. We present a compensation approach to counteract such an influence, which yields the result matching that by the S_{21} method. The retrieval method involving only S_{21} is a more broadband approach than the others utilizing S_{11}, particularly for these low reflection cases. It also deserves to be mentioned that the retrieval method from only one of the S-parameters may be unstable when the desired permittivity varies over a large dynamical scale, since the algorithm utilized to seek complex roots of Eq. (5) and (6) is sensitive to the initial guess. In particular, at the transparent window when S_{11} equals zero, the ε_{eff} can be separately calculated using the EWR method, which provides a good validation for other retrieval techniques.

For the infinite lattice, the spatial dispersion is smaller than the deviations from the static Rayleigh prediction, shown in Figs. 6 and 8. This phenomenon gives us the possibility of defining a dynamic effective permittivity different from the static one and yet relatively independent of the propagation direction in the quasi-dynamic range.

Finally, the quasi-static approximation limits f_L/f_{20} are calculated for the composites with similar geometry but different permittivity contrasts and inclusion volume fractions, according to the criterion that $|\varepsilon_{eff} - \varepsilon_{Ray}| / \varepsilon_{Ray} \leq 1\%$. Unfortunately, we fail to establish such a definition of the limit that becomes parameter-independent for these composites. It is, however, interesting to find out that when the frequency increases, the stronger the interactions among inclusions are, the quicker the quasi-static approximation will lose its predictive power for the ε_{eff} of the mixtures, if clusters are not allowed. A supplementary 1D lattice is analogically studied to confirm our conclusion. Our parallel work [19] focuses on the influence of finite slab thickness on the homogenization and the characterization of different layers comprising the slab, whose geometry setup is shown in Fig. 1.

ACKNOWLEDGMENT

This work is partially supported by the Academy of Finland.

REFERENCES

[1] G. W. Milton, *The Theory of Composites*, Cambridge University Press, Cambridge, 2002.

[2] A. I. Căbuz, D. Felbacq, and D. Cassagne, "Spatial dispersion in negative-index composite metamaterials," *Phys. Rev. A*, vol. 77, pp. 0138071-01380711, 2008.

[3] J. A. Kong, *Electromagnetic Wave Theory*, EMW Publishing, Cambridge, 2008.

[4] A. Sihvola, *Electromagnetic Mixing Formulas and Applications*, IEE, London, 1999.

[5] J. Zhou, L. Zhang, G. Tuttle, T, Koschny, and C. M. Soukoulis, "Negative index materials using simple short wire pairs," *Phys. Rev. B*, vol. 73, pp. 0411011-0411014, 2006.

[6] T. C. Yang, Y. H. Yang, and T. J. Yen, "An anisotropic negative refractive index medium operated at multiple-angle incidences," *Opt. Express*, vol. 17, pp. 24189-24197, 2009.

[7] D. R. Smith, D. C. Vier, T. Koschny, and C. M. Soukoulis, "Electromagnetic parameter retrieval from inhomogeneous metamaterials," *Phys. Rev, E*, vol. 71, pp. 0366171-03661711, 2005.

[8] C. Menzel, T. Paul, C. Rockstuhl, T. Pertsch, S. Tretyakov, and F. Lederer, "Validity of effective material parameters for optical fishnet metamaterials," *Phys. Rev. B,* vol. 81, pp. 0353201-0353205, 2010.

[9] R. A. Shore and A. D. Yaghjian, "Traveling waves on two- and three- dimensional periodic arrays of lossless scatterers," *Radio Sci.*, vol. 42, pp. RS6S211- RS6S2140, 2007.

[10] Computer Simulation Technology AG, *CST Microwave Studio 2009*, www.cst.com, 2009.

[11] D. Escot, D. Poyatos, I. Montiel, and M. Patricio, "Soft Computing Techniques for Free-Space Measurements of Complex Dielectric Constant," *ACES Journal*, vol. 24, pp. 324-331, 2009.

[12] A. M. Nicolson and G. F. Ross, "Measurement of the intrinsic properties of materials by time-

domain techniques," *IEEE Trans. Inst. Meas.*, vol. 19, pp. 377-382, 1970.

[13] W. B. Weir, "Automatic measurement of complex dielectric constant and permeability at microwave frequencies," *Proceedings of the IEEE*, vol. 62, pp. 33-36, 1974.

[14] D. R. Smith, S. Schultz, P. Markoš, and C. M. Soukoulis, "Determination of effective permittivity and permeability of metamaterials from reflection and transmission coefficients," *Phys. Rev. B*, vol. 65, pp. 1951041-1951045, 2002.

[15] X. Chen, T. M. Grzegorczyk, B.-I. Wu, J. Pacheco, and J. A. Kong, "Robust method to retrieve the constitutive effective parameters of metamaterials," *Phys. Rev. E*, vol. 70, pp. 166081-166087, 2004.

[16] J. D. Joannopoulos, R. D. Meade, and J. N. Winn, *Photonic Crystals*, Princeton University Press, New Jersey, 1995.

[17] C. R. Simovski, "Material parameters of metamaterials," *Opt. and Spectrosc.*, vol. 107, pp. 726-753, 2009.

[18] S. Tretyakov, *Analytical Modeling in Applied Electromagnetics*, Artech House, London, 2003.

[19] H. Kettunen, J. Qi, H. Wallén, and A. Sihvola, "Homogenization of thin dielectric composite slabs: techniques and limitations," Submitted to *ACES Journal*.

Jiaran Qi was born on October 19, 1981, in Harbin, China. He received the B.E. (Communication Engineering) and M.E. degrees (Electromagnetics and Microwave Technology) from Harbin Institute of Technology, China in 2004 and 2006, respectively. He is currently working toward the D.Sc. degree at the Department of Radio Science and Engineering in Aalto University School of Science and Technology (the former Helsinki University of Technology), Finland. His current research interests include electromagnetic wave interaction with complex media, modeling of complex materials, such as composites and metamaterials.

Henrik Kettunen was born in Orimattila, Finland, in 1980. He received the M.Sc. (Tech.) and Lic.Sc. (Tech.) degrees in Electrical Engineering from the Helsinki University of Technology (TKK), Espoo, Finland, in 2006 and 2009, respectively. He is currently working toward the D.Sc. (Tech.) degree in Electrical Engineering at the Aalto University School of Science and Technology, Finland. His research interests include electromagnetic modeling of complex materials.

Henrik Wallén was born in 1975 in Helsinki, Finland. He received the M.Sc. (Tech.) and D.Sc. (Tech.) degrees in Electrical Engineering in 2000 and 2006 from the Helsinki University of Technology (which is now part of Aalto University). He is currently working as a Postdoctoral Researcher at the Aalto University School of Science and Technology, Department of Radio Science and Engineering in Espoo, Finland. He is Secretary of the Finnish National Committee of URSI (International Union of Radio Science). His research interests include electromagnetic theory, modeling of complex materials, and computational electromagnetics.

Ari Sihvola was born on October 6th, 1957, in Valkeala, Finland. He received the degrees of Diploma Engineer in 1981, Licentiate of Technology in 1984, and Doctor of Technology in 1987, all in Electrical Engineering, from the Helsinki University of Technology, Finland.

Besides working for TKK and the Academy of Finland, he was a visiting engineer in the Research Laboratory of Electronics of the Massachusetts Institute of Technology, Cambridge, in 1985–1986, and in 1990–1991, he worked as a visiting scientist at the Pennsylvania State University, State College. In 1996, he was a visiting scientist at the Lund University, Sweden, and in 2000–2001 he was visiting professor at the Electromagnetics and Acoustics Laboratory of the Swiss Federal Institute of Technology, Lausanne. In the summer of 2008, he was visiting professor at the University of Paris XI, France. Ari Sihvola is professor of electromagnetics in Aalto University School of Science and Technology (before 2010 Helsinki University of Technology) with interest

in electromagnetic theory, complex media, materials modeling, remote sensing, and radar applications. He is Chairman of the Finnish National Committee of URSI (International Union of Radio Science) and Fellow of IEEE. He was awarded the five-year Finnish Academy Professor position starting August 2005. Starting January 2008, he is director of the Graduate School of Electronics, Telecommunications, and Automation (GETA).

Multi-Frequency Higher-Order ADI-FDTD Solvers for Signal Integrity Predictions and Interference Modeling in General EMC Applications

Nikolaos V. Kantartzis

Department of Electrical and Computer Engineering, Faculty of Technology
Aristotle University of Thessaloniki, GR-54124 Thessaloniki, Greece
kant@auth.gr

Abstract ─ The precise and wideband modeling of electromagnetic interferences and their effect on the signal integrity of microwave structures is presented in this paper, via an efficient 3-D dispersion-optimized method. Introducing a novel frequency-dependent alternating-direction implicit finite-difference time-domain algorithm in general curvilinear coordinates, the technique establishes a consistent multi-frequency higher-order stencil management formulation. Moreover, for arbitrary geometric discontinuities and abrupt curvatures, a field projection scheme is devised. Thus, the detrimental dispersion errors of existing approaches are drastically minimized and time-steps can now greatly exceed the stability condition at any frequency range. The proposed method leads to affordable simulations and very accurate results, as proven by a variety of electromagnetic compatibility problems.

Index Terms ─ EMC analysis, EMI prediction, higher-order ADI-FDTD methods, signal integrity.

I. INTRODUCTION

An essential issue in the electromagnetic compatibility (EMC) realization of modern electronic equipment is the fulfillment of certain immunity and emission standards. To this aim, the role of electromagnetic interference (EMI) is deemed critical since it can seriously affect the signal integrity of most microwave devices. Actually, this issue has become the topic of a constant research for the design of proficient components with the highest possible sensitivity and confined intermodulation distortions [1-11]. Considering that these structures may receive many expensive reconfigurations before their final form, the need for a cost-effective and robust approach offering fast and rigorous EMI estimations, is indeed of major importance. However, this task is rather cumbersome, especially on a broadband basis, as most of the devices have a lot of geometric details, arbitrary discontinuities, or involve dispersive materials which call for fine meshes and prolonged simulations. For these difficulties to be overcome, the combination of the alternating-direction implicit (ADI) concept with the finite-difference time-domain (FDTD) method [12] can be proven a powerful means [13, 14]. Nonetheless, extensive studies revealed that the original algorithm suffers from rapidly growing dispersion errors as time-steps increase, a fact that led to several noteworthy algorithms for its correction [15-25].

The key objective of this paper is the development of an accuracy-adjustable class of dispersion-reduction ADI-FDTD solvers for the enhanced analysis of signal integrity and EMI interactions in contemporary EMC applications. Being fully wideband, the 3-D algorithm associates new higher-order frequency-dependent spatial/temporal forms with optimal stencils that produce generalized dual curvilinear grids. Furthermore, for the manipulation of small-scale structural details or irregularities, a conformal field projection on preselected planes is introduced. On the other hand, to preserve consistency amid neighboring areas, a family of boundary and continuity conditions is employed to ensure smooth transition. In view of its controllable formal precision and unconditional stability, the multi-frequency technique provides certain advantages over conventional approaches. Particularly, it permits the choice of time-steps well above the Courant limit, without creating prohibitive dispersion artifacts and enables the construction of coarse, yet

sufficiently adaptable, lattices. Therefore, intermodulation deformations are thoroughly resolved and signal integrity is reliably estimated. These properties are numerically validated by an assortment of different EMC arrangements, like waveguides, resonators, cavities, junctions, specialized antennas, metamaterial structures, and anechoic/reverberation test facilities.

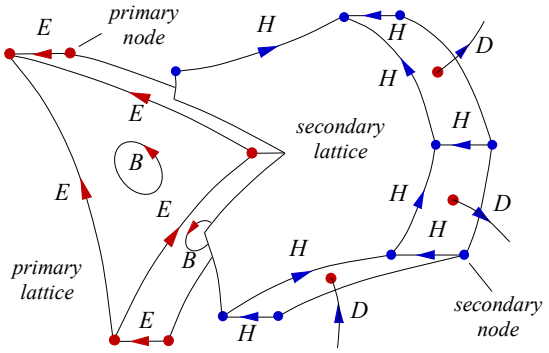

Fig. 1. Geometry of the dual mesh tessellation.

II. HIGHER-ORDER OPERATORS

The central contribution of our formulation focuses on the development of a high-precision non-orthogonal ADI-FDTD technique, whose actual performance – unlike several existing approaches – does not depend on dispersion errors as time-steps exceed the Courant limit. Moreover, the novel algorithm is intended to be fully generalized in terms of adaptive meshing, geometric details, and material modeling to successfully simulate all intricate wave interactions without needing excessive computational resources.

A. Discretization and dual-lattice construction

Starting from the correct interpretation of the underlying physical problem, the proposed discretization framework is based on highly-accurate spatial/temporal interpolation schemes and dual adaptive grids, as those of Fig. 1. More specifically, the construction of these meshes is based on the selection of the appropriate coordinate system that leads to cells of optimal quality [24-27]. To this aim, we start with an adaptive primary lattice, whose refinement is conducted according to the geometric details of the structures, under study, and the achievement of the minimum reflection error at neighboring cell interfaces. This local refinement process on the primary grid yields a finite number of uniquely defined local patterns [28, 29], which, if properly assembled at their adjacent vertices, enable the formation of an equally consistent secondary grid (see Fig. 1). Next and via a dual mesh notion, magnetic field **H** components are placed at secondary edge centers, to remain in absolute staggering with electric field **E** components located at primary edge centers [30-32]. Note that all quantities required for the update of the proposed algorithm are evaluated through a field flux concept across cell faces [7] which preserves the hyperbolic nature of Maxwell's equations and saves a lot of numerical effort.

B. Accuracy-controllable operators

Let us assume a general coordinate system (u,v,w) defined by the corresponding $g(u,v,w)$ metrical coefficients, which describe all of its implementation issues. In our formulation, spatial and temporal derivatives are evaluated by a new Lth-order accurate operator, whose expressions are, respectively, given by

$$S_\eta\left[f\big|_{u,v,w}^{t}\right]=\frac{e^{L\Delta\eta/4}}{\sqrt{\pi}\Delta\eta}Q_\eta^L\left[f\big|_{u,v,w}^{t}\right]+\sum_{s=1}^{3}\left(1+\frac{\Delta\eta}{4s}\right)f\big|_{\eta\pm s\Delta\eta}^{t}, \quad (1)$$

$$\mathcal{T}\left[f\big|_{u,v,w}^{t}\right]=\frac{1}{\Phi(\Delta t)}\left(f\big|_{u,v,w}^{t+\Delta t/2}-f\big|_{u,v,w}^{t-\Delta t/2}\right)-q\frac{\partial^3 f}{\partial t^3}\bigg|_{u,v,w}^{t}, \quad (2)$$

where $\eta\in(u,v,w)$, $\Delta\eta\in(\Delta u,\Delta v,\Delta w)$ is the spatial increment and Δt the time-step. Parameter q controls the impact of extra nodes due to higher-order derivatives [7, 10]. After some algebra, one obtains

$$q=(a+2)(\Delta\eta)^{L-1}-(a-1)(\Delta\eta)^{L}, \quad (3)$$

for $a\in[0,1]$ being a weighting coefficient relative to the frequency spectrum of our approximation.

Proceeding to the analysis of (1), special attention must be drawn to the contribution of the novel multi-frequency operator $Q_\eta[.]$. Its extra degree of freedom D denotes the suitable stencil size and introduces auxiliary nodes that allow the satisfactory modeling of abrupt waves or fine geometric details. In particular,

$$Q_\eta^L\left[f\big|_{u,v,w}^{t}\right]=\frac{g(u,v,w)}{\Psi(k_\eta\Delta\eta)}\sum_{l=1}^{L}Y_l\left\{\sum_{d=1}^{D}V_{l,d}\left[f\big|_{u,v,w}^{t}\right]\right\}. \quad (4)$$

Coefficients Y_l (with a total sum of 1/2) improve grid consistency, primarily in signal integrity estimations, whereas correction functions $\Phi(\Delta t)$ and $\Psi(k_\eta\Delta\eta)$ of (2) and (4), enhance the accuracy of derivative approximation. In wideband EMI simulations, which are rather demanding for most time-domain schemes, these functions are proven very

effective. Essentially, they consider the excitation frequency content and subdue all oscillatory modes that can corrupt propagating waves. Note that for low-frequency applications, where strong coupling phenomena occur, this behavior is retained, as well. Such an issue is deemed critical for EMC optimization due to the important influence of the excitation on the final design. In this context, function $\Psi(k_\eta\Delta\eta)$, with k_η the k_u, k_v, or k_w component of wavevector **k**, gives the best nodal pattern for the construction of the mesh. To acquire their arguments, the $\mathcal{S}_\eta\,[e^{jk\eta}]/\partial_\zeta e^{jk\eta} \rightarrow 1$ constraint should be satisfied, which in higher-order realizations becomes $\mathcal{S}_\eta\,[e^{jk\eta}]/\partial_\eta\, e^{jk\eta} \approx 2[\cos(k_\eta\Delta\eta) - 1]$; a strict requirement for minimizing dispersion errors, not easily achieved by traditional techniques [31]. So, suitable $k_\eta\Delta\eta$ are derived by the Fourier transform of already computed components at fixed positions near geometric details and the mean value of the estimated frequency spectrum. Herein, the two functions are selected to be the combination of exponential and hyperbolic terms

$$\Phi(\Delta t) = \frac{e^{\Delta t/2}}{2\Delta t - 3}\sinh\left[\Delta t\sqrt{1-(\Delta t/2)^2}\right], \tag{5}$$

$$\Psi(k_\eta\Delta\eta) = e^{5\sqrt{2p-1}}\Delta\eta\cosh\left(\Delta\eta\sqrt{p+2}\right), \tag{6}$$

with $p = k_\eta\Delta\eta/2$. To complete the theoretical description, operators $V_{l,d}[.]$, in (4), must be defined. Basically, they are responsible for the combination of the nodal patterns introduced by (4). In contrast to Yee's method that involves only two lattice points for derivative computation, the specific scheme employs a complete set of nodes which yield coarse but very robust grids [34]. A typical w-directed (for $D = 5$) $V_{l,d}[.]$ operator receives the compact expression of

$$V_{l,d}\left[f\big|^t_{u,v,w}\right] = \frac{(\Delta w)^l}{5l+1} \times\sum_{r=-1}^{+1}\left[f\big|^t_{u-\Delta u,v+\Delta v,w+r\Delta w} - f\big|^t_{u+\Delta u,v-\Delta v,w-r\Delta w}\right]. \tag{7}$$

The purpose of r is the consistent treatment of regions near perfectly electric conducting outer walls or composite media interfaces, i.e. cases where stencils extend at least two nodes on each side of a mesh point.

Observing the multi-frequency algorithm, presented above, it is stated that (1), (2), (4), and (7) launch a class of 3-D higher-order spatial and temporal forms with advanced dispersion-reduction assets. In fact, it is the structural consistency of (4) and (7) that increases the overall performance. Consequently, the latter operators subdue the typical discretization defects created during the modeling of most microwave structures and especially of electrically large ones. Moreover, their auxiliary nodes guarantee the correct representation of laborious geometries, so evading severe inaccuracies [30-34]. Given that lengthy propagation paths in several EMC setups are related to multiple interactions from compound interfaces, the extraction of wideband update formulas is expected to be a considerable contribution. However, one must be aware of the regularly encountered discontinuities with non-zero tangential quantities that demand notable overheads. This is, also, drastically alleviated by (1)-(7), which, except for their superior precision, can be applied to frequency-dependent problems. Thus, in the next sections, we extract novel unconditionally-stable expressions, able to offer an optimal phase velocity, mainly independent of lattice reflection errors.

III. GENERALIZED ADI-FDTD ALGORITHM

For the development of the frequency-dependent methodology, one must start from magnetic, $\mathbf{B} = [B_u, B_v, B_w]^T$, and electric, $\mathbf{D} = [D_u, D_v, D_w]^T$, flux densities

$$\mathbf{B} = \mu(\omega)\mathbf{H} = \mu_0\mathbf{H} + \mathbf{M}, \tag{8}$$

$$\mathbf{D} = \varepsilon(\omega)\mathbf{E} = \varepsilon_0\mathbf{E} + \mathbf{P}, \tag{9}$$

where $\mathbf{H} = [H_u, H_v, H_w]^T$, $\mathbf{E} = [E_u, E_v, E_w]^T$ represent magnetic and electric field intensities and $\mathbf{M} = [M_u, M_v, M_w]^T$, $\mathbf{P} = [P_u, P_v, P_w]^T$ the auxiliary magnetic and electric polarizations that consider the dispersive nature (Debye, Lorentz or Drude) of every material with constitutive parameters $\varepsilon(\omega)$, $\mu(\omega)$. Application of (1)-(7) to Faraday's and Ampere's laws, gives

$$\Xi^{\mathrm{E}}\mathcal{S}[\mathbf{E}] = -\mathcal{T}[\mathbf{B}], \tag{10}$$

$$\Xi^{\mathrm{H}}\mathcal{S}[\mathbf{H}] = \mathcal{T}[\mathbf{D}] + \sigma\mathbf{E} + \mathbf{J}, \tag{11}$$

where σ denotes the electric losses, $\mathbf{J} = [J_u, J_v, J_w]^T$ is the electric current density source used for external excitation, and $\Xi^{\mathrm{E,H}}$ are 3×3 dual metric tensors whose elements, expressed as functions of $g(u,v,w)$, characterize the (u,v,w) coordinate system selected for our analysis. On the other hand, $\mathcal{S} = [\mathcal{S}_u\ \mathcal{S}_v\ \mathcal{S}_w]^T$ is the non-orthogonal curl operator, described by

$$\mathcal{S}[.] = \mathrm{CURL}[.] = \begin{bmatrix} 0 & -S_w & S_v \\ S_w & 0 & -S_u \\ -S_v & S_u & 0 \end{bmatrix}. \quad (12)$$

The proposed ADI-FDTD algorithm retains the simplicity of the common approach [13-18] and circumvents the defects of regular finite-difference configurations. Thus, it divides the original iteration of a component into two sub-iterations, namely, for time forwarding from the nth to the $(n + 1)$th time-step, we get: the first sub-iteration from n to $n + 1/2$ and the second one from $n + 1/2$ to $n + 1$. It is emphasized that for the sake of symmetry during the ADI splitting process, the electric current density terms in (11) are replaced with judiciously adjusted temporal averages. For instance, at time-step $n + 1/2$,

$$\sigma \mathbf{E}^{n+1/2} = \sigma\left[(\mathbf{E}^{n+1/2} + \mathbf{E}^{n}) + (\mathbf{E}^{n+1} + \mathbf{E}^{n+1/2})\right]/4, \quad (13)$$

$$\mathbf{J}^{n+1/2} = (\mathbf{J}^{n+1/4} + \mathbf{J}^{n+3/4})/2, \quad (14)$$

from which the $\sigma(\mathbf{E}^{n+1/2} + \mathbf{E}^{n})/4$, $\mathbf{J}^{n+1/4}/2$ terms belong to the first and the $\sigma(\mathbf{E}^{n+1} + \mathbf{E}^{n+1/2})/4$, $\mathbf{J}^{n+3/4}/2$ terms to the second sub-iteration of the method. Let us, now, take into account the dual structure of Fig. 1 and focus on the unconditionally-stable update of the E_u component. In the first sub-iteration, the u-directed part of the dispersion-optimized Ampere's law, (11), yields

$$\mathcal{T}\left[D_u\big|_{\mathrm{A}}^{n+1/2}\right] + \frac{\sigma}{4}\left(E_u\big|_{\mathrm{A}}^{n+1/2} + E_u\big|_{\mathrm{A}}^{n}\right) + \frac{1}{2}J_u\big|_{\mathrm{A}}^{n+1/4} = \Xi_w^{\mathrm{H}} S_v\left[H_w\big|_{\mathrm{A}}^{n+1/2}\right] - \Xi_v^{\mathrm{H}} S_w\left[H_v\big|_{\mathrm{A}}^{n}\right], \quad (15)$$

with the subscript A = $(i + 1/2, j, k)$. Using (2) for the expansion of the temporal operator, one derives

$$D_u\big|_{\mathrm{A}}^{n+1/2} = D_u\big|_{\mathrm{A}}^{n} + \Phi(\Delta t)\left\{\Xi_w^{\mathrm{H}} S_v\left[H_w\big|_{\mathrm{A}}^{n+1/2}\right] - \Xi_v^{\mathrm{H}} S_w\left[H_v\big|_{\mathrm{A}}^{n}\right] - \frac{\sigma}{4}\left(E_u\big|_{\mathrm{A}}^{n+1/2} + E_u\big|_{\mathrm{A}}^{n}\right) - \frac{1}{2}J_u\big|_{\mathrm{A}}^{n+1/4} + \Lambda_D\right\}, \quad (16)$$

for Λ_D a weighting function that contains all higher-order (HO) temporal differentiations of D_u conducted at n or earlier time-steps [19-23]. Combined with the $\Phi(\Delta t)$ of (5) and the enhanced spatial operators, this extra degree of freedom leads to a large suppression of the dispersion mechanism, even when the Courant stability criterion has been appreciably exceeded.

As observed from (16), partial derivative $S_v[H_w]$ at $n + 1/2$ must be implicitly calculated, as it involves only unknown H_w values at A = $(i \pm 1/2, j + 1/2, k)$ nodes, while its $S_w[H_v]$ counterpart can be explicitly given by the already computed H_v quantities at the nth time-step. To eliminate H_w, the same ADI notion is implemented in the w-directed part of Faraday's law, (10), thus concluding to

$$\mu\mathcal{T}\left[H_w\big|_{\mathrm{B}}^{n+1/2}\right] = \Xi_u^{\mathrm{E}} S_v\left[E_u\big|_{\mathrm{B}}^{n+1/2}\right] - \Xi_v^{\mathrm{E}} S_u\left[E_v\big|_{\mathrm{B}}^{n}\right], \quad (17)$$

with B = $(i \pm 1/2, j \pm 1/2, k)$. Again, expanding $\mathcal{T}[.]$

$$H_w\big|_{\mathrm{B}}^{n+1/2} = H_w\big|_{\mathrm{B}}^{n} + \frac{\Phi(\Delta t)}{\mu}\left\{\Xi_u^{\mathrm{E}} S_v\left[E_u\big|_{\mathrm{B}}^{n+1/2}\right] - \Xi_v^{\mathrm{E}} S_u\left[E_v\big|_{\mathrm{B}}^{n}\right] + \Lambda_H\right\}, \quad (18)$$

in which Λ_H is the corresponding function for the HO temporal derivatives of H_w based on known data [34]. Nevertheless, prior to the use of (18), we will deal with the final unknown of (16), i.e. the D_u at $n + 1/2$, attributed to the presence of the frequency-dependent materials in the computational domain. To treat this term, an unconditionally-stable Crank-Nicolson technique, applied to (9) is employed. Hence,

$$P_u\big|_{\mathrm{A}}^{n+1/2} = \frac{\varepsilon_0\omega_0\Phi(\Delta t)}{4+\Phi(\Delta t)}\left(E_u\big|_{\mathrm{A}}^{n+1/2} + E_u\big|_{\mathrm{A}}^{n}\right) + \frac{4-\Phi(\Delta t)}{4+\Phi(\Delta t)}P_u\big|_{\mathrm{A}}^{n} + \frac{\Lambda_P}{4+\Phi(\Delta t)}, \quad (19)$$

where Λ_P is again the suitable weighting function. Now, plugging (18), (19) into (16) gives the update expression (20) for E_u at $n + 1/2$ (bottom of page). Parameters χ_m (for m = 1,2,…,9) are defined in terms of spatial increments, function $\Phi(\Delta t)$, material constitutive properties and metrical coefficients $g(u,v,w)$. Since, χ_m have constant values, their evaluation – hardly affecting the total burden – is conducted only once and utilized during the update of the particular field quantity. Repetition, of (20) for every j along the v mesh direction, where the spatial alternation occurs, yields a sparse 3-band tridiagonal system of equations that is recursively solved through well-known techniques [13-15]. Upon acquiring E_u, the prior formulation is identically applied to E_v and E_w, while magnetic and electric polarizations are explicitly obtained via their higher-order FDTD expressions.

The second sub-iteration for the time advancing of E_u in the interval from $n + 1/2$ to $n + 1$ reverses the roles of $S_v[H_w]$ and $S_w[H_v]$, modifying (14) as

$$\mathcal{T}\left[D_u\big|_{\mathrm{A}}^{n+1/2}\right]+\frac{\sigma}{4}\left(E_u\big|_{\mathrm{A}}^{n+1}+E_u\big|_{\mathrm{A}}^{n+1/2}\right)+\frac{1}{2}J_u\big|_{\mathrm{A}}^{n+3/4}$$
$$=\Xi_w^{\mathrm{H}}S_v\left[H_w\big|_{\mathrm{A}}^{n+1/2}\right]-\Xi_v^{\mathrm{H}}S_w\left[H_v\big|_{\mathrm{A}}^{n+1}\right]. \quad (21)$$

The unknown variables, now, are H_v and D_u (after expanding $\mathcal{T}[.]$) at $n+1$. Eliminating these terms in a way similar to (17)-(19), one gets (22), shown below, with ψ_m the counterparts of χ_m. Once all electric quantities are computed, by solving the resulting systems, the remaining fields are explicitly evaluated and the algorithm continues with the next time-step.

A completely analogous strategy holds for media, whose frequency-dependent constitutive parameter is permeability μ. Notice, also, that the extension of the multi-frequency methodology to structures, comprising both types of dispersive media, is straightforward without any additional constraints.

$$\chi_1 E_u\big|_{i+1/2,j,k}^{n+1/2}-\chi_2 E_u\big|_{i+1/2,j+1,k}^{n+1/2}-\chi_3 E_u\big|_{i+1/2,j-1,k}^{n+1/2}=\chi_4 E_u\big|_{i+1/2,j,k}^{n}+\chi_5 J_u\big|_{i+1/2,j,k}^{n+1/4}+\chi_6 S_v\left[H_w\big|_{i+1/2,j+1/2,k}^{n}\right]$$
$$-\chi_7 S_w\left[H_v\big|_{i+1/2,j,k+1/2}^{n}\right]-\chi_8\left\{S_u\left[E_v\big|_{i,j+1/2,k}^{n}\right]+S_v\left[E_u\big|_{i,j-1/2,k}^{n}\right]\right\}+\chi_9 P_u\big|_{i+1/2,j,k}^{n+1/2}, \quad (20)$$

$$\psi_1 E_u\big|_{i+1/2,j,k}^{n+1}-\psi_2 E_u\big|_{i+1/2,j,k+1}^{n+1}-\psi_3 E_u\big|_{i+1/2,j,k-1}^{n+1}=\psi_4 E_u\big|_{i+1/2,j,k}^{n+1/2}+\psi_5 J_u\big|_{i+1/2,j,k}^{n+3/4}-\psi_6 S_w\left[H_v\big|_{i+1/2,j,k+1/2}^{n+1/2}\right]$$
$$+\psi_7 S_v\left[H_w\big|_{i+1/2,j+1/2,k}^{n+1/2}\right]+\psi_8\left\{S_v\left[E_w\big|_{i,j,k+1/2}^{n+1/2}\right]-S_w\left[E_v\big|_{i,j,k-1/2}^{n+1/2}\right]\right\}-\psi_9 P_u\big|_{i+1/2,j,k}^{n+1/2}, \quad (22)$$

Indeed, every material is rigorously modeled by the appropriate scheme regarding the variation of ε or μ [17]. Finally, it is important to stress that, aside from some limited storage needs, the novel procedure does not considerably increase the total CPU and memory requirements. On the contrary, its ability to accomplish dispersion-optimized simulations by letting temporal increments to be greatly augmented, leads to serious savings.

IV. STABILITY AND DISPERSION ANALYSIS

Pertaining to the stability of the proposed algorithm, the von Neumann method is applied [12]. Thus, the two sub-iterations are expressed in matrix form as

$$n\to n+1/2: \qquad \mathbf{Z}_1\mathbf{E}^{n+1/2}=\mathbf{\Theta}_1\mathbf{E}^{n}, \quad (23)$$

$$n+1/2\to n+1: \qquad \mathbf{Z}_2\mathbf{E}^{n+1}=\mathbf{\Theta}_2\mathbf{E}^{n+1/2}, \quad (24)$$

where sparse matrices $\mathbf{Z}_l$, $\mathbf{\Theta}_l$ (for $l=1,2$) are created by the proper χ_m and ψ_m parameters during the rearrangement of the system of equations. If (23) and (24) are combined into a single equation, one obtains

$$\mathbf{E}^{n+1}=\mathbf{Z}_2^{-1}\mathbf{\Theta}_2\mathbf{Z}_1^{-1}\mathbf{\Theta}_1\mathbf{E}^{n}=\mathbf{K}\mathbf{E}^{n}. \quad (25)$$

The eigenvalues of matrix $\mathbf{K}$ are found to be

$$\rho_{1,2}=1, \quad \rho_\tau=\left[\sqrt{G_1^2-7G_2^2}\pm j\left(G_2/5-2G_1\right)\right]/5G_2, \quad (26)$$

for $\tau=3,\ldots,6$ and coefficients G_1, G_2 depending on $(\Delta t/\Delta\eta)\sin(k_\eta\Delta\eta/2)$. After the required mathematics, it is proven that the magnitudes of (26) are always less or equal to unity, thus certifying the initial convention for the algorithm. In this manner, Δt can be safely selected far beyond the Courant limit, without the prohibitive influence of the detrimental lattice errors, now, decisively suppressed up to 10 orders. Such a performance implies that the specific ADI-FDTD technique is fully conservative and of high convergence, since it subdues anisotropy errors, as well.

On the other hand, it would be very instructive to examine the improvement of the dispersion relation and verify the large suppression of the relevant error, mainly when the time-step is larger than that dictated by the conventional stability criterion. Following a general framework, the dispersion error is defined as

$$e_{disp}=F_{ex}(u,v,w,t)-F_{num}(u,v,w,t)$$
$$=\int\alpha(\omega)e^{j\left[\mathbf{k}_{ex}(\omega)-\mathbf{k}_{num}(\omega)\right]\cdot\mathbf{r}}d\omega, \quad (27)$$

in which F_{ex} is the exact and F_{num} the numerical solution of the problem with their respective wavenumber vectors $\mathbf{k}_{ex}$ and $\mathbf{k}_{num}$. Functions $\alpha(\omega)$ are the amplitudes of the Fourier transform in (27), while $\mathbf{r}$

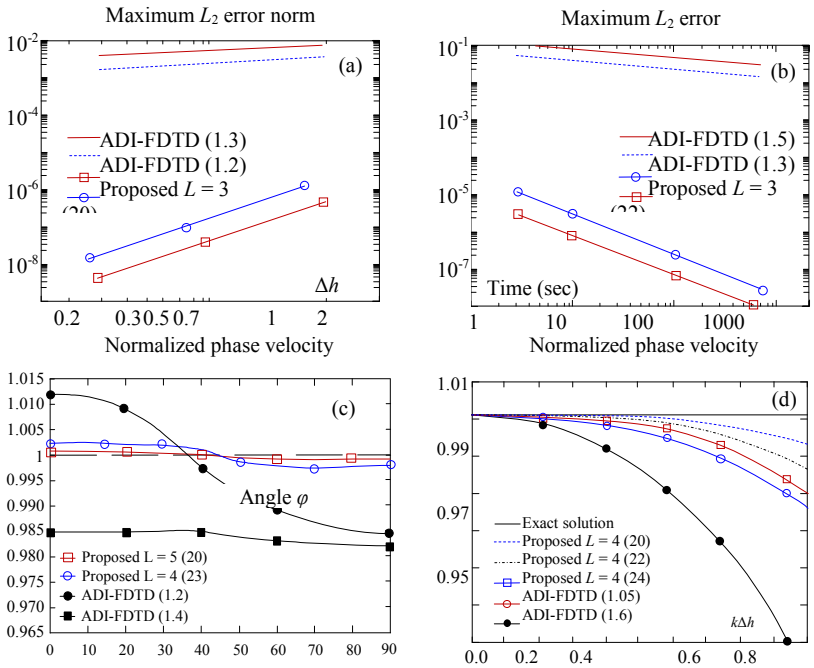

Fig. 2. Maximum L_2 error norm versus (a) spatial increment and (b) time. Normalized phase velocity versus (c) angle of propagation and (d) gridding density.

is a position vector in the (u,v,w) coordinate system. Note that F_{num} is the superposition of both propagating and evanescent waves. This idea is deemed more realistic, as it takes into account the strenuous evanescent waves that are customarily responsible for critical inaccuracies near discontinuities. In this context, the extraction of the dispersion error is based on the estimate of

$$\sum_{\zeta=u,v,w}\left|e^{j\left[k_{ex}(\omega)-k_{num}(\omega)\right]\zeta}\right| \le \sum_{\zeta=u,v,w}\left|k_{ex}(\omega)-k_{num}(\omega)\right|\left|\zeta\right|, \quad (28)$$

with $k_{ex}(\omega)=\omega$ the free-space dispersion relation and

$$k_{num}(\omega) \cong \omega\left\{1-\frac{2(\Delta t)^{L+3D}}{725}+O\left[(\Delta t)^{2L+3D}\right]\right\}, \quad (29)$$

the corresponding formula of the multi-frequency ADI-FDTD method. It is evident that (29) exhibits a significant enhancement, easily adjusted by the order of accuracy L and the complementary degree of freedom D. In the light of these considerations, e_{disp} becomes

$$e_{disp} \cong \frac{4+3(\Delta t)^{L+D}}{986}\omega\,. \quad (30)$$

To indicate the superiority of (29), for D = 3, over the typical ADI-FDTD dispersion relation, Fig. 2 presents the maximum L_2 error norm and the normalized phase velocity as a function of different parameters at a spectrum of 15 GHz. For notation compactness, we define the gauge CFLN = $\Delta t^{MT}/\Delta t^{FDTD}$ (MT = proposed or plain ADI-FDTD method) as the Courant-Friedrichs-Levy number, shown in parenthesis at the legend of every figure. Also, Table 1 summarizes the maximum dispersion error and the convergence rate of various implementations. Apparently, the higher-order methodology accomplishes a serious and wideband reduction of discretization errors, unlike the usual technique, whose performance deteriorates progressively as Δt depart from the stability condition. These benefits are more prominent for large CFLN, optimally handled by the pertinent L and D values.

Table 1: Maximum dispersion and convergence rate

Method	Grid density	Maximum dispersion	Convergence rate
ADI-FDTD (1.5)	1/40	3.84579	1.62412
ADI-FDTD (1.2)	1/25	2.465×10^{-1}	1.75679
FDTD (1.0)	1/15	1.532×10^{-2}	1.90304
Proposed L = 3 (18)	1/10	3.072×10^{-7}	3.18712
Proposed L = 5 (22)	1/9	5.068×10^{-10}	4.97021
Proposed L = 7 (25)	1/8	8.034×10^{-12}	7.01584

V. CURVED INTERFACE TREATMENT

The presence of curved media interfaces or geometric discontinuities with arbitrary cross sections in real-world EMC applications constitutes a principal modeling difficulty for the majority of numerical methods. Unfortunately, these geometric irregularities are proven detrimental for the simulation of EMI phenomena, since they arouse non-separable and highly oscillatory wavefronts that require extremely fine grid resolutions and excessive computational resources.

A. Dissimilar material boundaries

To retain consistency amid regions with media of different constitutive parameters, a set of continuity conditions with optimal sensitivity is developed. The process launches an adaptive concept, which employs extra nodes at both interface sides, in the area of node P, and follows the variation of the curvature as

$$\frac{1}{\varepsilon_1}\left(\sum_{real} s_{1,j}+\sum_{extra} s_{2,j}\right)=\frac{1}{\varepsilon_2}\left(\sum_{extra} s_{1,j}+\sum_{real} s_{2,j}\right), \quad (31)$$

where 1,2 are the dissimilar media, s differencing weights at real or extra nodes, and j the stencil for the summation around P [28-30]. Therefore, all sub-wavelength details are accurately tracked, while their contribution is directly integrated in Maxwell's equations in an exploitable form. This manipulation offers high levels of reliability and smooth regional transition without unexpected instabilities.

B. Irregular cross-sections and discontinuities

Presume the complex cross-section of Fig. 3, stretching over an angle θ_D with inner and outer mean

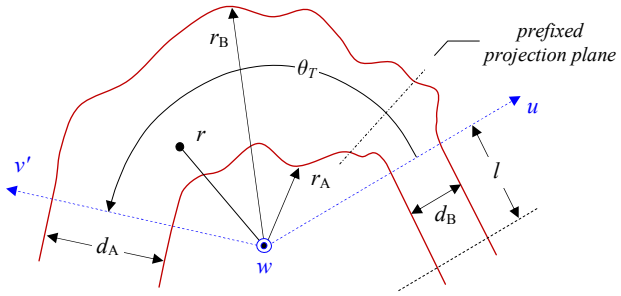

Fig. 3. An arbitrary geometric discontinuity.

radii r_1 and r_2. For its treatment, we separate every propagating mode at κ prefixed transverse planes, which satisfy all physical continuity conditions.

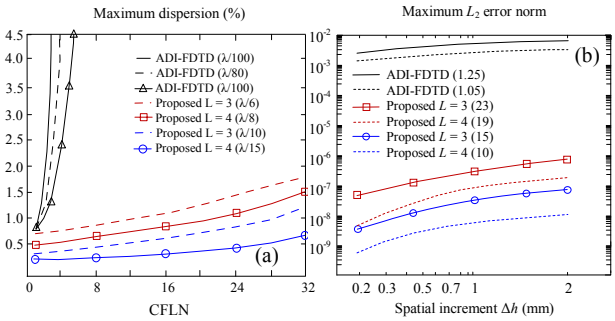

Fig. 4. (a) Maximum dispersion and (b) maximum L_2 norm variation for the parallel-plate waveguide.

Hence, each component f, defined at a local (ρ, θ, φ) system, can be expressed as

$$f(r,\theta,\varphi)=\sum\nolimits_{\kappa}\zeta_{\kappa}F_{\kappa}(r,\theta,\varphi), \quad (32)$$

with $$\zeta_{\kappa}=\frac{2}{r_M}\cos\left[\kappa\pi\left(\frac{r-r_1}{r_M}\right)\right],$$

$r_M = r_2 - r_1$, ζ_κ the corresponding eigenfunctions and F_κ known amplitude coefficients [3, 7]. The new scheme is purely conformal and provides consistent meshes via the choice of r_1, r_2. Two effectively smooth functions that fulfill this goal, with $\alpha_{\theta,\varphi}=(\theta-\varphi)/\theta_D$, $d=d_2-d_1$, and $d_2=1.5d_1$, are

$$r_1=d\left(\alpha_{\theta,\varphi}-1.65\right)+d_1-0.45d_2, \quad (33)$$

$$r_2=-d\left(\alpha_{\theta,\varphi}-1.75\right)+0.2d_1+0.35d_2. \quad (34)$$

After the prior mode decoupling, the next step is the projection of Maxwell's laws on the prefixed κ planes to obtain our differential equation model. Each solution is considered as a transverse intermediate excitation surface in the discontinuity. This approach maintains lattice quality near the geometric details, contrary to other renditions that cannot supply equivalent outcomes. In this way and using a matrix notation, Ampere's and Faraday's laws locally become

$$\partial_t\left[\varepsilon(\omega)\mathbf{E}\right]=\left(\mathbf{U}^{\mathrm{A}}+\mathbf{U}^{\mathrm{B}}\mathbf{U}^{\mathrm{C}}\right)\nabla\times\mathbf{H}-\mathbf{U}^{\mathrm{D}}\mathbf{P}, \quad (35)$$

$$\partial_t\left[\mu(\omega)\mathbf{H}\right]=-\mathbf{U}^{\mathrm{C}}\nabla\times\mathbf{E}+\mathbf{U}^{\mathrm{D}}\mathbf{H}-\mathbf{U}^{\mathrm{E}}\mathbf{M}, \quad (36)$$

in which all spatial and temporal derivatives are evaluated by means of (1) and (2). Also, the elements of $\mathbf{U}^i$ (i = A,…,E) structural matrices include the main mesh details in the vicinity of the cross-section, while their values are given by

$$U^{\mathrm{A}}_{\kappa\lambda}=(-1)^{\kappa+2\lambda}\kappa^2/\left(\kappa^2+\lambda^2\right), \qquad U^{\mathrm{B}}_{\kappa\lambda}=\kappa^2\lambda^2-1,$$

$$U^{\mathrm{C}}_{\kappa\lambda}=r_1+d/2, \qquad U^{\mathrm{D}}_{\kappa\lambda}=\kappa r_M-\lambda d/4,$$

$$U_{\kappa\lambda}^{\mathrm{E}} = (-1)^{2\kappa+\lambda} r_2 / \left(\kappa^2 + \lambda^2\right).$$

In fact, a careful choice of κ, improves the multi-frequency behavior of the entire method.

VI. NUMERICAL VERIFICATION

To substantiate the advantages of our method, we, start from a set of simple examples for which analytical solutions exist. Thus, proving its accuracy and numerical dispersion reduction capabilities, we will, then, proceed to more realistic EMC applications.

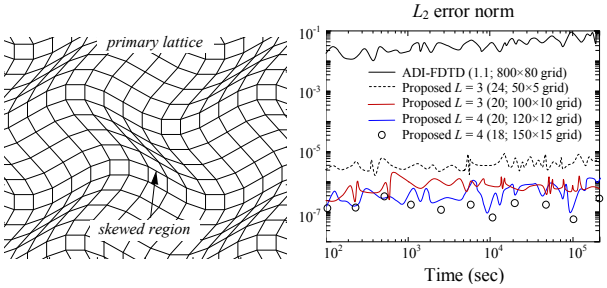

Fig. 5. Temporal variation of the L_2 norm for the parallel-plate waveguide discretized by a skewed mesh.

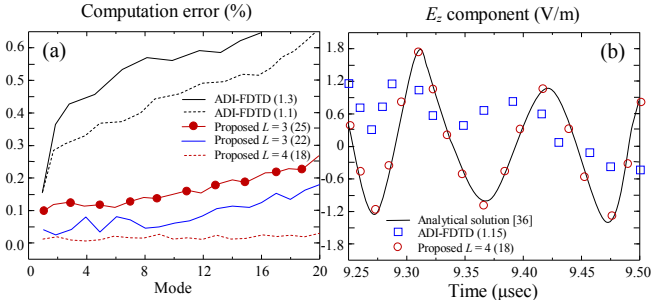

Fig. 6. (a) Computation error and (b) variation of the E_z component for the 3-D rectangular cavity.

The first test problem explores the propagation of the TM_1 mode in a parallel-plate 0.5×5.5 m waveguide. For the entire simulation, excitation and boundary field values – obtained from the analytical solution [35] – are assigned to both ports, while the device is truncated by a 12-cell perfectly matched layer [12]. The waveguide is highly elongated and, hence, considerable dispersion errors are expected to appear when employing traditional approaches or exceeding the Courant limit. Using various non-uniform grid sizes, ranging from 10×150 to 30×1200 cells, simulations are conducted until steady-state is attained. Figure 4a gives the maximum dispersion (%) versus CFLN; while, Fig. 4b gives the maximum L_2 error norm with respect to the spatial step. The large dispersion errors of the usual ADI-FDTD method as CFLN increase along with the superiority of the proposed technique are promptly discernible for all lattice resolutions.

Table 2: Resonant frequencies of the cylindrical dielectric cavity with $\varepsilon_r = 3.8$

Exact [35] (GHz)	Method	Comp. (GHz)	Error (%)	Maximum Dispersion
TE_{111} 9.896	ADI-FDTD	9.454	4.467	2.532×10^{-1}
	Proposed	9.894	0.011	5.471×10^{-11}
TM_{010} 11.235	ADI-FDTD	10.557	6.031	9.031×10^{-1}
	Proposed	11.231	0.035	8.964×10^{-11}
TM_{011} 12.211	ADI-FDTD	11.328	7.228	1.548
	Proposed	12.204	0.052	2.109×10^{-10}
TE_{112} 13.028	ADI-FDTD	11.776	9.605	3.042
	Proposed	13.019	0.068	7.286×10^{-10}
TM_{012} 14.899	ADI-FDTD	13.201	11.397	6.751
	Proposed	14.886	0.083	9.047×10^{-10}
TE_{211} 15.085	ADI-FDTD	12.843	14.862	8.984
	Proposed	15.068	0.107	4.103×10^{-9}

Additionally, the previous waveguide is revisited by means of a skewed mesh (Fig. 5) to examine the behavior of the new schemes in the case of discretization discontinuities responsible for several types of inaccuracies. From the outcomes of Fig. 5, illustrating the temporal variation of the local error and different orders of accuracy L, one can, easily, derive that our schemes remain very precise, even for large CFLN, unlike the existing second-order implementation.

Next, we move to some broadband problems and particularly to the computation of the first 20 resonant modes of a 3-D air-filled cavity with perfectly conducting walls. The modes are derived through a fast Fourier transform of the computed signals at prefixed locations. Figure 6a shows the error (%) of our calculations and Fig. 6b presents a comparison between the simulated and analytical waveform [36]. As observed, the conventional

Table 3: Maximum L_2 error for the TE_{11} mode

Lattice	ADI-FDTD	CPU time	Proposed	CPU time
10×5×90	68.43129	5.2 m	0.20421	17.35 s
32×16×288	24.58074	26.3 m	0.04372	1.46 m
56×28×504	16.04823	2.43 h	0.00347	7.72 m
78×39×702	3.94618	6.57 h	0.00025	21.89 m

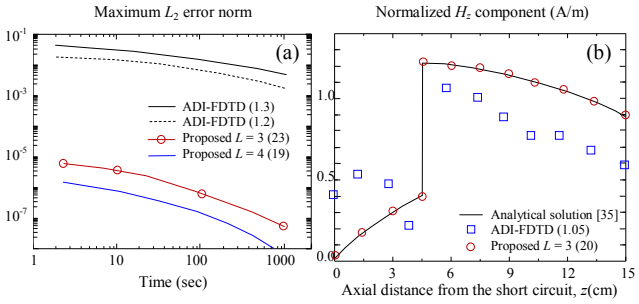

Fig. 7. (a) Maximum L_2 error norm and (b) normalized E_z component for the lossy-slab waveguide.

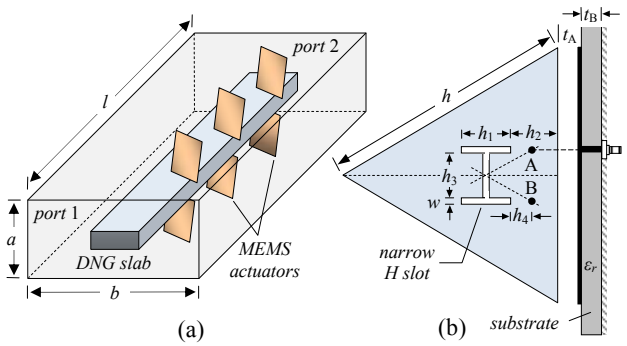

Fig. 8. (a) An RF MEMS-based coaxial waveguide and (b) a triangular H-slot microstrip antenna.

Table 4: Resonances of the coaxial waveguide

Ref. [8] (GHz)	Method	Comp. (GHz)	Error (%)	CPU Time	Maximum Dispersion
3 Actuators 11.781	ADI-FDTD	10.777	8.52	12.5 h	1.792×10^{-1}
	Proposed	11.779	0.01	51 m	3.082×10^{-11}
4 Actuators 14.205	ADI-FDTD	12.903	9.16	11.9 h	3.981
	Proposed	14.201	0.03	45 m	5.483×10^{-10}
5 Actuators 16.423	ADI-FDTD	14.647	10.81	10.9 h	6.432
	Proposed	16.235	0.05	36 m	3.561×10^{-10}

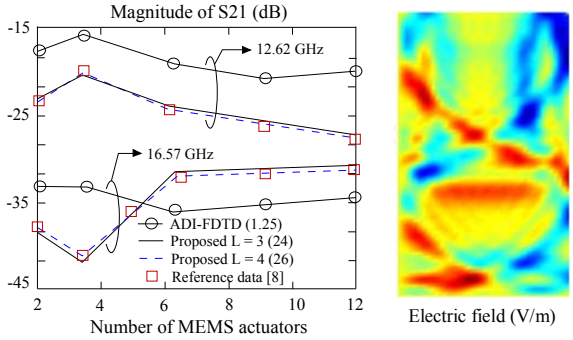

Fig. 9. Magnitude of the S_{21}-parameter versus the MEMS number and an electric field snapshot.

ADI-FDTD method lacks to provide reliable results, while our technique is, again, proven very efficient. In a similar manner, analysis moves to a parallel-plate cylindrical dielectric (ε_r = 3.8) resonator with a height of 15.75 mm and a radius of 5.35 mm. Table 2 gives the first six resonant frequencies of the structure obtained via the usual staircase ADI-FDTD method (CFLN = 1.16; grid: 180×180×360) and the proposed algorithm (CFLN = 18, L = 3; grid: 40×40×80). Herein, the conformal profile of the latter scheme leads to a 10-order dispersion error reduction.

Remaining in waveguides, let us, now, examine a 3-D air-filled 0.5×0.25×0.8 cm rectangular structure. The analytical solution [36] is inserted at the z = 0.8 cm port at all time steps together with the initial conditions. Using diverse lattices, Table 3 sums up the dispersion errors for the computation of the TE_{11} mode, from which the acceleration and the high accuracy of the enhanced method are deduced. Analogous conclusions are drawn from Fig. 7 for the same waveguide which, now, has a lossy ($\mu_r = 2 - j2$) slab with a length of 0.27 cm along the z axis. Note the inability of the regular ADI-FDTD scheme to model the material discontinuity in contrast to the new technique.

Having certified the performance of our methodology, we then investigate various realistic EMC setups in terms of EMI behavior and signal integrity prediction. Their selection has been mainly based on complexity, fine details, and electrical size. In fact such issues cannot be adequately manipulated by the usual staircase ADI-FDTD method either due to its insufficient discretization models or the need for prohibitively elongated steady-state simulations. All infinite domains are truncated by a modified 8-cell perfectly matched layer [12], while the results, whenever possible, are compared with reference/measurement data.

The first application is the coaxial waveguide of Fig. 8a, which involves a set of microelectromechanical (MEMS) actuators for selective mode propagation. Its inner slab is based on a double negative (DNG) metamaterial, described by a Drude model and the basic dimensions are: l = 11 mm, a = 1.7 mm, and b = 6.2 mm. The choice of such a problem is primarily attributed to the increasing use of complicated MEMS and DNG setups in several high-end arrangements. Table 4 gives the resonance frequencies for three cases (with L = 3) and several realizations. Moreover, the

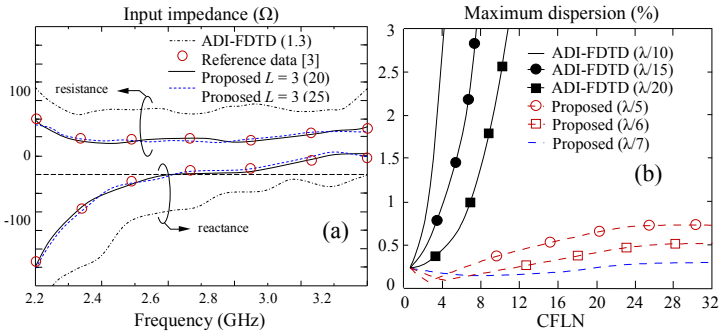

Fig. 10. (a) Input impedance and (b) maximum dispersion error for the *H*-slot microstrip antenna.

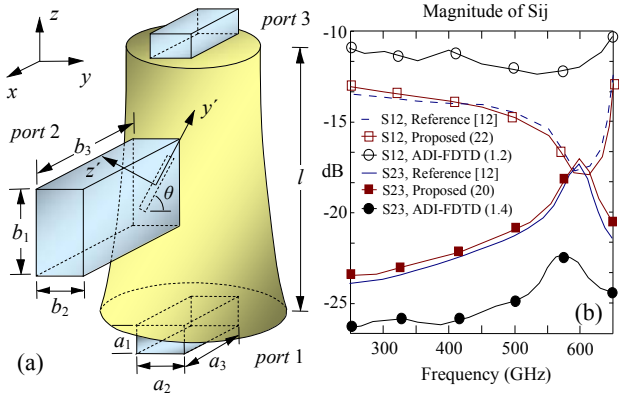

Fig. 11. (a) An inclined-slot three-port junction and (b) magnitude of *S*-parameters versus frequency.

variation of the S_{21}-parameter versus MEMS number is presented in Fig. 9 along with an indicative electric field snapshot directly above the actuators. It appears that, the proposed ADI-FDTD schemes are quite accurate and economical, attaining greatly diminished dispersion errors for large CFLN selections.

Subsequently, let us focus on the equilateral triangular *H*-slot microstrip (ε_r = 4.3) antenna of Fig. 8b, encountered in many up-to-date communication systems. Its dimensions are: h = 40 mm, h_1 = 12.2 mm, h_2 = 10.1 mm, h_3 = 12.8 mm, h_4 = 5.5 mm, t_A = 6.2 mm, t_B = 1.58 mm, and w = 1.2 mm. Figure 10a gives the input impedance, while Fig. 10b presents the maximum dispersion error versus CFLN for diverse resolutions. Note that the plain ADI-FDTD method (grid: 260×282×74; 62000 time-steps), cannot cope with this problem. Conversely, the optimized schemes are proven workable (81% coarser mesh and a maximum lattice reflection error of 2.398×10^{-10}), without the excessive CPU requirements of the usual algorithm.

Proceeding to the signal integrity of waveguide

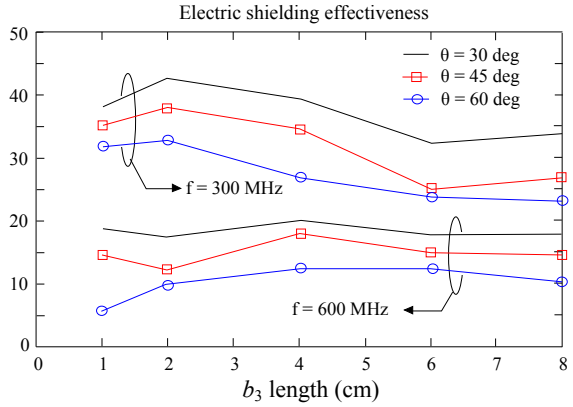

Fig. 12. Shielding effectiveness of the aperture.

junctions – a popular item in EMC applications – the next problem examines the elliptical cavity of Fig. 11a, which has a sidewall inclined slot, coupled to a rectangular waveguide. Typical dimensions are: a_1 = 6.52 mm, a_2 = 11.22 mm, a_3 = 21.35 mm, b_1 = 23.64 mm, b_2 = 11.52 mm, and l = 68.74 mm. For L= D = 3, in (1) and (3), the domain is discretized into 24×38 ×116 cells. Figure 11b gives the magnitude of two *S*-parameters, while Fig. 12 illustrates

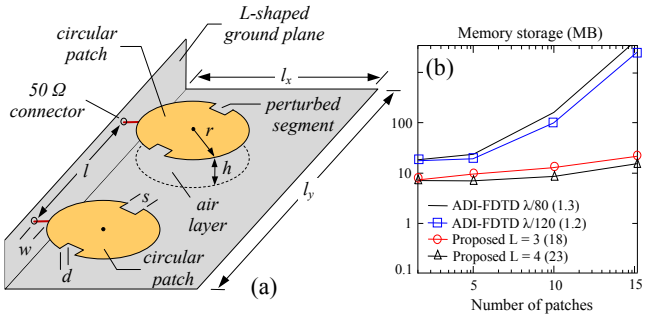

Fig. 13. (a) A wideband patch array and (b) memory storage versus the number of circular patches.

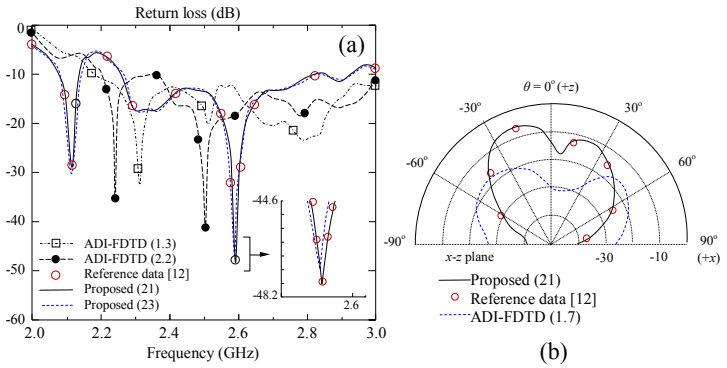

Fig. 14. (a) Return loss and (b) radiation pattern for the wideband 2×1 patch array.

the shielding effectiveness for diverse inclinations of the coupling slot and lengths of the b_3 side. As can be deduced, the enhanced ADI-FDTD technique – unlike its staircase counterpart – is able to manipulate this demanding simulation, even though the curved parts comprise a relatively large portion of the computational domain.

We, now, investigate the 2×1 patch array of Fig. 13a, with its cross-polarized profile attained by two perturbed segments (0.74% of the patch). Due to its frequent use in many systems, the optimal design of such an antenna will require a reliable simulation tool. Its dimensions are: l_x = 110 mm, l_y = 316 mm, r = 22 mm, l = 32 mm, h = 0.17 mm, w = 3.6 mm, d = 2.6 mm, and s = 5.7 mm. The mesh employs 68×110×26 cells (L = 3, D = 2), unlike the regular 91% larger grid. To verify the cost-effective profile of the new algorithm, Fig. 13b provides its memory needs versus the number of circular patches. As observed, its overhead remains relatively stable and in very low levels considering the complexity of the problem. Conversely, the usual ADI-FDTD method is proven far more expensive, especially above the typical value of 5 patches. Also, Fig. 14 shows the return loss and radiation pattern at 3.4 GHz. Again, our technique agrees very well with the reference data [3, 12] (actual accuracy: 0.0028% to 0.0032%), despite the large CFLN. In fact, this attains a dispersion error practically 9 orders of magnitude lower than the usual ADI-FDTD one (actual accuracy: 6.5312% to 8.9124%).

To this end, analysis moves to the coaxial four-port microwave splitter with a 2.4×0.8×0.6 mm DNG region (Fig. 15a). The outer conductor's cross-section is 6.3×5.7 mm and the inner's 1.3×0.9 mm. Figure 15b displays the return loss between ports 1 and 4, while Fig. 15c gives the variation of two S-parameters with regard to the number of used switches. Obviously, the wideband algorithm has a better performance for significantly lower CPU time, as indicated in Fig. 15d.

With regard to the modeling of electrically-large facilities, the next application is the inclined-wall dual reflector compact range anechoic chamber of Fig. 16. Being extremely expensive to construct, any effort toward the accurate estimation of its design parameters becomes really essential. Its

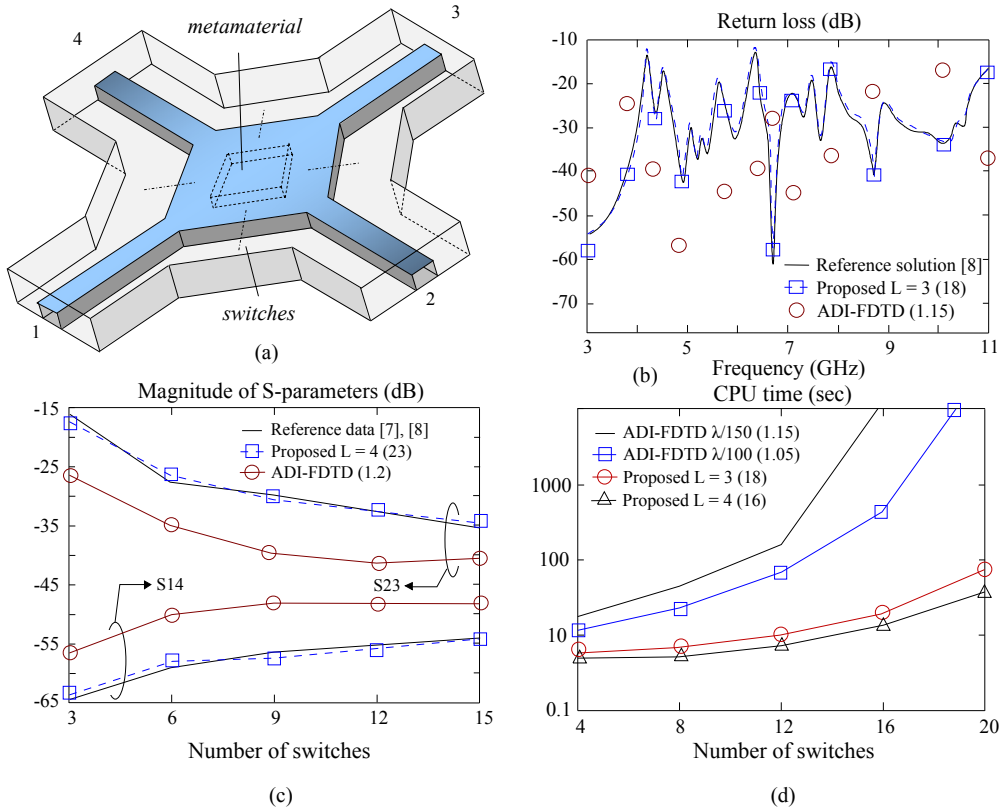

Fig. 15. (a) Geometry, (b) return loss, (c) magnitude of *S*-parameters, and (d) CPU time for a four-port microwave splitter with a DNG-based core.

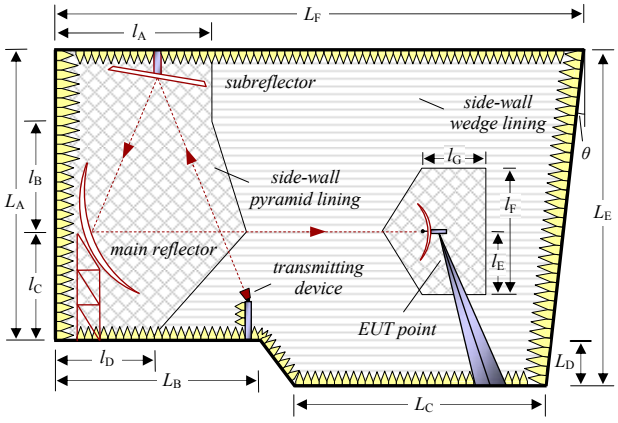

Fig. 16. A dual-reflector compact range anechoic chamber with an inclined rear wall.

width is 6.8 m, whereas L_A = 5.9 m, L_B = 4.1 m, L_C = 5.2 m, L_D = 1.5 m, L_E = 7.4 m, and L_F = 10.5 m. The diameters of the sub- and main reflector are 2.5 m and 3.9 m. Moreover, $\theta = 6^o$, l_A = 3.4 m, l_B = 2.6 m, l_C = 2.3 m, l_D = 2.1 m, l_E = 1.4 m, l_F = 2.8 m, and l_G = 1.3 m. The chamber is lined with different types of pyramids and wedges (Fig. 17b). Figure 17a presents the normalized site- attenuation of the facility's semi-anechoic version. Results indicate that notwithstanding its fine lattice, the simple ADI-FDTD method lacks to estimate the chamber's measurement suitability in contrast to our method which achieves an 85% overhead decrease. Similar outcomes are derived from Fig. 18, where the suitability of the facility's fully anechoic version is estimated. Notice, also, the impact of wedges on the performance of the semi-anechoic chamber in Fig. 19.

Finally, the signal integrity and EMI immunity of two nested reverberation chambers (Fig. 20) is analyzed. Their walls are covered by quadratic residue diffusers, i.e. a set of periodical phase gratings that diffract waves in extra directions. The movement of both stirrers is modeled with an interval of 20^o, while for each of their positions 60 time instants are sampled. The larger chamber has a length of 4.8 m, l_A = 3.72, l_B = 4.0 m and the smaller one a length of 2.44 m, l_C = 1.34 m, l_D= 1.78 m, with an aperture size of 0.32 m × 0.32 m. Figure 21 displays the shielding effectiveness of an 1.5 mm fiber-glass-fiber plate and a dielectric (ε_r = 3.4) cover. Once

more, our technique leads to very sufficient and wideband results, without critical dispersion errors due to high CFLN values.

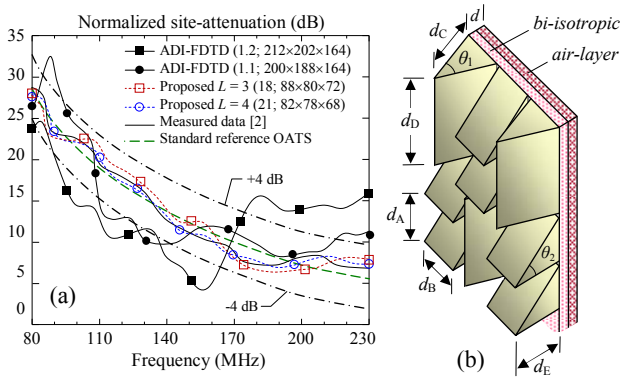

Fig. 17. (a) Normalized site-attenuation and (b) part of the absorptive wedges of the compact range chamber.

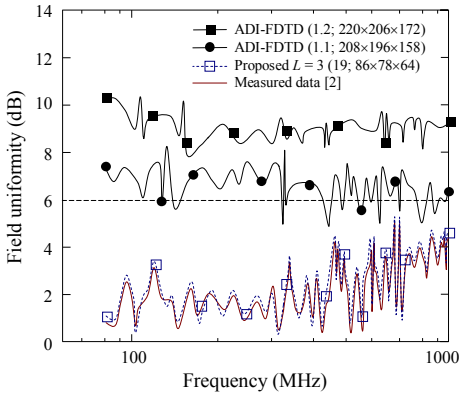

Fig. 18. Field uniformity of compact range facility .

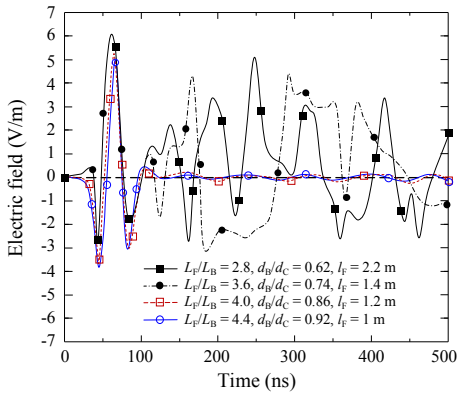

Fig. 19. Electric field variation in the compact range chamber for different structural parameters.

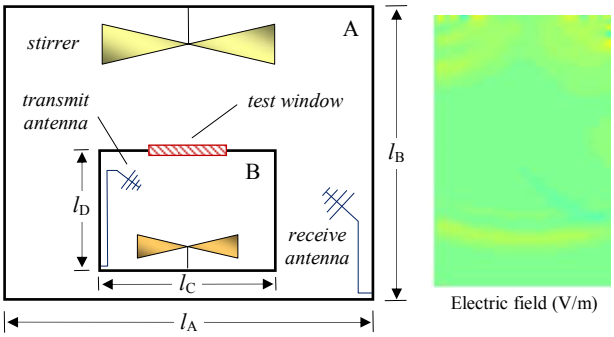

Fig. 20. A nested reverberation test facility along with a snapshot of the electric field near its wall diffusers.

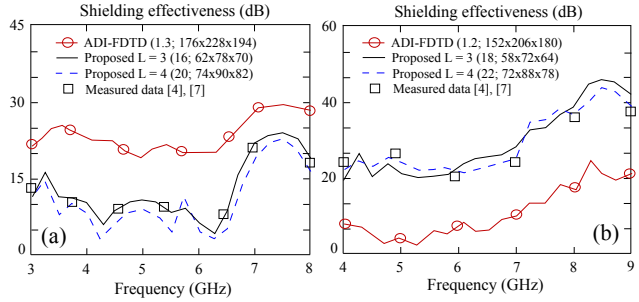

Fig. 21. Shielding effectiveness of (a) a 1.5 mm fiber-glass-fiber plate and (b) a dielectric (ε_r = 3.4) cover.

VII. CONCLUSION

A rigorous EMI analysis and signal integrity estimation of general EMC structures has been performed in this paper. To this aim, a new 3-D frequency-dependent higher-order ADI-FDTD method, incorporating a multi-frequency field projection scheme with an enhanced curvilinear nodal density, has been introduced and applied to a variety of problems, extending from waveguides, resonators, and antennas to large-scale test facilities. Their numerical simulations lead to very accurate and cost-effective realizations, even for coarse meshes and temporal increments that amply supersede the Courant stability condition.

REFERENCES

[1] C. Buccella, M. Feliziani, F. Maradei, and G. Manzi, "Magnetic field computation in a physically large domain with thin metallic shields," *IEEE Trans. Magn.*, vol. 41, no. 2, pp. 1708-1711, May 2005.

[2] C. Holloway, P. McKenna, R. Dalke, R. Perala, and C. Devor, "Time-domain modeling, characteriza-

tion, and measurements of anechoic and semi-anechoic electromagnetic test chambers," *IEEE Trans. Electromagn. Compat.*, vol. 44, no. 1, pp. 102-118, Feb. 2002.

[3] S. Lee, M. Vouvakis, and J.-F. Lee, "A non-overlapping domain decomposition method with non matching grids for modeling large finite arrays," *J. Comp. Phys.*, vol. 203, no. 1, pp. 1-21, Feb. 2005.

[4] C. Bruns and R. Vahldieck, "A closer look at reverberation chambers – simulation and experimental verification," *IEEE Trans. Electromagn. Compat.*, vol. 47, pp. 612-26, 2005.

[5] M. Sarto and A. Tamburrano, "Innovative test method for the shielding effectiveness measurement of thin films in wide frequency range," *IEEE Trans. Electromagn. Compat.*, vol. 48, no. 2, pp. 331-341, May 2006.

[6] Y. Song, N. Nikolova, and M. Bakr, "Efficient time-domain sensitivity analysis using coarse grids," *ACES J.*, vol. 23, no. 1, pp. 5-15, Mar. 2008.

[7] N. Kantartzis and T. Tsiboukis, *Modern EMC Analysis Techniques: Models and Applications*, Morgan & Claypool Publishers, San Rafael, CA, 2008.

[8] J. Muldavin, C. Bozler, S. Rabe, P. Wyatt, and C. Keast, "Wafer-scale packaged RF MEMS switches," *IEEE Trans. Microw. Theory Tech.*, vol. 56, pp. 522-529, Feb. 2008.

[9] S. Barmada, A. Gaggelli, P. Masini, A. Musolino, R. Rizzo, and M. Tucci, "Modeling of UIC cables in railway systems for their use as power line communication channels," *ACES J.*, vol. 24, no. 6, pp. 609-617, 2009.

[10] T. Ohtani, K. Taguchi, T. Kashiwa, Y. Kanai, and J. Cole, "Scattering analysis of large-scale coated cavity using the complex nonstandard FDTD method with surface impedance boundary condition," *IEEE Trans. Magn.*, vol. 45, no. 3, pp. 1296-1299, Mar. 2009.

[11] K. El Mahgoub, T. Elsherbeni, F. Yang, A. Elsherbeni, L. Sydänheimo, and L. Ukkonen, "Logo-antenna based RFID tags for advertising application," *ACES J.*, vol. 25, no. 3, pp. 174-181, Mar. 2010.

[12] A. Taflove and S. Hagness, *Computational Electrodynamics: The Finite-Difference Time-Domain Method*., Artech House, Norwood, MA, 2005.

[13] T. Namiki, "A new FDTD algorithm based on ADI method," *IEEE Trans. Microwave Theory Tech.*, vol. 47, no. 10, pp. 2003-2007, Oct. 1999.

[14] F. Zheng, Z. Chen, and J. Zhang, "An FDTD method without the Courant stability conditions," *IEEE Microw. Guided Wave Lett.*, vol. 9, no. 11, pp. 441-443, Nov. 1999.

[15] J. Mao, L. Jiang, and S. Luo, "Numerical formulations and applications of the ADI-FDTD method," *ACES Newsletter*, vol. 16, no. 3, pp. 12-18, Nov. 2001.

[16] M. Darms, R. Schuhmann, H. Spachmann, and T. Weiland, "Dispersion and asymmetry effects of ADI-FDTD," *IEEE Microw. Wireless Compon. Lett.*, vol. 12, pp. 491-493, 2002.

[17] S. Staker, C. Holloway, A. Bhobe, and M. Piket-May, "ADI formulation of the FDTD method: Algorithm and material dispersion implementation," *IEEE Trans. Electromagn. Compat.*, vol. 45, no. 2, pp. 156-166, May 2003.

[18] G. Sun and C. Truemann, "Efficient implementations of the Crank-Nicolson scheme for the FDTD method," *IEEE Trans. Microw. Theory Tech.*, vol. 54, no. 5, pp. 2275-84, May 2006.

[19] Erping Li, I. Ahmed, and R. Vahldieck, "Numerical dispersion analysis with an improved LOD–FDTD method," *IEEE Microw. Wireless Compon. Lett.*, vol. 17, pp. 319-321, 2007.

[20] E. Tan and D. Heh, "ADI-FDTD method with fourth order accuracy in time," *IEEE Microw. Wireless Compon. Lett.*, vol. 18, no. 5, pp. 296-298, May 2008.

[21] W. Fu and E. Tan, "Effective permittivity scheme for ADI-FDTD method at the interface of dispersive media," *ACES J.*, vol. 22, no. 2, pp. 120-125, June 2008.

[22] K. Jung, F. Teixeira, S. Garcia, and R. Lee, "On numerical artifacts of the complex envelope ADI-FDTD method," *IEEE Trans. Antennas Propag.*, vol. 57, pp. 491-498, Feb. 2009.

[23] Y. Zhang, S. Lu, and J. Zhang, "Reduction of numerical dispersion of 3-D higher order ADI-FDTD method with artificial anisotropy," *IEEE Trans. Microw. Theory Tech.*, vol. 57, no. 10, pp. 2416-28, Oct. 2009.

[24] H. Zheng and K. Leung, "A nonorthogonal ADI-FDTD algorithm for solving 2-D scattering problems," *IEEE Trans. Antennas Propag.*, vol. 57, no. 12, pp. 3981-3902, Dec. 2009.

[25] H. Zheng, L. Feng, and Q. Wu, "3-D nonorthogonal ADI-FDTD algorithm for the full-wave analysis of microwave circuit devices," *IEEE Trans. Microw. Theory Tech.*, vol. 58, no. 1, pp. 128-135, Jan. 2010.

[26] J.-F. Lee, R. Palendech, and R. Mittra, "Modeling three-dimensional discontinuities in waveguides using the nonorthogonal FDTD algorithm," *IEEE Trans. Microw. Theory Tech.*, vol. 40, no. 2, pp. 346-352, Feb. 1992.

[27] W. Yu, R. Mittra, and S. Dey, "Application of the nonuniform FDTD technique to analysis of coaxial discontinuity structures," *IEEE Trans. Microw. Theory Tech.*, vol. 49, pp. 207-209, Jan. 2001.

[28] S. Noelle, W. Rosenbaum, and M. Rumpf, "3D adaptive central schemes: Part I. Algorithms for assembling the dual mesh," *Appl. Numer. Math.*, vol.

56, no. 2, pp. 778-799, June 2006.
[29] P. Wang, "Modeling material responses by arbitrary Lagrangian Eulerian formulation and adaptive mesh refinement method," *J. Comput. Phys.*, vol. 229, pp. 1573-1599, Mar. 2010.
[30] R. Nilavalan, I. Craddock, and C. Railton, "Quantifying numerical dispersion in non-orthogonal FDTD meshes," *IEE Proc. Microw. Antennas Propag.*, vol. 149, pp. 23-27, 2002.
[31] N. Kantartzis and T. Tsiboukis, "A higher-order non-standard FDTD-PML method for the advanced modeling of complex EMC problems in generalized 3-D curvilinear coordinates," *IEEE Trans. Electromagn. Compat.*, vol. 46, no. 1, pp. 2-11, Feb. 2004.
[32] D. Firsov, J. LoVetri, O. Jeffrey, V. Okhmatovski, C. Gilmore, and W. Chamma, "High-order FVTD on unstructured grids using an object-oriented computational engine," *ACES J.*, vol. 22, no. 1, pp. 71-82, Mar. 2007.
[33] M. Hadi, "Wide-angle absorbing boundary conditions for low and high-order FDTD algorithms," *ACES J.*, vol. 24, no. 1, pp. 9-15, Feb. 2009.
[34] N. Kantartzis, T. Tsiboukis, and E. Kriezis, "An explicit weighted essentially non-oscillatory time-domain algorithm for the 3-D EMC applications with arbitrary media," *IEEE Trans. Magn.*, vol. 42, pp. 803-806, 2006.
[35] J. van Bladel, *Electromagnetic Fields*, IEEE Press, New York, NJ, 2007.
[36] D. Pozar, *Microwave Engineering*, John Wiley & Sons, New York, NJ, 2005.

Nikolaos V. Kantartzis received the Diploma and Ph.D. degrees from the Department of Electrical and Computer Engineering, Aristotle University of Thessaloniki, Greece, in 1994 and 1999, respectively. In 2001, he joined the same department, as a Postdoctoral Research Fellow, where, currently, he serves as an Assistant Professor. He has authored/co-authored 3 books, more than 50 referenced journals and over 60 conference papers. His main research interests include computational electromagnetics, EMC modeling, higher-order methods, metamaterials, and advanced microwave structures.

Improved Performance of FDTD Computation Using a Thread Block Constructed as a Two-Dimensional Array with CUDA

Naoki Takada[1], Tomoyoshi Shimobaba[2], Nobuyuki Masuda[2], and Tomoyoshi Ito[2]

[1]Department of Informatics and Media Technology,
Sony Institute of Higher Education, Shohoku College,
428 Nurumizu, Atsugi, Kanagawa 243-8501, JAPAN
ntakada@shohoku.ac.jp

[2]Graduate School of Engineering, Chiba University,
1-33 Yayoi-cho, Inage-ku, Chiba, Chiba 263-8522, JAPAN
shimobaba@faculty.chiba-u.jp, masdanb@faculty.chiba-u.jp, itot@faculty.chiba-u.jp

Abstract ― In a previous study, the authors proposed an finite-difference time-domain (FDTD) implementation for a compute unified device architecture (CUDA) compatible graphics processing unit (GPU) using a thread block constructed as a two-dimensional (2-D) array. However, it was found that the larger the computational domain of the 2-D FDTD simulation using the GPU, the slower the computational speed.

In the present paper, the authors investigated the computational performance with respect to the size of a thread block constructed as a 2-D array, and improved the performance of the implementation. Finally, regardless of the size of computational domain, the computational speed using a single GPU (NVIDIA GeForce GTX 280) achieved approximately 30.0 Gflops, which was approximately 20 times faster than that of a single core of a central processing unit (Intel 3.0-GHz Core 2 Duo). The improved performance was approximately 65% of the theoretical peak performance (47.23 Gflops) obtained by the theoretical memory bandwidth (141.7 GB/s).

Index Terms ― Finite-difference time-domain method, GPU computing, graphics processing unit, high-performance computing.

I. INTRODUCTION

A graphics processing unit (GPU) is equipped with a large-memory graphics accelerator board for use in a personal computer (PC). The GPU has many processors for 32-bit floating-point calculations. The theoretical peak performance of recent GPUs is greater than 1 Tflops (floating point operations per second). High performance/cost has been reported for the hierarchical N-body simulation using a PC cluster equipped with 256 GPUs [1].

Programs can be developed that allow GPUs to perform general numerical calculations using a high-level shader language (HLSL) (Microsoft HLSL, NVIDIA Cg [2], etc.) or a programming environment (Brook [3], the NVIDIA compute unified device architecture (CUDA) programming environment [4], etc.). Implementation of the finite-difference time-domain (FDTD) method [5-7] on a GPU using various programming environments has been reported [8-16]. The development of the GPU code written in HLSL requires technical knowledge of computer graphics (CG) [8]. In the FDTD simulation using the GPU code written in NVIDIA Cg, the Euclidean normalized error increased monotonously with respect to the time step [9]. The GPU-FDTD code written in Brook has also been reported [10]. In three-dimensional (3-D) FDTD simulation, 3-D to 2-D translation has been reported [11]. Translation from 3-D to 2-D becomes very complicated because the 3-D computational domain of the FDTD simulation is allocated to 2-D texture as a CG technique. Programming tools for the GPU based on CUDA

have been available since 2007. In CUDA, the programmer does not need to be conscious of the CG technique. The advantages of CUDA over Cg and HLSL is that CUDA allows source code to be written in a C-like language and the memory on the GPU board can be used easily. The GPU implementation for LU decomposition solvers using CUDA for computational electromagnetics application has been reported [17]. More GPU implementations of the FDTD method using CUDA have been provided and the computational performances of these implementations have been discussed [12-16]. The FDTD computation using GPU has been implemented with data reuse of the electromagnetic field, and the computational performance has been reported [12]. In [13], a thread block [4] was constructed as a 2-D array. The performance of the 2-D FDTD implementation using GPU was investigated with respect to the four arrays considered (4 × 4, 8 × 8, 12 × 12, and 16 × 16). The FDTD computation was fastest for the 16 × 16 array among the four arrays. The GPU implementations of 3-D FDTD computation using CUDA have been reported [14, 15]. A thread block was constructed as a 2-D array [14], and the size of the 2-D array was 16 × 16. However, the performance of the implementation was not investigated the other 2-D arrays. In [15], a thread block was constructed as a 1-D array, and GPU implementations based on two thread-to-cell mapping algorithms were considered. The performances of the implementations were investigated with respect to the number of threads per thread block. Thus, a 1-D array or a 2-D array is used as a thread block.

In a previous study, the authors proposed a GPU implementation for FDTD computation using a thread block constructed as a 2-D array [16]. The computational domain of the FDTD simulation is divided into subdomains. The electromagnetic field data of a subdomain is stored in shared memory [4]. A subdomain is adjacent to four neighbor subdomains. In this case, a subdomain requires four overlapping areas that include the electromagnetic field data of four neighbor subdomains required to calculate the electromagnetic field on the boundaries of a subdomain. The proposed implementation uses two different subdomains for the calculation of the electric field and the magnetic field, and reduces the number of overlapping areas from four to two in order to reduce the number of branches in the CUDA program. In performance evaluation of the proposed implementation, NVIDIA GeForce GTX 280 was used as a GPU, and a 16 × 16 2-D array was used as a thread block. However, the larger the computational domain of the 2-D FDTD simulation using the proposed implementation, the slower the computational speed.

In the present paper, the authors investigated the performance of the proposed GPU implementation with respect to the size of a thread block constructed as a 2-D array and improved the performance of the proposed implementation. As a result, the computational speed of the implementation in a computational domain of 8,192 × 8,192 peaked when the size of the thread block was 32 × 4. Regardless of the size of the computational domain, the computational speed using a single GPU (NVIDIA GeForce GTX 280) was approximately 30.0 Gflops, which is approximately 20 times faster than that of a single core of a central processing unit (CPU) (Intel 3.0-GHz Core 2 Duo), where the Intel C compiler was used as C compiler.

The remainder of the present paper is organized as follows. The proposed GPU implementation for FDTD computation using a thread block constructed as a 2-D array in a previous study is described in Section II. In Section III, the performance of the proposed GPU-FDTD implementation is described in detail with respect to the size of a thread block constructed as a 2-D array, and the performance of the proposed implementation is improved. Finally, in Section IV, conclusions are presented and future research is described.

II. GPU-FDTD IMPLEMENTATION [16]

CUDA is a parallel computing architecture. NVIDIA GeForce GTX 280 has 30 streaming multiprocessors (SMs), each of which is composed of eight streaming processors (SPs) for 32-bit floating-point calculation, 16,384 registers, and 16 KB of on-chip memory. The CUDA program consists of the CPU code and the GPU code. The GPU code, which is written in a C-like language, includes data-parallel functions, referred to collectively as the *kernel*. A kernel is executed as a *grid* of *thread blocks*. A thread block is an array of threads that can cooperate. Threads within the same thread block are synchronized and share data

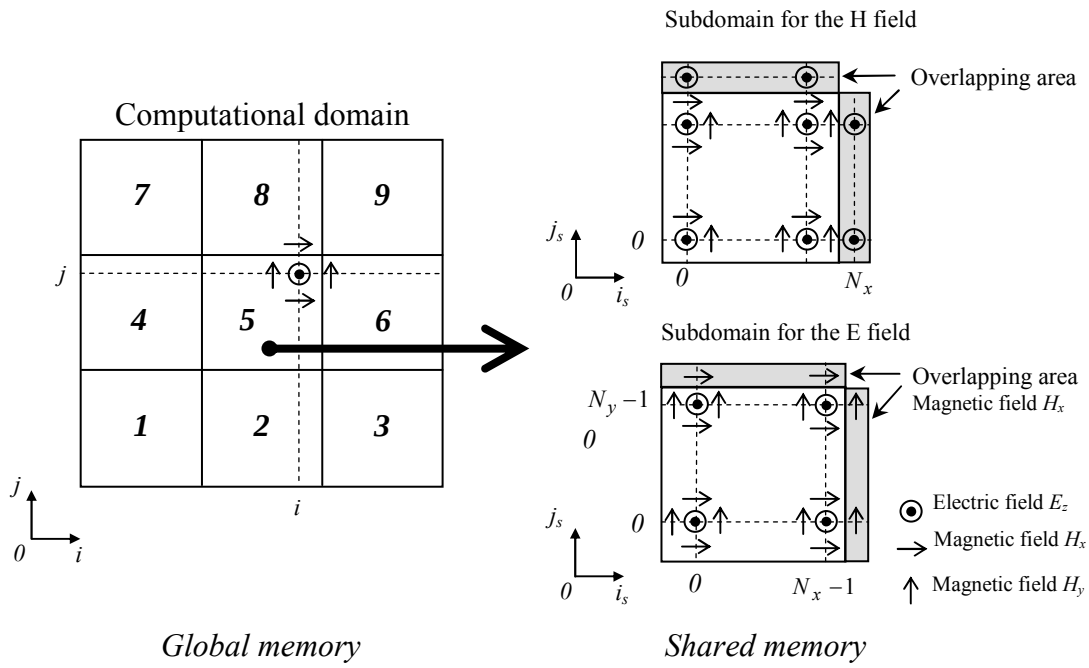

Fig. 1. Subdomains of the proposed GPU-FDTD implementation (TM case).

in the shared memory. The CPU code is written in the C language, and the CPU launches the GPU kernel.

In the case of the 2-D FDTD method, the equations in the transverse magnetic (TM) case are as follows:

$$H_x^{n+1/2}(i, j+1/2) = H_x^{n-1/2}(i, j+1/2) - \Delta t / \mu \Delta y \left\{ E_z^n(i, j+1) - E_z^n(i, j) \right\}, \quad (1)$$

$$H_y^{n+1/2}(i+1/2, j) = H_y^{n-1/2}(i+1/2, j) - \Delta t / \mu \Delta x \left\{ E_z^n(i+1, j) - E_z^n(i, j) \right\}, \quad (2)$$

$$E_z^{n+1}(i, j) = E_z^n(i, j) - \Delta t / \varepsilon \Delta y \left\{ H_x^{n+1/2}(i, j+1/2) - H_x^{n+1/2}(i, j-1/2) \right\} + \Delta t / \varepsilon \Delta x \left\{ H_y^{n+1/2}(i+1/2, j) - H_y^{n+1/2}(i-1/2, j) \right\}, \quad (3)$$

where $E_z^{n+1}(i, j)$ is the required value of the electric field at grid point (i, j) and the (n+1)-th time step, Δx and Δy are the sizes of the spatial division in the x and y directions, respectively, and Δt is the time increment. Parameters ε and μ are the electric permittivity and the magnetic permeability in the medium, respectively. A large quantity of electromagnetic field data in the computational domain for FDTD simulation is stored in the global memory as off-chip device memory on a CUDA-compatible graphics accelerator board. The CPU allocates the data of the electromagnetic fields to a global memory on the GPU board. The memory size of each electromagnetic field array in the program must be an integer multiple of 16 for coalesced global memory access [4]. If the memory size of each required electromagnetic field array in the computational domain is not an integer multiple of 16, the memory size, which is larger than that of each required array, is allocated in order to be equal to an integer multiple of 16. Shared memory enables faster data access than global memory and accounts for 16 KB of on-chip memory in the role of CPU cache memory. In the proposed implementation, a thread block is constructed as a 2-D array, and the computational domain of the FDTD simulation is divided into a small subdomain. The electromagnetic field data in each subdomain are stored in each shared memory as shown Fig. 1. Calculating the electric field data $E_z^{n+1}(i, j)$ in Region 5 requires the magnetic field data $H_y^{n+1/2}(i+1/2, j)$ in Region 6 and the magnetic field data $H_x^{n+1/2}(i, j+1/2)$ in Region 8. The required data of the magnetic field, which overlap neighboring subdomains as shown in Fig. 1, are also stored in each shared memory. Each subdomain of the proposed implementation includes two overlapping areas. In the CUDA

```
__global__ void maxwH( float *HX, float *HY, float *EZ)
{
  int tx=threadIdx.x;
  int ty=threadIdx.y;
  unsigned int x = blockIdx.x*blockDim.x + threadIdx.x;
  unsigned int y = blockIdx.y*blockDim.y + threadIdx.y;
  __shared__ float SH_EZ[NY+1][NX+1];
  float xx;
  if(ty==(NY-1))SH_EZ[ty+1][tx]=EZ[(y+1)*w+x];
  if(tx==(NX-1))SH_EZ[ty][tx+1]=EZ[y*w+x+1];
  SH_EZ[ty][tx]=EZ[y*w+x];
  xx=SH_EZ[ty][tx];
  HX[(y+1)*w+x]=HX[(y+1)*w+x]-dtdy*(SH_EZ[ty+1][tx]-xx);
  HY[y*w+x+1]=HY[y*w+x+1]+dtdx*(SH_EZ[ty][tx+1]-xx);
}
```

(a)

```
__global__ void maxwEZ( float *HX, float *HY, float *EZ, float *T)
{
    int tx=threadIdx.x;
    int ty=threadIdx.y;
    unsigned int x = blockIdx.x*blockDim.x + threadIdx.x;
    unsigned int y = blockIdx.y*blockDim.y + threadIdx.y;
    __shared__ float SH_HX[NY+1][NX+1];
    __shared__ float SH_HY[NY+1][NX+1];
    if(ty==(NY-1))SH_HX[ty+1][tx]=HX[(y+1)*w+x];
    if(tx==(NX-1))SH_HY[ty][tx+1]=HY[y*w+x+1];
    SH_HX[ty][tx]=HX[y*w+x];
    SH_HY[ty][tx]=HY[y*w+x];
    __syncthreads();
   if((x==511)&&(y==511)){
       T[0]+=dt;
      EZ[y*w+x]=am*sin(omega*T[0]);
   }else{
      EZ[y*w+x]=EZ[(y)*w+x]+dtdx*(SH_HY[ty][tx+1]-SH_HY[ty][tx])
                            -dtdy*(SH_HX[ty+1][tx]-SH_HX[ty][tx]);
   }
    if(x==0)EZ[(y)*w+x]=0;
    if(x==1023)EZ[(y)*w+x]=0;
    if(y==0)EZ[(y)*w+x]=0;
    if(y==1023)EZ[(y)*w+x]=0;
}
```

(b)

Fig. 2. GPU-FDTD code, (a) kernel for calculating the magnetic field, (b) kernel for calculating the electric field.

program, the size of each subdomain, excluding overlapping areas, is $N_x \times N_y$ when the size of the thread block constructed as a 2-D array is $N_x \times N_y$. In calculating the magnetic field data H_x and H_y (Equations (1) and (2)), all of the threads in each $N_x \times N_y$ thread block first store the data of electric field E_z of each subdomain in the shared memory, whereas no data of magnetic fields H_x and H_y of each subdomain are stored in the shared memory. Next, the same electric field data $E_z^n(i,j)$ required in Equations (1) and (2) are stored in the register only once [12]. After these procedures, all of the threads in a thread block are used to calculate Equations (1) and (2) in each subdomain. Finally, the calculated data of magnetic fields H_x and H_y are stored in the global memory, while the calculation of electric field E_z by Equation (3) at the following time step is performed in the same manner. The subdomain used to calculate the electric field E_z (Subdomain for the E field shown in Fig. 1) differs from that used to calculate the magnetic fields H_x and H_y (Subdomain for the H field shown in Fig. 1) in order to use the shared memory efficiently. Therefore, two kernels for the electric field and magnetic field calculations are required in the CUDA program. The number of time steps is counted and stored in the global memory by a particular SP in each kernel if the calculation of the electric field E_z or the magnetic field H_x or H_y requires the number of time steps for the boundary condition. The kernel codes of the proposed GPU-FDTD implementation are shown in Fig. 2.

III. PERFORMANCE

In the present paper, the authors used the NVIDIA CUDA programming environment for the GPU and a NVIDIA GeForce GTX 280 as the GPU board and timed the calculations required for a simple 2-D model, excluding for the absorbing boundaries, in order to investigate the basic performance of the proposed GPU-FDTD implementation. The propagation of electromagnetic waves from the line source in the TM case was used as the calculation model. The line source was located in the center of the 2-D computational domain. The authors compared the GPU implementation with the conventional CPU implementation. In the GPU implementation, the authors developed a GPU-FDTD code written in the C language and a kernel written in a C-like language for the instruction set of the GPU using the CUDA programming environment. A kernel can be embedded in the code written in the C language for the CPU. Two kernels in the FDTD code were used: a kernel to calculate the magnetic fields H_x and H_y and a kernel to calculate the electric field E_z. A CUDA driver (180.22) was used. The GPU-FDTD code was compiled using NVIDIA CUDA 2.1. In the CPU implementation, the conventional FDTD code was written in the C language. Here, FDTD computation was performed using a single core in the CPU. The code for the CPU was compiled using the Intel C-compiler (ver. 11.1) with "-msse –O3" as an optimized compiler option. The CPU-only computation used SSE instructions. In the CPU and GPU implementations, the authors used the

same PC equipped with an Intel Core 2 Duo E8400 (3.0 GHz) as the CPU, 2.0 GB of memory (DDR3-1333), and Fedora 9 as the Linux operating system and timed 1,000 iterations of the calculation by Equations (1) through (3) for the GPU and CPU-only computation.

In Equations (1) through (3), the authors replace $\Delta t/\mu\Delta x$, $\Delta t/\varepsilon\Delta x$, and $\Delta t/\varepsilon\Delta y$ with constants. As a result, the number of operations in Equations (1) through (3) is estimated to be 12. The theoretical peak performance of the FDTD simulation using the NVIDIA GeForce GTX 280 as a GPU is obtained as 47.23 Gflops = 141.7 GB/s ÷ 4 byte/word × 12 operations ÷ nine words, where the theoretical memory bandwidth is 141.7 GB/s, and the number of load/store data in Equations (1) through (3) is estimated to be nine words. On the other hand, the theoretical peak performance of the GPU is obtained as 933.12 Gflops = three operations/SP × 240 SP × 1.296 GHz, and the theoretical peak performance of the FDTD simulation using the GPU (47.23 Gflops) is smaller than in the latter example (933.12 Gflops). Therefore, the bottleneck of 2-D FDTD computation using the GPU is the memory bandwidth.

Here, T_{GPU} is the GPU computation time (s) in the computational domain of $L \times L$, and N_{itr} is the number of time steps of the FDTD simulation. Subsequently, the actual computational speed (flops) can be obtained as 12 operations $\times L \times L \times N_{itr}/T_{GPU}$ (N_{itr} = 1,000). When the size of the subdomain is 16 × 16, the two computational speeds of the GPU-FDTD simulation using shared and non-shared memory are shown in Fig. 3. In Fig. 3, the 'non-shared memory' indicates the basic GPU-FDTD computation without the subdomain for using shared memory, while 'shared memory' indicates the proposed GPU-FDTD implementation using shared memory. The larger the computational domain of the 2-D GPU-FDTD simulation, the slower the computational speed. In the computational domain of 8,192 × 8,192, the authors investigated the performances of two GPU-FDTD implementations with respect to the size of a thread block constructed as a 2-D array (Table 1). In 'shared memory', the thread block of size 32 × 4 achieved a peak speed (Table 1(a)). In the 'non-shared memory', the thread block of size 64 × 4 achieved a peak speed (Table 1(b)). In Table 1, the computation time using the

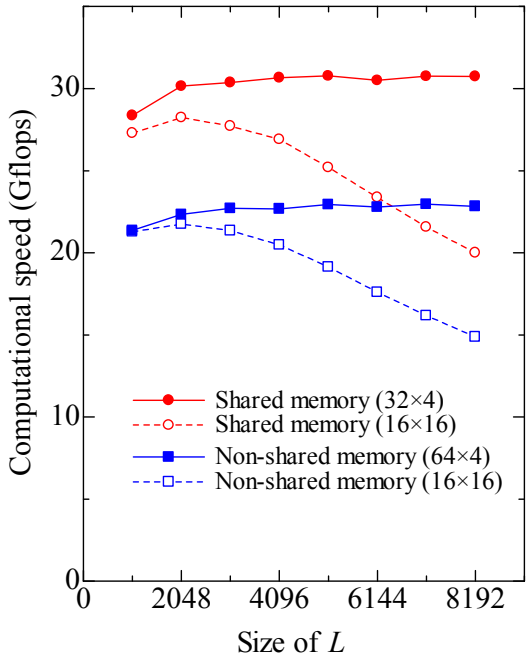

Fig. 3. Computation speed versus computational domain $L \times L$.

proposed GPU-FDTD implementation was very long when N_y was larger than or equal to N_x. The authors analyzed the performance of the proposed GPU-FDTD implementation using the NVIDIA CUDA Visual Profiler. Bank conflicts of shared memory occurred when $N_x \leq 8$ for all cases of the total number of threads per thread block considered herein. Therefore, the performance of the global memory overall throughputs, which is the sum of the global memory write throughput and the global memory read throughput, decreased markedly in the GPU computation of the electric field and the magnetic field. For all cases of the total number of threads per thread block, the number of divergent branches within a warp increased in the GPU computation of the electric field when $N_x \leq 16$. In the 'shared memory', the performance of the global memory overall throughputs was the best for the case in which the total number of threads per thread block is 128. In Table 1(a), a thread block of size 32 × 4 achieved a peak speed. In the case of the 32 × 4 thread block, the global memory overall throughput of the GPU computation of the electric field was 99.12 GB/s, while the global memory overall throughput of the GPU computation of the magnetic field was 126.70 GB/s. The

Table 1: Computation time for the GPU-FDTD implementations with respect to the size of the thread block constructed as a 2D-array ($N_x \times N_y$) in the computational domain: 8,192 × 8,192. (a) GPU-FDTD implementation with shared memory, (b) basic GPU-FDTD implementation without a subdomain for shared memory.

(a)

Total number of threads per thread block							
512		256		128		64	
$N_x \times N_y$	Time (ms)	$N_x \times N_y$	Time (ms)	$N_x \times N_y$	Time (ms)	$N_x \times N_y$	Time (ms)
512 × 1	34,910.91	256 × 1	30,332.19	128 × 1	29,208.40	64 × 1	31,378.07
256 × 2	27,860.34	128 × 2	26,828.33	64 × 2	26,546.84	32 × 2	31,021.64
128 × 4	27,023.15	64 × 4	26,404.10	**32 × 4**	**26,193.54**	16 × 4	32,172.59
64 × 8	28,329.08	32 × 8	27,766.32	16 × 8	31,641.55	8 × 8	49,528.76
32 × 16	31,408.21	16 × 16	40,315.71	8 × 16	81,558.07	4 × 16	151,044.05
16 × 32	43,464.29	8 × 32	92,666.19	4 × 32	179,097.02	2 × 32	334,621.00
8 × 64	99,550.48	4 × 64	201,960.70	2 × 64	462,255.13	1 × 64	1,156,390.13
4 × 128	240,642.34	2 × 128	513,940.38	1 ×128	1,135,948.50		
2 × 256	531,257.31	1 × 256	1,137,908.38				
1 × 512	1,142,198.88						

(b)

Total number of threads per thread block							
512		256		128		64	
$N_x \times N_y$	Time (ms)	$N_x \times N_y$	Time (ms)	$N_x \times N_y$	Time (ms)	$N_x \times N_y$	Time (ms)
512 × 1	36,148.74	256 × 1	35,712.13	128 × 1	35,765.40	64 × 1	36,315.55
256 × 2	35,523.61	128 × 2	35,412.05	64 × 2	35,463.31	32 × 2	35,510.76
128 × 4	35,283.57	**64 × 4**	**35,283.14**	32 × 4	35,446.44	16 × 4	36,006.95
64 × 8	36,126.11	32 × 8	36,836.52	16 × 8	41,499.72	8 × 8	72,708.84
32 × 16	41,103.40	16 × 16	54,172.49	8 × 16	103,208.16	4 × 16	188,353.81
16 × 32	60,904.04	8 × 32	117,666.61	4 × 32	219,635.84	2 × 32	434,315.56
8 × 64	133,583.14	4 × 64	259,646.30	2 × 64	571,017.06	1 × 64	1,445,463.25
4 × 128	299,888.72	2 × 128	632,672.88	1 × 128	1,410,071.50		
2 × 256	661,946.06	1 × 256	1,422,834.38				
1 × 512	1,442,981.13						

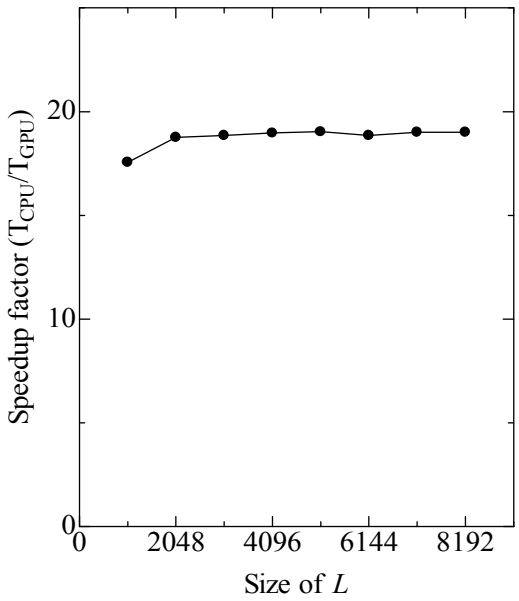

Fig. 4. Speedup factor (T_{CPU} / T_{GPU}) versus computational domain $L \times L$.

computational speeds using the 32 × 4 thread block in the 'shared memory' and the 64 × 4 thread block in the 'non-shared memory' are shown in Fig. 3. Regardless of the size of the computational domain, the computational speed of the proposed GPU-FDTD implementation achieved approximately 30.0 Gflops. The authors improved the performance of the GPU-FDTD simulation by using the optimum size of a thread block constructed as a 2-D array and compared the computation time of the GPU-FDTD simulation with that of CPU-only simulation. In Fig. 4, the speedup factor shows the ratio of the computation time of the CPU only (T_{CPU}) to that of GPU (T_{GPU}). The FDTD simulation using a single GPU was approximately 20 times faster than that using a single CPU core.

The authors estimated the effective performance (Fig. 5). As a result, the effective performance achieved approximately 65% of the

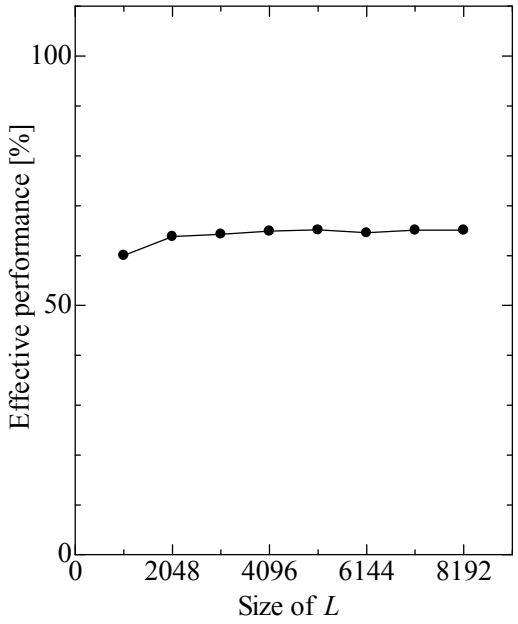

Fig. 5. Effective performance of the improved GPU-FDTD computation versus computational domain $L \times L$.

theoretical peak performance (47.23 Gflops) obtained using the theoretical memory bandwidth.

IV. Conclusion

The authors proposed GPU-FDTD implementation using a thread block constructed as a 2-D array in a previous study. However, in a 16 × 16 thread block, the larger the computational domain of 2-D GPU-FDTD simulation, the slower the computational speed. In the present paper, the authors investigated the computational performance with respect to the size of a thread block constructed as a 2-D array. As a result, the computational speed of the GPU-FDTD simulation peaked when the thread block size was 32 × 4. Regardless of the size of the computational domain, the computational speed of the GPU (NVIDIA GeForce GTX 280) was approximately 30.0 Gflops, which is approximately 20 times faster than that using a single core of the central processing unit (Intel 3.0-GHz Core 2 Duo). Finally, after improving the performance of the proposed GPU-FDTD implementation, the effective performance was approximately 65% of the theoretical peak performance of GPU-FDTD computation using an NVIDIA GeForce GTX 280 as a GPU.

In the future, the authors intend to apply the proposed method to 3-D FDTD simulation.

ACKNOWLEDGMENT

The present study was supported in part by a Grant-in-Aid for Young Scientists (B), 22700060, from the Ministry of Education, Culture, Sports, Science and Technology, Japan.

REFERENCES

[1] T. Hamada, T. Narumi, R. Yokota, K. Yasuoka, K. Nitadori, and M. Taiji, "42 TFlops hierarchical *N*-body simulations on GPUs with applications in both astrophysics and turbulence," *Proceedings of the Conference on High Performance Computing Networking, Storage and Analysis*, 2009.

[2] W. R. Mark, R. S. Glanville, K. Akeley, and M. J. Kilgard, "Cg: A system for programming graphics hardware in a C-like language," *ACM SIGGRAPH*, pp. 896-907, 2003.

[3] I. Buck, T. Foley, D. Horn, J. Sugerman, K. Fatahalian, M. Houston, and P. Hanrahan, "Brook for GPUs: stream computing on graphics hardware," *ACM SIGGRAPH*, pp. 777-786, 2004.

[4] NVIDIA, *NVIDIA CUDA Programming Guide version 2.1*, NVIDIA, 2008.

[5] K. S. Yee, "Numerical solution of initial boundary value problems involving Maxwell´s Equations in isotropic media," *IEEE Trans. Antennas Propagat*., vol. AP-14, pp. 302-307, 1966.

[6] A. Taflove, "Computational electrodynamics: the finite difference time domain method," *Artech House*, Inc., 1995.

[7] K. S. Kunz and R. J. Luebbers, "The finite difference time domain method for electromagnetics," *CRC Press*, Inc., 1993.

[8] N. Takada, N. Masuda, T. Tanaka, Y. Abe, and T. Ito, "A GPU implementation of the 2-D finite-difference time-domain code using high level shader Language," *ACES Journal*, vol. 23, no. 4, pp. 309-316, 2008.

[9] G. S. Baron, C. D. Sarris, and E. Fiume, "Fast and accurate time-domain simulations with commodity graphics hardware," *Proceedings of the Antennas and Propagation Society International Symposium*, July 2005.

[10] M. J. Inman and A. Z. Elsherbeni, "Programming video cards for computational electromagnetics application," *IEEE Antennas and Propagation Magazine*, vol. 47, no. 6, pp. 71-78, 2005.

[11] M. J. Inman, A. Z. Elsherbeni, J. G. Maloney, and B. N. Baker, "Practical implementation of a CPML absorbing boundary for GPU accelerated FDTD technique," *ACES Journal*, vol. 23, no. 1, pp. 16-22, 2008.

[12] N. Takada, T. Takizawa, Z. Gong, N. Masuda, T. Ito, and T. Shimobaba, "Fast computation of 2-D finite-difference time-domain method using graphics processing unit with unified shader," *IEICE Trans. Inf. Syst.*, vol. J91-D, no. 10, pp. 2562-2564, 2008.

[13] S. Ryoo, C. Rodrigues, S. Baghsorkhi, S. Stone, D. Kirk, and W. Hwu, "Optimization principles and application performance evaluation of a multithreaded GPU using CUDA," *Proc. of the 13th ACM SIGPLAN Symposium on Principles and Practice of Parallel Programming*, pp.73–82, 2008.

[14] P. Sypek, A. Dziekonski, and M. Mrozowski, "How to render FDTD computations more effective using graphics accelerator," *IEEE Trans. Magn.*, vol. 45, no. 3, pp. 1324-1327, 2009.

[15] V. Demir and A. Z. Elsherbeni, "Compute Unified Device Architecture (CUDA) based finite-difference time-domain (FDTD) implementation," *ACES Journal*, vol. 25, no. 4, pp. 303-314, 2010.

[16] N. Takada, T. Shimobaba, N. Masuda, and T. Ito, "High-speed FDTD simulation algorithm for GPU with compute unified device architecture," *Proc. 2009 IEEE AP-S Int. Symposium and USNC/URSI National Radio Science Meeting*, session 126, 126.9, 2009.

[17] M. J. Inman, A. Z. Elsherbeni and C. J. Reddy, "CUDA based LU decomposition solvers for CEM applications," *ACES Journal*, vol. 25, no. 4, pp. 339-347, 2010.

Naoki Takada received a B.E. degree and an M.S. degree in Electrical Engineering from Gunma University, Gunma, Japan in 1994 and 1996, respectively and a Ph.D. in Electrical Engineering from Gunma University in 2000. From 1996 to June 2001, he was a research associate at Oyama National College of Technology, Tochigi, Japan. From July 2001 to March 2005, he was a research scientist with the High-Performance Biocomputing Research Team, Bioinformatics Group, Genomic Science Center (GSC), Institute of Physical and Chemical Research (RIKEN), Yokohama, Japan and joined the "Protein Explorer Project" for a petaflops special-purpose computer (MDGRAPE-3) system for molecular dynamics simulation of proteins. This project was the Protein 3000 project supported by the Ministry of Education, Culture, Sports, Science, and Technology of Japan. He was a lecturer from April 2005 to 2009 and an associate professor from 2010, at Shohoku College, Atsugi, Japan.

His research interests are GPGPU, distributed and parallel computation including the FDTD method, a special-purpose computer for the FDTD method, numerical simulation including the FDTD method, the CIP method, and molecular dynamics, and electromagnetic theory. He is a member of ACES and IEICE.

Tomoyoshi Shimobaba received B.E. and M.E. degrees from Gunma University in 1997 and 1999. And he received a Ph.D. from Chiba University in 2002. From 2002 to 2005, he was a special postdoctoral researcher at RIKEN. From 2005 to 2009, he was an associate professor at the Graduate School of Science and Engineering, Yamagata University. He is currently an associate professor at the Graduate School of Engineering, Chiba University.

His research interests include 3D display, digital holography, and special-purpose computing using FPGA and GPU. He is a member of OSA, IEICE, and ITE.

Nobuyuki Masuda received a bachelor degree and a master degree in System Science from the University of Tokyo, Tokyo, Japan in 1993 and 1995, respectively, and a Ph.D. in System Science from the University of Tokyo in 1998. From 2000 to March 2004, he was a research associate at Gunma University, Gunma, Japan. Since April 2004, he has been a research associate at Chiba University, Chiba, Japan.

His research interests include a special-purpose computer for digital-holographic particle-tracking velocimetry and computer-generated holograms on GPU. He is a member of IEICE, IPSJ, and ASJ.

Tomoyoshi Ito received a B.E. degree, M.S. degree, and Ph.D. from the University of Tokyo, Tokyo, Japan in 1989, 1991, and 1994, respectively. He was a research associate from 1992 to 1994 and an associate professor from 1994 to 1999 at Gunma University, Gunma, Japan. From 1999 to 2005, he was an associate professor at Chiba University, Chiba, Japan, and since 2005, he has been a professor.

His research interests are high-performance computing and its applications. He was an initial member of the GRAPE project, which has produced special-purpose computers for astrophysics. He developed the first machine, GRAPE-1, in 1989 and the second machine with high accuracy, GRAPE-2, in 1990 and the third machine for protein simulation, GRAPE-2A, in 1991. From 1992, he has also designed and built special-purpose computers for holography named HORN. Using HORN computers, he is trying to develop a three-dimensional television. He is a member of OSA and IEICE.

A Single-Field FDTD Formulation for Electromagnetic Simulations

Gokhan Aydin [1], Atef Z. Elsherbeni [2], and Ercument Arvas [1]

[1] Department of Electrical Engineering and Computer Science
Syracuse University, Syracuse, NY 13244-1240, USA
goaydin@syr.edu, earvas@syr.edu

[2] Department of Electrical Engineering
University of Mississippi, University, MS 38677-1848, USA
atef@olemiss.edu

Abstract ─ A set of general purpose single-field finite-difference time-domain (FDTD) updating equations for solving electromagnetic problems is derived. The formulation uses a single-field expression for full-wave solution. This formulation can provide numerical results similar to those obtained using the traditional Yee algorithm with less computer resources. The traditional FDTD updating equations are based on Maxwell's curl equations whereas the single-field FDTD updating equations, used here, are based on the vector wave equation. Performance analyses of the single–field formulation in terms of CPU time, memory requirement, stability, dispersion, and accuracy are presented. It was observed that the single-field method is significantly efficient relative to the traditional one in terms of speed and memory requirements.

Index Terms ─ FDTD, single-field approach.

I. INTRODUCTION

The first paper on finite-difference time-domain (FDTD) was published in 1966 by Yee [1]. Since then, the FDTD has become widely used in computational electromagnetics [2]. Extensive research has been reported to improve the accuracy and speed of the method and different absorbing boundary conditions (ABCs) are developed to provide more accurate results [3, 4, 5]. An improvement in speed of the method, however, has relied almost solely on progresses in computer hardware and software architecture.

This paper investigates the single-field approach based on the vector wave equation (VWE) to derive the FDTD updating equations in a way that only one field component will be calculated and updated inside the iteration loop to eliminate iteration steps required to update the other field component. Since one field (E or H) can be calculated from the other field, whenever needed, the proposed method, hence, is able to provide simulation results similar to that obtained from traditional FDTD updating equations.

There is not much published work investigating VWE-based updating equations as a complete alternative to the traditional Yee algorithm; Aoyagi et al. investigated a possible combination of scalar and vector wave equations as well as scalar wave equation and Maxwell's equations [6], however both approaches lose generality since they require partitioning of the problem domain; Okoniewski discussed the application of the vector wave equation approach to inhomogeneous wave-guide structure in terms of stability by using transverse field components [7]. Chu et al. studied the FDTD modeling of optical guided-wave devices based on the Yee algorithm and investigated scalar wave equation and its semivectorial version for the simulation of optical guided-wave devices, but the vector nature of the electromagnetic waves is either completely or partially ignored [8,9].

The single-field FDTD is an effort at reduction of FDTD variables in a Yee grid to only the three components of a single field variable, either E or H, while maintaining the ability to analyze full vector source injection. To compare the proposed updating equations with the traditional Yee algorithm, 2D TM, TE, and 1D electromagnetic problems are solved. Results of performance analyses: CPU time, memory requirement, stability, dispersion, and accuracy, are presented. It was observed that for 1D and 2D problems, the single-field method has advantages over the traditional one in terms of speed and memory requirements.

II. FORMULATIONS

The single-field formulation is derived by starting with Maxwell's curl equations:

$$\nabla \times \boldsymbol{E} = -\mu \frac{\partial \boldsymbol{H}}{\partial t} - (\boldsymbol{M}_i + \sigma^m \boldsymbol{H}), \quad (1)$$

$$\nabla \times \boldsymbol{H} = \varepsilon \frac{\partial \boldsymbol{E}}{\partial t} + (\boldsymbol{J}_i + \sigma^e \boldsymbol{E}). \quad (2)$$

where $\boldsymbol{E}$ is the electric field strength, $\boldsymbol{H}$ is the magnetic field strength, $\boldsymbol{J_i}$ is the impressed electric current density, $\boldsymbol{M_i}$ is the impressed magnetic current density, ε is the permittivity, and μ is permeability, σ^e and σ^m are the electric and magnetic conductivity, respectively. Taking the curl of (1) we have:

$$\nabla \times \nabla \times \boldsymbol{E} = -\mu \frac{\partial}{\partial t}(\nabla \times \boldsymbol{H}) - \nabla \times \boldsymbol{M}_i - \sigma^m (\nabla \times \boldsymbol{H}). \quad (3)$$

Replacing the curl of $\boldsymbol{H}$ in (3) with the right hand side of (2), (3) can be rewritten as:

$$\nabla \times \nabla \times \boldsymbol{E} = -\mu \frac{\partial}{\partial t}\left(\varepsilon \frac{\partial \boldsymbol{E}}{\partial t} + (\boldsymbol{J}_i + \sigma^e \boldsymbol{E})\right) - \nabla \times \boldsymbol{M}_i - \sigma^m \left(\varepsilon \frac{\partial \boldsymbol{E}}{\partial t} + (\boldsymbol{J}_i + \sigma^e \boldsymbol{E})\right). \quad (4)$$

Alternatively, taking the curl of (2) we have:

$$\nabla \times \nabla \times \boldsymbol{H} = \varepsilon \frac{\partial}{\partial t}(\nabla \times \boldsymbol{E}) - \nabla \times \boldsymbol{J}_i - \sigma^m (\nabla \times \boldsymbol{E}). \quad (5)$$

Replacing the curl of $\boldsymbol{E}$ in (5) with the right hand side of (1), (5) can be written as:

$$\nabla \times \nabla \times \boldsymbol{H} = \varepsilon \frac{\partial}{\partial t}\left(-\mu \frac{\partial \boldsymbol{H}}{\partial t} - (\boldsymbol{M}_i + \sigma^m \boldsymbol{H})\right) - \nabla \times \boldsymbol{J}_i - \sigma^m \left(-\mu \frac{\partial \boldsymbol{H}}{\partial t} - (\boldsymbol{M}_i + \sigma^m \boldsymbol{H})\right). \quad (6)$$

To implement (4) or (6) as FDTD updating equations, we have to write them in scalar form for each Cartesian component.

A. 2D single-field E-based updating equations

If we assume no variation with respect to the *z* direction, i.e. $\frac{\partial}{\partial \boldsymbol{z}} = \boldsymbol{0}$, the *x*-component of the electric field from (4) is given as:

$$\frac{\partial^2 E_x}{\partial y^2} - \frac{\partial^2 E_y}{\partial x \partial y} = \sigma^m \sigma^e E_x + (\mu \sigma^e + \varepsilon \sigma^m)\frac{\partial E_x}{\partial t} + \mu\varepsilon \frac{\partial^2 E_x}{\partial t^2} + \frac{\partial M_{zi}}{\partial y} + \sigma^m J_{ix} + \mu \frac{\partial J_{ix}}{\partial t}. \quad (7)$$

To derive the FDTD updating equations for the *x*-component of the electric field, we have to evaluate all the spatial derivatives in (7) at their corresponding electric field node, i.e. E_x. Central difference formula is used to discretize the derivatives. Care must be taken for $\frac{\boldsymbol{\partial^2 E_y}}{\boldsymbol{\partial x \partial y}}$ term. Four field components need to be used to evaluate the second derivative of E_y at the corresponding electric field node as shown in Fig. 1.

$$\frac{\partial^2 E_y(i,j)}{\partial x \partial y} = \frac{E_y^n(i+1,j) - E_y^n(i+1,j-1) - E_y^n(i,j) + E_y^n(i,j-1)}{\Delta x \Delta y}. \quad (8)$$

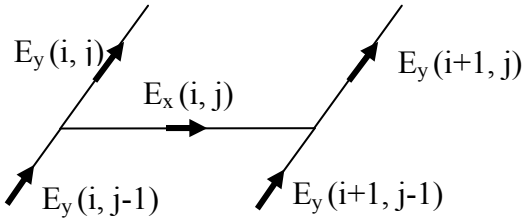

Fig. 1. Electric field components in 2D.

$$\begin{aligned} E_x^{n+1}(i,j) = {} & C_{ex}^{ex,n}(i,j)[E_x^n(i,j)] \\ & + C_{ex}^{ex,n-1}(i,j)[E_x^{n-1}(i,j)] \\ & + C_{ex}^{ex,n,y}(i,j)[E_x^n(i,j+1) + E_x^n(i,j-1)] \\ & + C_{ex}^{ey,n,xy}(i,j)[E_y^n(i+1,j) - E_y^n(i,j) \\ & \quad - E_y^n(i+1,j-1) + E_y^n(i,j-1)] \\ & + C_{ex}^{Mz,n,y}(i,j)\left[M_{i,z}^n(i,j) - M_{i,z}^n(i,j-1)\right] \\ & + C_{ex}^{Jx,n}(i,j)\left[J_{i,x}^n(i,j)\right] \\ & + C_{ex}^{Jx,t}(i,j)\left[J_{i,x}^{n+1}(i,j) - J_{i,x}^{n-1}(i,j)\right]. \end{aligned} \quad (9)$$

The final expression of the updating equation for the *x*-component of the electric field is given in (9), where the *C* terms are constant coefficients as given in Appendix A. The source terms are only included at the source locations whereas the field terms are included in the updating equation throughout the entire problem domain.

Similarly, updating equations for E_y and E_z can be derived in the same manner and are given below for completeness.

$$\begin{aligned}E_y^{n+1}(i,j) = {} & C_{ey}^{ey,n}(i,j)\left[E_y^n(i,j)\right] \\ & + C_{ey}^{ey,n-1}(i,j)\left[E_y^{n-1}(i,j)\right] \\ & + C_{ey}^{ey,n,x}(i,j)\left[E_y^n(i+1,j) + E_y^n(i-1,j)\right] \\ & + C_{ey}^{ex,n,xy}(i,j)[E_x^n(i,j+1) - E_x^n(i,j) \\ & \qquad - E_x^n(i-1,j+1) + E_x^n(i-1,j)] \\ & + C_{ey}^{Mz,n,x}(i,j)\left[M_{i,z}^n(i,j) - M_{i,z}^n(i-1,j)\right] \\ & + C_{ey}^{Jy,n}(i,j)\left[J_{i,y}^n(i,j)\right] \\ & + C_{ey}^{Jy,t}(i,j)\left[J_{i,y}^{n+1}(i,j) - J_{i,y}^{n-1}(i,j)\right]. \end{aligned} \quad (10)$$

and

$$\begin{aligned}E_z^{n+1}(i,j) = {} & C_{ez}^{ez,n}(i,j)[E_z^n(i,j)] \\ & + C_{ez}^{ez,n-1}(i,j)[E_z^{n-1}(i,j)] \\ & + C_{ez}^{ez,n,x}(i,j)[E_z^n(i+1,j) + E_z^n(i-1,j)] \\ & + C_{Ez}^{ez,n,y}(i,j)[E_z^n(i,j+1) + E_z^n(i,j-1)] \\ & + C_{ez}^{Miy,n,x}(i,j)\left[M_{i,y}^n(i,j) - M_{i,y}^n(i-1,j)\right] \\ & + C_{ez}^{Mix,n,y}(i,j)\left[M_{i,x}^n(i,j) - M_{i,x}^n(i,j-1)\right] \\ & + C_{ez}^{Jz,n}(i,j)\left[J_{i,z}^n(i,j)\right] \\ & + C_{ez}^{Jiz,t}(i,j)\left[J_{i,z}^{n+1}(i,j) - J_{i,z}^{n-1}(i,j)\right]. \end{aligned} \quad (11)$$

B. 1D single-field E-based updating equations

FDTD updating equations for the one-dimensional field components can be easily obtained from the two-dimensional updating equations by further assuming $\frac{\partial}{\partial y} = 0$. The *y*-component of the electric field is then given as:

$$\begin{aligned}\frac{\partial^2 E_y}{\partial x^2} = \sigma^e\sigma^m E_y + (\mu\sigma^e + \varepsilon\sigma^m)\frac{\partial E_y}{\partial t} + \mu\varepsilon\frac{\partial^2 E_y}{\partial t^2} - \\ \frac{\partial M_{i,z}}{\partial x} + \sigma^m J_{iy} + \mu\frac{\partial J_{i,y}}{\partial t}, \end{aligned} \quad (12)$$

which yields the following updating equation

$$\begin{aligned}E_y^{n+1}(i) = {} & C_{ey}^{ey,n}(i)\left[E_y^n(i)\right] \\ & + C_{ey}^{ey,n-1}(i)\left[E_y^{n-1}(i)\right] \\ & + C_{ey}^{en,n,x}(i)\left[E_y^n(i+1) + E_y^n(i-1)\right] \\ & + C_{ey}^{Mz,n,x}(i)\left[M_{i,z}^n(i) - M_{i,z}^n(i-1)\right] \\ & + C_{ey}^{Jy,n}(i)\left[J_{i,y}^n(i)\right] \\ & + C_{ey}^{Jy,t}(i)\left[J_{i,y}^{n+1}(i) - J_{i,y}^{n-1}(i)\right]. \end{aligned} \quad (13)$$

Similarly, updating equations for E_z, H_y, and H_z can be derived in the same manner.

In the solution of 2D and 1D electromagnetic problems, one can utilize the proper updating equation to find the field in the problem domain at each time step. Moreover, frequency domain solution and scattering parameters can also be obtained by using the time domain field solution.

III. PERFORMANCE ANALYSIS

A. Memory/speed analysis of a 1D problem

Next, we examine a one-dimensional electromagnetic problem given in [10]. The electric field components, due to a *z*-directed electric current sheet placed at the center of a problem space filled with air between two parallel perfect electric conducting plates extending to infinity in *y* and *z* directions, are computed. Figure 2 shows the comparison of the CPU time required by the single-field and the traditional formulations for the same cell size and number of cells. The required number of floating-point addition operation per node (FLAOPn), floating-point multiplication operation per node (FLMOPn), and memory allocation needed for the field terms per node (MAFTn) are tabulated in Table 1.

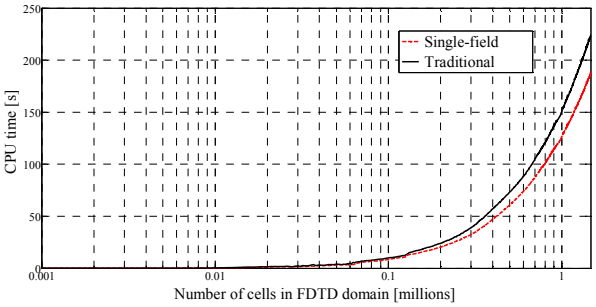

Fig. 2. Comparison of performance in 1D.

B. Memory/speed analysis of a TM problem

A two-dimensional problem is constructed as free space with a *z*-directed impressed electric current located at the origin. The current density has a Gaussian waveform with magnitude of 1 [Amp/m]. Electric field generated by the

traditional and the single-field formulations are compared in time and frequency domains, the stability and dispersion analyses are also performed for both. Since the real benefit of the single-field formulation is the time required to run the simulation and required memory size, the two formulations are compared for different domain sizes. Figure 3 shows the CPU time verses domain size for both formulations for the same cell size and number of cells. To get a better insight for the simulation time and memory usage, the required number of FLAOPn, FLMOPn, and (MAFTn) are tabulated in Table 1. As for the memory allocation, only the field terms and their coefficients are taken into account since the source terms are updated at only source points, therefore the required memory for the source terms and their coefficients are negligible compared to the field terms.

C. Memory/speed analysis of a TE problem

A two dimensional problem is constructed as free space with a *z*-directed impressed magnetic current located at the origin. The current density has a Gaussian waveform with magnitude of 1 [V/m]. Magnetic field generated by the traditional and the single-field formulations are compared in time and frequency domains, stability and dispersion analyses are, also, performed for both. Due to the symmetry in the formulation and duality in the problem, merits for CPU time, memory requirements, stability, and dispersion are the same as the previous TM problem. Therefore, Fig. 3 and Table 1 show the performance of the single-field formulation for 2D TE problems as well.

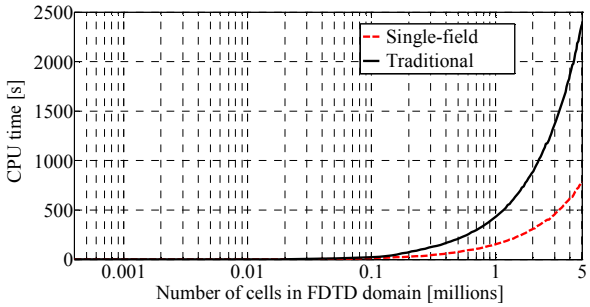

Fig. 3. Comparison of performance in 2D.

A speed up factor is calculated according to the formula given in (14) for different problem sizes and plotted in Fig. 4.

$$\text{Speed up Factor} = \frac{CPU\ Time\ (Traditional)}{CPU\ Time\ (Single-field)}. \quad (14)$$

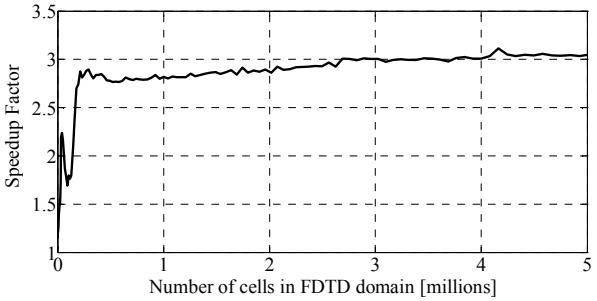

Fig. 4. Speed up factor in 2D.

The single-field formulation appears to be faster than the traditional one, especially for greater domain sizes.

Table 1: Summary of the required number of FLAOPn, FLMOPn, and MAFTn

Formulation	# FLAOPn	# FLMOPn	# MAFTn
2D Single-field	5	4	6
2D Traditional	8	7	10
1D Single-field	3	3	5
1D Traditional	2	4	6

D. Numerical validation

An infinite line of a constant electric current is placed parallel and in the vicinity of a circular conducting cylinder of infinite length. We will examine the scattering of the cylindrical waves by the cylinder for $\rho \geq \rho'$. The analytical solution for the total electric field is given in [11] as

$$E_\rho^t = E_\varphi^t = 0, \quad (15)$$

$$E_z^t = -\frac{\beta^2 I_e}{4\omega\varepsilon}\sum_{n=-\infty}^{+\infty} H_n^{(2)}(\beta\rho) \left[J_n(\beta\rho) - \frac{J_n(\beta a)}{H_n^{(2)}(\beta\rho')} H_n^{(2)}(\beta\rho')\right] e^{jn(\varphi-\varphi')}, \quad (16)$$

where ρ is the distance from the center of the cylinder to the field point, its range is 0.1-1.1 m, ρ' is the distance from the center of the cylinder to

the source point, its value is 0.1 m, φ is the azimuth angle of the field point, and φ' is the azimuth angle of the source point; its value is 0, a is the radius of the conducting cylinder and its value is 0.01 m. For the numerical simulation, the spatial and temporal steps used are $\Delta x = \Delta y = 1$ mm and $\Delta t = 2.2407$ ps. The cylinder is modeled in FDTD domain by stair-casing. Electric field is computed with the single-field and the traditional formulation at 1000 different spatial points in time domain and converted to frequency domain to compare with the analytical solution results. The single-field and the traditional formulation show similar performance in terms of accuracy as shown in Figs. 5 and 6.

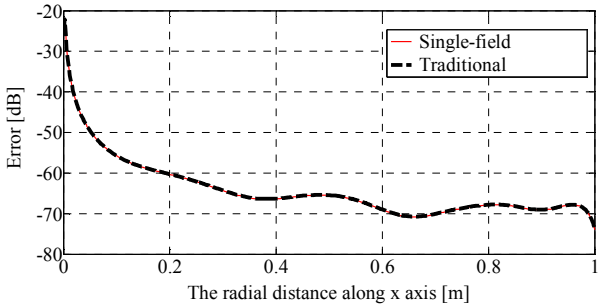

Fig. 5. Comparison of the numerical solutions with the analytical solution; magnitude.

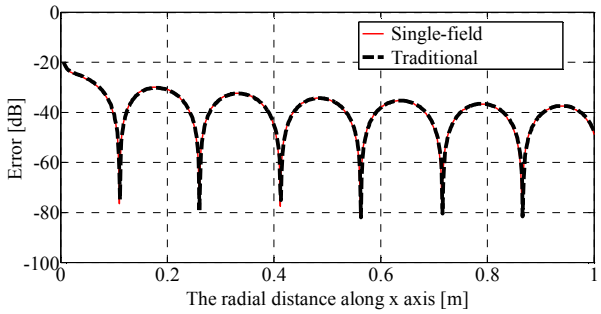

Fig. 6. Comparison of the numerical solutions with the analytical solution; phase.

E. Stability comparison

Stability comparison was conducted by changing the value of the time-increment (Δt) and observing the change in the field values generated by the single-field and the traditional formulations.

The Courant-Friedrichs-Lewy (CFL) condition [12] requires that the time increment Δt be 2.35 ps for a stable result if the space increments in both directions, Δx and Δy, are 1 mm. Figure 7 shows the field comparison of such stable simulation results calculated at point (8, 8) mm in a 20 mm x 20 mm free-space problem domain as described in Section B. If we set Δt to 2.37 ps, the single-field and the traditional formulation shows divergence from optimum field values. Figure 8 shows the divergence in terms of absolute value of the field versus time step. The single-field formulation provides comparatively less divergent results than the traditional formulation does, since it requires less numerical computation.

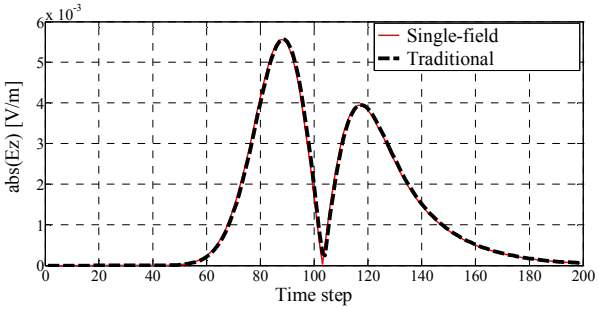

Fig. 7. Field comparison for $\Delta t = 2.35$ ps.

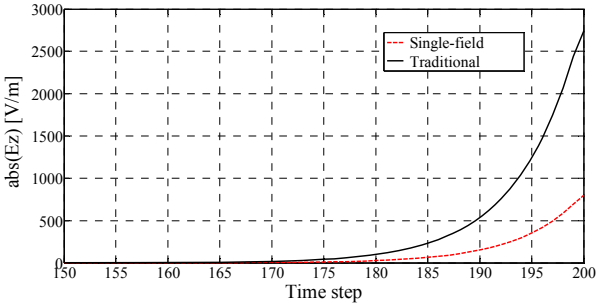

Fig. 8. Field comparison for $\Delta t = 2.37$ ps.

F. Dispersion analysis

Dispersion is defined as the variation of a propagating wave's velocity with frequency. The analysis is done for E_z component of the electric field for 2D case under the assumption of lossless medium and monochromatic traveling wave solution

$$E_z^n(i,j) = E_{z0} e^{j(\omega n \Delta t - k_x i_x \Delta_x - k_y i_y \Delta_y)}, \qquad (17)$$

where k_x and k_y are the x and y components of the numerical wavevector, i_x and i_y are space indices. By substituting this field expression into the electric field updating equation for E_z, and using the points per wavelength discretization (PPW) $= \frac{\lambda_n}{h}$, $c = \frac{1}{\sqrt{\mu_0 \varepsilon_0}}$ and $\frac{c\Delta t}{h} = 0.5$, one may obtain

$$\frac{c_n}{c_0} = \frac{\lambda_n}{\lambda} = \frac{2PPW}{\pi}\sin^{-1}\left[\frac{1}{4} - \left[\frac{1}{4}\cos\left(\frac{\pi}{PPW}(\cos\alpha + \sin\alpha)\right)\cos\left(\frac{\pi}{PPW}(\cos\alpha - \sin\alpha)\right)\right]\right]^{1/2}. \quad (18)$$

where c_n is the numerical velocity, λ_n is the numerical wavelength, and α is the angle between the direction of the propagating wave and the positive *x*-axis. Equation (18) gives the ratio of the velocities or wavelengths as a function of PPW and α for the 2D case. Figure 9 shows the variation of the normalized numerical phase velocity (c_p/c_0) versus PPW in two-dimensional FDTD grid for a plane wave travelling at 0 degree angle i.e., $\alpha = 0$.

Dispersion performance of the single-field formulation shows a characteristic identical to the traditional formulation as given in [13].

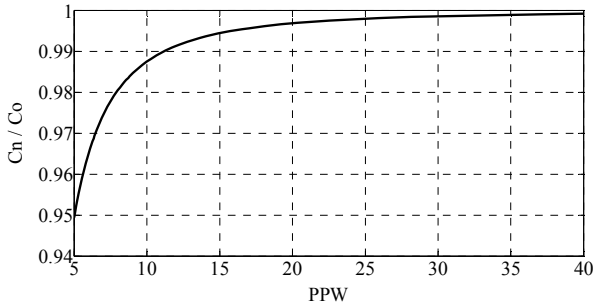

Fig. 9. Dispersion performance of the single-field formulation.

IV. CONCLUSION

The single-field finite-difference time-domain updating equations have been derived for two and one dimensional electromagnetic problems. In the traditional approach, electric field components are updated at integer time increments whereas magnetic field components need to be updated after a half-time-increment. Since the proposed updating equations are based on a single field only, updating field components takes place only at integer time increments [14]. Liao's ABCs are used for both formulations in the verification of the examples presented [4]. One-dimensional case of the single-field formulation is evaluated with example geometry, and it is observed that the single-field formulation is about 20% faster than the traditional one, and provides around 20% memory reduction for solving the same size problem. The single-field formulation has great advantage in the two-dimensional case. A two-dimensional TM_z problem is constructed with an electric current source, and the field away from the source is calculated by the single-field and the traditional formulations. First, the stability and dispersion analyses are performed. Then, the speed and memory analyses follow; the single-field formulation happens to be around three times faster for reasonably big problem sizes and requires around 43% less memory than its traditional counterpart. A two-dimensional TE_z problem evaluation is also discussed to show that the single-field formulation is advantageous for two-dimensional TM_z as well as TE_z problems. The 3D case is being worked on for non-dispersive and dispersive media. The results will be reported in a future article.

APPENDIX A

The Complete Expressions of the Coefficients

$$C_x(i,j) = -\frac{2(\Delta t)^2}{\Delta t(\mu\sigma^e + \varepsilon\sigma^m) + 2\mu\varepsilon} \quad (19)$$

$$C_{ex}^{ex,n}(i,j) = C_x(i,j)\left(\frac{2}{(\Delta y)^2} - \frac{2\mu\varepsilon}{(\Delta t)^2} + \sigma^m\sigma^e\right) \quad (20)$$

$$C_{ex}^{ex,n-1}(i,j) = C_x(i,j)\left(\frac{\mu\varepsilon}{(\Delta t)^2} - \frac{(\mu\sigma^e + \varepsilon\sigma^m)}{2\Delta t}\right) \quad (21)$$

$$C_{ex}^{ex,n,y}(i,j) = -C_x(i,j)\left(\frac{1}{(\Delta y)^2}\right) \quad (22)$$

$$C_{ex}^{ey,n,xy}(i,j) = C_x(i,j)\left(\frac{1}{\Delta x\Delta y}\right) \quad (23)$$

$$C_{ex}^{mz,n,y}(i,j) = C_x(i,j)\left(\frac{1}{\Delta y}\right) \quad (24)$$

$$C_{ex}^{jx,n}(i,j) = C_x(i,j)(\sigma^m) \quad (25)$$

$$C_{ex}^{jx,t}(i,j) = C_x(i,j)\left(\frac{\mu}{2\Delta t}\right) \quad (26)$$

$$C_y(i,j) = -\frac{2(\Delta t)^2}{\Delta t(\mu\sigma^e + \varepsilon\sigma^m) + 2\mu\varepsilon} \quad (27)$$

$$C_{ey}^{ey,n}(i,j) = C_y(i,j)\left(\frac{2}{(\Delta x)^2} - \frac{2\mu\varepsilon}{(\Delta t)^2} + \sigma^m\sigma^e\right) \quad (28)$$

$$C_{ey}^{ey,n-1}(i,j) = C_y(i,j)\left(\frac{\mu\varepsilon}{(\Delta t)^2} - \frac{(\mu\sigma^e + \varepsilon\sigma^m)}{2\Delta t}\right) \quad (29)$$

$$C_{ey}^{ey,n,x}(i,j) = -C_y(i,j)\left(\frac{1}{(\Delta x)^2}\right) \quad (30)$$

$$C_{ey}^{ex,n,xy}(i,j) = C_y(i,j)\left(\frac{1}{\Delta x\Delta y}\right) \quad (31)$$

$$C_{ey}^{mz,n,y}(i,j) = -C_y(i,j)\left(\frac{1}{\Delta x}\right) \quad (32)$$

$$C_{ey}^{jy,n}(i,j) = C_y(i,j)(\sigma^m) \quad (33)$$

$$C_{ey}^{jy,t}(i,j) = C_y(i,j)\left(\frac{\mu}{2\Delta t}\right) \quad (34)$$

$$C_z(i,j) = -\frac{2(\Delta t)^2}{\Delta t(\mu\sigma^e + \varepsilon\sigma^m) + 2\mu\varepsilon} \quad (35)$$

$$C_{ez}^{ez,n}(i,j) = C_z(i,j)\left(\frac{2}{(\Delta x)^2} + \frac{2}{(\Delta y)^2} - \frac{2\mu\varepsilon}{(\Delta t)^2} + \sigma^m\sigma^e\right) \quad (36)$$

$$C_{ez}^{ez,n-1}(i,j) = C_z(i,j)\left(\frac{\mu\varepsilon}{(\Delta t)^2} - \frac{(\mu\sigma^e + \varepsilon\sigma^m)}{2\Delta t}\right) \quad (37)$$

$$C_{ez}^{ez,n,x}(i,j) = -C_z(i,j)\left(\frac{1}{(\Delta x)^2}\right) \quad (38)$$

$$C_{ez}^{ez,n,y}(i,j) = -C_z(i,j)\left(\frac{1}{(\Delta y)^2}\right) \quad (39)$$

APPENDIX B

2D Single-Field H-Based Updating Equations

If we assume no variation with respect to the *z* direction, i.e. $\frac{\partial}{\partial z} = 0$, the *x*-component of the magnetic field from (6) is given as:

$$\frac{\partial^2 H_x}{\partial y^2} - \frac{\partial^2 H_y}{\partial x \partial y} = \sigma^m\sigma^e H_x + (\mu\sigma^e + \varepsilon\sigma^m)\frac{\partial H_x}{\partial t} + \mu\varepsilon\frac{\partial^2 H_x}{\partial t^2} + \frac{\partial J_{i,z}}{\partial y} + \sigma^E M_{i,x} + \mu\frac{\partial M_{i,x}}{\partial t}. \quad (12)$$

To derive the FDTD updating equations for the *x*-component of the magnetic field, we have to evaluate all the spatial derivatives in (12) at their corresponding magnetic field node, i.e. H_x. Central difference formula is used to discretize the derivatives.

The final expression of the updating equation for the *x*-component of the magnetic field becomes

$$\begin{aligned} H_x^{n+1}(i,j) = {} & C_{hx}^{hx,n}(i,j)[H_x^n(i,j)] \\ & + C_{hx}^{hx,n-1}(i,j)[H_x^{n-1}(i,j)] \\ & + C_{hx}^{hx,n,y}(i,j)[H_x^n(i,j+1) + H_x^n(i,j-1)] \\ & + C_{hx}^{hy,n,xy}(i,j)[H_y^n(i+1,j) - H_y^n(i,j) \\ & \quad - H_y^n(i+1,j-1) + H_y^n(i,j-1)] \\ & + C_{hx}^{Jiz,n,y}(i,j)\left[J_{i,z}^n(i,j) - J_{i,z}^n(i,j-1)\right] \\ & + C_{hx}^{Mix,n}(i,j)\left[M_{i,x}^n(i,j)\right] \\ & + C_{hx}^{Mix,t}(i,j)\left[M_{i,x}^{n+1}(i,j) - M_{i,x}^{n-1}(i,j)\right], \end{aligned} \quad (14)$$

where the *C* terms are constant coefficients. Similarly, updating equations for H_y and H_z can be obtained in the same manner and their final expressions are

$$\begin{aligned} H_y^{n+1}(i,j) = {} & C_{hy}^{hy,n}(i,j)H_y^n(i,j) \\ & + C_{hy}^{hy,n-1}(i,j)\left[H_y^{n-1}(i,j)\right] \\ & + C_{hy}^{hy,n,y}(i,j)\left[H_y^n(i,j+1) + H_y^n(i,j-1)\right] \\ & + C_{hy}^{hy,n,xy}(i,j)[H_y^n(i,j+1) - H_y^n(i,j) \\ & \quad - H_y^n(i-1,j+1) + H_y^n(i-1,j)] \\ & + C_{hy}^{Jiz,n,x}(i,j)\left[J_{i,z}^n(i+1,j) - J_{i,z}^n(i,j)\right] \\ & + C_{hy}^{Miy,n}(i,j)\left[M_{i,y}(i,j)\right] \\ & + C_{hy}^{Miy,t}(i,j)\left[M_{i,y}^{n+1}(i,j) - M_{i,y}^{n-1}(i,j)\right]. \end{aligned} \quad (15)$$

$$\begin{aligned} H_z^{n+1}(i,j) = {} & C_{hz}^{hz,n}(i,j)[H_z^n(i,j)] \\ & + C_{hz}^{hz,n-1}(i,j)[H_z^{n-1}(i,j)] \\ & + C_{hz}^{hz,n,x}(i,j)[H_z^n(i+1,j) + H_z^n(i-1,j)] \\ & + C_{hz}^{hz,n,y}(i,j)[H_z^n(i,j+1) + H_z^n(i,j-1)] \\ & + C_{hz}^{Jy,n,x}(i,j)\left[J_{i,y}^n(i+1,j) - J_{i,y}^n(i,j)\right] \\ & + C_{hz}^{Jx,n,y}(i,j)\left[J_{i,x}^n(i,j+1) - J_{i,x}^n(i,j-1)\right] \\ & + C_{hz}^{Miz,n}(i,j)\left[M_{i,z}(i,j)\right] \\ & + C_{hz}^{Miz,t}(i,j)\left[M_{i,z}^{n+1}(i,j) - M_{i,z}^{n-1}(i,j)\right]. \end{aligned} \quad (16)$$

APPENDIX C

The Computing System Information

All of the simulations presented in this paper are performed using a system whose specifications are given in the table below.

Table 2: The computing system specifications

Processor	Intel(R) Core(TM) i7 CPU 920 @ 2.67 GHz
Memory	6.00 GB
System Type	64-bit OS
Operation System	Windows 7 Pro
Programming Language	Matlab R2009a (32-bit)

REFERENCES

[1] K. Yee, "Numerical solution of initial boundary value problems involving Maxwell's equations in isotropic media," *IEEE Trans. Antennas Propagation*, vol. AP-14, pp. 302-307, May 1966.

[2] K. L. Shlager and J. B. Schneider, "A selective survey of the finite-difference time-domain literature," *IEEE Antennas and Propagation Magazine*, vol. 37, pp. 39-57, August 1995.

[3] G. Mur, "Absorbing boundary conditions for the finite-difference approximations of the time-domain electromagnetic field equations," *IEEE Trans. Electromagnetic Compatibility*, vol. EMC-23, pp. 1073-1077, Nov. 1981.

[4] Z. P. Liao, H. L. Wong, B. Yang, and Y. Yuan, "A transmitting boundary for transient wave analysis," *Sci. Sin., Ser. A*, vol. 27, pp. 1063–1076, 1984.

[5] J. P. Berenger, "A perfectly matched layer for the absorption of electromagnetic waves," *Journal of Computational Physics*, vol. 114, pp. 185–200, 1994.

[6] P. H. Aoyagi, Jin-Fa Lee, and R. Mittra, "A hybrid Yee algorithm/scalar-wave equation approach," *IEEE Trans. on Microwave Theory and Techniques,* vol. 41, pp. 1593–1600, September 1993.

[7] M. Okoniewski, "Vector wave equation 2D-FDTD method for guided wave problems," IEEE *Microwave and Guided Wave Letters,* vol. 3, pp. 307–309, September 1993.

[8] W. P. Huang, S. T. Chu, and S. K. Chaudhuri, "A semivectorial finite-difference time-domain method (optical guided structure simulation)," *IEEE Photonics Technology Letters,* vol. 3, pp. 803–806, September 1991.

[9] S. T. Chu and S. K. Chaudhuri, "A finite-difference time-domain method for the design and analysis of guided-wave optical structures," *Journal of Lightwave Technology,* vol. 7, pp. 2033–2038, 1989.

[10] A. Elsherbeni and V. Demir, *The Finite-Difference Time-Domain Method for Electromagnetics with MATLAB Simulations*, section 1.5 Raleigh, NC: SciTech Publishing, 2009.

[11] C. A. Balanis, *Advanced Engineering Electromagnetics*, section 11.5.5, NY: John Wiley, 1982.

[12] R. Courant, K. Friedrichs, and H. Lewy, "On the Partial Difference Equations of Mathematical Physics," *IBM Journal of Research and Development*, vol. 11, no. 2, pp. 215-234, 1967.

[13] A. M. Abdin, "Fourth Order Accurate FDTD Technique and Its Applications in Electromagnetics and Microwave Circuits," Dissertation, pp. 88, January 1998.

[14] G. Aydin, A. Z. Elsherbeni, and E. Arvas, "A New Finite-Difference Time-Domain Formulation for Electromagnetic Simulations," *ACES Conference*, Finland, 2010.

Gokhan Aydin received the B.S. in Electrical and Electronics Engineering from Gaziantep University in 2005 and the M.S. in Electrical Engineering from Syracuse University in 2008. He is currently working towards his Ph.D. degree in the Department of Electrical Engineering and Computer Science at Syracuse University.

He worked as an Interoperability Engineer at Sonnet Software, Inc. during 2008-2009. He has been a Teaching Associate at Syracuse University since 2009. His research interest includes Scientific Computing and RF/Microwave Circuit Design. He is a student member of IEEE and ACES.

Atef Z. Elsherbeni is a Professor of Electrical Engineering and Associate Dean of Engineering for Research and Graduate Programs, the Director of The School of Engineering CAD Lab, and the Associate Director of The Center for Applied Electromagnetic Systems Research (CAESR) at The University of Mississippi. In 2004, he was appointed as an adjunct Professor, at The Department of Electrical Engineering and Computer Science of the L.C. Smith College of Engineering and Computer Science at Syracuse University. In 2009, he was selected as Finland Distinguished Professor by the Academy of Finland and Tekes.

Dr. Elsherbeni is a Fellow member of the Institute of Electrical and Electronics Engineers (IEEE) and a Fellow member of The Applied Computational Electromagnetics Society (ACES). He is the Editor-in-Chief for the ACES Journal and a past Associate Editor to the Radio Science Journal.

Ercument Arvas received the B.S. and M.S. degrees from METU, Ankara, Turkey, in 1976 and 1979, respectively, and the Ph.D. degree from Syracuse University, Syracuse, New York, in 1983, all in Electrical Engineering. Between 1984 and fall of 1987, he was with the Electrical Engineering Department of Rochester Institute of Technology, Rochester, New York. He joined the Electrical Engineering and Computer Science Department of Syracuse University in 1987, where he is currently a Professor. His research interest includes numerical electromagnetics, antennas, and microwave circuits. He is a fellow of IEEE.

Bandwidth Control of Optimized FDTD Schemes

Theodoros T. Zygiridis

Department of Informatics and Telecommunications Engineering
University of Western Macedonia, Kozani 50100, Greece
tzygiridis@uowm.gr

Abstract ─ We investigate the potential of controlling the wideband behavior of finite-difference time-domain (FDTD) methods, which adopt extended spatial operators while maintaining the standard temporal updating procedure. Specifically, single-frequency optimization is performed first, while wider bands are then treated with the aid of the least-squares technique. The proposed methodology is applied to various discretization schemes with different stencil sizes and shapes, thus verifying its versatile character. Theoretical as well as numerical results are presented, which demonstrate that the optimization process has a beneficial impact on the efficiency of FDTD algorithms, and yields attractive alternatives for reliable multi-frequency simulations.

Index Terms ─ Finite-difference time-domain (FDTD) methods, high-order schemes, least squares, performance optimization.

I. INTRODUCTION

When solving wideband electromagnetic problems, a common feature in Yee's finite-difference time-domain (FDTD) method [1-4] and other standard techniques is that low-frequency components are modeled more reliably than those at higher frequencies. This phenomenon is due to the use of finite-difference operators that originate from truncated Taylor series. Experience has shown that such general approximations do not necessarily produce the lowest errors. In addition, Taylor-based schemes may be inefficient, when different orders of spatial and temporal differencing are combined. For instance, to ensure adequate performance for the (2,4) FDTD method, one should use significantly smaller time steps, compared to the stability limit [5]. On the other hand, a class of computational alternatives comprises schemes that exhibit optimized behavior, even if their formal accuracy order is not maximized. In contrast with conventional solutions, their frequency response is adjustable to problem-related needs. Usually, single-frequency optimization is realized [6–9], which cannot always ensure satisfactory wideband characteristics or control of the optimization bandwidth. Yet, there exist approaches that directly deal with the challenging issue of multi-frequency error control. For instance, one-dimensional suppression of phase errors, integrated over the wavenumbers of practical interest, is proposed in [10]. Another choice is to minimize numerical dispersion at one frequency, while applying additional constraints to the finite-difference coefficients [11]. The algorithms presented in [12, 13] accomplish their goals by introducing frequency-dependent quantities in the update equations, eventually altering the size of the operator stencil. Another solution [14] combines error reduction at selected wavelengths and directions of propagation. Note that we will not be concerned with inaccuracies due to geometric modeling, which can be handled with other approaches, such as subgridding techniques [15, 16].

In the present study, we focus on FDTD approaches that preserve the time advancing of Yee's method, so practically only the spatial-differencing process is modified (yet, it is shown that high convergence rates are still feasible). In order to remedy algorithmic reliability over extended frequency bands, we exploit the fact that optimum performance – according to a specific criterion – can be ensured at one frequency point. In essence, after determining a consistent error

formula, single-frequency correction is translated into a set of linear equations. The unknowns in these equations are constant coefficients, introduced by the spatial operators. An augmented system is formulated afterwards, by repeating this procedure for a number of frequency points within the band of interest. The new system is overdetermined; hence, it is solved approximately with the least-squares method. Being generalized, the proposed formulation is applied to five discretization schemes, leading to different levels of reliability. The dispersion and anisotropy flaws of the modified approaches are examined theoretically, and numerical simulations are executed to demonstrate the qualities of the new techniques.

II. METHODOLOGY

A. The case of $(2,2N)$ schemes

The present study is concerned with the two-dimensional Maxwell's equations. In the first case examined, partial derivatives with respect to space variable u ($u = x, y$) are approximated at point $i\Delta u$ by the parametric operator

$$\mathrm{D}_u\left[f_i\right]=\frac{1}{\Delta u}\sum_{\ell=1}^{N}C_\ell\left(f_{i+\frac{2\ell-1}{2}}-f_{i-\frac{2\ell-1}{2}}\right). \qquad (1)$$

In this expression, the number of considered field samples is $2N$, N = 1, 2, 3, and the unknown C_ℓ coefficients are determined later. As mentioned in the introduction, time marching is performed using the second-order leapfrog scheme:

$$\mathrm{D}_t\left[f^n\right]=\frac{1}{\Delta t}\left(f^{n+\frac{1}{2}}-f^{n-\frac{1}{2}}\right). \qquad (2)$$

Thus, the updating procedure is similar to that of the classic FDTD method. For instance, the H_z component is updated according to

$$H_z\Big|_{i+\frac{1}{2},j+\frac{1}{2}}^{n+\frac{1}{2}}=H_z\Big|_{i+\frac{1}{2},j+\frac{1}{2}}^{n-\frac{1}{2}}+\frac{\Delta t}{\mu_0}\left(\mathrm{D}_y\left[E_x\Big|_{i+\frac{1}{2},j+\frac{1}{2}}^{n}\right]-\mathrm{D}_x\left[E_y\Big|_{i+\frac{1}{2},j+\frac{1}{2}}^{n}\right]\right). \qquad (3)$$

We label these algorithms $(2,2N)$, indicating the temporal/spatial structure of the corresponding discretization scheme. The key idea is to reduce the inherent error as isotropically as possible at one frequency, and then tune the operators' response within wider bands. To exemplify the derivation of the x-operator, we start from the equation

$$\varepsilon\frac{\partial E_y}{\partial t}+\frac{\partial H_z}{\partial x}=0. \qquad (4)$$

Admitting plane-wave forms similar to the exact solutions for both field components in the discrete form of (4) yields

$$\epsilon\left(\omega,\tilde{k},\varphi\right)=\frac{\Delta x}{c_0\Delta t}\sin\left(\frac{\omega\Delta t}{2}\right)\cos\phi-\sum_{\ell=1}^{N}C_\ell\sin\left(\frac{2\ell-1}{2}\tilde{k}_x\Delta x\right)=0, \qquad (5)$$

where $\tilde{k}_x=\tilde{k}\cos\phi$ is the x-component of the numerical wavenumber $\tilde{k}$, and ϕ denotes the propagation angle. If $\tilde{k}=k=\omega/c_0$ is additionally enforced, then (5) does not remain valid, as numerical and exact wavenumbers do not coincide in general, due to discretization artifacts. Nevertheless, given that $\epsilon(\omega,k,\phi)=0$ corresponds to the ideal scenario of an error-free algorithm, an acceptable representation of the continuous problem should be feasible, as long as C_ℓ values that render $\epsilon(\omega,k,\phi)$ close to zero are selected. We refrain from specifying individual values for ϕ, since all directions can be treated rather equally, by exploiting the error's trigonometric expansion:

$$\epsilon\left(\omega,k,\varphi\right)=\frac{\Delta x}{c_0\Delta t}\sin\left(\frac{\omega\Delta t}{2}\right)\cos\phi-2\sum_{\ell=1}^{N}C_\ell\sum_{i=0}^{\infty}(-1)^i J_{2i+1}\left(\tfrac{2\ell-1}{2}k\Delta x\right)\cos\left[(2i+1)\phi\right]. \qquad (6)$$

Evidently, small values for ϵ can be easily accomplished at a designated angular frequency ω_0 through the vanishing of the first N terms in (6). In this way, a $N\times N$ system of equations is formed,

$$\left[a_{ij}(\omega_0)\right]\left[\mathrm{C}\right]=\left[b_i(\omega_0)\right], \qquad (7)$$

where

$$a_{ij}=J_{2i-1}\left(\frac{2j-1}{2}\frac{\omega\Delta x}{c_0}\right)\quad (1\le i,j\le N) \qquad (8)$$

$$b_1=\frac{\Delta x}{c_0\Delta t}\sin\left(\frac{\omega\Delta t}{2}\right) \qquad (9)$$

$$b_i=0\quad (i\ne 1), \qquad (10)$$

$J_n(x)$ denotes Bessel functions of the first kind, and [C] is the vector of the C_ℓ coefficients. As expected, the C_ℓ values calculated from (7) depend on spatial as well as temporal increments. For instance, the two necessary equations in the case of the $(2,4)$ scheme are:

$$\begin{bmatrix} J_1(\frac{k\Delta x}{2}) & J_1(\frac{3k\Delta x}{2}) \\ J_3(\frac{k\Delta x}{2}) & J_3(\frac{3k\Delta x}{2}) \end{bmatrix} \begin{bmatrix} C_1 \\ C_2 \end{bmatrix} = \begin{bmatrix} \frac{\Delta x}{2c_0\Delta t}\sin(\frac{\omega\Delta t}{2}) \\ 0 \end{bmatrix}. \quad (11)$$

Given that the described procedure relies on the selection of a specific frequency ω_0, it is expected that error decrease will be confined to the corresponding part of the spectrum. To pursue a more wideband performance tuning, we propose the application of a least-squares approach. Let's assume that the band of interest is described by $\omega_{\min} \le \omega \le \omega_{\max}$. Then, an extended set of equations can be derived by introducing a partition $\Omega = \{\omega_1, \omega_2, \ldots, \omega_M\}$ of the interval $[\omega_{\min}, \omega_{\max}]$. For each point $\omega_i \in \Omega$ ($i = 1, \ldots, M$), the corresponding equations from (7) are obtained, and all of them are assembled, in order to build a new – overdetermined – system:

$$[\mathcal{A}][\mathrm{C}] = [\mathcal{B}], \quad (12)$$

where

$$[\mathcal{A}] = \begin{bmatrix} [a_{ij}(\omega_1)] \\ [a_{ij}(\omega_2)] \\ \vdots \\ [a_{ij}(\omega_M)] \end{bmatrix}, \quad [\mathcal{B}] = \begin{bmatrix} [b_i(\omega_1)] \\ [b_i(\omega_2)] \\ \vdots \\ [b_i(\omega_M)] \end{bmatrix}. \quad (13)$$

An approximate solution to (12) is calculated by applying the least-squares method:

$$[\mathrm{C}] \simeq \left([\mathcal{A}]^{\mathrm{T}}[\mathcal{A}]\right)^{-1}\left([\mathcal{A}]^{\mathrm{T}}[\mathcal{B}]\right). \quad (14)$$

The operators acquired in this way are expected to perform well, within the prescribed band.

It is noted that the case of *y*-operators can be handled in the same manner, starting from

$$\varepsilon\frac{\partial E_x}{\partial t} - \frac{\partial H_z}{\partial y} = 0. \quad (15)$$

B. The case of $(4,2N)$ schemes

From the above description it appears that the generalized character of the proposed methodology permits further applications. Therefore, we extend the optimization procedure to FDTD schemes, which practically adopt a modified version of the fourth-order leapfrog integrator [17]. Recall that time integration based on the fourth-order leapfrog approach introduces temporal operators with the following form:

$$\mathrm{D}_t[f^n] = \frac{f^{n+\frac{1}{2}} - f^{n-\frac{1}{2}}}{\Delta t} - \frac{\Delta t^2}{24}\mathrm{D}_t^{(3)}[f^n], \quad (16)$$

where $\mathrm{D}_t^{(3)}$ stands for a second-order approximation of the third-order temporal derivative, calculated with the proper use of spatial formulae. It can be easily shown that the structure of such algorithms is equivalent to a combination of the standard second-order leapfrog scheme with extended, two-dimensional, spatial operators. We denote these algorithms as $(4,2N)$, N = 2, 3, and the geometric configuration of their spatial expressions can be identified in Fig. 1. Analytically, the parametric expression of the D_x operator now becomes

$$\mathrm{D}_x\left[f_{i,j}\right] = \frac{1}{\Delta x}\sum_{\ell=1}^{N} C_\ell\left(f_{i+\frac{2\ell-1}{2},j} - f_{i-\frac{2\ell-1}{2},j}\right) + \frac{1}{\Delta x}C_{N+1}\left(f_{i+\frac{1}{2},j+1} + f_{i+\frac{1}{2},j-1} - f_{i-\frac{1}{2},j+1} - f_{i-\frac{1}{2},j-1}\right). \quad (17)$$

Compared to the formula in (1), an extra degree of freedom has been added (C_{N+1}), which weights nodal values appearing on both sides of the differentiation axis. Following the methodology applied to $(2,2N)$ schemes, we define a similar error expression, whose trigonometric expansion is

$$\epsilon(\omega,k,\phi) = \frac{\Delta x}{c_0\Delta t}\sin\left(\frac{\omega\Delta t}{2}\right)\cos\phi - 2\sum_{\ell=1}^{N} C_\ell\sum_{i=0}^{\infty}(-1)^i J_{2i+1}\left(\tfrac{2\ell-1}{2}k\Delta x\right)\cos\left[(2i+1)\phi\right] - 4C_{N+1}\sum_{i=0}^{\infty}(-1)^i J_{2i+1}\left(\tfrac{k\Delta\chi}{2}\right)\cos\left[(2i+1)\phi_0\right]\cos\left[(2i+1)\phi\right],$$

where

$$\Delta\chi = \sqrt{4(\Delta x)^2 + (\Delta y)^2}, \ \tan\phi_0 = 2\Delta x/\Delta y. \quad (18)$$

Now, a $(N+1)\times(N+1)$ system is formulated by zeroing the first $(N+1)$ error terms. For example, we give the three necessary equations for the single-frequency design of the (4,4) scheme:

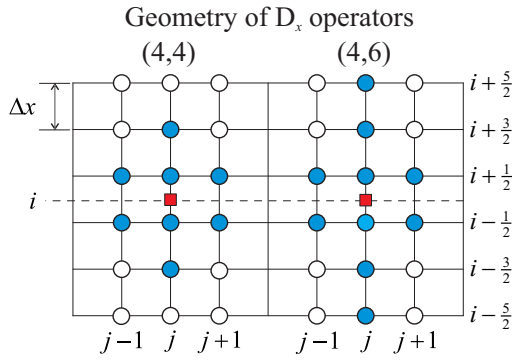

Fig. 1. Nodal arrangement of the operators used for spatial differencing by the $(4,2N)$ schemes.

$$\begin{bmatrix} J_1(\frac{k\Delta x}{2}) & J_1(\frac{3k\Delta x}{2}) & 2J_1(\frac{k\Delta \chi}{2})\cos\phi_0 \\ J_3(\frac{k\Delta x}{2}) & J_3(\frac{3k\Delta x}{2}) & 2J_3(\frac{k\Delta \chi}{2})\cos 3\phi_0 \\ J_5(\frac{k\Delta x}{2}) & J_5(\frac{3k\Delta x}{2}) & 2J_5(\frac{k\Delta \chi}{2})\cos 5\phi_0 \end{bmatrix} \begin{bmatrix} C_1 \\ C_2 \\ C_3 \end{bmatrix} = \begin{bmatrix} \frac{\Delta x}{2c_0\Delta t}\sin(\frac{\omega\Delta t}{2}) \\ 0 \\ 0 \end{bmatrix}. \quad (19)$$

Then, the wideband optimization is carried out with the application of the least-squares method, as presented in detail in Section II-A.

III. THEORETICAL ASPECTS

For simplicity, we assume $\Delta x = \Delta y = \Delta h$. In the case of the $(4,2N)$ schemes, the stability criterion is described by

$$\Delta t \le \frac{\Delta h}{c_0\sqrt{2}\left(\sum_{\ell=1}^{N}|C_\ell| - 2C_{N+1}\right)}, \quad (20)$$

while the corresponding numerical dispersion relation, which will be utilized later for theoretical tests, is

$$\left(\frac{\Delta h}{c_0\Delta t}\right)^2 \sin^2\left(\frac{\omega\Delta t}{2}\right) = \mathcal{X}^2 + \mathcal{Y}^2, \quad (21)$$

where

$$\mathcal{X} = \sum_{\ell=1}^{N} C_\ell \sin\left(\frac{2\ell-1}{2}\tilde{k}\cos\phi\Delta h\right) + 2C_{N+1}\sin\left(\frac{1}{2}\tilde{k}\cos\phi\Delta h\right)\cos\left(\tilde{k}\sin\phi\Delta h\right) \quad (22)$$

$$\mathcal{Y} = \sum_{\ell=1}^{N} C_\ell \sin\left(\frac{2\ell-1}{2}\tilde{k}\sin\phi\Delta h\right) + 2C_{N+1}\sin\left(\frac{1}{2}\tilde{k}\sin\phi\Delta h\right)\cos\left(\tilde{k}\cos\phi\Delta h\right). \quad (23)$$

Formulae (20)-(23) apply in the case of $(2,2N)$ schemes as well, considering that it is $C_{N+1} = 0$ for those algorithms. Hereafter, the time-step size is described by Q, where $Q = \sqrt{2}c_0\Delta t / \Delta h$. Note that the maximum value of Q is 1 for the standard (2,2) and (4,4) techniques, 6/7 for the standard (2,4) and 120/149 for the standard (2,6) scheme. To assess algorithmic accuracy via the numerical phase velocity $\tilde{c}$, the following error definition is used,

$$\mathcal{E}(\omega) = \frac{1}{2\pi c_0}\int_0^{2\pi}\left|c_0 - \tilde{c}(\omega,\phi)\right| d\phi, \quad (24)$$

which is a measure of the mean-error value for all possible propagation angles.

Starting from $(2,2N)$ algorithms, the variation of $\mathcal{E}$ as a function of the grid density is illustrated in Figs. 2(a)-(c). We consider two different cases: in the first one, the band of interest ranges from 25 to 35 cells per wavelength, and from 20 to 40 cells per wavelength in the second case. When $N = 1$ (Q = 0.99 is selected for the optimized techniques), moderate error reduction can be noted. On the other hand, substantial improvement is obtained when N = 2 (Q = 0.85), and even more precise results are observed in the case of six-point operators (Q = 0.7). The latter value of Q is selected due to stability purposes. As deduced from these examples, the accomplished accuracy amendment tends to concentrate toward smaller wavelengths. This is deemed a desirable feature, for high-frequency inaccuracies have the most serious impact.

Next, the $(4,2N)$ schemes are investigated in a similar fashion. Now, the desired frequency band corresponds to 30-60 cells per wavelength, and the calculated error curves appear in Fig. 3. We can verify that the modified leapfrog integration leads to smaller error fluctuations within the prescribed frequency band. In addition, it can be safely concluded that the extra degree of freedom provided by the (4, 6) scheme, compared to the (4, 4) counterpart, allows further upgrade.

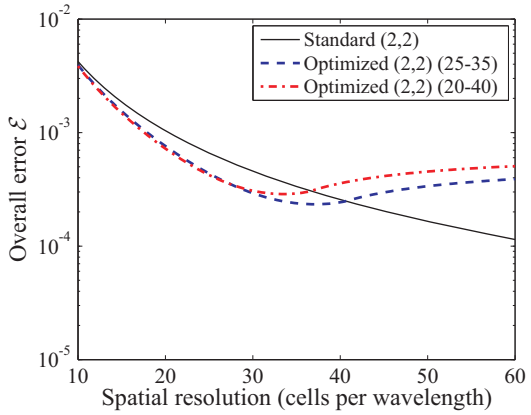

(a)

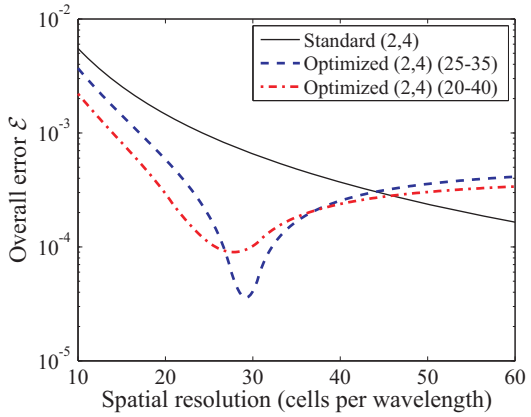

(b)

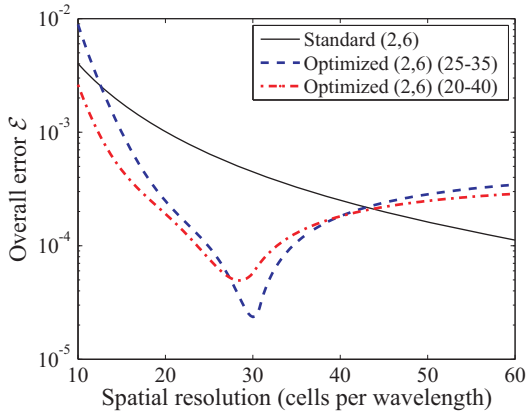

(c)

Fig. 2. Error $\mathcal{E}$ versus spatial grid resolution for $(2,2N)$ schemes: (a) $N=1$, (b) $N=2$, (c) $N=3$. Optimization is performed within either 25-35 or 20-40 cells per wavelength.

As mentioned in the introduction, a known property of schemes with lower temporal than spatial error (such as the standard (2,4) method) is the capability to improve their performance, when small time-step sizes (down to a specific limit) are selected. It is now examined whether the optimized (4, 6) technique exhibits an improved response, provided that small values for Δt are used. If we refer to Fig. 4, we may verify that this distinct feature is exhibited by the optimized (4,6) scheme as well, since a denser temporal sampling can lead to a quite equally distributed error suppression over the designated frequencies of interest.

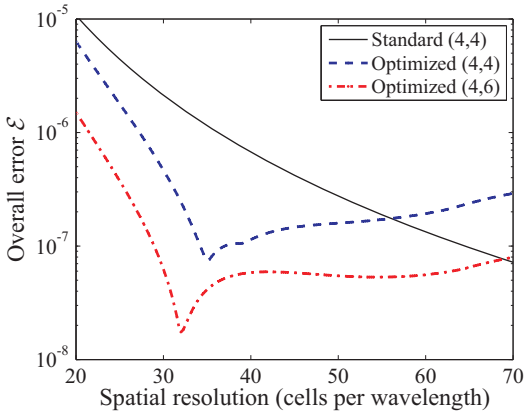

Fig. 3. Error $\mathcal{E}$ versus spatial resolution, in the case of the (4,4) and (4,6) schemes. The optimization bandwidth is 30-60 cells per wavelength.

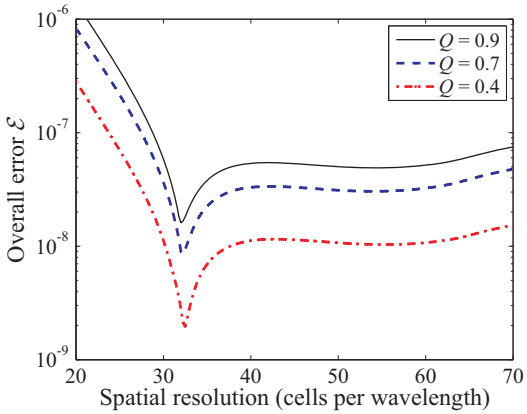

Fig. 4. Error $\mathcal{E}$ versus spatial resolution for varying time-step size, in the case of the (4,6) scheme.

IV. NUMERICAL RESULTS

In the first examples, the performance of $(2,2N)$ schemes is investigated. We initially test the narrowband optimization ensured by (7)-(10), by calculating the maximum L_2 error regarding the H_z component, when single-mode excitation is enforced in a 10 cm × 5 cm rectangular cavity with

perfectly conducting boundaries. The selected mode is TE_{22}, with a resonant frequency of 6.704 GHz. Standard as well as optimized techniques are tested considering grids with different resolutions, and the results are presented in Fig. 5. It is noted that maximum allowable time steps are selected in all cases. As anticipated, the Taylor-based algorithms exhibit second-order behavior even when extended stencils are utilized, as their low temporal accuracy dominates. On the other hand, the optimization practice treats the combined space-time errors efficiently, hence resulting in higher convergence rates. For reference, we mention that when $\Delta h = 0.568$ mm, the computational times for $N = 2, 4, 6$ is 48.8, 57.3, and 62.4 sec, respectively.

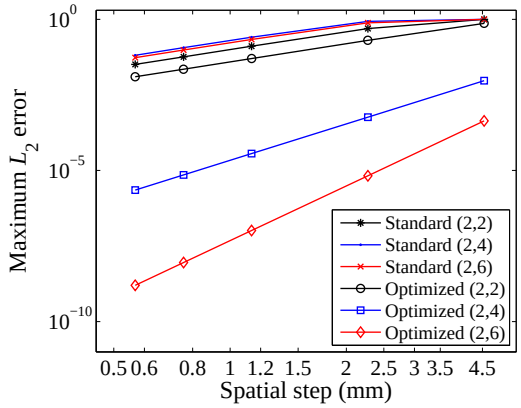

Fig. 5. Maximum L_2 error versus spatial-step size in the cavity problem with single-mode excitation.

Next, multi-modal excitation is introduced into the cavity of the previous example. Specifically, the excited modes are: TE_{11} at 3.352 GHz, TE_{31} at 5.405 GHz, and TE_{12} at 6.181 GHz. Now, the wideband optimization based on the least-squares approach is applied. The results depicted in Fig. 6 are consistent with the theoretical findings, and indicate that all schemes converge at a second-order rate (maximum time steps are again chosen). The level of error reduction in the case of Yee's method is approximately 25%. When $N = 2$, the performance upgrade appears more considerable, as 10-time lower errors are produced, compared to the conventional solution. The wideband (2, 2) and (2, 4) schemes produce the same computational times as the standard ones (9.1 and 11.3 sec, respectively, when $\Delta h = 1.14$ mm). Even better results are computed when $N = 3$; yet, the six-point operators call for reduced time steps when finer lattices are considered, which slightly increase the computational burden. Specifically, the simulation time increases from 12.5 sec to 18.9 sec, when $\Delta h = 1.14$ mm. Nevertheless, the accuracy gain is high, and the optimized (2,6) algorithm remains more efficient than the standard version.

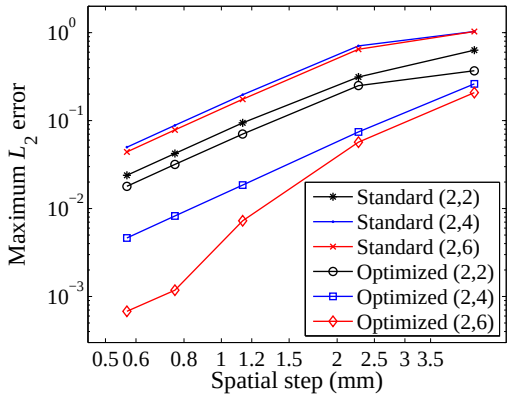

Fig. 6. Maximum L_2 error versus spatial-step size in the cavity problem with multi-modal excitation.

We, also, investigate the achievable rates of convergence, when the errors due to the low-order leapfrog updating are controlled with the use of sufficiently small time steps. For instance, the standard (2, 4) method can be fourth-order accurate, provided that the reduction of Δh by a factor of α is combined with a time-step reduction by α^2. We use the previous numerical test to determine whether the new (2, 4) and (2, 6) algorithms possess this property as well. As illustrated in Fig. 7, high convergence rates (consistent with the size of the spatial stencil) are recovered for standard as well as optimized schemes. Yet, the latter exhibit extra accuracy enhancement, which is estimated close to a factor of 10 in this example.

Proceeding with the $(4,2N)$ techniques, a 50 cm × 5 cm parallel-plate waveguide is modeled. In this configuration, three different modes are excited: TM_1 at 4.5 GHz, TM_2 at 7.5 GHz, and TM_3 at 10.5 GHz. The accuracy of various schemes is tested with grids of 200 × 20 cells, 400 × 40 cells, and 800 × 80 cells. Comparisons are made against the standard (4, 4) method. The results shown in Table 1 verify fourth-order convergence in all cases. However, error improvement by 6.8 and 8.8 times is reported, when the standard (4, 4) method is compared to the optimized (4, 4) and (4, 6) algorithms, respectively. In the case of the denser grid,

the computational time is practically the same for the standard and optimized (4,4) schemes, while the wideband (4,6) method slightly increases the simulation's duration by approximately 6 %, due to smaller time step.

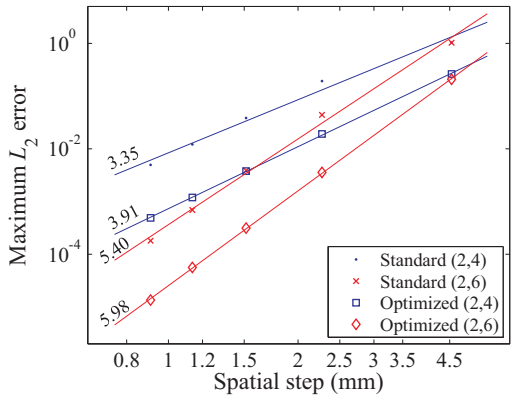

Fig. 7. Maximum L_2 error versus spatial-step size in the cavity problem with multi-modal excitation, when sufficiently small time steps are used. The convergence rates are also shown.

Table 1: Maximum L_2 errors in the parallel-plate waveguide problem

Δh (mm)	Standard (4,4)	Opt. (4,4)	Opt. (4,6)
2.5	3.15e–5	4.61e–6	3.72e–6
1.25	1.98e–6	2.88e–7	2.25e–7
0.625	1.24e–7	1.80e–8	1.39e–8

In the last test, a 5 cm × 5 cm cavity is considered, whose resonant frequencies within the band 2.998 GHz – 18.961 GHz are detected. The selected mesh comprises 25 × 25 cells, and the total simulation time corresponds to 131,072 time steps. A sufficiently narrow Gaussian pulse is used for the introduction of electromagnetic energy in the cavity. The errors concerning the $(2,2N)$ methods are shown in Fig. 8a, while Fig. 8b plots the corresponding error curves in the case of the $(4,2N)$ schemes. Moreover, an explicit reference to the numerical error values is made in Table 2. As seen, the theoretically predicted wideband upgrade of the algorithms' performance is verified, as high-frequency components are now modeled in a more reliable fashion. Note that the error of the optimized (4,6) scheme is dictated by the resolution of field samples in the frequency domain, rather than the – highly accurate – discretization process.

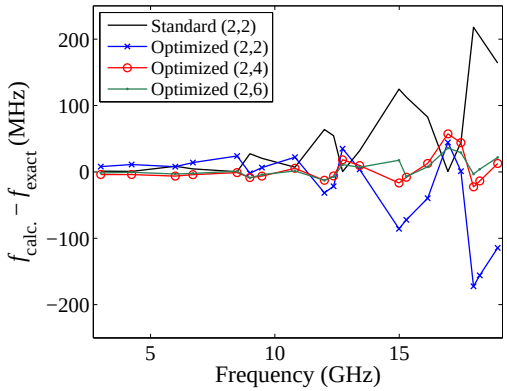

(a)

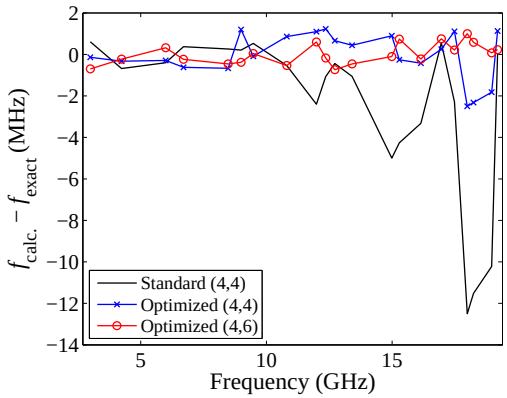

(b)

Fig. 8. Errors in the calculation of a cavity's resonant frequencies: (a) $(2,2N)$ schemes, (b) $(4,2N)$ schemes.

Table 2: Errors of various algorithms in the detection of a cavity's resonant frequencies

Method	$\max\{\lvert\Delta f\rvert\}$ (MHz)	$\max\left\{\frac{\lvert\Delta f\rvert}{f_{exact}}\right\}\cdot 100\%$
Standard (2,2)	217.9	1.21
Opt. (2,2)	172.4	0.96
Opt. (2,4)	57.35	0.34
Opt. (2,6)	35.95	0.21
Standard (4,4)	12.5	0.069
Opt. (4,4)	2.5	0.014
Opt. (4,6)	1	0.023

V. CONCLUSION

We have presented a systematic methodology that facilitates performance control of FDTD approaches over a selected frequency range. It has been pointed out, both theoretically and computationally, that algorithms based on the leapfrog integrator can be optimized within designated frequency bands, by solving an over determined sys-

tem with the least-squares method. In this way, FDTD schemes with $(2,2N)$ structure have been rendered efficient, even when operated close to stability limits. Moreover, high-order convergence has been exhibited by optimized $(4,2N)$ techniques in multi-frequency problems, ensuring improvement over standard counterparts. Compared to classic analogues, the new operators suppress errors in a broadband fashion, without extra computational burden. The proposed practice is generic and can be applied to several FDTD schemes, as long as the proper error analysis is performed.

REFERENCES

[1] K. S. Yee, "Numerical solution of initial boundary value problems involving Maxwell´s equations in isotropic media," *IEEE Trans. Antennas Propag*., vol. 14, pp. 302-307, 1966.

[2] A. Taflove and M. E. Brodwin, "Numerical solution of steady-state electromagnetic scattering problems using the time-dependent Maxwell's equations," *IEEE Trans. Microw. Theory Tech.*, vol. 23, no. 8, pp. 623-630, Aug. 1975.

[3] A. Taflove, "Application of the finite-difference time-domain method to sinusoidal steady-state electromagnetic-penetration problems," *IEEE Trans. Electromagn. Compat.*, vol. 22, no. 3, pp. 191-202, Aug. 1980.

[4] A. Taflove and S. C. Hagness, *Computational Electrodynamics: The Finite-Difference Time-Domain Method, 3rd ed.* Norwood, MA: Artech House, 2005.

[5] A. Yefet and P. G. Petropoulos, "A staggered fourth-order accurate explicit finite difference scheme for the time-domain Maxwell's equations," *J. Comput. Phys.*, vol. 168, pp. 286–315, 2001.

[6] J. B. Cole, "A high-accuracy realization of the Yee algorithm using non-standard finite differences," *IEEE Trans. Microw. Theory Tech.*, vol. 45, no. 6, pp. 991-996, June 1997.

[7] E. A. Forgy and W. C. Chew, "A time-domain method with isotropic dispersion and increased stability on an overlapped lattice," *IEEE Trans. Antennas Propag.*, vol. 50, no. 7, pp. 983-996, July 2002.

[8] I.-S. Koh, H. Kim, J.-M. Lee, J.-G. Yook, and C. S. Pil, "Novel explicit 2-D FDTD scheme with isotropic dispersion and enhanced stability," *IEEE Trans. Antennas Propag.*, vol. 54, no. 11, pp. 3505-3510, Nov. 2006.

[9] A.-X. Zhao, B.-K. Huang, and W.-B Wang, "Study of low-dispersion ADI-FDTD method with isotropic finite difference," *IEEE Antennas Wireless Propag. Lett.*, vol. 8, pp. 275-278, 2009.

[10] C. K. W. Tam and J. C. Webb, "Dispersion-relation-preserving finite difference schemes for computational acoustics," *J. Comput. Phys.*, vol. 107, no. 2, pp. 262-281, 1993.

[11] H. E. A. El-Raouf, E. A. El-Diwani, A. El-Hadi Ammar, and F. M. El-Hefnawi, "A FDTD hybrid "$M3d_{24}$" scheme with subgridding for solving large electromagnetic problems," *ACES Journal*, vol. 17, no. 1, pp. 23-29, Mar. 2002.

[12] S. Wang and F. L. Teixeira, "Dispersion-relation-preserving FDTD algorithms for large-scale three-dimensional problems," *IEEE Trans. Antennas Propag.*, vol. 51, no. 8, pp. 1818–1828, Aug. 2003.

[13] T. Ohtani, K. Taguchi, T. Kashiwa, Y. Kanai, and J. B. Cole, "Nonstandard FDTD method for wide-band analysis," *IEEE Trans. Antennas Propag.*, vol. 57, no. 8, pp. 2386–2396, Aug. 2009.

[14] Y. Liu and M. K. Sen, "A new time-space domain high-order finite-difference method for the acoustic wave equation," *J. Comput. Phys.*, vol. 228, no. 23, pp. 8779-8806, 2009.

[15] P. Monk, "Sub-gridding FDTD schemes," *ACES Journal*, vol. 11, no. 1, pp. 37-46, Mar. 1996.

[16] S. Wang, "Numerical examinations of the stability of FDTD subgridding schemes," *ACES Journal*, vol. 22, no. 2, pp. 189-194, July 2007.

[17] H. Spachmann, R. Schuhmann, and T.Weiland, "Higher order time integration schemes for Maxwell's equations," *Int. J. Numerical Modeling: Electron. Networks, Devices and Fields*, vol. 15, pp. 419–437, 2002.

Theodoros T. Zygiridis received the Diploma and Ph.D. degrees in Electrical and Computer Engineering from Aristotle University of Thessaloniki, Greece, in 2000 and 2006, respectively. He is now a Lecturer at the Department of Informatics and Telecommunications Engineering, University of Western Macedonia, Greece. His research interests lie in the area of Computational Electromagnetics, and currently focus on finite-difference time-domain algorithms, high-order techniques, and dispersion-relation-preserving methodologies.

A Small Dual Purpose UHF RFID Antenna Design

A. Ali Babar[1], Leena Ukkonen[1], Atef Z. Elsherbeni[2], and Lauri Sydanheimo[1]

[1] Department of Electronics
Tampere University of Technology, Rauma Research Unit
Kalliokatu 2, FI-26100, Rauma, Finland
abdul.babar@tut.fi, leena.ukkonen@tut.fi, lauri.sydanheimo@tut.fi

[2] Department of Electrical Engineering
The University of Mississippi, University, MS 38677-1848, USA
atef@olemiss.edu

Abstract ─ In this paper, designs and development of a small dual purpose UHF RFID planar antenna and an RFID tag antenna for small wireless application devices are presented. The planar antenna resonates at both the European and US RFID bands. It has a reasonable gain on both RFID bands with an omni-directional radiation pattern. The RFID tag antenna is designed for the European UHF RFID band. Experimental results for radiation pattern, input impedance reflection coefficient, and tag antenna realized gain confirmed the validity of the designs based on numerical simulations.

Index Terms ─ Antenna, dual band antennas, microstrip, miniaturized, planar, reader antenna, RFID, tag antenna.

I. INTRODUCTION

The growing demand for small compact wireless devices has increased the need for small antennas that can be integrated while providing acceptable overall performance. Apart from the size of the antenna and the wireless device, the cost is one of the most important aspects to consider in developing a wireless system. Thus, small low-cost antenna models are needed. The European RFID band (865 MHz - 868 MHz) and the US RFID band (902 MHz - 928 MHz) can also be used for small wireless applications. This includes various wireless sensor networks and other small indoor consumer electronic systems.

Throughout the antenna design process in this paper, the main objective was to develop a low-cost small antenna model, with reasonable performance, for the UHF RFID European and US bands. This work is an extension to the previous antenna designed and presented in [1]. The current antenna design can be useful for developing reader antennas, as well as RFID tags [2-5]. Directionality of the antenna is a result of the patch part of the antenna which radiates more than the rest of the antenna components. Since the antenna operates for both European RFID and US RFID bands, it becomes a good candidate for use in low-cost global wireless devices. It is small in size and can be embedded and integrated in several small wireless units.

Similarly, the same antenna design can be utilized to operate as a tag antenna, with an omni-directional radiation pattern and reasonable gain. The tag antenna is designed by mirroring the top part of the planar antenna and eliminating the ground plane, leading to a symmetric dipole type structure. The tag antenna is designed to operate at the European UHF RFID band. The structure of the tag antenna makes it highly sensitive to any geometrical or dielectric change. This sensitivity behavior can be exploited to make the antenna work as a sensor tag. The antenna can also be tuned to work on other frequency bands, as well as multiple frequency bands, by changing some of its configuration parameters.

Planar antenna design techniques are discussed in Section II. Section III concentrates on

utilizing the same design to make a UHF RFID tag antenna. This is followed by the simulation and measurement process and results of the planar antenna and the RFID tag antenna in Section IV. Section V discusses the sensitivity of the RFID tag antenna relative to its geometrical parameters. This is followed by the conclusions in Section VI.

II. ANTENNA DESIGN

The antenna is designed and simulated with the help of Ansoft HFSS V. 12 [6]. A 1.6 mm thick FR-4 double-sided substrate with a relative dielectric constant of 4.1 is used. The outer dimension of the antenna is 42 mm in height and 30 mm in width. The patch or lower part of the antenna has copper on both sides of the substrate, whereas the upper part of the antenna has no copper under the substrate. The feed of the antenna (using SMA connector) is connected between the feeding block of width *'a'* and height *'b'* and the ground plane as shown in Fig. 2.

The antenna structure is fabricated on a low-cost FR4 substrate to provide a low-cost solution. Various miniaturization techniques were used to tune the microstrip antenna design to the desired frequency [7]. Extra lumped components, such as capacitors and inductors were avoided in order to reduce the anticipated gain and efficiency losses from these elements. This also simplifies the manufacturing process and reduces the cost of the antenna production.

The antenna design uses the miniaturization technique of shorting the antenna structure with the ground plane, similar to PIFA designs presented in [8-9]. The shorted antenna models have a great dependency on the ground plane, which itself works as part of an asymmetrical dipole structure.

Therefore, designing a small shorted antenna model, with a small ground plane, makes the ground plane a more effective radiator. This fact is exploited in the design to achieve an antenna that radiates more on one of its poles towards the negative 'y' axis. The upper part of the antenna, along the positive 'y' axis, which consists of microstrip lines, helps in matching the antenna to the desired operating frequencies [10]. For example, line '*k*', is divided into two microstrip lines *'m1'* and '*m2*', enabling the antenna to resonate at two different frequency bands.

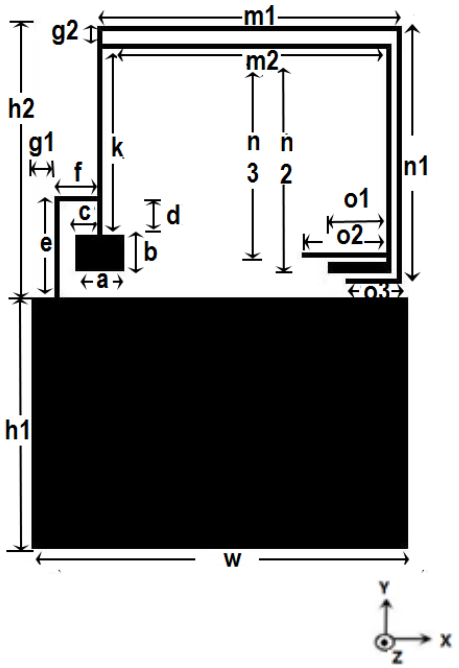

Fig. 1. Antenna configuration.

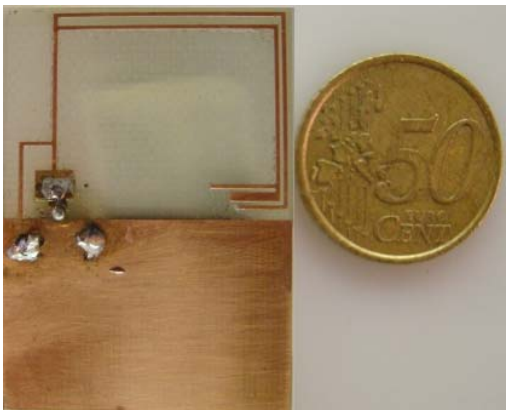

Fig. 2. Fabricated antenna model.

Furthermore, line '*m2*' is divided into two lines, '*o1*' and '*o2*'. The distance between the lines, at various places, plays a major role in matching the antenna. This also helps in lowering the resonance frequency of the antenna, by utilizing the current-vector alignment technique [11]. According to this, closely coupled lines with a current vector in-phase and in the same direction, increase the self-inductance of the antenna. This eventually reduces the resonance frequency of the antenna.

Table 1: The geometrical dimensions of the antenna in Fig. 1

Line (mm)	Length (mm)	Width (mm)
a	4	
b	3	
c	1.75	
d	2.5	0.5
e	8	0.5
f	3.45	0.5
g1	2	
g2	0.9	0.5
h1	20	
h2	21.5	
k	14.6	0.5
m1	24.25	0.5
m2	22.45	0.5
n1	20.5	0.5
n2	18.3	0.5
n3	17	0.5
o1	5.5	1
o2	6.7	0.5
o3	5	0.5
w	30	

III. TAG ANTENNA DESIGN

The RFID tag antenna is an extension of the small antenna design presented above [12]. The tag is designed using a 3.175mm thick Rogers RT/duroid 5880 [13] with a relative dielectric constant of 2.2 and 35µm copper cladding. Higgs 3 IC, manufactured by Alien Technology [14], is used in this tag antenna design. The antenna's configuration parameters were determined using numerical simulation based on Ansoft HFSS V.12. The size of the antenna is 44mm (height) x 30mm (width). The design of the tag antenna is similar to the planar small antenna, presented in Fig. 1 with slight changes in the structure. The changes are required to tune the tag antenna to the desired European UHF RFID frequency band (865 MHz - 868 MHz).

Figure 3, shows the design of the tag antenna, achieved by mirroring the planar antenna in Fig. 1. This makes the tag antenna a quasi symmetric dipole structure. There is no copper under the substrate, to achieve an omni-directional radiation pattern. The IC of the tag antenna lies in the middle of the two '*a*' lines. Line '*g*' connects both arms of the dipole to enhance the input inductance of the antenna. Some parameters of the planar antenna are modified to match the tag antenna to the desired frequency band and the input impedance of the IC. The resonance frequency of the tag antenna can be tuned to the desired frequency by changing the length of the tuning lines '*o*' and '*i*'. The length of line '*g*' also plays a great role in changing the resonance of the antenna and improving the antenna's return loss. Similar to the antenna design shown in Fig. 1, the coupling between the parallel lines reduces the size of the antenna. The closely coupled parallel lines increase the self inductance of the antenna, when the current vector is in-phase and in the same direction. The tag antenna design can also be tuned to operate on multiple frequency bands. This tuning can be done by varying the lengths of '*l*' and '*o*'. The dimensions of the tag geometrical parameters are listed in Table 2.

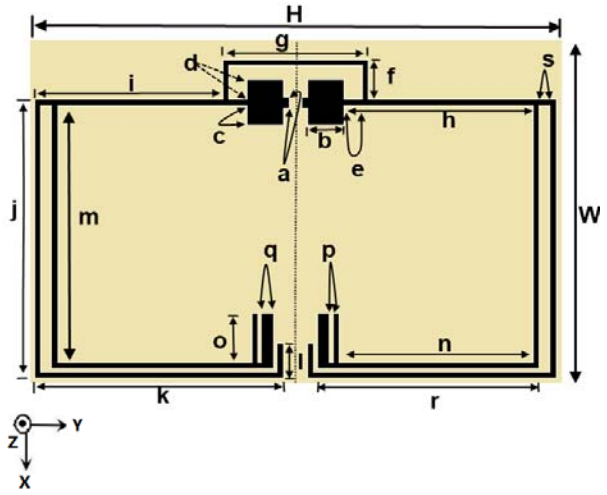

Fig. 3. UHF RFID tag antenna design.

The transfer of power between the IC (complex load impedance) and the tag antenna (complex source impedance), can be analyzed based on equation (1). The ratio of power available from the tag antenna (P_{tag}) and the power reflected back (P_{rfl}) is called the power reflection coefficient [15], [16].

$$\frac{P_{rfl}}{P_{tag}} = \left| \frac{Z_{ic} - Z_a^*}{Z_{ic} + Z_a} \right|^2 . \qquad (1)$$

Table 2: The geometrical dimensions of the antenna in Fig. 3

Line (mm)	Length (mm)	Width (mm)
a	0.5	1
b	3	
c	1.75	
d	1.75	
e	1.5	0.5
f	3.45	0.5
g	12	0.5
h	15.6	0.5
i	15.5	0.5
j	24.3	0.5
k	20.5	0.5
l	3	0.5
m	22.45	0.5
n	16	0.5
o	3.3	0.5
p	0.3	
q	1	
r	18.3	0.5
s	0.9	0.5
H	44	
W	30	

In equation (1), $Z_a=R_a+jX_a$ is the impedance of the tag antenna, whereas $Z_{ic}=R_{ic}+jX_{ic}$ is the impedance of the tag chip. The superscript (*) denotes the complex conjugate. For optimal power transfer and maximum read range, it is desirable to have a lower value for the power reflection coefficient at the operating frequency band.

IV. RESULTS

A. Planar antenna design

The antenna is fabricated with the help of a milling machine, and the S_{11} is measured by an Agilent 8358 (VNA series) Network Analyzer [17]. The radiation pattern and gain of the antenna are measured by Satimo's StarLab [18]. In Fig. 4, the simulated and measured S_{11} of the antenna are shown with resonances at both the European and the US RFID bands.

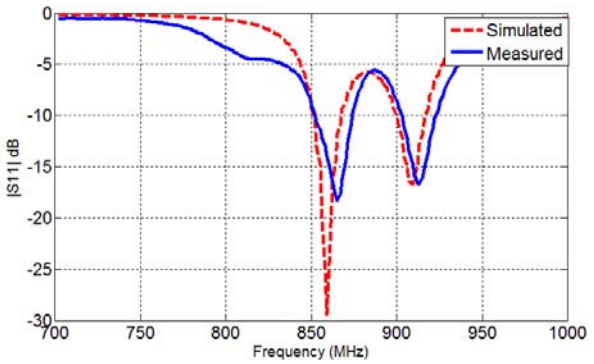

Fig. 4. Simulated and measured S_{11} (dB) of the planar antenna.

Figures 5 and 6 show the radiation patterns of the H (x-z) and E (x-y) planes of the antenna, respectively, for both 865MHz and 915MHz operating frequencies. No significant variations can be considered between the patterns at these two frequencies. Furthermore, one can observe that the directional characteristics of the antenna pattern lies in the half space below the x-z plane. The maximum deviation from the omni-directional characteristics in the H-plane is about 4dB. For the E-plane patterns, the side lobe level is in the order of -8dB, and the back lobe level is about -10dB, and -14dB for 865MHz and 915MHz, respectively. Figures 7 and 8 show the measured 3-D gain radiation patterns of the planar antenna at 865MHz and 915MHz, respectively. Similar patterns are observed, but with higher gain value at the higher frequency.

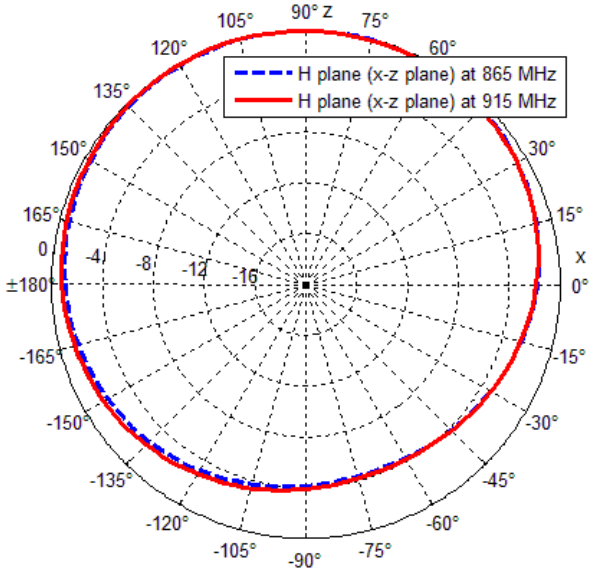

Fig. 5. Measured H-plane normalized gain (dB) of the planar antenna at 865 and 915MHz.

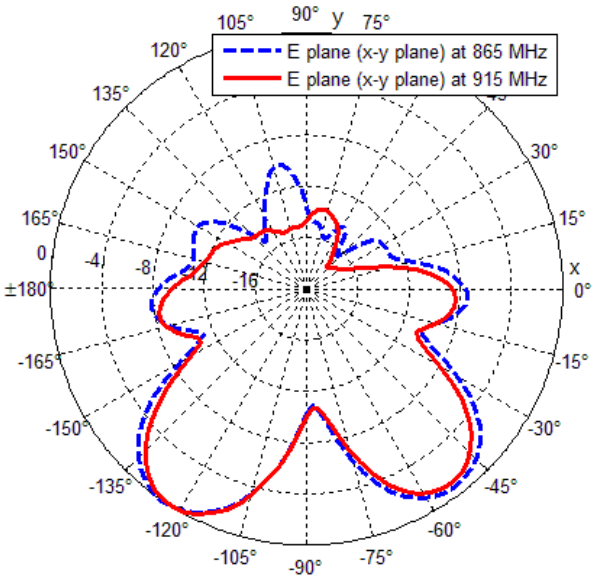

Fig. 6. Measured E-plane normalized gain (dB) of the planar antenna at 865 and 915MHz.

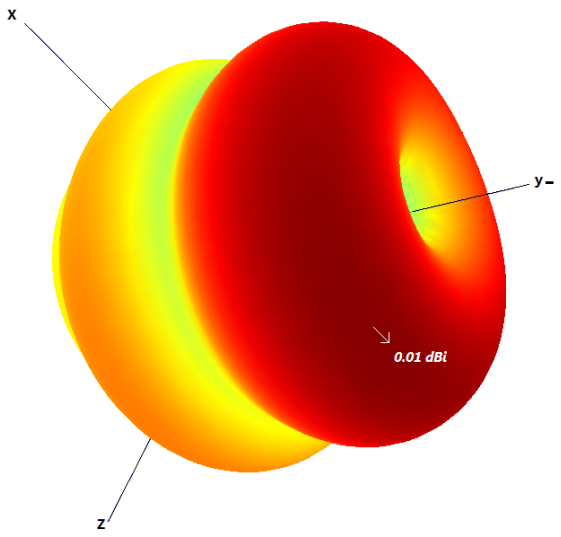

Fig. 7. Measured 3-D gain (dBi) radiation pattern of the planar antenna at 865MHz.

B. Tag antenna design

Figure 9 shows the power reflection coefficient of the tag antenna, resonating at the European UHF RFID band (865 MHz – 868 MHz). The centre frequency is set to 866 MHz. The figure illustrates that the tag antenna has a narrow bandwidth. This feature can be useful in applications where sensitive RFID tags are required. These applications include some of the RFID sensor applications, such as temperature and humidity sensors [19]. The input impedance of the chip and the tag antenna are shown in Fig. 10.

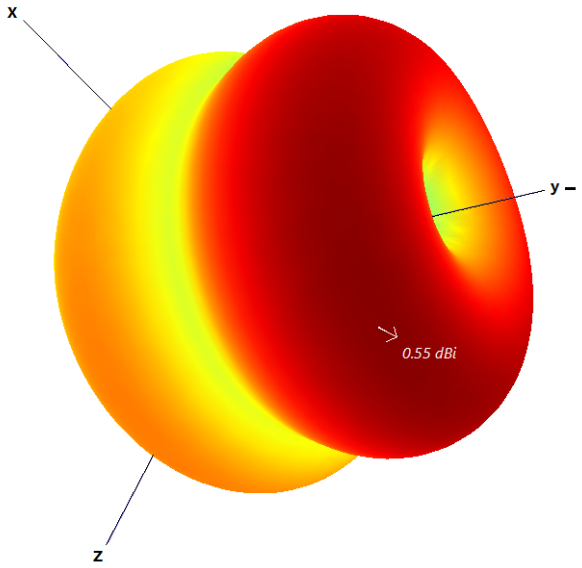

Fig. 8. Measured 3-D gain (dBi) radiation pattern of the planar antenna at 915MHz.

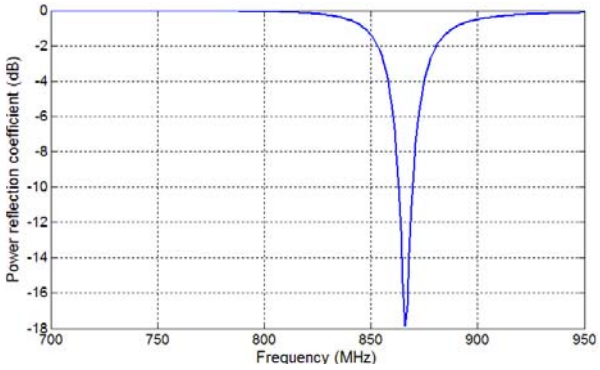

Fig. 9. Simulated power reflection coefficient of the tag antenna.

Figure 10 shows how the tag antenna parameters are carefully designed to provide a good conjugate match with the chip impedance. This is required to minimize the reflection loss at this junction, and hence improve the power transmission and maximize the read range.

The simulated normalized radiation patterns of the tag antenna are shown in Figs. 11 and 12 for the E and H planes, respectively. The radiation patterns show that the tag antenna has the typical radiation pattern of a dipole antenna.

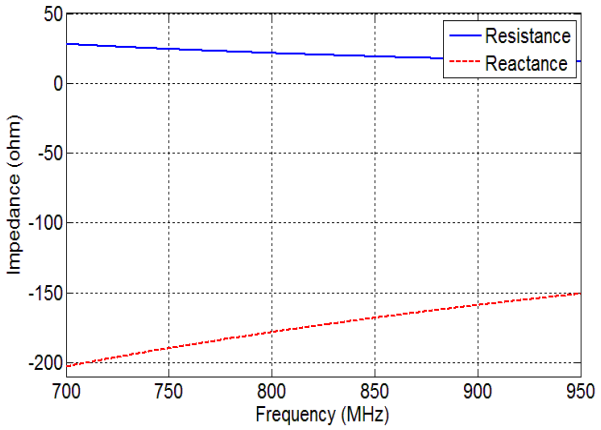

(a)

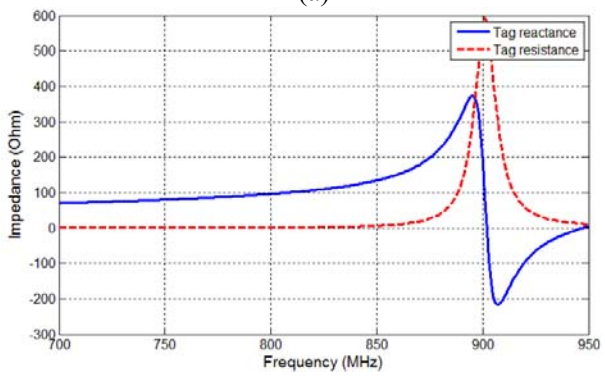

(b)

Fig. 10. Impedance versus frequency (a) chip impedance, (b) tag impedance.

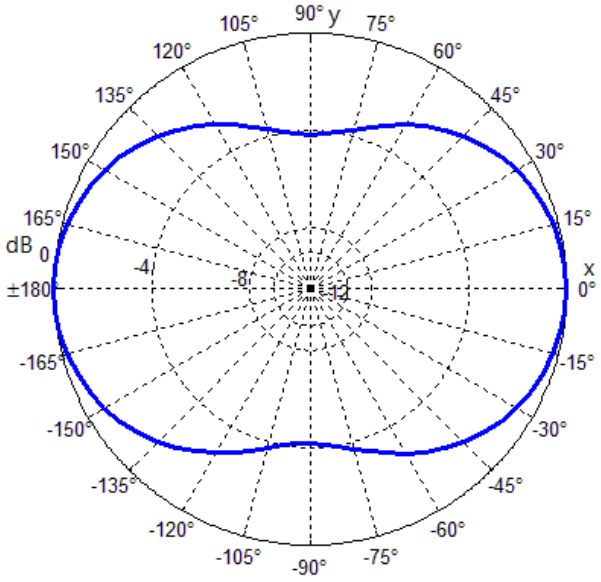

Fig. 11. Simulated E-plane (xy-plane) normalized gain (dB) of the radiation pattern of the tag antenna at 866MHz.

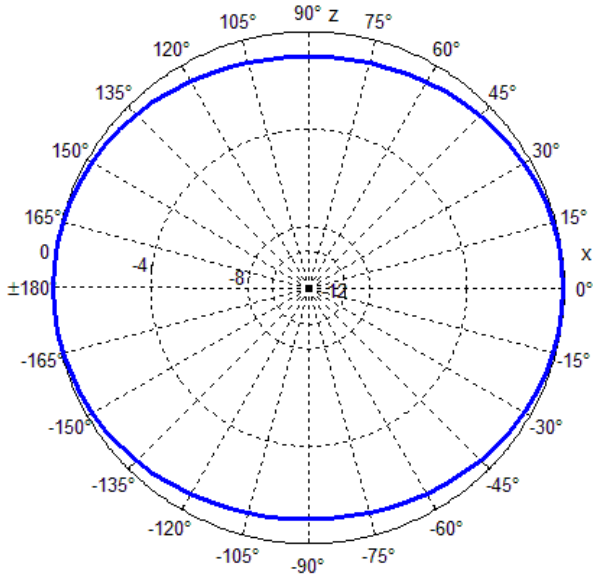

Fig. 12. Simulated H-plane (xz-plane) normalized gain (dB) of the radiation pattern of the tag antenna at 866MHz.

In Fig. 13, a 3-D view of the simulated radiation pattern of the tag antenna is shown, at 866MHz. As shown in the figure, the maximum simulated realized gain of the tag antenna at 866 MHz is approximately 1.4dBi, with asymmetric doughnut shape. The radiation pattern is not perfectly round, radiating slightly more along the x axis than that along the z axis.

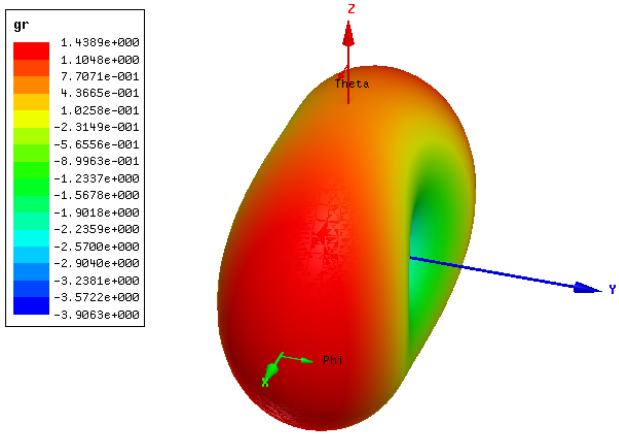

Fig. 13. 3-D view of the simulated realized gain (dBi) at 866MHz.

The fabricated model of the UHF RFID tag antenna model is shown in Fig. 14. This prototype was fabricated on Rogers 5880 substrate, with a

dielectric constant of 2.2. There is no copper on the opposite side of the substrate. This enables the tag antenna to achieve an almost omni-directional radiation pattern as shown in Fig. 13.

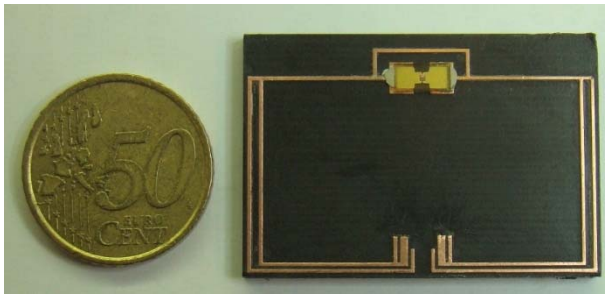

Fig. 14. Fabricated UHF RFID tag antenna.

A Tagformance RFID measurement device was used to measure the tag antenna in a specialized anechoic chamber suited for UHF RFID tag antennas [20]. The chamber contains a linearly polarized reader antenna, with a rotating disc to measure the radiation pattern of the tag. A linearly polarized reader antenna is connected to the Tagformance measurement device by Voyantic.

The theoretical read range of the tag antenna was calculated by using the measured results from the Tagformance, with the help of the following equation [23]:

$$d_{tag} = \frac{\lambda}{4\pi}\sqrt{\frac{1.64P_{ERP}}{L_{fwd}P_{th}}}. \qquad (2)$$

In the above equation, 'd_{tag}' is the theoretical read range of the tag antenna. 'L_{fwd}' is the measured path loss from the generator's output port to the input port of a hypothetic isotropic antenna placed at that tag's location. The forward path loss was achieved from the measured calibration data using the Tagformance measurement. The European effective radiated power 'P_{ERP}' value was considered equal to 2W (33dBm) according to [21]. The parameter 'P_{th}' is the measured threshold power in the forward direction from the transmitter to the tag. This is the minimum continuous wave power transmitted to enable the tag to send a response to EPC Gen 2 protocol's query command. The resulting theoretical read range of the tag antenna, calculated based on measured results, is shown in Fig. 15.

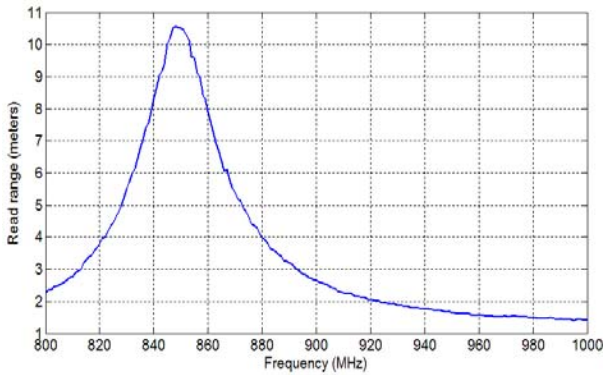

Fig. 15. Theoretical read range [d_{tag}] of the tag antenna.

In Fig. 15, the maximum read range is approximately 10.5m and is slightly shifted from 866MHz to 850MHz. This tag antenna is meant to be highly sensitive to structural changes. This nature of the tag antenna can be responsible for the shift of the frequency. The structural change can reasonably be caused by the inaccuracy of the fabrication process. Several other factors might also be responsible for the frequency shift including the process of attaching the IC strap to the tag antenna. This can be tuned by reducing the size of the two lines with length '*o*', by 1 - 2mm.

The maximum measured realized gain of the tag antenna can be analyzed by utilizing the path loss measurement data from the Tagformance measuring equipment. This can be described as [23],

$$G_r = \frac{P_{ic}}{L_{fwd} \cdot P_{th}}, \qquad (3)$$

where 'P_{ic}' is the sensitivity of the IC, which is equal to -18dBm, 'L_{fwd}' is the forward path loss from the transmitter to the tag antenna, and 'P_{th}' represents the threshold power. The estimated maximum simulated and measured gain of the tag antenna can be seen in Fig. 16. The difference between the simulated and measured realized gain can be due to several reasons. This includes the difficulty of simulating the actual substrate losses, and the inaccuracy of fabricating the tag. However, it is obvious that the maximum

measured gain is almost the same as the simulated gain at the desired operating frequency, 850MHz.

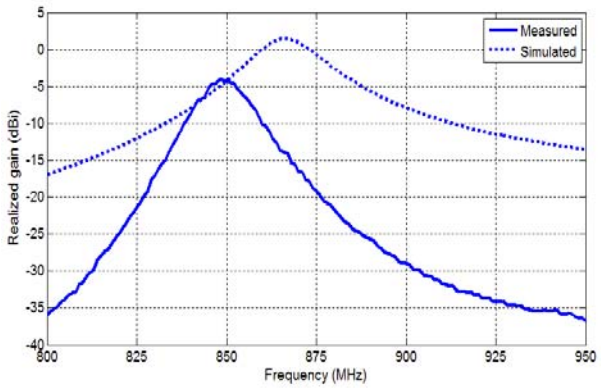

Fig. 16. Measured and simulated maximum realized gain of the tag antenna.

The measured normalized gain patterns at the E and H planes of the tag antenna are shown in Figs. 17 and 18, respectively. These measured radiation patterns resemble the simulated radiation patterns in Figs. 11 and 12, respectively, although at a slightly different frequency.

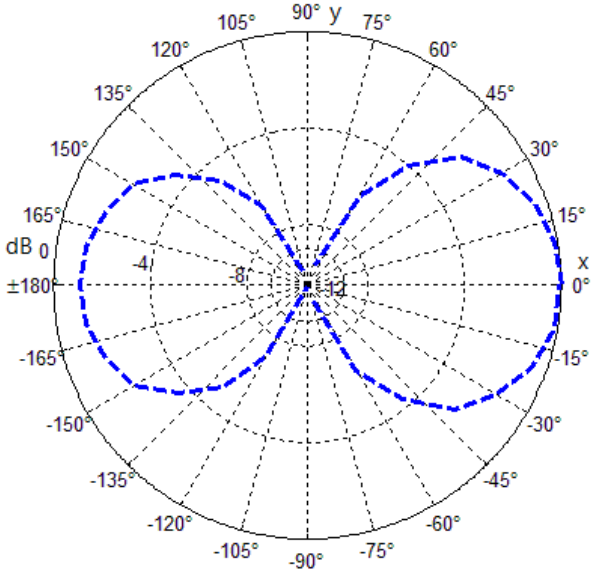

Fig. 17. Measured E-plane (xy-plane) normalized gain (dB) radiation pattern of the tag antenna at 850MHz.

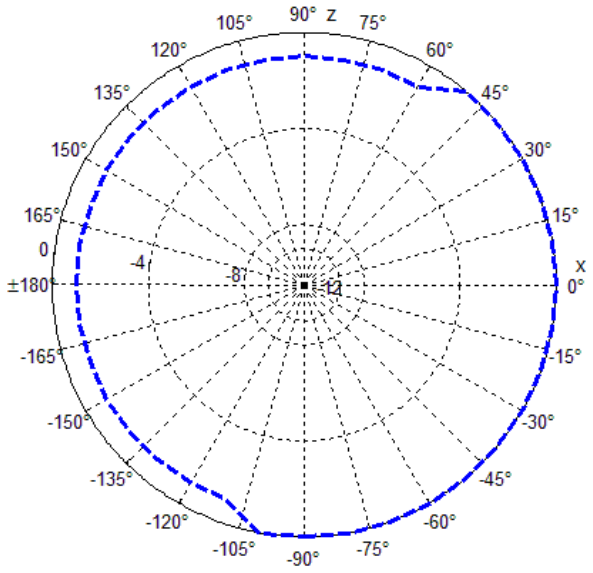

Fig. 18. Measured H-plane (xz-plane) normalized gain (dB) radiation pattern of the tag at 850MHz.

The measured normalized gain radiation pattern shown in Figs. 17 and 18, show an almost omni-directional radiation pattern as required for this application.

V. TAG SENSITIVITY ANALYSIS

Several parameters are useful for tuning the antenna to the desired frequency. Some of these are the substrate thickness, the shorting line '*g*', and the tuning lines '*l*' and '*o*'.

In Fig. 19, the resonance shift of the tag antenna, due to different substrate thicknesses is shown. According to the figure, reduction in the substrate thickness increases the resonance frequency of the tag antenna and vice versa. The rate of change of the resonance frequency is higher, with a decrease in the substrate thickness.

The length of the shorting line '*g*' can also be very useful in tuning the antenna. In Fig. 20, the effect of various lengths of the shorting line on the resonance frequency of the tag antenna is shown. According to the figure, a slight change in the length of the shorting line '*g*', directly influences the inductance and thus affects the resonance of the tag antenna.

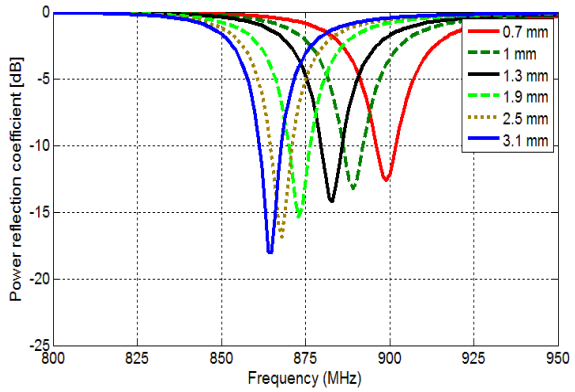

Fig. 19. Simulated power reflection coefficient of the tag antenna, due to various substrate thicknesses.

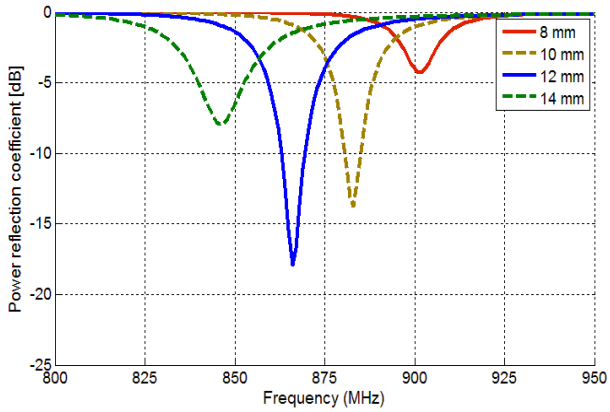

Fig. 20. Simulated power reflection coefficient of the tag antenna, due to various lengths of shorting lines '*g*'.

The tuning lines of length '*l*' and '*o*', can greatly help in fine tuning of the tag antenna. In Fig. 21, there is a gradual decrease in the resonance frequency, with an increase in the length of the tuning line '*l*'.

Similarly, the length '*o*' of the lines, can also be useful in tuning the tag antenna operating frequency. This effect is shown in Fig. 22, where the resonance frequency gradually changes with the increase in the length '*o*'. The lengths of the two lines equal to '*o*' are always kept same. The gap '*p*' between the two lines is also kept constant.

The above numerical results based on parametric study show that an antenna with small thin lines and small spacing between the lines helps miniaturize the antenna structure. However, such tag antennas exhibit narrowband characteristics and become sensitive to structural changes. These types of tag antennas can be useful for various sensing applications [22].

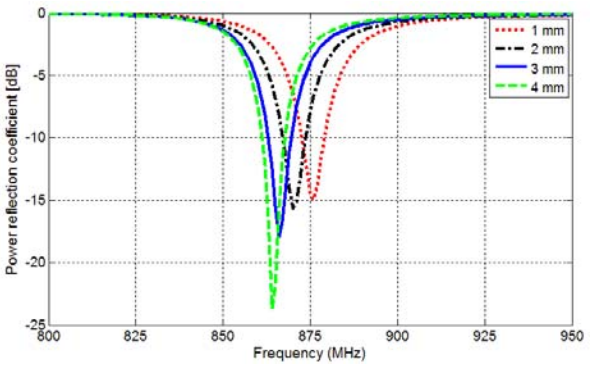

Fig. 21. Simulated power reflection coefficient shift of the tag antenna, due to various lengths of tuning line '*l*'.

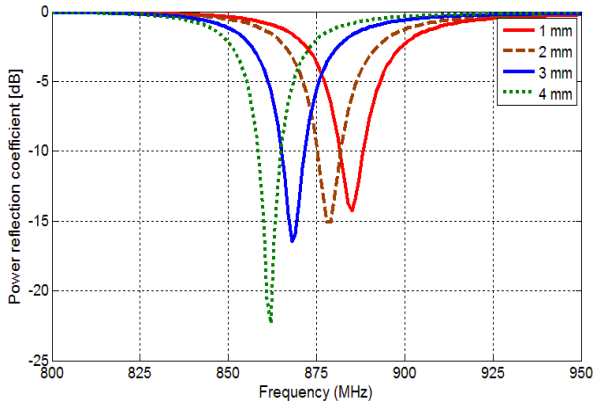

Fig. 22. Simulated power reflection coefficient of the tag antenna, due to various lengths of line '*o*'.

VI. CONCLUSION

In this paper, a small dual purpose planar RFID antenna design was discussed. The same antenna design is used as a shorted planar antenna, and as an RFID tag antenna. The planar shorted antenna works on both European and US RFID bands. Different miniaturization techniques helped in reducing the resonance frequency of the antennas. In the planar antenna model, the shorting technique and the close coupled lines helped in reducing the size of the antenna. The RFID tag antenna design's self inductance was increased with the help of the shorting line (loop) and the closely coupled lines, using current vector alignment technique. This indicates that the antenna structure can be reduced with the help of thin closely coupled lines. However, it makes the antenna more narrowband and sensitive. The

sensitivity of the antenna to the structural deformations can be utilized for various sensing tag antenna applications.

ACKNOWLEDGMENT

This research work has been funded by the Finnish Funding Agency for Technology and Innovation (TEKES), the Academy of Finland and the Centennial Foundation for Finnish Technology Industries, Finnish Cultural Foundation, Nokia Foundation and High Technology Foundation of Satakunta, Finland. The authors would also like to thank Toni Björninen for his assistance in conducting the measurements of the UHF RFID tag antenna.

REFERENCES

[1] A. A. Babar, L. Ukkonen, A. Z. Elsherbeni, and L. Sydanheimo, "Miniaturized Dual Band Planar Antenna," *26th Annual Review of Progress in Applied Computational Electromagnetics,* April, 2010.

[2] J. Landt, "The history of RFID," *IEEE Potentials*, vol. 24, no. 4, pp. 8-11, Oct. - Nov. 2005.

[3] K. Finkenzeller, *RFID Handbook, Radio-Frequency Identifications Fundamentals and Applications,* 2nd Ed. New York: Wiley, 2003.

[4] J.-P. Curty, N. Joehl, C. Dehollain, and M. J. Declercq, "Remotely powered addressable UHF RFID integrated system," *Solid-State Circuits, IEEE Journal*, vol. 40, no. 11, pp. 2193- 2202, Nov. 2005.

[5] W. C. Brown, "The history of power transmission by radio waves," *IEEE Trans. Microwave Theory Tech*., vol. MTT-32, no. 9, pp. 1230-1242, Sept., 1984.

[6] ANSYS, Ansoft HFSS, http://www.ansoft.com/products/hf/hfss/

[7] P. Bhartia, I. Bahl, R. Garg, and A. Ittipiboon, *Microstrip Antenna Design Handbook*, *Artech House,* Inc. 2001.

[8] A. K. Skrivervik, J. –F. Zurcher, O. Staub, and J. R. Mosig, "PCS Antenna Design: The Challenge of Miniaturization," *IEEE Antennas and Propagation Magazine,* vol. 43, no. 4 August 2001.

[9] T. Taga and K. Tsunekawa, "Performance analysis of a built-in planar inverted-F antenna for 800MHz hand portable hand units," IEEE J. Select. Areas Commun., vol. 5, pp. 921-929, June 1987.

[10] K. –L. Wong, *Planar Antennas for Wireless Communications*, Wiley series in Microwave and Optical Engineering, 2003.

[11] S. R. Best and J. D. Morrow, "On the Significance of Current Vector Alignment in Establishing the Resonant Frequency of Small Space-Filling Wire Antennas," IEEE Antennas and Wireless Propagation Letters, vol. 2, 2003.

[12] D. M. Dopkins, The RF in RFID: Passive UHF RFID in Practice, Newline, 2008.

[13] Rogers corporation, Rogers RT/duroid 5880 high frequency laminates datasheet, http://www.rogerscorp.com/documents/606/acm/RT-duroid-5870-5880-Data-Sheet.aspx

[14] Alien technologies, Higgs 3 datasheet.

[15] http://www.alientechnology.com/docs/products/DS_H3.pdf

[16] K. Kurokawa, "Power Waves and the Scattering Matrix," Microwave Theory and Techniques, IEEE Transactions on, vol. 13, no. 2, pp. 194-202, Mar. 1965.

[17] P. V. Nikitin, K. V. S. Rao, S. F. Lam, V. Pillai, R. Martinez, and H. Heinrich, "Power reflection coefficient analysis for complex impedances in RFID tag design," Microwave Theory and Techniques, IEEE Transactions, vol. 53, no. 9, pp. 2721- 2725, Sept. 2005.

[18] Agilent Technologies, http://www.agilent.com

[19] Satimo Starlab, http://www.satimo.com

[20] J. Virtanen, L. Ukkonen, T. Björninen, and L. Sydänheimo, "Printed humidity sensor for UHF RFID systems," IEEE Sensors Applications Symposium (SAS), pp. 269-272, 23-25 Feb. 2010, Limerick, Ireland.

[21] Voyantic, RFID measurements solutions, http://www.voyantic.com

[22] EPC frequency regulations UHF, http://www.epcglobalinc.org/tech/freq_reg/RFID_at_UHF_Regulations_20100824.pdf

[23] A. Rida, L. Yang, and M. Tentzeris, RFID-Enabled Sensor Design and Applications, Artech House, Inc. 2010.

[24] J. Virtanen, T. Björninen, L. Ukkonen, and L. Sydänheimo, "Passive UHF Inkjet Printed Narrow Line RFID Tags," IEEE Antennas and Wireless Propagation Letters, vol. 9, pp. 440-443, May 2010.

Abdul Ali Babar received his M.Sc. in Radio Frequency Electronics (Electrical Engineering), from Tampere University of Technology in 2009 and works as a Research Scientist in RFID research group, Tampere University of Technology. He is currently working on his Ph.D. degree in the Department of Electronics in Tampere University of Technology. His area of research includes RFID systems, RFID reader and Tag antennas, miniaturized antenna and other Radio Frequency systems and their integration in wireless systems.

Leena Ukkonen received the M.Sc. and Ph.D. degrees in Electrical Engineering from Tampere University of Technology (TUT) in 2003 and 2006, respectively. She is currently leading the RFID research group at TUT Department of Electronics, Rauma Research Unit. She, also, holds Adjunct Professorship in Aalto University School of Science and Technology. She has authored over 90 scientific publications in the fields of RFID antenna design and industrial RFID applications. Her research interests are focused on RFID antenna development for tags, readers, and RFID sensors.

Lauri Sydänheimo received the M.Sc. and Ph.D. degrees in Electrical Engineering from Tampere University of Technology (TUT). He is currently a Professor with the Department of Electronics, TUT, and works as the Research Director of Tampere University of Technology's Rauma Research Unit. He has authored over 120 publications in the field of RFID tag and reader antenna design and RFID system performance improvement.
His research interests are focused on wireless data communication and radio frequency identification (RFID), especially RFID antennas and sensors.

Dr. Atef Z. Elsherbeni is a Professor of Electrical Engineering and Associate Dean of Engineering for Research and Graduate Programs, the Director of The School of Engineering CAD Lab, and the Associate Director of The Center for Applied Electromagnetic Systems Research (CAESR) at The University of Mississippi. In 2004, he was appointed as an adjunct Professor, at The Department of Electrical Engineering and Computer Science of the L.C. Smith College of Engineering and Computer Science at Syracuse University. In 2009, he was selected as Finland Distinguished Professor by the Academy of Finland and Tekes.

Dr. Elsherbeni is the co-author of the book "*The Finite Difference Time Domain Method for Electromagnetics With MATLAB Simulations*", SciTech 2009, the book "*Antenna Design and Visualization Using Matlab*", SciTech, 2006, the book "*MATLAB Simulations for Radar Systems Design*", CRC Press, 2003, the book *"Electromagnetic ScatteringUsing the Iterative Multiregion Technique"*, Morgan & Claypool, 2007, the book *"Electromagnetics and Antenna Optimization using Taguchi's Method"*, Morgan & Claypool, 2007, and the main author of the chapters "*Handheld Antennas"* and "*The Finite Difference Time Domain Technique for Microstrip Antennas"* in Handbook of Antennas in Wireless Communications, CRC Press, 2001.

Dr. Elsherbeni is a Fellow member of the Institute of Electrical and Electronics Engineers (IEEE) and a Fellow member of The Applied Computational Electromagnetic Society (ACES). He is the Editor-in-Chief for ACES Journal and an Associate Editor to the Radio Science Journal.

Evaluation of EM Absorption in Human Head with Metamaterial Attachment

Mohammad Rashed I. Faruque [1, 2], Mohammad Tariqul Islam [1], and Norbahiah Misran [1, 2]

[1]Institute of Space Science (ANGKASA)

[2]Dept. of Electrical, Electronic and Systems Engineering
Faculty of Engineering and Built Environment
Universiti Kebangsaan Malaysia, 43600 UKM, Bangi, Selangor, Malaysia
rashedgen@yahoo.com, titareq@yahoo.com, bahiah@vlsi.eng.ukm.my

Abstract ─ The reduction of electromagnetic (EM) absorption with metamaterial is performed by the finite-difference time-domain method with lossy-Drude model by CST Microwave Studio in this paper. The metamaterials can be achieved by arranging split ring resonators (SRRS) periodically. The SAR value has been observed by varying the distances between head model to phone model, different distance, different thickness, and different size of metamaterial design. Metamaterial has achieved 53.94% reduction of the initial SAR value for SAR 10 gm.

Index Terms ─ Antenna, human head model, lossy-Drude model, metamaterial, symmetry, SAR, SRRS.

I. INTRODUCTION

Radio frequency (RF) safety guidelines have been issued to stop undue electromagnetic-field exposure. The guidelines are given in terms of the specific absorption rate (SAR). The revelation of the human head to the near field of a mobile phone has been evaluated by measuring the SAR in a human-head phantom, or by calculating it using a human-head numerical result.

The interaction of handset antennas with the human body is a great consideration in cellular communications. The user's body, especially the head and hand, influence the antenna voltage standing wave ratio (VSWR), gain, and radiation patterns. Furthermore, thermal effects, when tissues are exposed to unlimited electromagnetic energy, can be a serious health hazard. Therefore, standard organizations have set exposure limits in terms of SAR [1, 2]

Specifically, the problems to be solved in SAR reduction need to be a correct representation of the cellular phone; anatomical representation of the head; alignment of the phone and the head and suitable design of metamaterial [3-10].

In [7], for the SAR in human head, an effective approach is the use of a planar antenna integrated onto the back side (away from the head) of a phone model, but it brings additional design difficulties especially in achieving the required frequency bandwidth and radiation efficiency. Another approach is the use of a directional or reflectional antenna [10-15].

SAR is a measure of the rate at which radio frequency (RF) energy is absorbed by the body when exposed to radio-frequency electro-magnetic field. SAR is used to measure exposure to field between 100 KHz and 10 GHz [16-20]. It is commonly used to measure power absorbed from mobile phones and during MRI scans. The value will be defined heavily on the geometry of the part of the body that is exposed to the RF energy and on the exact location and geometry of the RF source. Metamaterials have inspired great interests due to their unique physical properties and novel application [10, 12].

Recently, there are many interests on metamaterial with split ring resonators (SRRS) structure were proposed to reduce the SAR value [4-12]. The SRRS was introduced by Pendry et al.

in 1999 [3] and subsequently used by Smith et al. for synthesis of the first left-handed artificial medium [7-9], [12-16]. A lot of effort worldwide has been spent studying single negative metamaterials, double negative metamaterials, their properties [12], applications in antennas [13], and other microwave devices. The negative permittivity can be obtained by arranging the metallic thin wires periodically [9]. On the other hand, an array of SRRS can exhibit negative effective permeability.

Some numerical results have implied that the peak 1 gm averaged SAR value (SAR 1 gm) may exceed the safety limits when a portable telephone is placed extremely close on reducing the SAR distribution in human head. At first, metamaterials are placed between an antenna and a human head. In order to study SAR reduction of antenna operated at the GSM 900 band, the effective medium parameter of metamaterials is set to negative at 900 MHz. Different positions, sizes, and negative medium parameters of metamaterials for SAR reduction effectiveness are also analyzed.

II. SIMULATION MODEL AND TECHNIQUES

The simulation model which includes the handset with the helix type of antenna and the SAM phantom head provided by CST Microwave Studio (CST MWS) is shown in Figure 1. Complete handset model composed of the circuit board, LCD display, keypad, battery, and housing was used for simulation. The relative permittivity and conductivity of individual components were set to comply with industrial standards. In addition, definitions in [18-22] were adopted for material parameters involved in the SAM phantom head. In order to accurately characterize the performance over a broad frequency range, dispersive models for all the dielectrics were adopted during the simulation [18]. The electrical properties of materials used for simulation are listed in Table 1. Helix type antenna constructed in a helical sense operating at 900MHz for GSM application was used in the simulation model. In order to obtain high-quality geometry approximation for such helical structure, a predictable meshing scheme used in FDTD method usually requires a large number of hexahedrons which in turn makes it extremely challenging to get converged results within a reasonable simulation time.

Fig. 1. Complete model used for simulation including handset and SAM phantom head.

Table 1: Electrical properties of materials used for simulation

Phone Materials	ε_r	$\sigma(S/m)$
Circuit Board	4.4	0.05
Housing Plastic	2.5	0.005
LCD Display	3.0	0.02
Rubber	2.5	0.005
SAM Phantom Head		
Shell	3.7	0.0016
Liquid @ 900MHz	40	1.42

CST MWS, which adopted the finite integral time-domain technique (FITD) proposed by Weiland in 1976 [19], was used as the main simulation instrument In permutation of the perfect boundary approximation (PBA) and thin sheet technique (TST), significant development in geometry approximation with computation speed is achieved with squashy highly accurate results. The non-uniform meshing scheme was adopted so that major computation endeavor was dedicated to regions along the inhomogeneous boundaries for fast and perfect analysis. The minimum and maximum mesh sizes were 0.3mm and 1.0 mm, respectively. A total of 2,097,152 mesh cells were generated for the complete model, and the simulation time was 1163 seconds (including mesh generation) for each run on an Intel Core ™ 2 Duo E8400 3.0 GHz CPU with 4 GB RAM system.

Figure 2 shows a portable telephone model at 900 MHz for the present study. It was considered

to be a quarter wavelength PIFA antenna mounted on a rectangular conducting box. The conducting box was 10 cm tall, 4 cm wide, and 3 cm thick. The PIFA antenna was located at the top surface of the conducting box. A space domain enclosing the human head and the phone model is also shown in Fig. 2. The time-stepping was performed for about eight sinusoidal cycles in order to reach a steady state. To absorb the outgoing scattered waves, the second order Mur absorbing boundaries acting on electric fields were used.

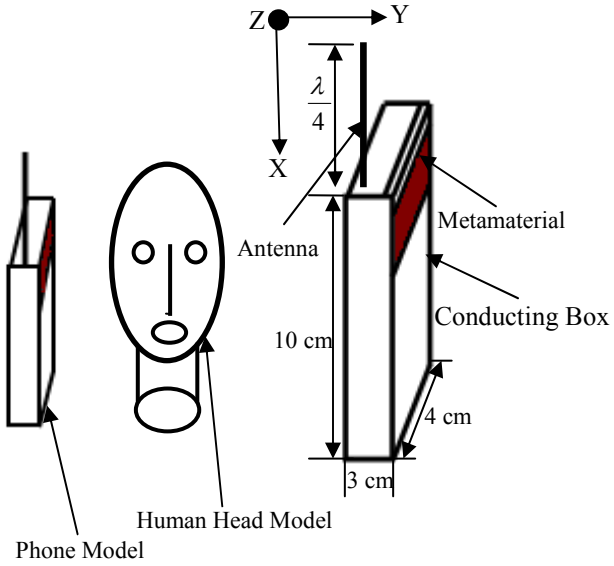

Fig. 2. The head and antenna model for SAR calculation.

The analysis workflow started from the design of the antenna with complete handset model in free space. The antenna was designed such that the S_{11} response was less than -10 dB over the frequency band of interest. SAM phantom head was then included for SAR calculation using the standard definition as

$$SAR = \frac{\sigma}{2\rho} E^2,$$

where E is the induced electric field (V/m); ρ is the density of the tissue (kg/m^3) and σ is the conductivity of the tissue (S/m). The resultant SAR values averaged over 1 gm and 10 gm of tissue in the head were denoted as SAR 1 gm and SAR10 gm, respectively. These values were used as a benchmark to appraise the effectiveness in peak SAR reduction.

III. REDUCTION OF SAR USING METAMATERIAL

The SAR in the head can be reduced by placing the metamaterial between the antenna and the human head. The metamaterial is on a scale less than the operating wavelength. The structures are resonant due to internal capacitance and inductance. The stop band can be designed at operation bands of cellular phone radiation. The metamaterial are designed on a printed circuit board so it may be easily integrated to the cellular phone. By arranging sub-wavelength resonators periodically, we get the metamaterial.

A. SRRS configuration

We establish that metamaterials can be used to reduce the peak SAR 1gm and SAR 10gm in the head from the FDTD analysis. In this section, the metamaterials operated at 900 and 1800 MHz bands of the cellular phone were considered.

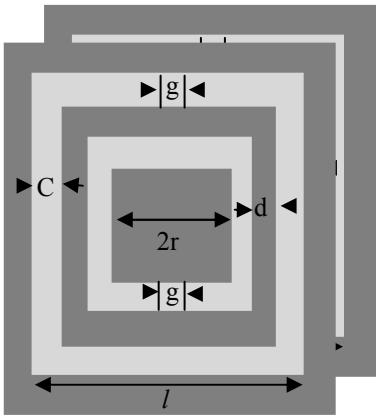

Fig. 3. The structure of SRRS.

The SRRS structure consists of two concentric annular of conductive material. There is a gap on each ring, and each ring is situated opposite to the gap on the other ring. The schematics of the SRRS structure that we used in this study are shown in Figure 3. The significant frequency of SRRS can be varied toward higher or lower frequency band by appropriately choosing these structure parameters.

B. SRRS design and simulation

The metamaterials with a negative permeability medium can be obtained by arranging SRRS periodically. The resonant frequency ω is very sensitive to small changes in the structure parameters of SRRS. The frequency response can be scaled to higher or lower frequency depending on properly choosing these geometry parameters by utilizing the following equation (1) in [9]:

$$\omega^2 = \frac{3 l c_0^2}{\pi \ln \frac{2c}{d} r^3}. \quad (1)$$

Numerical simulations could predict the transmission properties depending on various structure parameters of this system. Simulations of this complex structure are performed with the FDTD method. To construct the SRRS for SAR reduction, the SRRS that lie in the *x-z* plane are considered. The EM wave propagates along the y direction. The electric polarization is kept along the z-axis, and magnetic field polarization is kept along x axis. Periodic boundary conditions are used to reduce the computational domain and absorbing boundary condition is used at the propagation regions. The total-field/scatter-field formulation was used to excite the plane wave. The region inside of the computational domain and outside of the SRRS was assumed to be vacuums.

From this study, it is found that both of the two incident polarizations can produce a stop band. As shown in [23-27], the stop band corresponds to a region where either the permittivity or permeability is negative. When the magnetic field is polarized along the split ring axes, it will produce a magnetic field that may either oppose or enhance the incident field. A large capacitance in the region between the rings will be generated and the electric field will be powerfully concentrated. There is strong field coupling between the SRRS and the permeability of the medium will be negative at the stop band. Because the magnetic field is parallel to the plane of SRRS, we imagine the magnetic effects are small, and that permeability is small, positive, and slowly varying. In this condition, these structures can be viewed as arranging the metallic wires periodically.

The stop bands of SRRS are designed to be 900 MHz and 1800 MHz. The periodicity along x, y, z axes are L_x = 63mm, L_y = 1.5mm and L_z = 63mm, respectively. On the other hand, to obtain a stop band at 1800 MHz, the parameters of SRRS are chosen as c =1.8mm, d = 0.6mm, g =0.6mm, and r =12.9mm.The periodicity along x, y, z axes are L_x =50mm, L_y =1.5mm, and L_z = 50mm, respectively Both the thickness and dielectric constant of the circuit boards for 900 MHz and 1800 MHz are 0.508mm (Rogers 4003) and 3.38, respectively. After properly choosing geometry parameters, the SRRS medium can display a stop band around 900 MHz and 1800 MHz, respectively. From FDTD simulation, it is observed that the ring size is an important factor for operating frequency. The stop band can be shifted towards the lower frequency band by increasing the ring size.

We have tried to use a high impedance surface configuration [21] to reduce the peak SAR. However, we found that when these structures operate at 900 MHz, the sizes of these structures are too large for cellular phone application. A negative permittivity medium can also be constructed by arranging the metallic thin wires periodically [26-29]. However, we found that when the thin wires operate at 900 MHz, the size is also too large for practical application. Because the SRRS structures are significant due to internal capacitance and inductance, they are on a scale less than the wavelength of radiation. In this study, it is established that the SRRS can be designed at 900 MHz while the size is similar to that of a cellular phone.

IV. IMPACT OF SAR BY METAMATERIAL ATTACHMENT

The SAR reduction effectiveness and antenna performance with different positions, sizes, and materials properties of metamaterials will be analyzed. The head models used in this study was obtained from the MRI-based head model through the whole brain Atlas website. Six types of tissues, i.e., bone, brain, muscle, eye ball, fat, and skin were involved in this model [9-10].

Numerical simulation of SAR value was performed by the FDTD method. The parameters for FDTD computation were as follows. In our

lossy-Drude simulation model, the domain were 128 × 128 × 128 cells in FDTD method. The cell sizes were set as $\Delta x = \Delta y = \Delta z$ = 1.0 mm. The computational domain was terminated with 8 cells PML. A helix antenna was modeled for this paper by thin-wire approximation. Simulations of materials and metamaterials are performed by FDTD method with lossy-Drude model [12]. The method is utilized to understand the wave propagation characteristics of metamaterials.

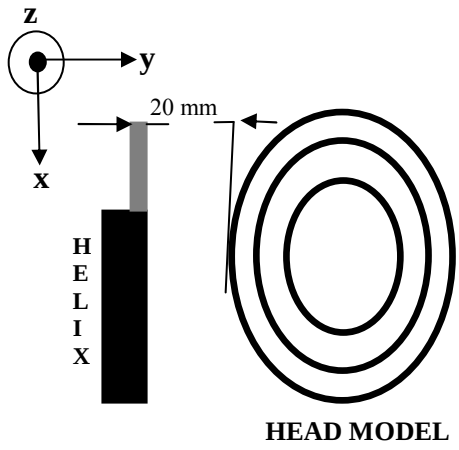

Fig. 4. The head and antenna models for SAR calculation.

Figure 4 shows the simulation model which includes the handset with a monopole type of helix antenna and the SAM phantom head that was provided by CST Microwave Studio® (CST MWS).

The dispersive models for all the dielectrics were adopted during the simulation in order to accurately characterize the metamaterials. The antenna was arranged in parallel to the head axis; the distance is varied from 5 mm to 20 mm; and finally, 20 mm was chosen for comparison with metamaterial. Besides that, the output power of the mobile phone models need to be set before SAR is simulated. In this paper, the output power of the cellular phone is 500 mW at the operating frequency of 0.9 GHz. In the real case, output power of the mobile phone will not exceed 250 mW for normal use, while the maximum output power can reach till 1W or 2W when the base station is far away from the mobile station (cellular phone). The SAR simulation is compared with the results in [11], for validation, as shown in Table 2. The calculated peak SAR 1 gm value is 2.002 W/Kg, and SAR10gm value is 1.293W/Kg when the phone model is placed 20mm away from the human head model without metamaterial. This SAR value we achieved is better compared with the result reported in [11], which is 2.43W/Kg for SAR 1 gm. The metamaterial is utilized in between the phone and head models, and it is found that the simulated value of SAR 1 gm is 1.16079 W/Kg, but in [11] they have reported 1.89 W/Kg. It is found that the use of metamaterials in this paper can reduce the peak SAR 1 gm by about 42.12% compared with the result of the SAR without attaching metamaterial where as the design reported in [11] has been achieved 22.63%. This is realized due to the consideration of different antenna, and different size of metamaterial and different positions, and it is because the electromagnetic source is being moved away from the head. Figures 5-9 show the SAR value in the distance between phone and head models without metamaterial, with metamaterial, distance between antenna and metamaterial 3-6 mm, thickness of metamaterial

Table 2: Comparisons of peak SAR without metamaterial

Tissue	SAR value (W/kg)
SAR value for [11]	2.43
SAR value in this work for 1 gm	2.002

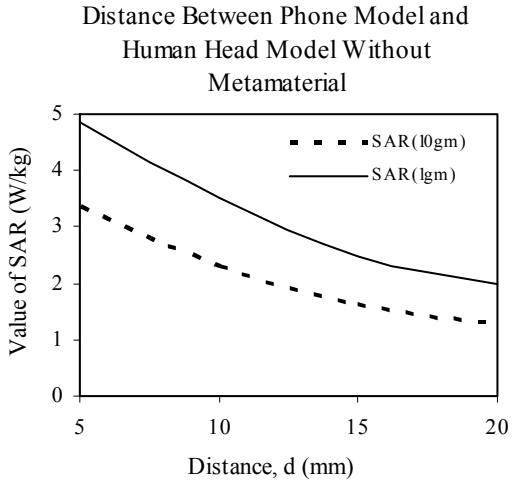

Fig. 5. SAR value compared the distance between phone model and human head model without metamaterial.

between 6-3 mm and size of metamaterial between 48 × 48 to 56 × 56 mm, respectively.

The reduction efficiency of the SAR depends on its thickness and ring size of metamaterials. In order to definitely confirm this, 1 gm and 10 gm average SARs versus distance, thickness, and sizes are plotted in the Figs. 5-9. In Figure 5, it is shown that if the distance between phone and human head models is varied then SAR value decreases. This is because dielectric constant, conductivity, density, and magnetic tangent losses are also varied. In Figure 6, it can be observed that the SAR value reduces with the attachment of metamaterial.

As shown in Figure 7, the distance between the antenna and metamaterials was changed from 3 mm to 6 mm. Figure 8 shows that the metamaterial thickness was reduced from 6 mm to 3 mm. It is found that both the peak SAR 1 gm and power absorbed by the head increase with the increase of distance or the decrease of thickness. The results imply that only suppressing the maximum current on the front side of the conducting box contributes significantly to the reduction of spatial peak SAR. This is because the

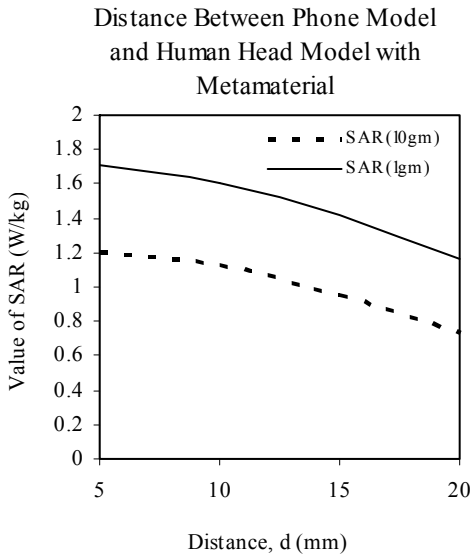

Fig. 6. SAR value compared the distance between phone model and human head model with metamaterial.

decreased quantity of the power absorbed in the head is considerably larger than that dissipated in the metamaterial and it is because the electromagnetic source is being moved away from the head. Figure 9 shows that, the size of the metamaterial was increased from 48 mm × 48 mm to 56 mm × 56 mm. It can be noted that the peak SAR 1 gm is reduced significantly.

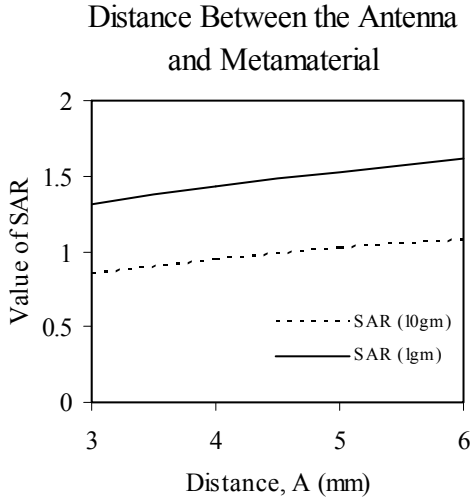

Fig. 7. SAR value compared the distance between the antenna and metamaterial.

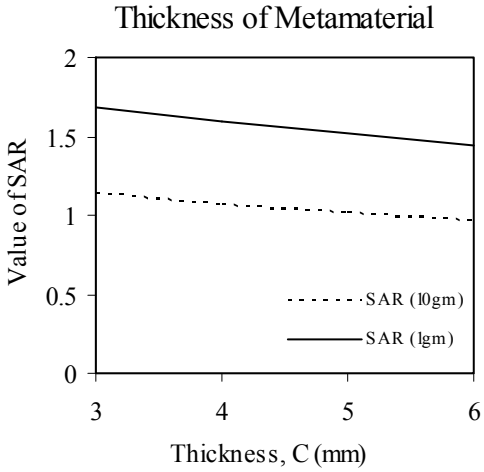

Fig. 8. SAR value compared the thickness of metamaterial.

The metamaterials can be obtained by arranging SRRS periodically [9-11]. The metamaterials were placed between the antenna and the human head. The distance between the antenna feeding point and the edge of metamaterials was 3 mm. The size of metamaterials in *x*-*z*-plane was 48 mm × 48 mm and the thickness was 6mm.

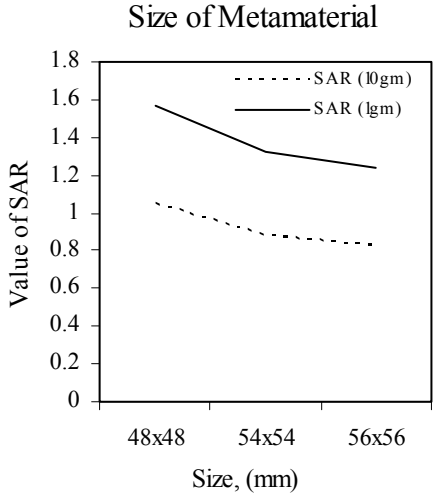

Fig. 9. SAR value compared the size of the metamaterial.

Different negative medium parameters for SAR reduction effectiveness were analyzed. We placed negative permittivity mediums between the antenna and the human head. First, the plasma frequencies of the mediums were set to be $\omega_{pe} = 9.309 \times 10^9$ rad/s, which give mediums with μ = 1 and ε = -3 at 900 MHz. The mediums with larger negative permittivity μ= 1, and ε = -5; μ= 1, and ε = -7 were also analyzed. We set $\Gamma_e = 1.2 \times 10^8$ rad/s, suggesting the mediums have losses. The peak SAR 1 gm becomes 1.0697 W/kg with μ = 1 and ε = -3 mediums. Compared to the condition without metamaterials, the radiated power is reduced by 13.9% while the SAR is reduced by 53.43%. With the use of and mediums, the SAR reduction effectiveness is decreased. However, the radiated power from the antenna is less affected.

Comparisons of the SAR reduction effectiveness with different positions and sizes of metamaterials were analyzed. Simulation results are shown in Table 3. In case 1, the distance between the antenna and metamaterial was changed from 3 mm to 6 mm. In case 2, the metamaterial thickness was reduced from 6 mm to 3 mm. It is found that both the peak SAR 1 gm and power absorbed by the head increases with the increase of distance or the decrease of thickness. In case 3, the size of the metamaterial was increased from 48 mm × 48 mm to 56 mm × 56 mm. It can be noted that the peak SAR 1 gm is reduced significantly while the terrible conditions on the radiated power due to metamaterial is insignificant. To further examine whether the metamaterial affected the antenna performance or not, the radiation pattern of the PIFA antenna with the μ = 1 and ε = -3 metamaterial was analyzed.

Table 3: Effects of sizes and positions of metamaterials on antenna performances and SAR values

	Z_R (Ω)	P_R (mW)	P_{abs} (mW)	SAR 1 gm (W/Kg)
Without material	63.39+j94.53	600	268.83	2.002
μ=1, ε =-3	51.43+j99.68	514.6	211.95	1.0697
Case 1	58.37+j95.35	539.4	253.53	1.6105
Case 2	62.19+j96.86	557.2	258.74	1.6893
Case 3	69.15+j107.38	573.33	216.83	1.2346

Table 4: Comparisons of SAR reduction techniques with different materials

	Z_R (Ω)	P_R (mW)	SAR 1 gm (W/Kg)
μ= 1, ε = -3	51.43+j99.68	514.6	1.0697
PEC reflector	66.83+j32.23	509.3	4.6803
Ferrite sheet	169.33+j153.69	519.3	1.043

The use of metamaterials was also compared with other SAR reduction techniques. A PEC reflector and a ferrite material are commonly used in SAR reduction. The PEC reflector and ferrite sheet were analyzed. The relative permittivity and permeability of the ferrite sheet were ε =7.0-j0.58

and μ=2.83-j3.25, respectively. Numerical results are shown in Table 4.

A PEC placed between the human head and the antenna is studied. It can be found that the peak SAR 1 gm is increased with the use of a PEC reflector. This is because the EM wave can be induced in the neighbor of a PEC reflector due to scattering. When the size of the PEC sheet is small compared to the human head, the head will absorb more EM energy. Similar results of peak SAR increase with PEC placement were also reported in [14]. The use of a ferrite sheet can reduce the peak SAR 1 gm effectively. However, the degradation on radiated power from the antenna is also significant. In addition, compared to the use of a ferrite sheet, the metamaterials can be designed on the circuit board so they may be easily integrated to the cellular phone.

To study the effect of SAR reduction with the use of metamaterials, the radiated power from the PIFA antenna with μ=1 and ε = -3 mediums was fixed at 600 mW. Numerical results are shown in Table 5. It is found that the calculated SAR value at 900 MHz, without the metamaterial, is 2.002 W/kg for SAR 1 gm and with the metamaterial, the reduction of the SAR 1 gm value is 1.16079 W/kg and SAR 10 gm value is 0.737 W/kg. The reduction is 42.12% for SAR 1 gm and 53.94% for SAR 10 gm.

Table 5: Effects of comparisons with metamaterials on SAR reduction (P_R = 0.5 w for 900 MHz)

	900MHz	
	Without material	μ=1, ϵ =-3
SAR 1 gm value for [11]	2.43	1.89
SAR 1 gm value in this work	2.002	1.16079

To study the effect of SAR reduction with the use of metamaterials, it can be observed that the metamaterials can reduce peak SAR effectively and the antenna performances can be less affected. The metamaterials resonate due to internal capacitance and inductance.

V. CONCLUSION

The EM interaction between the antenna and the human head with metamaterials has been discussed in this paper. Utilizing metamaterial SAR value is achieved about 1.16079 W/Kg for SAR 1gm and 0.737 W/kg for SAR 10 gm. Based on the 3-D FDTD method with the lossy-Drude model, it is found that the peak SAR 1 gm of the head can be reduced by placing the metamaterials between the antenna and the human head. Metamaterials were designed from periodical arrangement of SRRS. Numerical results can provide useful information in designing communication equipment for safety compliance.

ACKNOWLEDGEMENT

The authors would like to thank the Institute of Space Science (ANGKASA), Universiti Kebangsaan Malaysia (UKM) and the MOSTI Secretariat, Ministry of Science, Technology and Innovation of Malaysia, Science fund: 01-01-02-SF0612, for sponsoring this work.

REFERENCES

[1] IEEE C 95.1 – 2005, "IEEE Standards for safety levels with respect to Human Exposure to Radio Frequency Electromagnetic fields, 3KHz to 300GHz," *Institute of Electrical and Electronics Engineers*, Inc. New York, NY 2005.

[2] International Non-Ionizing Radiation Committee of the International Radiation Protection Association, "Guidelines on Limits on exposure to radio frequency electromagnetic fields in the frequency range from 100 KHz to 300 GHz," *Health Physics*, vol.54, no. 1, pp. 115-123, 1988.

[3] J. B. Pendry, A. J. Holen, D. J. Robbins, and W. J. Stewart, "Magnetism from conductors and enhanced nonlinear phenomena," *IEEE Trans. Microwave Theory Tech.*, vol. 47, no. 11, pp. 2075–2084, Nov. 1999.

[4] M. T. Islam, M. R. I. Faruque**,** and N. Misran, *"*Reduction of specific absorption rate (SAR) in the human head with ferrite material and metamaterial*," Progress In Electromagnetics Research, PIER C, vol.* 9, pp. 47-58, 2009.

[5] J. Wang and O. Fujiwara, "Reduction of electromagnetic absorption in the human head for portable telephones by a ferrite

sheet attachment," *IEICE Trans. Commun.*, vol. E80b, no. 12, pp. 1810-1815, Dec. 1997.

[6] M .R. I. Faruque, M. T. Islam, and N. Misran, "Electromagnetic (EM) absorption reduction in a muscle cube with metamaterial attachment," Med. Eng. & Phys., (Elsevier) (In Press), Doi:10.1016/j.medengphy.2010.12.004.

[7] B. Wu, W. Wang, J. Pacheco, X. Chen, T. Grzegorczyk, and J. A. Kong, "A study of using metamaterials as antenna substrate to enhance gain," *PIER*, vol. 51, pp. 295-328, 2005.

[8] M. M. Sigalalas, C. T. Chan, K .M. Ho, and Soukoulis, "Metallic photonic band gap materials*," Phys. Rev. B*.,vol. 52, no. 16, pp. 11744-11760, 2001.

[9] D. R. Smith and N. Kroll, "Negative refractive index in left handed materials," *Phys. Rev. Lett*., 85-14 2933-2936, 2000.

[10] K. H. Chan, K. M. Chow, L. C. Fung, and S. W. Leung, "Effects of using conductive materials for SAR reduction in mobile phones," *Microwave Opt. Technol, Lett.*, vol. 44, no. 2, pp. 140-144, Jan. 2005.

[11] J. N. Hawang and F.-C. Chen, "Reduction of the peak SAR in the Human Head with Metamaterials*," IEEE Trans. on Antenna and Propagation,* vol. 54 (12) pp. 3763-3770, Dec. 2006.

[12] R. W. Ziolkowski, "Design, fabrication, and testing of double negative metamaterials," *IEEE Trans. Antennas Propagation.*, vol. 51, no. 7, pp. 1516–1529, Jul. 2003.

[13] B. Bandlow, R. Schuhmann, G. Lubkowski, and T. Weiland, "Analysis of single-cell modeling of periodic metamaterial structures," *IEEE Trans. Magn*., vol. 44, no. 6, pp. 1662-1665, Jun. 2008.

[14] A. Erentok, P. L. Luljak, and R. W. Ziolkowski, "Characterization of a volumetric metamaterial realization of an artificial magnetic conductor for antenna applications," *IEEE Trans. Antennas Propag.*, vol. 53, pp. 160–172, Jan. 2005.

[15] A. Hirata, M. Fujimoto, T. Asano, J. Wang, O. Fujiwara, and T. Shiozawa, "Correlation between max temperature and SAR with average schemes," *IEEE Trans. Electromagn. Compat*., vol. 48, pp. 569-78, Aug. 2006.

[16] A. Lai, C. Caloz, and T. Itoh, "Transmission line based metamaterials for microwave applications," *IEEE Microw. Mag.*, vol. 5, pp. 34-50, Sep. 2004.

[17] L. C. Fung, S. W. Leung, and K. H. Chan, "Experimental study of SAR reduction on commercial products and shielding materials in mobile phone applications," *Microwave and Optical Technology Letters*, vol. 36, no. 6, pp. 419-422, March. 2003.

[18] M. T. Islam, M. R. I. Faruque, and N. Misran, "Design analysis of ferrite sheet attachment for SAR reduction in human head," *Progress In Electromagnetics Research (PIER),* vol. 98, pp. 191-205, 2009.

[19] J. B. Pendry, "Negative refraction makes a perfect lens," *Phy. Rev. Lett*., vol. 85, no. 18, pp. 3966-3969, 30 October 2000.

[20] A. Alù, F. Bilotti, N. Engheta, and L. Vegni, "Subwavelength, compact, resonant patch antennas loaded with metamaterials," *IEEE Trans. Antennas & Propag*., vol. 55, no. 1, pp. 13-25, Jan. 2007.

[21] D. M. Sullivan, "Electromagnetic simulation using the FDTD method", *IEEE Press Series on RF and Microwave Technology*. Roger D. Pollard and Richard Booton Series Editors, First Edition (July 6, 2000).

[22] D. Sounas and N. Kantartzis, "Systematic Surface Waves Analysis at the Interfaces of Composite DNG/SNG Media," *Optics Express*, vol. 17, no. 10, pp. 8513-8524, 2009.

[23] P. Bernardi, M. Cavagnaro, S. Pisa, and E. Piuzzi, "A graded-mesh FDTD code for the study of human exposure to cellular phones equipped with helical antennas," *ACES Journal*, vol. 16, no. 2, pp. 90-96, 2001.

[24] M. T. Islam, M. R. I. Faruque, and N. Misran, "Study of specific absorption rate (SAR) in the Human Head by metamaterial attachment," *IEICE*

Electronics Express, vol. 7, no. 4, pp. 240-246, 2010.

[25] R. W. Ziolkowski, "The design of Maxwellian absorbers for numerical boundary conditions and for practical applications using engineered artificial materials," *IEEE Trans Antennas and Propagation*, vol. 45 (4), pp. 656-671, April 1997.

[26] R. W. Ziolkowski and F. Auzanneau, "Artificial molecule realization of a magnetic wall," *J. Appl. Phys.*, vol. 82, no. 7, pp. 3192-3194, October 1997.

[27] F. Auzanneau and R. W. Ziolkowski, "Theoretical study of synthetic bianisotropic smart materials," *Journal of electromagnetic Waves and Applications,* vol. 12, no. 3, pp. 353-370, March 1998.

[28] D. Sounas, N. Kantartzis, and T. Tsiboukis, "Focusing efficiency analysis andoptimization performance of arbitrarily sized DNG metamaterial slabs withlosses," *IEEE Trans. Microw. Theory Tech.*, vol. 54, no. 12, pp. 4111-4121, Dec. 2006.

[29] J.-Y. Lee, J.-H. Lee, H. Kim, N. Kang, and H. Jung, "Effective medium approach of left-handed material using a dispersive FDTD method," *IEEE Trans. Magn*., vol. 41, no. 5, pp. 1484-1487, May 2005.

Mohammad Rashed Iqbal Faruque was born in Chittagong, Bangladesh in 1974. He received the B.Sc. and M. Sc. Degree in Physics from University of Chittagong, Chittagong, Bangladesh in 1998 and 1999, respectively. From July 2000 to until 2008, he worked as a lecturer at Chittagong University of Engineering and Technology (CUET), Chittagong, From June 2007 to November 2008; he was a part time Lecturer at University of Information Technology and Sciences (UITS), Chittagong. From February 2009, he is a doctorate student in Telecommunication Engineering Research Group (TERG), Electrical, Electronic and Systems Engineering Department, UKM. He has authored or coauthored approximately 12 referred journals and conference papers. His research interests include the RF, electromagnetic field and propagation, FDTD analysis, and electromagnetic compatibility.

Mohammad Tariqul Islam was born in Dhaka, Bangladesh in 1975. He received the B.Sc. and M. Sc. Degrees in Applied Physics and Electronics from University of Dhaka, Dhaka, Bangladesh in 1998 and 2000, respectively, and the Ph.D. degree in Telecommunication Engineering from the Universiti Kebangsaan Malaysia (UKM) in 2006. In August 2000, he became an Adjunct Research Fellow, at Bose Research Center, University of Dhaka, Dhaka. From September 2000 until June 2002, he worked as a lecturer at International Islamic University Chittagong (IIUC), Dhaka. Also in August 2006, he became an Assistant Professor at IIUC. He has served as a faculty at the Multimedia University (MMU), Malaysia from May 2007 until May 2008. He has joined UKM as a Senior Lecturer at the Universiti Kebangsaan Malaysia in June 2008. He is currently an Associate Professor at the Institute of Space Science (ANGKASA), UKM, Malaysia. He has been very promising as a researcher with the achievement of several International Gold Medal awards, Best Invention in Telecommunication award and Special Award from Vietnam for his research. He has filed 6 patents and 2 patent applications are in process for filing. He has authored and coauthored approximately 65 referred journals, 100 international and local conference papers, 3 books, and 2 book chapters. He has been awarded "Best Young Researcher Award" in 2010 at UKM, Malaysia. His research interests concerns the enabling technology for RF, antenna technology, smart antenna receiver, MIMO, and electromagnetic radiation. He is now handling many research projects from the Ministry of Science, Technology and Environmental of Malaysia.

Norbahiah Misran was born in Selangor, Malaysia in 1976. She received her B.Eng. degree in Electrical, Electronic & System Engineering from the Universiti Kebangsaan Malaysia in 1999 and the Ph.D. degree in Communication Engineering from the Queen's University of Belfast, UK in 2004. From 1999 to 2004, she was a Lecturer at the Universiti Kebangsaan Malaysia. She is currently an Associate Professor at the same universiti since 2009. Her current research interests include antennas, RF design, and ionospheric studies.

CAD Technique for Microwave Chemistry Reactors with Energy Efficiency Optimized for Different Reactants

Ethan K. Murphy[1] and Vadim V. Yakovlev[2]

[1] Applied Mathematics, Inc., Gales Ferry, CT 06335, USA
ethan.kane.murphy@gmail.com

[2] Department of Mathematical Sciences, Worcester Polytechnic Institute, Worcester, MA 01609, USA
vadim@wpi.edu

Abstract ― Upgrading successful processes of microwave-assisted organic synthesis to the level of industrial technology is currently slowed by difficulties in experimental development of large-scale and highly-productive reactors. This paper proposes to address this issue by developing microwave chemistry reactors as microwave systems, rather than as black-box-type units for chemical reactions. We suggest an approach based on the application of a neural network optimization technique to a microwave system in order to improve its coupling (and thus energy efficiency). The RBF network optimization with CORS sampling introduced in our earlier work and capable of exceptionally quick convergence to the optima due to a dramatically reduced number of underlying 3D FDTD analyses, is upgraded here to account for an additional practically important condition requiring optimal design of the reactor for different reactants. Viability of the approach is illustrated by three examples of finding the geometry of a conventional 99% energy efficient microwave reactor for 3/3/6 different materials; with 1/5/1 liter reactants, seven-parameter optimization yields the best configurations taking only 16/38/115 hours of CPU time of a regular PC.

Index Terms ― FDTD simulation, microwave reactor, neural network, optimization, scaling up.

I. INTRODUCTION

Microwave (MW)-assisted organic synthesis (MAOS) has recently become a frontline methodology in chemistry programs of pharmaceutical, agrochemical, and biotechnology industries due to its ability to significantly speed up chemical reactions [1-3]. With specialized systems for MW chemistry now available, particular attention is currently paid to the problem of development of controlled MAOS featuring new reaction routes for organic synthesis resulting in large-scale production of chemical substances [3]. In order for MAOS to become a widely accepted industrial technology, there is a need to develop techniques routinely producing new chemical entities on a scale of dozens/hundreds of kilograms. However, surveying the contemporary literature, one may notice that progress in this direction is fairly slow. While scaling up successful processes of MW chemistry is commonly acknowledged to be a key issue of the current state of the field, this problem is being addressed via essentially trial-and-error experiments aiming, with no way to measure the temperature inside the reactant, to catch correlation between the input parameters of the scaled up MW reactors and the output chemical characteristics of the products [4].

Comprehensive modeling of interactions of the reactants with the electromagnetic field in closed systems appears to be a powerful tool applicable to the MW chemistry reactors. Specifically, modeling can be used for determining reflections (i.e., for finding energy efficiency of the reactors) as well as spatial distributions of dissipated power in the reactant; application of an appropriate computational procedure to MW systems suitable for MAOS is exemplified, e.g., in [5]. There are also electromagnetic modeling techniques that compute

temperature fields in the processed materials by taking into account thermal dependence of material parameters [6]. Some multiphysics computational technologies couple electromagnetic and thermodynamic simulations of heated materials with temperature-dependent electromagnetic and thermal material parameters [7, 8]. Moreover, there are modeling-based procedures that optimize MW applicators for energy efficiency [9] and synthesize optimal processes, resulting in homogeneous temperature fields [10, 11]. Despite being known and used in other MW power applications, these advanced computational approaches seem to not be utilized in microwave chemistry. Examples of employing computer simulation in design of MAOS reactors as MW systems are rare [12, 13] and limited to insufficiently accurate analysis (rather than optimization or synthesis) of the reactor's operational regimes.

Computational schemes using neural network techniques and allowing for direct designing MW devices (by providing the system geometry for a given electromagnetic specification) have been described in [14-17]. In this paper, we present an original technique for direct computer-aided design (CAD) of MW reactors of a desirable scale and sufficiently high energy efficiency to process different reactants. The approach is based on the radial basis function (RBF) network optimization algorithm originally introduced in [14] and principally upgraded in [16], featuring

(i) an objective function (OF) measuring the bandwidth of the frequency characteristic of the reflection coefficient over a specified frequency range and

(ii) the constrained optimization response surface (CORS) technique [18] selecting additional sample points in the dynamic training of the network.

This algorithm, backed by 3D FDTD data, is characterized by very quick convergence to the optima and a dramatic reduction in the required number of underlying analyses. Due to these features, it has strong potential for viable optimization of complex MW systems and/or structures with a large number of design variables.

Here, the technique [16] is upgraded by incorporating an additional practically important condition requiring optimality of the reflection coefficient for different processed materials. Functionality of the resulting algorithm is illustrated by finding the optimal designs of a conventional reactor containing vessels with 1 and 5 liter reactants. It is shown that for finding the best configurations of the system (suitable for three and six different reactants) from seven-parameter optimizations, only a few dozen/hundred simulations are required.

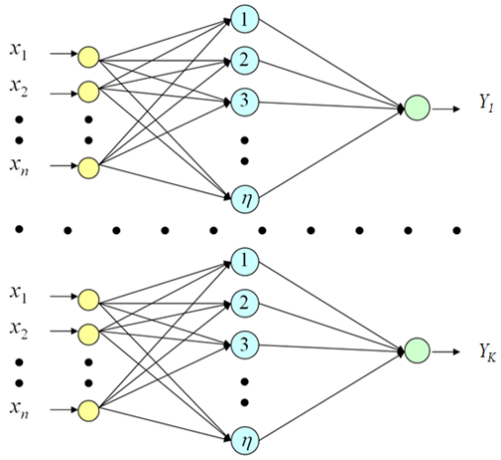

Fig. 1. Architecture of a decomposed RBF ANN with η hidden neuron [14, 16].

II. OPTIMIZATION TECHNIQUE: RBF NETWORK AND OBJECTIVE FUNCTIONS

In accordance with [16], the decomposed RBF artificial neural network (ANN) shown in Fig. 1 and denoted as F: $X \rightarrow Y$ works with input vectors $X_i = [x_1\ x_2\ \ldots\ x_N]$, where $x_1, \ldots, x_N$ are design variables for $i = 1, \ldots, P$, and P is the number of input-output pairs of modeling data. In the upgraded version of the algorithm proposed in this paper, the network output is obtained by taking frequency characteristics of an S-parameter over specified frequency range(s) (f_1, f_2) given by the formula

$$Y_i = \max_{1 \le k \le L} \left[\left[BW_r(S_k, T) + 1 \right]^{-1} \right], \qquad (1)$$

where

$$S_k = S(f_1 \le f \le f_2, X_i, \varepsilon_k', \sigma_k),$$

and T is the tolerance defined for the jth frequency interval. The function BW_r (associated with the system's bandwidth BW) is calculated over the

specified frequency interval and outputs relative bandwidth in the range [0, 1], and L is the number

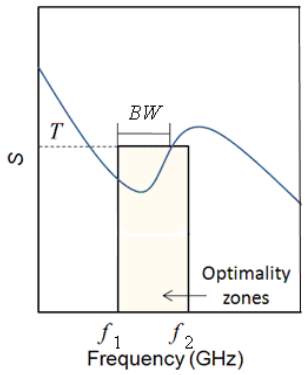

Fig. 2. Parameters of objective function (1) with S representing S_{11}.

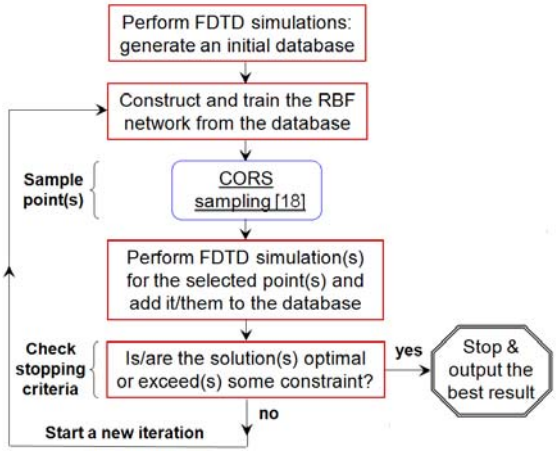

Fig. 3. RBF network optimization algorithm with CORS sampling.

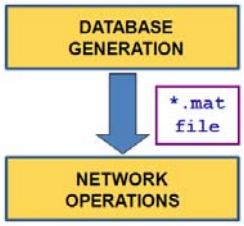

Fig. 4. Modules of the algorithm's MATLAB implementation.

of materials for which the system is to be optimized; we maximize over k to use the worst of the L samples with the dielectric constant ε' and electric conductivity σ. This OF represents a typical pract-ical need of MW optimization to search not just the minimum of S, but rather the maximum BW_r in a certain frequency range (as illustrated in Fig. 2). Motivations for the choice of the shape of the optimality zone (i.e., the values of f_1, f_2, and T) for problems of MW power engineering are discussed in [9]. The RBF used in the network is a thin plate spline defined as

$$\varphi_l^{(i)} = \begin{cases} \| X_i - c_l \|_2^2 \log(\| X_i - c_l \|_2), & \| X_i - c_l \|_2 > 0, \\ 0, & \| X_i - c_l \|_2 = 0, \end{cases} \quad (2)$$

where $l = 1, \ldots, N_c$, N_c is the number of RBFs, c_l are the centers of $\varphi_l^{(i)}$. The training set is the set of centers chosen. The network is coupled with a linear model, and the weights are constructed by solving the corresponding linear system.

A brief general description of the algorithm is given by the flow chart in Fig. 3. Given some initial data, we construct and train the RBF network $F(X)$, perform CORS sampling, simulate the sampled point, check stopping criteria, and repeat the cycle, if necessary. The critical part of the algorithm is the choice of additional points: CORS sampling balances the goal of finding the minimum with exploring unknown regions of the domain [18]. This is accomplished by selecting a parameter β ($0 \le \beta \le 1$) and finding the minimum of $F(X)$, subject to $\|X - X_i\| \ge \beta\Delta$ for $1 \le i \le P$, where $\Delta = \max_X(\min_{1 \le i \le P}\|X - X_i\|)$. The Δ is approximated by picking the maximum from a random sampling of points in the domain. This seems to be sufficient because the aim of Δ is to measure the spacing of points in the current database. In other words, the algorithm searches for minima forced away from previously sampled points based on the percentage (or fraction) given by β.

The stopping criteria chosen to be a set maximum number of database points are applied if the solution has 100% BW_r or some lower predefined value.

III. COMPUTER IMPLEMENTATION

The option of RBF network optimization for a number of different materials that is formulated in the OF (1) has been realized in this work as an upgraded MATLAB code implementing the algorithm [16].

Data for the network are generated by an FDTD model of a MW device; with an appropria-

tely applied pulse excitation, the model produces frequency responses of *S*-parameters. In our implementation, the data is produced with the use of the 3D conformal FDTD simulator *QuickWave-3D*

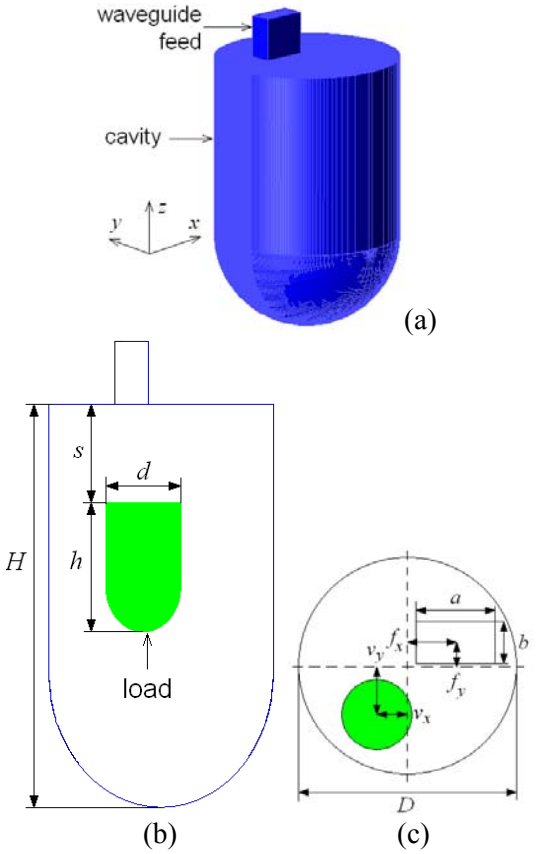

Fig. 5. General 3D view (a) and geometrical parameters of the considered reactor (b), (c).

(*QW-3D*) [19]; all CPU times are given below for a 64-bit Windows XP Intel Xeon 3.2-GHz PC.

The code consists of two modules as shown in Fig. 4. Database Generation calls *QW-3D* and constructs an initial database (DB) for the specified optimization problem and stopping criteria. This module produces a problem-specific mat-file which is then used as input data for network operations. The latter module runs optimization iterations for the chosen/specified OF, sampling technique, and RBF.

IV. NUMERICAL RESULTS: A MAOS REACTOR OPTIMIZED FOR DIFFERENT REACTANTS

Here, we consider a MW system resembling the shape of a typical MAOS reactor (Fig. 5). The cavity is constructed by combining a hemisphere and cylinder. Inside the cavity, there is a thin-wall hemisphere-bottom cylindrical vessel with a liquid reactant whose volume V is assumed to be specified. The reactor is excited by a rectangular waveguide which may be offset in the x- and y-directions by f_x and f_y, respectively. The vessel also may be offset from the z-axis by v_x and v_y, and is located a distance s from the top of the cavity. The CAD goal is: given the height of the system H and a set of L reactants to be processed in the reactor, find the configuration of the whole system, i.e., diameter D, internal dimensions of the vessel (d and h), its position in the cavity (s, v_x and v_y), and a position of the waveguide (f_x and f_y), that yields less than T % of reflected microwave energy (i.e., the reflection coefficient $|S_{11}| < 0.1\sqrt{T}$) in BW_r^k % (k = 1, …, L) of the frequency range (f_1, f_2) for reactants A, …, L, respectively.

Table 1: Material parameters of the reactants at 2.45 GHz (adapted from [1]).

Reactant	Dielectric constant, ε'	Electric conductivity, σ(S/m)
(A) Ethyl acetate	6.2	0.1468
(B) Methylene chloride	9.1	0.0582
(C) Acetone	20.6	0.1178
(D) Ethanol	24.6	0.1808
(E) Methanol	32.7	4.1882
(F) Acetonitrile	36.0	3.2291

A. One liter load and three reactants

In the first illustration, we solve this problem for a load of V = 1 liter and with the height of the reactor H = 300 mm. We consider L = 3 (the materials (A), (B), and (D) specified in Table 1), T = 1 % (i.e., energy efficiency 99 %), BW_r^A = … = BW_r^D = 100 %, f_1 = 2.4 GHz, and f_2 = 2.5 GHz. While the waveguide dimensions are considered constant (a = 72 mm, b = 36 mm), seven design variables are allowed in the intervals:

$$-35 \le f_x, f_y \le 35 \text{ mm}, \; -24 \le v_x, v_y \le 24 \text{ mm},$$
$$80 \le d \le 110 \text{ mm}, \; 75 \le s \le 110 \text{ mm},$$
$$200 \le D \le 300 \text{ mm}. \qquad (3)$$

The procedure starts with a generation of an initial DB of 50 random points in the specified domain for each of the three reactants. Aiming to keep CPU time in this illustrative optimization reasonable, the chosen underlying FDTD model is

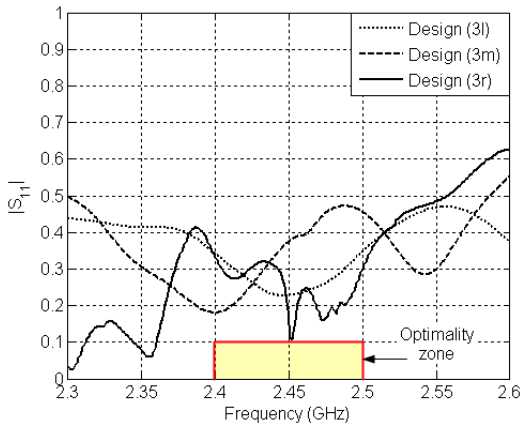

Fig. 6. Typical non-optimized characteristics of the system in Fig. 5 with Reactant (D): design variables chosen at the left-end (Design (3l)), mid- (3m), and right-end points (3r) of the intervals (3).

Table 2: Reactor configurations optimized for reactants (A), (B), and (D)

V (liters)	1	5
f_x, mm	-23.4	75.8
f_y, mm	11.0	83.2
v_x, mm	-5.3	50.0
v_y, mm	20.0	-36.0
d, mm	108.0	164.0
s, mm	94.8	145.4
D, mm	209.0	395.2
DB size/No of FDTD analysis	99/297	65/195

relatively rough: built with a non-uniform conformal mesh, it consists of 308,000 to 555,000 cells with size ranging from a maximum of 2.7 mm in the reactant to 7 mm in air. The cell size of the load is selected for materials with high dielectric constants ((D)-(F) in Table 1) and is kept the same for the materials with low ε'. The analysis of the system involves 10,000 time-steps (1.7 to 3.0 min of CPU time).

Characteristics of the reflection coefficient in the non-optimized reactor computed for all the reactants yield energy efficiency of about 75-85 % (see, e.g., Fig. 6). Our optimization procedure achieves what seems to be the "best" solution producing 99 % efficiency ($BW_r^A = 79$ %, $BW_r^B = 83$ %, and $BW_r^D = 100$ %) with 99 × 3 = 297 FDTD analyses (Fig. 7). Corresponding design

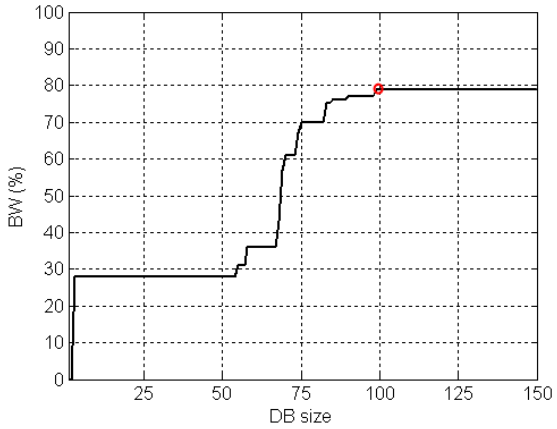

Fig. 7. Optimization convergence for the reactor designed for T = 1% and three one-liter reactants (A), (B), and (D); 99th iteration is marked by (○).

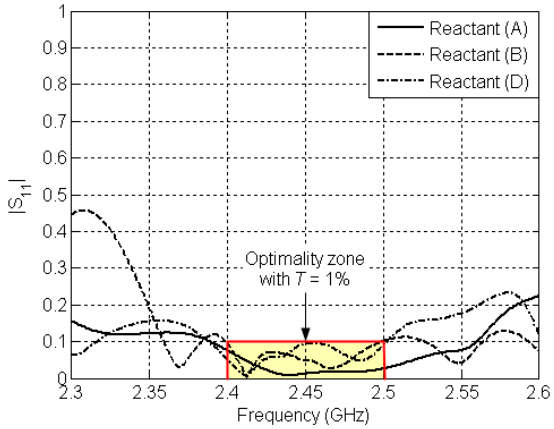

Fig. 8. Reflection coefficient in the reactor optimized for three one-liter reactants (A), (B), and (D).

variables are given in Table 2 and frequency characteristics of $|S_{11}|$ resulting from this geometry are shown in Fig. 8: it is seen that, for the reactants (A), (B), and (D), this optimized configuration provides the desirable efficiency in 79 % of the 2.4 to 2.5 GHz frequency range.

B. Five liter load and three reactants

The next example illustrates a capability of the proposed optimization technique in situations when scaling up of a successful MAOS process is

of key interest. Here, we solve the optimization problem for a reactor of the same design and constructed for the same reactants (L = 3), but of a 5-liter volume. With H = 513 mm, T = 1 %, BW_r^A = … = BW_r^D = 90 %, f_1 = 2.4 GHz, and f_2 = 2.5

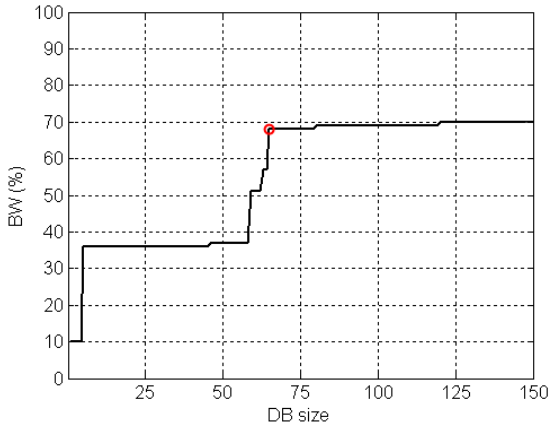

Fig. 9. Optimization convergence for the reactor designed for T = 1% and three five-liter reactants (A), (B), and (D); 65th iteration is marked by (○).

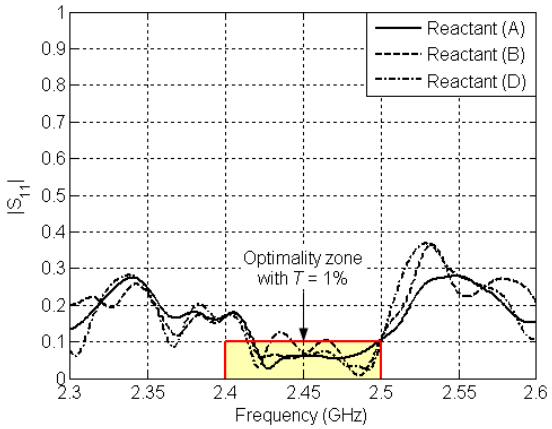

Fig. 10. Reflection coefficient in the reactor optimized for three five-liter reactants (A), (B), and (D).

GHz, the seven design variables are allowed in the intervals:

$$-85 \le f_x, f_y \le 85 \text{ mm}, \; -50 \le v_x, v_y \le 50 \text{ mm},$$
$$159 \le d \le 172 \text{ mm}, \; 80 \le s \le 300 \text{ mm},$$
$$340 \le D \le 510 \text{ mm} \qquad (4)$$

Similarly, the procedure starts with an initial DB of 50 random points in the domain (4). The model consists of 1,380,000 to 2,394,000 cells of maximum size 3 mm in the reactant to 7 mm in air – due to the larger volume of the reactant, the domain discretized with 3 mm cells is also larger. Likewise, the analysis requires 10,000 time-steps (8.6 to 14.4 min of CPU time).

In the case of a 5-liter reactant, as seen from Fig. 9, the best solution (BW_r^A = 80 %, BW_r^B = 77 %, and BW_r^C = 70 %) is achieved with 119 DB points, but for the preceding very close result (with the worst BW_r^C = 68 %) the procedure needs only 65 points (195 analyses). Corresponding design variables are also given in Table 2 and $|S_{11}|$ characteristics resulting from this geometry are shown in Fig. 10: this optimized configuration provides 99 % energy efficiency for all three reactants in the 70 % of the 2.4 to 2.5 GHz frequency range.

It is seen that the optimized geometry of the 5 liter reactor is fairly different from a proportionally increased one of the 1 liter system, and the "qualities" of both best solutions are not alike. This appears to be consistent with theoretically expected (and observed in many experiments [13]) strongly non-linear alterations in a reactor's performance with variations of its geometrical parameters and material characteristics of the reactants.

C. One liter load and six reactants

In the last illustration, the proposed CAD technique is tested with double the number of reactants (L = 6), i.e., all the materials specified in Table 1 and differing in a dielectric constant by about 6 times and in the conductivity by about 70 times. We assume V = 1 liter, H = 300 mm, f_1 = 2.4 GHz, f_2 = 2.5 GHz, and set the goal values BW_r^A = … = BW_r^F = 100 %. The same seven design variables are allowed in the intervals given by (3). The underlying FDTD model and its CPU times are the same as in the first example above (sub-section IV.A).

First, we solve the problem for T = 2.5 %. The procedure starts with a generation of an initial DB of 50 points for each of the six reactants. The "best" optimal solution producing 97.5 % efficiency (BW_r^A = … = BW_r^D = 100 %, BW_r^E = 93 %, and BW_r^F = 95 %) is achieved very quickly with only 14 additional DB points; this requires a total of 384 FDTD analyses. The convergence to

this solution is illustrated in Fig. 11 for each reactant. Corresponding design variables are given in the last column of Table 3 along with the values produced from the previous 4 optimization iterations. Frequency characteristics of $|S_{11}|$ resulting from the 64th optimal solution are shown

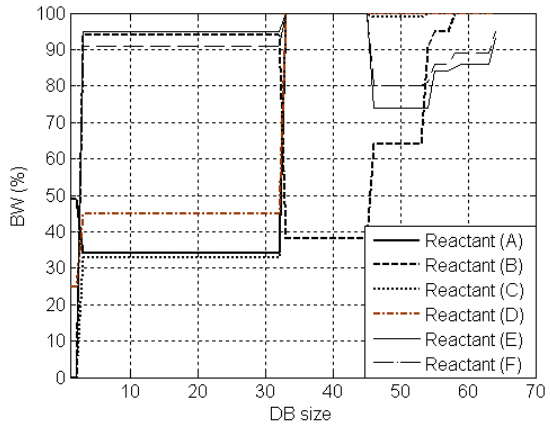

Fig. 11. Optimization convergence for the reactor designed for T = 2.5% and six one-liter reactants (A)-(F).

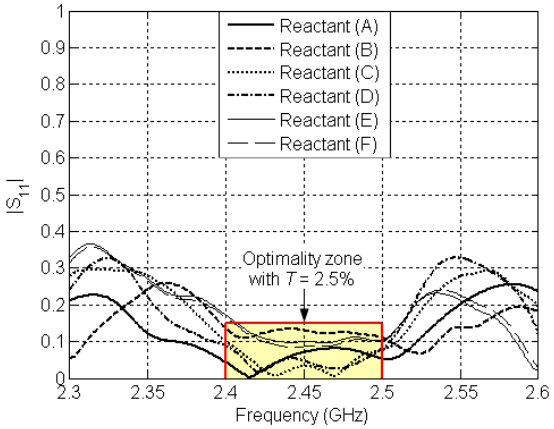

Fig.12. Reflection coefficient in the reactor optimized for six one-liter reactants (A)-(F).

Table 3: Optimal solutions of the final stage of optimization for 97.5% energy efficiency with six reactants (A)-(F).

Iter.	60	61	62	63	64
f_x, mm	-1.3	-2.6	-3.1	-2.9	-2.6
f_y, mm	-24.5	-22.1	-22.8	-22.3	-22.5
v_x, mm	-19.8	-19.6	-18.0	-18.4	-17.9
v_y, mm	-9.1	-9.0	-8.6	-8.5	-10.0
d, mm	101.6	101.4	101.2	100.9	101.2
s, mm	81.2	81.6	83.2	82.2	82.3
D, mm	242.3	242.6	242.3	242.6	243.4

in Fig. 12: for all the reactants (A)-(F), this optimized configuration provides desirable efficiency in 93 % of the 2.4 to 2.5 GHz frequency range.

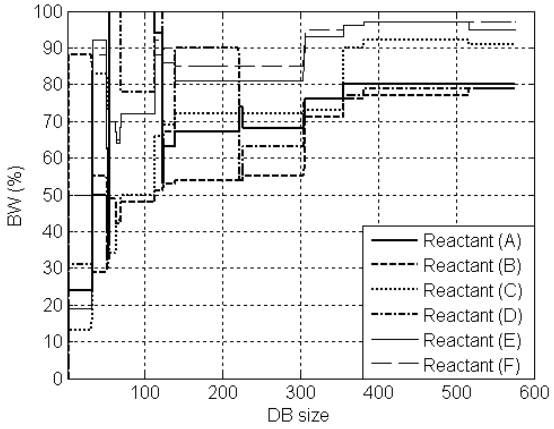

Fig. 13. Optimization convergence for the reactor designed for T = 1 % and six one-liter reactants (A)-(F).

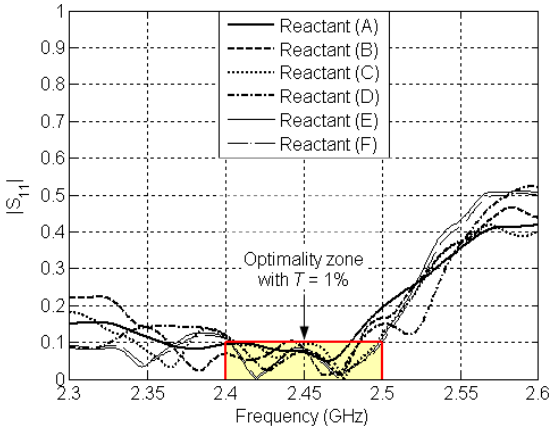

Fig. 14. Reflection coefficient in the reactor optimized for three 1-liter reactants (A)-(F).

Table 4: Optimal solutions of the final stage of optimization for 99 % energy efficiency with six reactants (A)-(F) .

Iter.	572	573	574	575	576
f_x, mm	10.6	10.5	9.6	9.6	9.4
f_y, mm	-22.1	-22.1	-22.2	-22.2	-22.1
v_x, mm	-21.7	-22.1	-21.9	-21.8	-21.8
v_y, mm	4.5	4.4	4.2	4.2	4.1
d, mm	92.8	93.0	92.5	92.4	92.5
s, mm	95.2	95.0	94.9	94.9	95.1
D, mm	250.6	250.2	249.6	249.6	249.6

With only a 64-point DB required to find the geometry of a 97.5% efficient reactor, in another test we attempt the more challenging task of finding the optimal solution for T = 1 %. By applying this more tough constraint (and simultaneously keeping the bandwidth goal values set to 100%), we are interested in seeing the capability of the optimization technique in searching for an optimal solution with bigger BW_r. Here, an initial DB, also, contains 50 points for each of the six reactants. The "best" optimal solution producing 99 % efficiency is BW_r^A = 80%, BW_r^B = 79 %, BW_r^C = 91 %, BW_r^D = 79 %, BW_r^E = 95 %, and BW_r^F = 97 %, and it is achieved with 527 DB points requiring 3,456 FDTD simulations. Graphs in Fig. 13 show the natural effect of quicker convergence for the reactants with higher loss factors ((E) and (F)) than with a lower one (B). Corresponding design variables are given in the last column of Table 4 which also shows how the "best" optimal solution was finally approached in the course of optimization. Frequency characteristics of $|S_{11}|$ resulting from the 576th solution are shown in Fig. 14: for all the reactants (A)-(F), this configuration provides 99 % efficiency in the 79 % of the 2.4 to 2.5 GHz frequency range.

V. CONCLUSION

In this paper, we have introduced an original modeling-based approach for CAD and scaling up of MAOS reactors. A computer code implementting the proposed technique allows for finding the geometry of a large-scale reactor that guarantees the highest possible energy efficiency for different reactants. The procedure of RBF ANN optimization backed by full-wave (3D conformal FDTD) simulations has been applied to a conventional MW reactor to find the best design for processing of 1- and 5-liter reactants. It has been demonstrated that, with the developed technique, seven-parameter optimization of this system that aims to guarantee 99 % efficiency takes only 297 and 195 FDTD analyses (i.e., about 16 and 37.5 h of CPU time of a regular PC), respectively. The optimization technique remains operational and viable when it is used for a larger number of materials – e.g., it requires 3,456 simulations when working with the same seven design variables for six different reactants.

The advanced functionality of the presented optimization technique is eloquently illustrated by the output of our earlier paper [20] showing, with the use of the technique [16], that a MW applicator optimized for only one load may behave unsatisfactorily for the other ones. On the other hand, our RBF optimization procedures are straightforwardly applicable to those systems with loads whose material parameters strongly depend on temperature. This has been already shown, in a simplified manner, in [21] where the technique [16] was applied to loads with different values of uniformly distributed complex permittivity. In a more accurate way, the temperature dependence can be handled by the optimization technique described in this paper if it is backed by *QW-3D* which pro-vides a regime of operating the FDTD solver with a cell-by-cell modification of media parameters as a function of dissipated power.

The results, presented in this paper, stay in strong favor of CAD of high-productive large-scale MAOS reactors and suggest that application of the developed modeling-based optimization procedure in efficient designing of systems of MW chemistry may be useful and practical.

REFERENCES

[1] P. Lidstrom, J. Tierney, B. Wathey, and J. Westman, "Microwave assisted organic synthesis – a review," *Tetrahedron*, vol. 57, pp. 9225-9283, 2001.

[2] D. Bodgal, *Microwave-Assisted Organic Synthesis*, Elsevier, 2005.

[3] C. O. Kappe and A. Stadler, *Practical Microwave Synthesis for Organic Chemists: Strategies, Instruments, and Protocols,* Wiley-VCH, 2009.

[4] J. M. Kremsner, A. Stadler, and C. O. Kappe, "The scale-up of microwave-assisted organic synthesis," *Top Curr Chem*, vol. 266, pp. 233-278, 2006.

[5] V. V. Komarov and V. V Yakovlev, "CAD of efficient TM_{mn0} single-mode elliptical applicators with coaxial excitation," *J. Microwave Power & Elec-tromag. Energy*, vol. 40, no. 3, pp. 174-185, 2007.

[6] M. Celuch, W. K. Gwarek, and M. Sypniewski, "A novel FDTD system for microwave heating and thawing analysis with automatic time-variation of enthalpy-dependent media parameters," *Advances in Microwave and Radio-Frequency Processing*, pp. 199-207, 2006.

[7] P. Kopyt and M. Celuch, "Coupled electromagnetic thermodynamic simulations of microwave heating

problems using the FDTD algorithm," *J. Microwave Power & Electromag. Energy*, vol. 41, no. 1, pp. 18-29, 2007.

[8] M. Celuch and P. Kopyt, "Modeling microwave heating of food," *Development of Packaging and Products for Use in Microwave Ovens*, pp. 307-350, 2009.

[9] V. A. Mechenova and V. V. Yakovlev, "Efficiency optimization for systems and components in microwave power engineering," *J. Microwave Power & Electromag. Energy*, vol. 39, no. 1, pp. 15-29, 2004.

[10] B. G. Cordes and V. V. Yakovlev, "Computational tools for synthesis of a microwave heating process resulting in the uniform temperature field," *Proc. 11th AMPERE Conf. Microwave and High Frequency Heating,* pp. 71-74, September 2007.

[11] E. E. Eves, B. G. Cordes and V. V. Yakovlev, "Modeling-based synthesis of a microwave heating process producing homogeneous temperature field," *Proc. 24th Annual Review of Progress in Applied Computational Electromagnetics,* pp. 542-544, 2008.

[12] S. Kalhori, N. Elander, J. Svennebrink, and S. Stone-Elander, "A re-entrant cavity for microwave-enhanced chemistry," *J. Microwave Power & Electromag. Energy*, vol. 38, no. 2, pp. 125-135, 2004.

[13] K.-M. Huang, Z. Lin, and X.-Q. Yang, "Numerical simulation of microwave heating of chemical reaction in dilute solution," *Progress in Electromagnetics Research (PIER)*, vol. 49, pp. 273-289, 2004.

[14] E. K. Murphy and V. V. Yakovlev, "RBF network optimization of complex microwave systems represented by small FDTD modeling data sets," *IEEE Trans. Microwave Theory Tech.*, vol. 54, no. 7, pp. 3069-3083, 2006.

[15] H. Kabir, Y. Wang, M. Yu, and Q. J. Zhang, "Neural network inverse modeling and applications to microwave filter design," *IEEE Trans. Microwave Theory and Tech.,* vol. 56, no. 4, pp. 867–879, 2008.

[16] E. K. Murphy and V. V. Yakovlev, "Reducing a number of full-wave analyses in RBF neural network optimization of complex microwave structures," *IEEE MTT-S Intern. Microwave Symp. Dig.*, pp. 1253-1256, June 2009.

[17] H. Kabir, Y. Wang, M. Yu, and Q. J. Zhang, "Advances of neural network modeling methods for RF/microwave applications," *ACES Journal,* vol. 25, no. 5, pp. 423–432, 2010.

[18] R. G. Regis and C. A. Shoemaker, "Constrained global optimization of expensive black box functions using radial basis functions," *J. Global Optim.,* vol. 31, no. 1, pp. 153–171, 2005.

[19] *QuickWave-3D*, QWED, http://www.qwed/com/pl, 1997-2009.

[20] E. K. Murphy and V. V. Yakovlev, "RBF network optimization with CORS sampling for practical CAD of microwave applicators," *Proc. 12th AMPERE Conf. Microwave and High Frequency Heating*, pp. 79-82, September 2009.

[21] E. K. Murphy and V. V. Yakovlev, "Efficiency optimization for microwave thermal processing of materials with temperature-dependent media parameters," *Proc. Progress in Electromagnetics Research Symp.*, pp. 400-401, August 2009.

Ethan K. Murphy received the M.S. degree in Industrial Mathematics from Worcester Polytechnic Institute (WPI), Worcester, MA in 2003 and the Ph.D. degree in Mathematics from Colorado State University, Fort Collins, CO in 2007. He then held two post-doc positions – at the WPI's Department of Mathematical Sciences (2008-2009) and at the Department of Biomedical Engineering at Rensselaer Polytechnic Institute, Troy, NY (2009-2010). He is currently with Applied Mathematics, Inc. His research interests include inverse problems, microwave optimization, microwave imaging, diffuse optical tomography, and electric impedance tomography. He has authored more than 20 papers in referred journals and conference proceedings. Dr. Murphy is a member of the American Mathematical Society and Pi Mu Epsilon.

Vadim V. Yakovlev received his Ph.D. degree in Radio Physics from the Institute of Radio Engineering and Electronics (IRE) of the Russian Academy of Sciences (RAS), Moscow, Russia in 1991. From 1984 to 1996, he was with IRE RAS as Junior Research Scientist, Research Scientist, and Senior Research Scientist. In 1993, he worked as Visiting Researcher at Electricité de France (Centre "Les Renardières").

In 1996, he joined the Department of Mathematical Sciences, Worcester Polytechnic Institute, Worcester, MA and currently holds there a position of Research Associate Professor. Dr. Yakovlev is a head of the Industrial Microwave Modeling Group which he established in 1999 as a division of the WPI's Center for Industrial

Mathematics and Statistics. Dr. Yakovlev's research interests in computational electromagnetics include neural-network-based optimization, microwave imaging, multiphysics modeling, microwave power engineering, and broadband/multiband antennas. He is an author of more than 120 papers in referred journals and conference proceedings. Dr. Yakovlev is a senior member of the IEEE, a member of the Technical Advisory Board of International Microwave Power Institute (IMPI), a member of Association for Microwave Power in Europe for Research and Education (AMPERE) and a member of the Massachusetts Institute of Technology (MIT) Electromagnetics Academy. He serves as a reviewer for several journals and as a member of program committees of several conferences.

Dynamic Simulation of Electromagnetic Actuators Based on the Co-Energy Map

A. Espírito Santo, M. R A. Calado, and C. M. P. Cabrita

Department of Electromechanical Engineering
University of Beira Interior, Covilhã, 6201-001, Portugal
aes@ubi.pt, rc@ubi.pt, cabrita@ubi.pt

Abstract ─ The development of new and efficient control methodologies demands the availability of mathematical models for the electromagnetic device under control. These models must be solved with great accuracy and speed. The finite element method (FEM) gives truthful results but computational demanding increases with device geometrical complexity. This paper proposes a new method for dynamic behavior simulation that uses FEM software at its early stage, to obtain the co-energy map for devices concerning static positions for different excitation currents. Inductance and force maps are derived from the co-energy map. A numerical model of a case study is built with Matlab© to obtain device dynamic response. The software implementation procedure is described in detail. The achieved results are compared with the ones obtained from the FEM tool analysis. The small computation effort required by the proposed analysis method makes possible that complex control methodologies can be developed and tested based on the proposed model.

Index Terms ─ Co-energy maps, dynamic behavior, electromagnetic actuator, numerical method.

I. INTRODUCTION

The electromagnetic actuators behavior analysis is nowadays, as in the past [1], a concerning subject for control in engineering areas as robotics or precision actuation. With the introduction of some simplifications, as ignoring material magnetic non-linearity, the analytical analysis of electromagnetic devices is possible only for the simplest geometries. The analysis tasks of actuators with higher structural complexity, with multi-excitation, or intricate geometry is very complex, and it is difficult to obtain an analytical solution. For these situations, the option is always to find the solution through the application of methodologies based on numerical analysis [2-10]. The dynamic behavior of an actuator can also be obtained through the experimental knowledge of the magnetic characteristics, as proposed in [11, 12].

The design of electromechanical devices requires the prediction of the developed force. This knowledge is often derived from field solutions obtained through numerical analysis, based upon different approaches, such as in [13-16]: (1) classical virtual work; (2) Maxwell stress tensor; (3) Coulomb's virtual work. These methods are currently used within the application of finite element analysis [17], but some care must be observed in their application. The mentioned methods can be classified depending on the number of required solutions. The classic method of virtual work requires two or more solutions, turning it computationally demanding. The Maxwell stress tensor and the Coulomb virtual work methods both require only one solution of the problem, making them more computationally efficient.

An issue with the application of the classic virtual work method is that if the moving part of the device performs a small displacement, the variation observed in the co-energy of the system is also small; as a result, a round-off error is introduced. On the other hand, if the displacement is large, a substantial error in the differentiation process is also introduced. These two problems cannot be simultaneously minimized, because one of them cannot be minimized without penalizing the other.

The choice of the method to be used is conditioned by factors such as the computational cost, data consistency, and precision requirements for the results.

The finite element analysis is a widely used numerical method to study electromagnetic problems with irregular and not homogeneous geometries. Finite element algorithms implementations are extremely efficient and commercially available. Nevertheless, these software tools are very expensive and require a large computation time. As a result, these characteristics make the execution of a high number of simulations difficult, with the aim of developing an optimal control strategy.

The aim of the presented work is the development of a new methodology that, applied to an electromechanical device, allows its electrodynamics study. Applying the method proposed here, it is possible to obtain a device dynamical model, based on the co-energy map [18-19]. The method is called dynamic modeling co-energy map (DMC).

This paper is structured as follows: in Section II, a theoretical analysis, based on device electromechanical energy conversion, is presented. The theoretical model possesses two components that describe the energy conversion process. The first one characterizes the electromagnetic process, taking into account the variation in magnetic induction depending on both mechanical displacement and current value. The second one describes the mechanical system. Section III presents a numerical analysis of the electromagnetic actuator, based on a 2D FEM, for the specific knowledge of the device. Several static simulations, for each device's relative position and for different current levels are performed, allowing the construction of a three-dimensional co-energy map. This map is the basis for the knowledge of the attraction force, magnetic flux, and inductance, which define the device numerical model, required for the development of the DMC method. Section IV presents the development details in Matlab© of the proposed method used to observe device dynamical response, in which computation demands are completely independent of the model geometry complexity. In Section V, the results obtained with the application of the proposed methodology, to a chosen case study, are presented. That analysis allows the comparison of the obtained results with the ones obtained with the application of the finite elements tool, when the iron losses are ignored. This allows the validation of the proposed method. Section VI outlines the conclusions.

II. ELECTROMECHANICAL ENERGY CONVERSION

An electromechanical device can convert electrical energy into mechanical energy, or vice--versa. This process is made through the device magnetic field. Different kinds of devices appeal to this principle, and operate according to similar physical processes, for example: transducers used in instrumentation, as the linear variable differential transformer, or actuators used in the electromechanical drives, generally called motors, if they produce force or torque, or generators, in case of producing electrical energy.

Some of the methods to produce force through the use of the electric energy are the following ones: interaction of two magnetic fields, such as a conductor carrying current in a magnetic field; ferromagnetic materials that moves to reduce the reluctance of the magnetic circuit; magnetostriction or deformation of a ferromagnetic material in a magnetic field; piezoelectric effect in the application of an electric potential to a piezoelectric crystal.

The magnetic actuator can be considered as a complete system composed by three sub-systems: (1) the electrical system; (2) the mechanical system; and (3) the coupling field. Note that in spite of the here adopted case study (electrovalve) only allowing longitudinal motion, the device possesses the three previously mentioned sub--systems, and its analysis can provide valuable information about the operation of more complex electro-magneto-mechanical devices.

Looking to the operation principles of an electromechanical device, and the respective process of energy conversion, it can be assumed that, from the energy point of view, three main advantages are presented [20]: (1) the problem formulation is simplified; (2) the analysis methodologies can easily be deduced; and (3) the experimental analysis can be made in order to confirm adopted analysis. For beyond the previous advantages, the application of the classic method of virtual work makes the problem formulation independent from the geometric complexity of the actuator, which can be considerable in some devices.

A mechanical component, free to be moved, develops mechanical work by the action of a force

produced by electrical means [21]. The energy conservation law, together with governing laws of magnetism, electrical and mechanical equations, makes this possible to obtain the energy balance equation for the system, as follows:

$$W_e = W_{le} + W_{fe} + W_{em}, \tag{1}$$

where W_e is the input energy, W_{le} the energy losses, W_{fe} the stored magnetic field energy, and W_{em} the mechanical energy output. Note that the expressed mechanical and electrical quantities are positive for motor operation and negative for generator operation. Because frequency and speed are relatively low, a quasi-stationary electromagnetic field can be assumed and electromagnetic radiation losses can be neglected. Some fraction of the mechanical output is lost (W_{fw}), while the other part is stored in the mechanical system as kinetic energy (W_{sm}). Thus, the effective mechanical energy output is W_m, and is expressed as:

$$W_m = W_{em} - W_{fw} - W_{sm}. \tag{2}$$

The losses in the system can be caused by distinct causes, like losses in electrical conductors (I^2R losses), friction and ventilation (mechanical losses) and magnetic losses in the coupling field. A small and therefore ignored fraction of the loss is caused by the dielectric effect in the electrical insulating material. Thus, the following expression is obtained for the final energy balance equation:

$$W_e = \left(W_{le} + W_{fw}\right) + \left(W_{fe} + W_{sm}\right) + W_m. \tag{3}$$

Differential energy dW_e supplied by the source, neglecting magnetic losses, is given in (4), where voltage e is the reaction from the coupling field over the electrical system, u_s the coil supply voltage, R a resistance connected in series with the coil, and i the circuit current. Equation (4) shows also the relation between voltage e and magnetic linkage flux λ as follows:

$$dW_e = \left(u_s i - R i^2\right) dt = ie dt = i\, d\lambda. \tag{4}$$

Thus, as can be seen, if a change in flux linkage occurs, the system energy will also change. This variation can be promoted by means of a variation in excitation, a mechanical displacement, or both. The coupling field can be understood as a reservoir of energy, that receives it from the entrance system, the electrical system, and delivers it to the exit system, the mechanical system. Coupling field energy intakes brings on a reaction expressed by an induced voltage as:

$$e = \frac{d\lambda}{dt}. \tag{5}$$

Energy is a state function on a conservative system. If losses are ignored, balance energy can be written as in (6), where f_{em} is the mechanical force that produces the mechanical work dW_{em}, when a differential displacement dx occurs. Energy W_e, in a lossless device, with only one coil, depends on λ and x, as follows:

$$dW_e = dW_{fe} + f_{em}\, dx \;\Leftrightarrow\; dW_{fe} = i\, d\lambda - f_{em}\, dx. \tag{6}$$

A different energy entity, defined as co-energy W'_{fe}, with no physical meaning, can be expressed as follows:

$$W'_{fe}(i,x) = i\lambda - W_{fe}. \tag{7}$$

After mathematical manipulation of (7) and considering (6), one obtains (8), where it can be seen that the co-energy W'_{fe} depends on current i and position x:

$$\begin{aligned} dW'_{fe}(i,x) &= \lambda\, di + f_{em}\, dx \\ &= \frac{dW'_{fe}(i,x)}{\partial i}\, di + \frac{dW'_{fe}(i,x)}{\partial x}\, dx. \end{aligned} \tag{8}$$

Because i and x are independent variables, λ and f_{em} are given by the following equations, where L is the device magnetic inductance:

$$\begin{cases} \lambda = \dfrac{dW'_{fe}(i,x)}{\partial i} \Leftrightarrow L = \dfrac{\lambda}{i} \\ f_{em} = \dfrac{dW'_{fe}(i,x)}{\partial x} \end{cases}. \quad (9)$$

III. FINITE ELEMENTS MODELLING

For validation purposes, the proposed numerical methodology is used to analyze an electrovalve as a case study. The device is modelled through Flux2D©, from Cedrat [22]. It is assumed that the coil of the electrovalve has 1136 turns, with a resistance of 43 Ω. An exploded view of the device can be observed in Fig. 1. The axial view and respective physical dimensions are shown in Fig. 2.

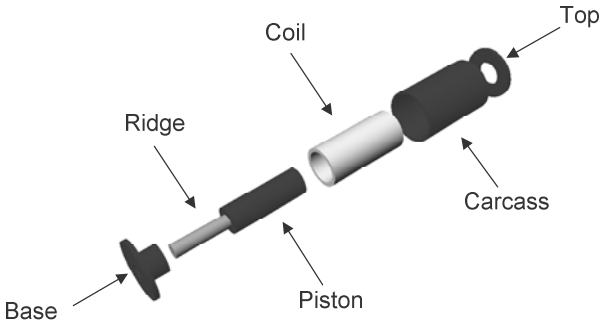

Fig. 1. Electrovalve exploded view.

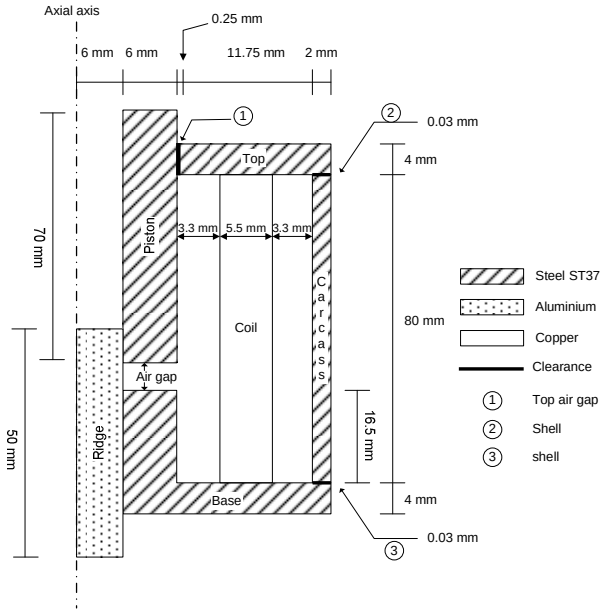

Fig. 2. Electrovalve axial view with physical dimensions.

A constructive detail of the finite element model is shown in Fig. 3. The different regions that compose this model are identified on it.

Concerning the introduction of materials connected with the different elements of the model, it is possible to recourse to a set of properties. For magnetic steels, the magnetization curve B - H is defined by means of the following relation:

$$B(H) = \mu_0 H + \frac{2J_s}{\pi} a\tan\left(\frac{\pi(\mu_r - 1)\mu_0 H}{2J_s}\right), \quad (10)$$

where μ_0 is the magnetic permeability of free space, μ_r the relative permeability and J_s the saturated magnetization. The expression is generally valid, but some errors can appear for curve values corresponding to the transition from the linear to the saturation region.

The finite element model has an infinite region with a half-circular form due to the device symmetry characteristic (see Fig. 4a), which is automatically generated as an extension of the classic analysis domain. The circular infinite region automatically receives cyclical conditions, making it physically dependent on the model limits; simultaneously, the inner part of the infinite region must present null Dirichlet conditions.

It is necessary to assign a specific property for each model region. All magnetic circuit parts are assumed as being steel made, while the screw thread and surrounding air regions are assumed as having the properties of vacuum (μ_r = 1), without any kind of associated current source. The coil region was also assigned the properties of vacuum, differing from the previous referred ones in the fact that a current source was considered. Each shell region (designated as 1 and 2 in Fig. 2) was assigned a constant and uniform thickness of 0.03 mm, with properties identical to the ones of the vacuum. Boundary conditions were also imposed for the analysis of the domain limit. Magneto-static problems formulation uses Dirichlet or Newmann boundary conditions, as in Fig. 4b. The circular infinite region automatically receives cyclical conditions, making it physically dependent on the model limits; simultaneously, the inner part of the infinite region must present null Dirichlet conditions.

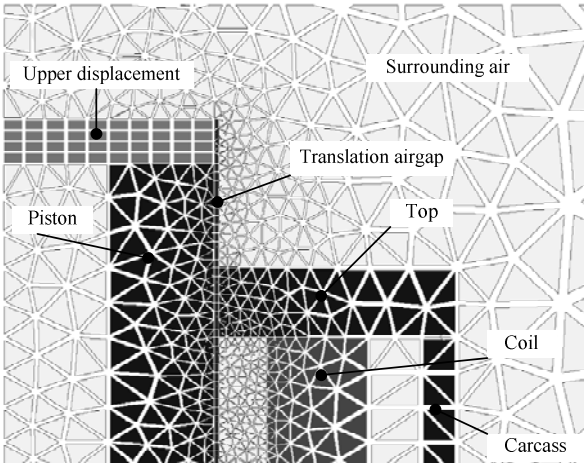

Fig. 3. Electrovalve FEM constructive detail.

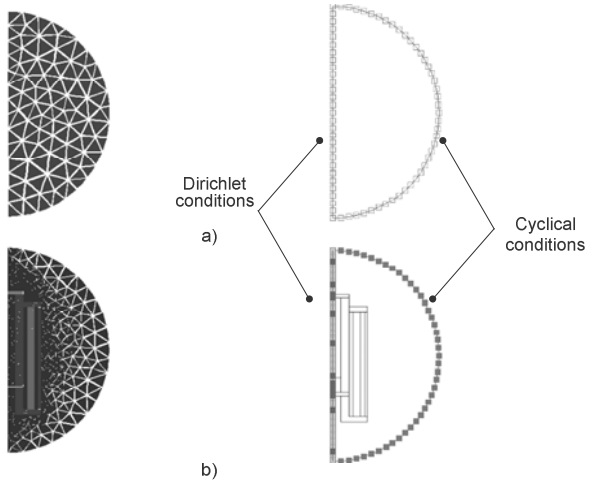

Fig. 4. Finite element mesh and boundary conditions: a) infinite region; b) electrovalve domain analysis.

The problem that authors intend to solve is a magneto-static problem, being all the computation carried out considering a steady-state situation. This fact means that neither the current nor the model geometry change during problem solving. Several static simulations have been performed. For each relative position x of the plunger, the finite elements model was analyzed, considering different excitation currents i. This task was performed using batch file programming under Flux2D©, which automatically reconfigures model parameters like plunger position x and current i, redefines model geometry and elements mesh, and collects the obtained data from the simulation process, saving it on computer hard disk for later processing proposes.

Data collected from simulations allowed the construction of a three-dimensional co-energy map, and from it, the attraction force, flux and inductance maps are properly derived, using (9). These characteristics are shown in Fig. 5, and can completely characterize the device behavior. Based on them, device numerical model can also be constructed and used to carry out the dynamical analysis. Each point of the co-energy map requires a static FEM simulation that takes approximately one minute. Notice that the case study is very simple, more complex geometries obviously will require more time. Another detail that must be observed is the co-energy map resolution. Some devices could require more points than others to define the map surface with a good resolution.

If devices geometrical parameters do not change, with the exception of the airgap length, there is no need to run the finite elements simulation again. Because the numerical model is implemented in a programming language (Matlab©) [23], simulation is more versatile and fast, in contrast with the finite elements tool.

IV. DMC NUMERICAL MODEL DEVELOPMENT

The proposed numerical model is based on the obtained values of the inductance and force maps. Using a representation of order $O(h^4)$ it is possible to obtain the centered difference expression (11) for the first derivative [24].

$$f'(x_i)=\frac{-f(x_{i+2})+8f(x_{i+1})-8f(x_{i-1})f(x_{i-2})}{12h}. \quad (11)$$

Derivative results can be improved either diminishing the step h or using a problem formulation of higher order with more points. Alternately, Richardson extrapolation uses two derivative values, obtained with different steps, to determine a third result. According to that, the extrapolation from expression (12) uses step $h_2 = h_1/2$.

$$f'(x_i)\approx\frac{4}{3}f'(x_i,h_2)-\frac{1}{3}f'(x_i,h_1). \quad (12)$$

The applied differentiation procedure returns as a result the force, flux, and inductance maps, which are shown in Fig. 5. The device non-

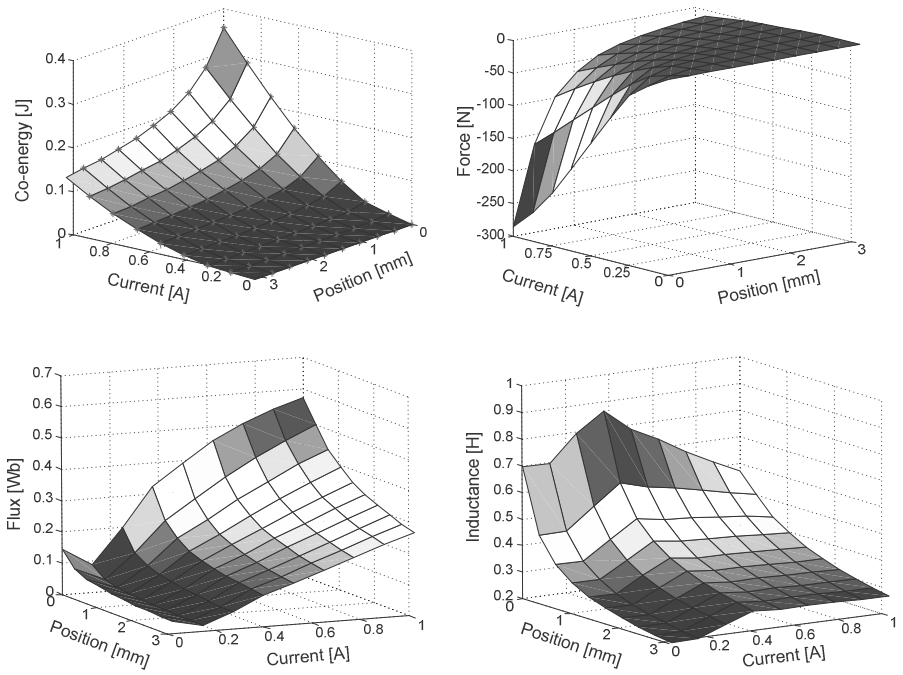

Fig. 5. Electrovalve three-dimensional maps: co-energy, force, flux and inductance.

linearity characteristic is shown in the previously referred maps. It is observable that inductance $L(i,x)$ and force $F(i,x)$ change not only with position x, but also with current i, exhibiting a strong influence of the magnetic circuit saturation. If these maps are used for device modeling, then simulation will take into account the actuator non-linearity.

The equation (13) describes the electromagnetic electrovalve behavior, being R the coil resistance and u_s the applied voltage:

$$u_s = R\, i(t) + \frac{dL(i,x)\, i(t)}{dt}. \qquad (13)$$

Because the inductance $L(i,x)$ is a function of the current i and position x, and in turn both function of time, the differentiation is carried through t, being terms di/dt and dx/dt placed in evidence, resulting:

$$u_s = \frac{di}{dt}\left[L(i,x) + i(t)\frac{\partial L(i,x)}{\partial i} \right] + . \\ + \frac{di}{dt}\left[i(t)\frac{\partial L(i,x)}{\partial x} \right] + Ri(t) \qquad (14)$$

Introducing parameters α and β as in:

$$\begin{cases} \alpha = L(i,x) + i\dfrac{\partial\ L(i,x)}{\partial i} \\ \beta = i\dfrac{\partial\ L(i,x)}{\partial x} \end{cases}, \qquad (15)$$

equation (14) becomes:

$$u_s = \alpha\frac{di}{dt} + \beta\frac{dx}{dt} + R\, i(t). \qquad (16)$$

Mathematical expressions (17) and (18) describe the dynamics of the electromechanical actuator, in which x, y, and a are, respectively, the plunger position, the velocity, and the acceleration, being M the plunger mass and F the produced attraction force.

$$a = \frac{1}{M} F \Leftrightarrow \frac{dy}{dt} = \frac{1}{M} F. \quad (17)$$

$$\frac{dx}{dt} = y. \quad (18)$$

The problem here under consideration is solved with Matlab© in two distinct steps. First, the plunger is allowed to move freely, and begins to do it from the considered initial position; this situation is described through the differential equations system (19). After, when stroke reaches its final position, it is considered that the movement is absent, and the velocity and acceleration will be zero. This situation is described by the differential equations system (20).

$$\begin{cases} \frac{dx}{dt} = y \\ \frac{dy}{dt} = \frac{1}{M} F \\ \frac{di}{dt} = -\frac{v_s - y\,\beta - R\,i}{\alpha} \end{cases}. \quad (19)$$

$$\begin{cases} \frac{dx}{dt} = 0 \\ \frac{dy}{dt} = 0 \\ \frac{di}{dt} = -\frac{v_s - y\,\beta - R\,i}{\alpha} \end{cases}. \quad (20)$$

The traditional solving methods for differential equations do not keep memory of the past solutions. Others, like the Adam family formulas for non-stiff problems and backward differences for stiff problems, take advantage from remembering past solutions. This formulations interpolate not only the solutions y_i, y_{i+1}, y_{i-p}, previously found, but also the new solution y_{i+1} using a polynomial $P(t)$. The solution at t_{i+1} is approached by the derivative of the following polynomial:

$$\left.\frac{dP}{dt}\right|_{t=t_{i+1}} = f\left(t_{i+1}, P\left(t_{i+1}\right)\right) = f\left(t_{i+1}, y_{i+1}\right) \quad . \quad (21)$$

The backward difference finite (BDF) family of formulas is obtained substituting the polynomial derivative at t_{i+1}, introducing coefficients α_p:

$$h\, f\left(t_{i+1}, y_{i+1}\right) = \bar{\alpha}_0\, y_{i+1} + \bar{\alpha}_1\, y_i + \ldots + \bar{\alpha}_p\, y_{i+1-p}. \quad (22)$$

The numerical differentiation formulas (NDF), defined by (23), and very close to the BDF, introduces some advantages. Here, k is a scalar parameter and the coefficients γ_k are given by $\gamma_k = \sum_{j=1}^{k} \frac{1}{j}$. Matlab© software implements NDF solving methodology in function ODE15S.

$$\sum_{m=1}^{n} \frac{1}{m} \nabla_{m+1}^{m} - h\, F\left(t_{n+1}, y_{n+1}\right) - k\, \gamma_k \left(y_{n+1} - y_{n+1}^{(0)}\right) = 0. \quad (23)$$

This function, or others like the ODE23, beyond solving with efficiency stiff problems, also has a good performance in solving non-stiff problems [23-25]. For each problem solving iteration, the values of α and β are obtained applying Spline interpolation and differential methods to the induction map. The dynamic simulation problem is solved using

```
[t,u,tev,uev,ie] = ode15s(@odemodelo_val1,
[0 tfim],uev,options,[],M,R,V1,interp_met);
```

where the parameter *odemodelo_val1* identifies the file that contains the numerical formulation made by a system of differential equations describing problem first phase. Before the system of differential equations can be evaluated, it is necessary to compute parameter $a(i,x)$ (α parameter), $b(i,x)$ (β parameter) and attraction force $f(i,x)$ for a specific system status (i,x). These operations are performed by the function *@odemodelo_val1* applying the previously described theoretical formulation. The determination of these parameters solves the system of differential equations for each problem phase. Equations (19) and (20) are described in Matlab as follows:

Problem phase I

```
dudt=zeros(size(u));
dudt(1)=u(2);
dudt(2)=f/M;
dudt(3)=(V1-u(2)*b-R*u(3))/a;
```

Problem Phase II

```
dudt=zeros(size(u));
dudt(1)= 0;
dudt(2)= 0;
dudt(3)=(V1-u(2)*b-R*u(3))/a;
```

The integration range is defined by vector [0 *tfim*], being the simulation end defined by *tfim*. Initial conditions are defined by the vector *uev* = [*x0 v0 i0*], where *x0* is the piston initial position, *v0* is the piston initial velocity, and *i0* the current in the solenoid coil at t = 0. The options of the ODE15s function are set with the *odeset* function:

```
options = odeset('OutputFcn',@odeplot,
'events',@events,'MaxStep',1e-4);
```

This function defines the output function *odeplot* that will represent the results graphically. The simulation process can be stopped by an event that is defined by the function *events*. This function is executed whenever it is necessary to check if the piston position reached the end of problem phase I, defined by *Vxcomuta*.

```
function [value,isterminal,direction] =
events(t,u,varargin)
    global VXcomuta;
    value = u(1)-VXcomuta;
    isterminal=1;
    direction=0
```

Finally, the parameter *MaxStep* defines the maximum integration step allowed. The *odemodelo_val1* also receives piston height (*M*), coil resistance (*R*), voltage source (*V1*), and the interpolation method to be used to collect data form maps.

At the end of problem phase I the following solution vectors are obtained: time (*t*), solution (*u*), event time (*tev*), last values of solution (*uev*), and wish event was occurred (*ie*). This information is saved and used as initial conditions of problem phase II. Now, the ODE15S function is used with the following configuration.

```
[t,u] = ode15s(@odemodelo_val2,
[tev tfim],uev,options,[],M,R,V1,interp_met);
```

This new problem stage is described by function *odemodelo_val2*.

After solving, the problem is possible to compute temporal evolution of the remaining variables associated with the electromechanical process of energy conversion. This task is performed applying interpolation methods in the respective variable map for each system state (*t*,*i*,*x*). This process allows us to compute the co-energy (*cw*), inductance (*l*), attraction force (*f*), and magnetic flux (*fl*).

Matlab application ends with the graphical exhibition of the dynamical results simulation. The solving process is shown in Fig. 6.

The process starts by loading the problem data and the initial approach to solve the problem, which corresponds to the plunger movement. When the plunger's stroke ends, another situation starts, and from this point forward to the end of the simulation, the plunger remains immobilized. Both problem stages are solved using ODE15S.

V. RESULTS ANALYSIS

The results obtained from the application of the proposed methodology to the case study can be visualized and compared with the ones obtained with the application of the finite elements tool, ignoring magnetic and iron losses. The results obtained considering the losses are also presented. The simulation was carried out considering a plunger mass *M* of 0.2 kg, an airgap length of 2.5 mm, and a DC voltage source of 30V, feeding a coil with 1136 turns and a resistance of 43 Ω. The plunger was initially considered immobilized, so that initial velocity and current were null. The established time for simulation was 70 msec, being 0.1 msec the maximum time step allowed in the FEM tool.

Results obtained from the proposed numerical model simulation are shown in Fig. 7, being also shown the ones obtained from Flux2D© simulation. The comparison between these results allows us to conclude that the first ones are closely fitting the second ones, corresponding to when the losses are neglected.

The DMC method allows that, after a non-

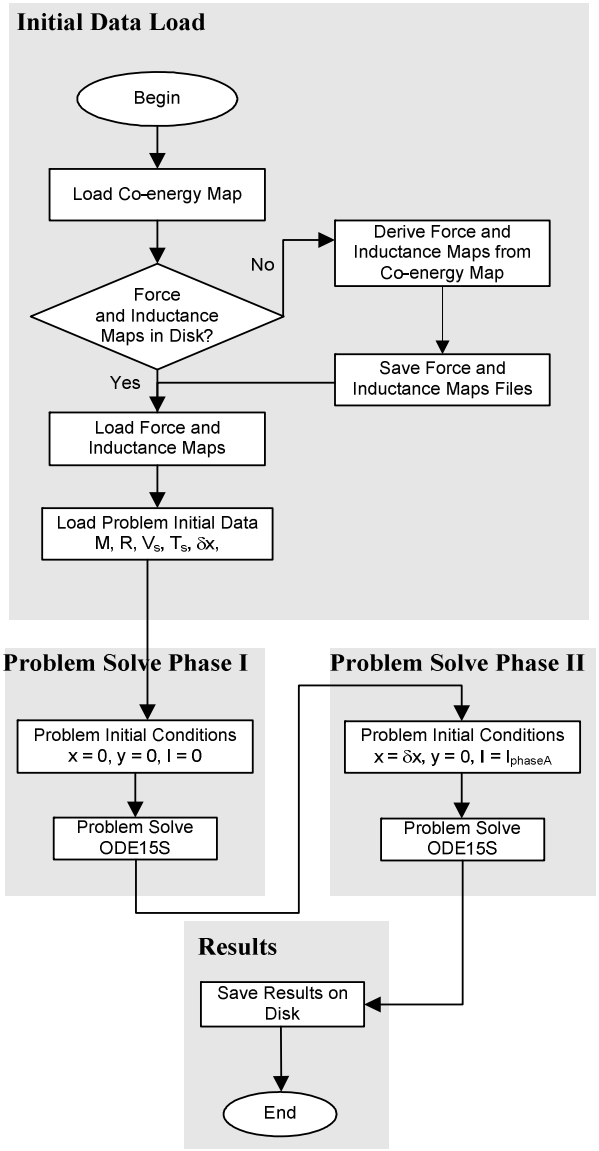

Fig. 6. Problem solving flowchart.

-geometric parameter change, like in voltage or coil resistance, the simulation can easily be repeated without solving the FEM model again. The proposed method is computationally efficient, taking less than two minutes, while the FEM tool takes about one hour to give equivalent results. Because the DMC problem is implemented using a high level programming language, changes can easily be introduced, allowing the validation of the device control strategy, for example.

The application of this methodology to a more complex device analysis, with more coils and/or a higher geometry complexity is not difficult, and the computation demands are completely independent from those complexities. From the analysis of Fig. 7, it can be noticed that the initial plunger movement is very small. As can be seen, current increases very quickly at this stage, but inductance stays almost constant. After reaching a first maximum, current decreases because inductance increases very quickly. When plunger movement stops, the current starts to increase again until it reaches a steady-state value, and because saturation effects are taken into account, inductance value decreases.

V. CONCLUSION

Dynamical simulation of electromagnetics actuators is usually accomplished with finite element tools. These kinds of tools appeal for high computational performance, are expensive, and take a long time to accomplish the simulation. Furthermore, FEM model complexity has high influence in the computation time and depends from the device's geometrical complexity. The previously described context turns the development and improvement of control methodologies hard to accomplish with FEM tools. Moreover, the development of advanced control methodologies could take advantage from an integration of electromagnetic device simulation with a numerical programming language.

This work proposes a simulation method to perform the dynamic behavior analysis of the electromagnetic actuators. This methodology uses a FEM software package at an early stage. After FEM model generation, several static simulations are performed to obtain the device co-energy map. The co-energy map must be obtained for each specific device. This approach is application specific to the electromagnetic actuator.

The co-energy map could be obtained through other methods like tube flux or experimentally. If device geometrical structure does not change, there is no need to run a new finite element model again. This data is used to make a device numerical model that, after being implemented in Matlab©, is used to observe the dynamical response of a case study device. From method implementation, we can conclude that computation effort to solve the problem is completely independent from the model geometry complexity. Introducing small changes, the proposed model could be easily applied to an actuator with a more

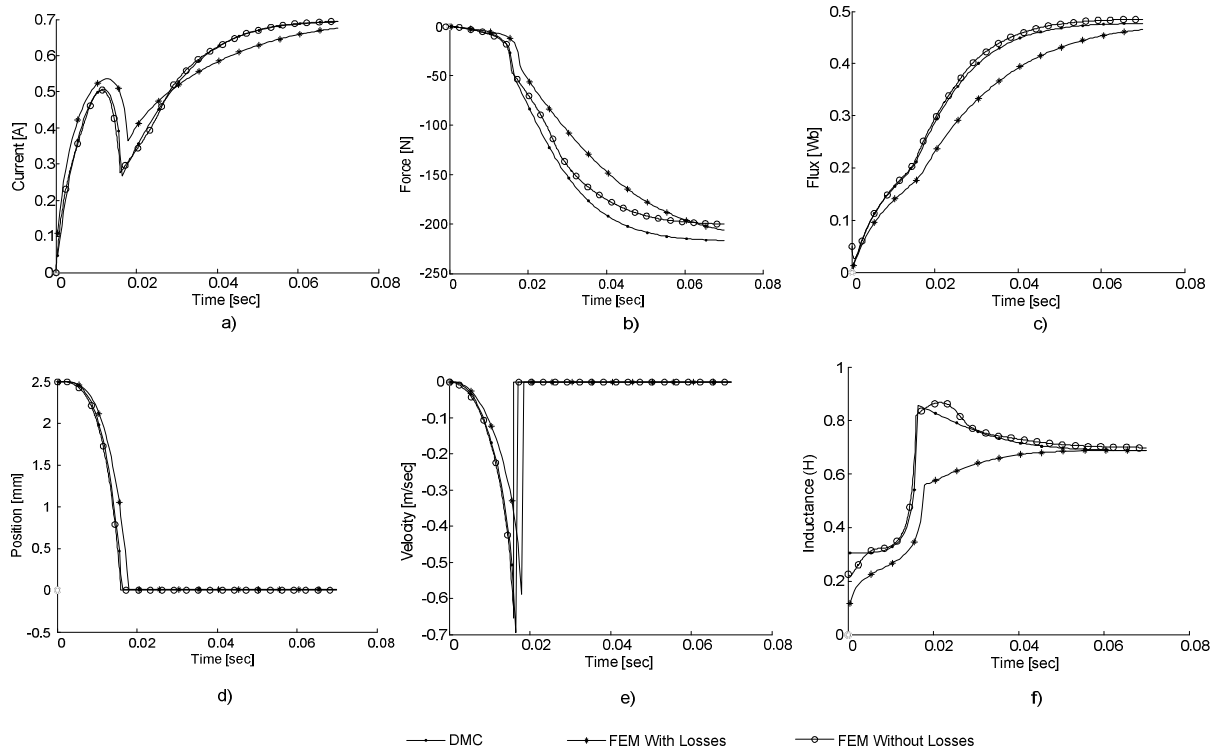

Fig. 7. Results as functions of time for a stroke of 2.5mm, with $u_s = 30\text{V}$, $R = 43\ \Omega$ and $M = 0.2$ Kg: a) current; b) force; c) flux; d) position; e) velocity; f) inductance.

complex geometry or with several excitation coils. The results can contribute to optimize actuator control methodology, with less computational effort. The mechanical load subsystem can be easily changed to simulate different mechanical loads or introduce friction effects.

REFERENCES

[1] H. C. Roters, *Electromagnetic Devices,* John Wiley and Sons, 1941.

[2] K. Srairi and M. Féliachi, "Electromagnetic Actuator Behavior Analysis Using Finite Element and Parameterization Methods," *IEEE Trans. Transactions on Magnetics*, vol. 31, no. 6, pp. 3497-3499, November 1995.

[3] G. Asche and Ph. K. Sattler, "Numerical Calculation of the Dynamic Behaviour of Electromagnetic Actuators," *IEEE Transactions on Magnetics*, vol. 26, no. 2, pp. 979-982, March 1990.

[4] K. Srairi and M. Féliachi, "Numerical Coupling Models for Analyzing Dynamic Behaviors of Electromagnetic Actuators," *IEEE Transactions on Magnetics*, vol. 34, no. 5, pp. 3608-3611, September 1998.

[5] Y. Xu and B. Jones, "A Simple Means of Predicting the Dynamic Response of Electromagnetic Actuators," *Mechatronics,* vol. 7, no. 7, pp. 589-598, October 1997.

[6] J. Faiz, J. Raddadi, and John W. Finch, "Spice-Based Dynamic Analysis of a Switched Reluctance Motor with Multiple Teeth per Stator Pole," *IEEE Transactions on Magnetics*, vol. 38, no. 4, pp. 1780-1788, July 2002.

[7] T. Tsukii, K. Nakamura, and O. Ichinokura, "SPICE Simulation of SRM Considering Nonlinear Magnetization Characteristics," *Electrical Engineering in Japan,* vol. 142, no. 1, pp. 50-56, 2003.

[8] U. Deshpande, "Two-Dimensional Finite-Element Analysis of a High-Force-Density Linear Switched Reluctance Machine Including Three-Dimensional Effects," *IEEE Transactions on Industry Applications*, vol. 36, no. 4, pp. 1047-1052, July/August 2000.

[9] X. D. Xue and K. W. E. Cheng, "A Self-Training Numerical Method to Calculate the Magnetic Characteristics for Switched Reluctance Motors Drives," *IEEE Transactions on Magnetics*, vol. 40, no. 2, pp. 734-737, March 2004.

[10] S. Kurz, J. Fetzer, T. Kube, G. Lehner, and W. M. Rucker, "BEM-FEM Coupling in Electromagnetics: A 2-D Watch Stepping Motor

Driven by A Thin Wire Coil," *ACES Journal*, vol. 12, no. 2, pp. 135-139, 1997.

[11] B. Parreira, S. Rafael, A. J. Pires, and P. J. Branco, "Obtaining the Magnetic Characteristics of an 8/6 Switched Reluctance Machine: From FEM Analysis to the Experimental Tests," *IEEE Transactions on Industrial Electronics*, vol. 52, no. 6, pp. 1635-1643, December 2005.

[12] K.Takayama, Y. Takasakiomoyuki, R. Ueda, and T. Sonoda, "Thrust Force Distribution on the Surface of Stator and Rotor Poles of Switched Reluctance Motor," *IEEE Transactions on Magnetics*, vol. 25, no. 5, pp. 3997-3999, September 1989.

[13] I. Boldea and S. A. Nasar, *Linear Electric Actuators and Generators*, Cambridge University Press, UK, 1997.

[14] S. Mcfee and D. A. Lowther, "Towards accurate and consistent force calculation in finite element based computational magnetostatics," *IEEE Transactions on Magnetics*, vol. 23, no. 5, pp. 3771-3773, September 1987.

[15] W. Muller, "Comparison of different methods of force calculation," *IEEE Transactions on Magnetics*, vol. 26, no. 2, pp. 1058-1061, March 1990.

[16] J. L. Coulomb, "A methodology for the determination of global electromechanical quantities for a finite element analysis and its application to the evaluation of magnetic forces, torques and stiffness," *IEEE Transactions on Magnetics*, vol. 19, no. 6, pp. 2514-2519, November 1983.

[17] P. P. Silvester and R. L. Ferrari, *Finite elements for electrical engineer*, Cambridge University Press, 1996.

[18] A. E. Santo, M. R. A. Calado, and C. M. P. Cabrita, "Variable Reluctance Linear Actuator Dynamics Analysis Based on Co-energy Maps for Control Optimization," *the Linear Drives for Industry Application*, Kobe-Awaji, Japan, September 2005.

[19] A. E. Santo, M. R. A. Calado, and C. M. P. Cabrita, "On the Influence of the Pole and Teeth Shapes on the Performance of Linear Switched Reluctance Actuator," *The International Journal for Computation and Mathematics in Electrical and Electronic Engineering* (accepted for publication), 2010.

[20] I. P. Hammond (1981): Energy Methods in Electromagnetism, *Oxford Science Publications*.

[21] A. E. Fitzgerald, *Electric machinery: The processes, devices, and systems of electromechanical energy conversion*, 3rd edition, McGraw-Hill, 1971.

[22] Flux2D (Version 7.40), *Translating motion tutorial*, Cedrat, 1999.

[23] C-M. Ong, Dynamic Simulation of Electric Machinery using Matlab/Simulink, *Englewood Cliffs, NI: Prentice-Hall*, 1998.

[24] S. C. Chapra, *Numerical methods for engineers*, McGraw-Hill International Editions, 1990.

[25] L. F. Shampine and M. W. Reichelt, "The MATLAB ODE Suite," *SIAM Journal on Scientific Computing*, vol. 18, pp. 1-22, 1997.

A. Espírito Santo received the Electrical Engineering degree from Universidade de Coimbra (FCTUC), Coimbra, Portugal, in 1996, the M.Sc. degree from the same institution, in 2002, and the Ph.D. degree from University of Beira Interior, Covilhã, Portugal, in 2008. He is currently Assistant Professor at UBI, Department of Electromechanical Engineering (DEM). His research area is instrumentation and control of actuators.

M. R. A. Calado received the Electrical Engineering degree from the Instituto Superior Técnico (IST), Lisbon, Portugal, in 1991, the M.Sc. equivalent degree and the Ph.D. degree from University of Beira Interior, Covilhã, Portugal, in 1996 and 2002, respectively.
She is currently Professor at UBI, Department of Electromechanical Engineering (DEM). She has about 50 scientific publications. Her research interests include electrical machines and actuators and numerical methods.

C. M. P. Cabrita received the Electrical and Computer Engineering and the Ph.D. degrees from the IST, Lisbon, in 1976 and 1988, respectively.
He was with Portuguese Railways from 1977 to 1978, in the electrical rolling stock division, and from 1978 to 1997, he was with IST, in the Electrical Machines Department. Since 1997, he has been with UBI, DEM, where currently he is a Full Professor. From 1978, he has also been a Consultant Engineer. He has about one hundred scientific publications. His research areas are electric traction and electrical machines and actuators.

Mutual Coupling Reduction in Dielectric Resonator Antenna Arrays Embedded in a Circular Cylindrical Ground Plane

S. H. Zainud-Deen, H. A. Malhat, and K. H. Awadalla

Department of Electronics and Electrical Communications Engineering
Faculty of Electronic Engineering, Menoufia University, Egypt
anssaber@yahoo.com, er_honida@yahoo.com

Abstract ─ In this paper, the radiation characteristics and the mutual coupling between two identical cylindrical dielectric resonator antennas embedded in a cylindrical structure in different configurations are calculated. To reduce the mutual coupling between the two antennas, the surface of the cylinder ground plane is defected by cutting slots, or inserting quarter wavelength grooves between the two antennas. The finite element method and the method based on the finite integration technique are used to calculate the radiation characteristics of the antenna.

Index Terms ─ Antenna arrays, dielectric resonator antenna, finite element method, mutual coupling.

I. INTRODUCTION

Dielectric resonator antennas (DRAs) have been widely discussed since they were introduced by Long et al. [1] in 1983. DRAs have many attractive features in terms of high radiation efficiency, light weight, small size, and low profile [2-7]. A comparison between the DRA and the microstrip antenna was presented in [8]. The development of antennas on curved surfaces is of great interest in aerospace and modern communication applications. Analysis of mutual coupling between elements mounted on cylinders using high-frequency or more analytical techniques are introduced in [9,10]. The mutual coupling or isolation between closely packed antenna elements is important in a number of applications [11]. Researchers have found that mushroom-like electromagnetic band gap structures (EBG) and the defected ground structure (DGS) are able to reduce the mutual coupling between elements [12, 13]. The objective of this paper is to analyze the radiation characteristics as well as the mutual coupling reduction between DRAs embedded in a cylindrical structure. The finite element is used to calculate the radiation characteristics of the antenna and the method based on finite integration technique is used to validate the results.

II. METHOD OF SOLUTION

A. Finite element method (FEM)

FEM is a numerical method that is used to solve boundary-value problems characterized by partial differential equations and a set of boundary conditions [14]. The geometrical domain of a boundary-value problem is discretized using sub-domain elements, called the finite elements (often triangles or quadrilaterals in 2D and tetrahedral, bricks, or prisms in 3D), and the differential equation is applied to a single element after it is brought to a "weak" integro-differential form. A set of shape functions is used to represent the primary unknown variable in the element domain. A set of linear equations is obtained for each element in the discretized domain. A global matrix system is formed after the assembly of all elements. FEM is one of the most successful frequency domain computational methods for electromagnetic simulations. It combines geometrical adaptability and material generality

for modeling arbitrary geometries and materials of any composition. More details about FEM can be found in [15].

B. Finite integration technique (FIT)

The finite integration technique (FIT) with the perfect boundary approximation (PBA) is a generalization of the finite-difference time-domain (FDTD). In this method, the integral form of Maxwell's equations in time domain is discretized instead of the differential ones. The PBA mesh has excellent convergence properties. The simulation doesn't require a huge memory to be carried out. Accordingly, using the PBA mesh is suitable to simulate the large structures as the simulated results can be obtained in a very short time [16, 17]. Comparing the PBA with the staircase mesh and the tetrahedral mesh, it is considered the best one in terms of the low memory requirements. The tetrahedral mesh, also, has excellent convergence properties but it requires large memory and a long computing time if large structures are to be simulated. As for the staircase mesh, it is suitable for simple structures without curved structures as it will not converge in a reasonable computing time.

The FEM is used for the parametric study as it uses the tetrahedral mesh which is accurate because the simulation is repeated at each frequency. In FIT (i.e. time domain method), a wideband pulse is used to excite the antenna, and the solution is transformed to the frequency domain to determine the input impedance over a wide band of frequencies [18].

III. NUMERICAL RESULTS

Figure 1 shows the two identical CDRA embedded in a hollow circular cylindrical ground plane. A single-element cylindrical dielectric resonator antenna (CDRA) embedded in a hollow circular cylindrical ground plane with a shallow cavity is shown in Fig.1*a* and Fig.1b. A CDRA with dielectric constant (ε_r) 12 is used. It has radius, "a" of 4.2 mm and a height, "b" of 3 mm. A coaxial probe with radius of 0.2 mm excites the antenna and is located off the center by distance d_f = 3.5 mm and height, "h_f" of 2.4 mm. The coaxial cable is located inside the hollow circular cylindrical ground plane. This CDRA is designed to operate around 10.36 GHz. The CDRA is centrally housed in a shallow cavity with radius r =8.4 mm and depth H = 4 mm. The length of the circular cylindrical ground plane, "L" is 100 mm, with radius R_C of 15mm. The thickness of the cylindrical conductor sheet is 0.6 mm.

Figure 2 shows the magnitude of S_{21} plotted as a function of separation, in wavelength, for both E – plane coupling and H – plane coupling at f=10.32 GHz. The coupling decreases faster for the H – plane configuration than for the E – plane with increasing separation between them "S". Figure 3 shows the magnitude S_{21} versus frequency with R_C=15mm and S=14.53 mm. The radiation patterns for the coupled antennas, CDRAs, in different orientations using the same input voltage excitations at f= 10.32 GHz are plotted in Fig. 4.

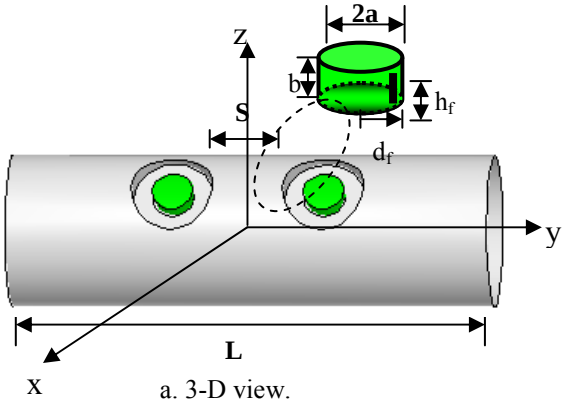

a. 3-D view.

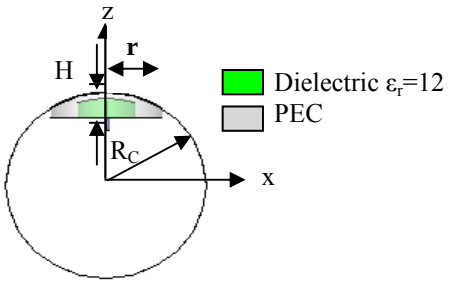

b. Side view.

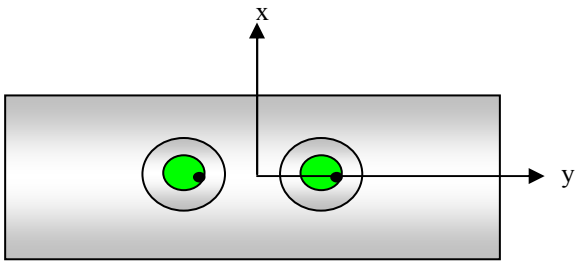

c. E-plane coupling, 2D.

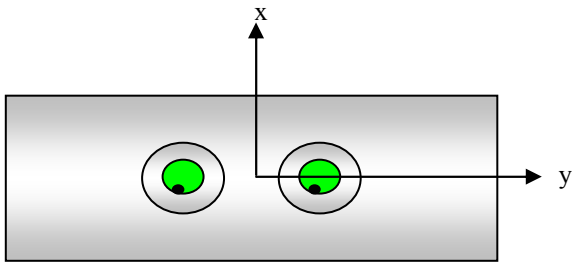

d. H-plane coupling, 2D.

Fig. 1. The construction of two identical CDRAs embedded in a hollow circular cylindrical ground plane in E-plane and H-plane.

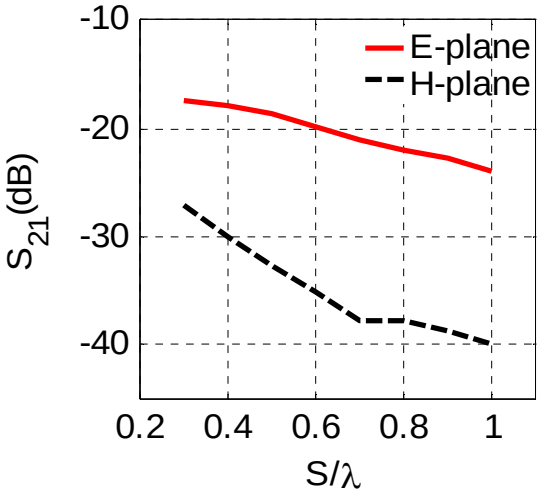

Fig. 2. Mutual coupling coefficient (S_{21}) versus separation in wavelengths for the E-plane coupling and H-plane coupling of two identical embedded CDRAs at f=10.32 GHz.

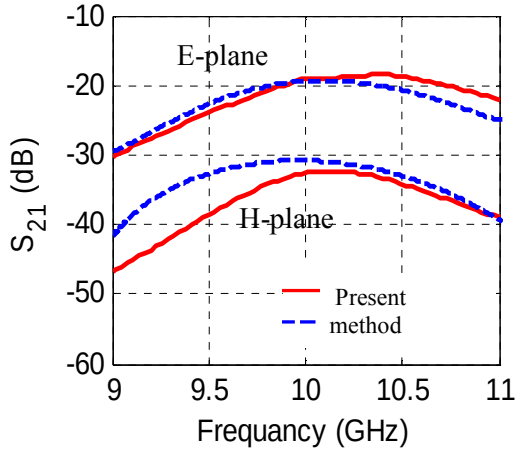

Fig. 3. Mutual coupling coefficient (S_{21}) versus frequency for the E-plane coupling and H-plane coupling two identical embedded CDRAs at S=14.53mm.

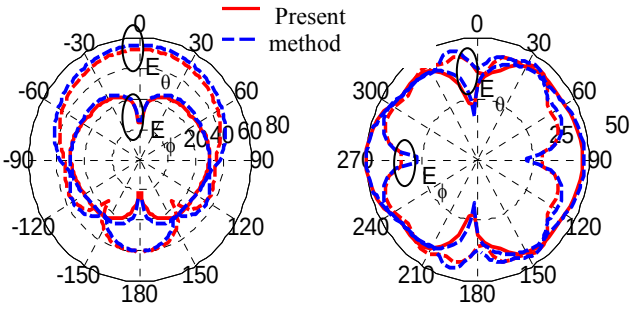

a. E- plane coupling.

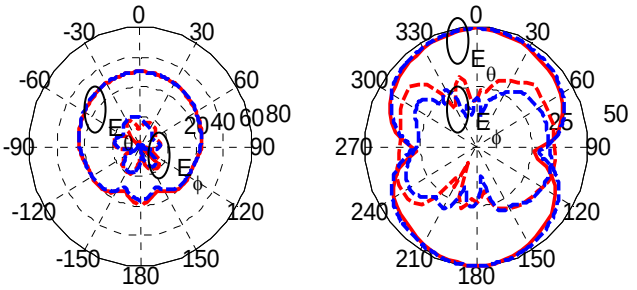

b. H- plane coupling.

Fig. 4. The radiation pattern for two identical embedded CDRAs with tilted defected ground plane structure at 10.32 GHz.

Figure 5 shows two identical CDRA embedded in a hollow circular cylindrical shape with defected ground plane structure (DGS). The DGS is composed of cutting slots in surface of the cylinders (case 1). The axis of the slot is perpendicular to the cylinder axis. The slot radial length L_s, width W_s, depth H_s, and the slots separation d_s. These dimensions are designed for their stop-band around 10.32 GHz. The mutual coupling coefficient S_{21} between two identical CDRAs (with dimensions as in Fig.1) versus frequency for one slot, two slots, and three slots is shown in Fig. 6. The optimized dimensions are L_s=0.5λ, W_s=0.01λ, d_s=0.05 λ, S=0.5 λ, and R_C=15 mm at the operating frequency 10.32 GHz. The results are compared with that calculated with a solid conventional cylindrical ground plane (without defect ground plane). It is observed that, the isolation of the defected ground plane provides a significant improvement of isolation of 5.46 dB for one slot, 6.66 dB for two slots, and 5.53 dB for three slots in the cylindrical ground plane at 10.32

GHz. The mutual coupling is increased in the case of using three slots due to the redistribution of the surface current on the cylinder between the two DRAs. Figure 7 shows the radiation patterns in different planes for one slot, two slots, and three slots at 10.32 GHz. Little effect on the radiation patterns for different numbers of the slots is observed.

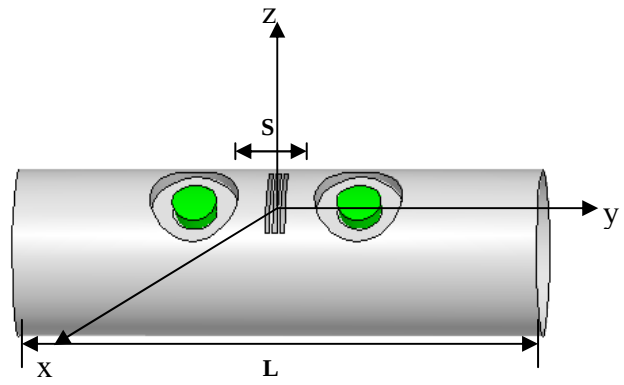

a. 3-D view.

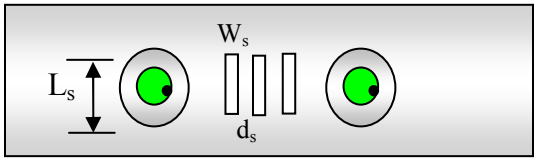

b. E-plane.

Fig. 5. The construction of two identical CDRA embedded in a hollow circular cylindrical shape with defected ground plane structure.

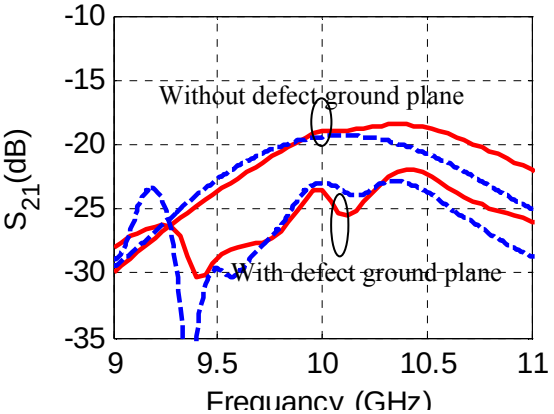

b. Two slots.

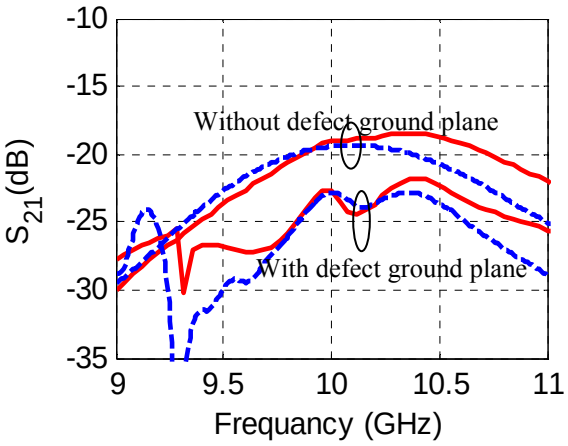

c. Three slots.

Fig. 6. The mutual coupling coefficient S_{21} between two identical embedded CDRAs versus frequency.

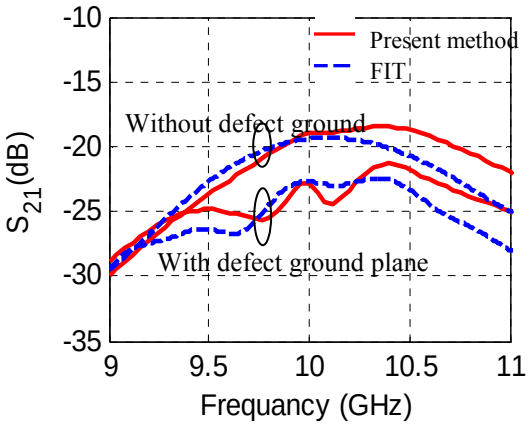

a. One slot.

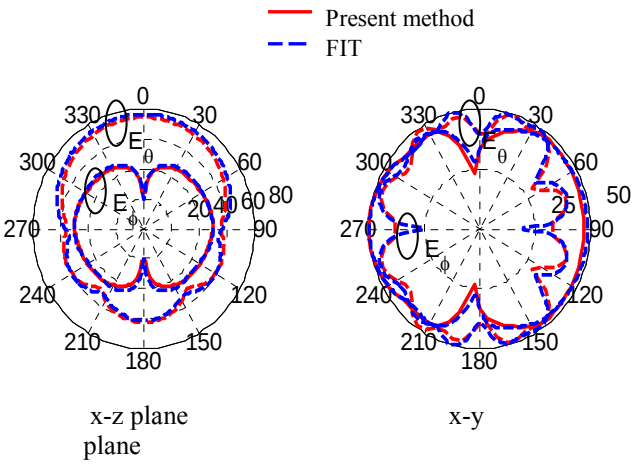

plane

a. One slot.

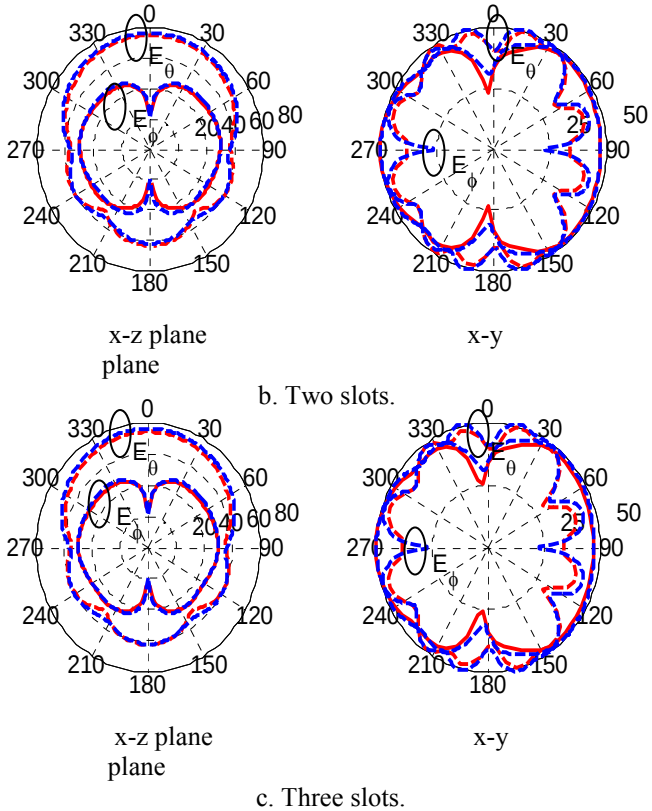

Fig. 7. The radiation pattern for two identical embedded CDRAs with tilted defected ground plane structure at 10.32 GHz.

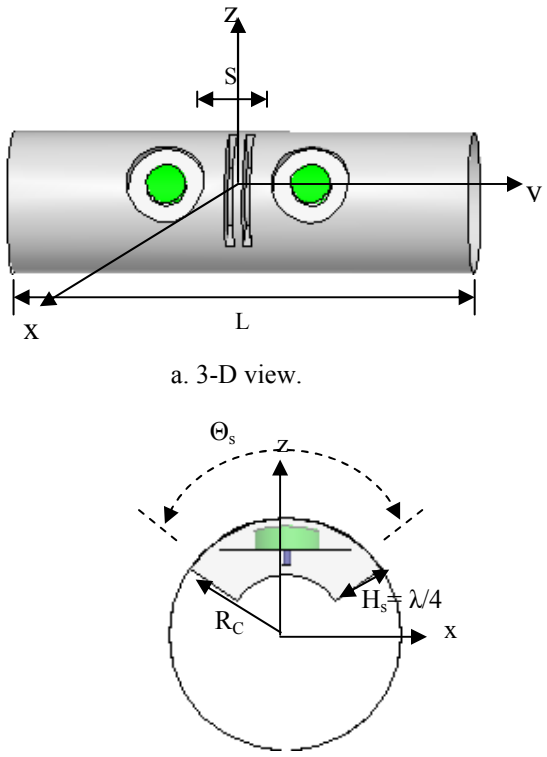

Fig. 8. The construction of two identical CDRAs embedded in a hollow cylindrical shape with tilted defect cylindrical ground plane.

Another shape for the cutting slots (with metallic grooves) are shown in Fig.8. The cutting slot (quarter wavelength groove) is tilted and its bottom is made cylindrical with the same axis of the ground cylinder (case 2). The depth $H_s = \lambda/4$(the metallic grooves depth) and $\theta_s = 60.3^o$ with $W_s = 0.02\lambda$, and $d_s = 0.1\lambda$ at the center frequency 10.32 GHz. Figure 9 shows S_{21} versus frequency for one slot and two slots. The separation distance S=14.53 mm, cylinder radius R_C=15 mm. An isolation of 4.07 dB for one slot and 12.14 dB for two slots over the solid conventional ground plane is obtained. The radiation patterns at 10.32 GHz and R_C=15 mm for one slot in different planes are plotted in Fig. 10.

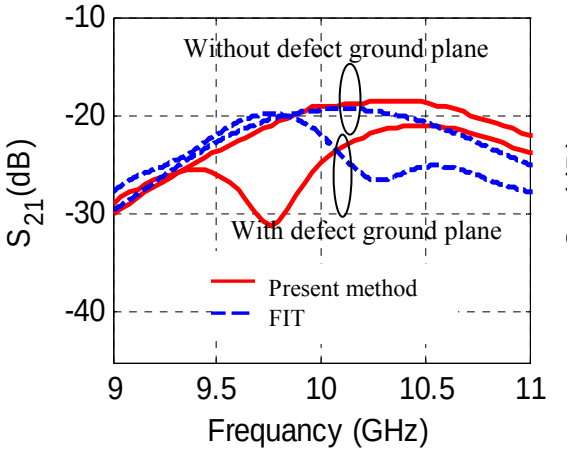

a. One slot.

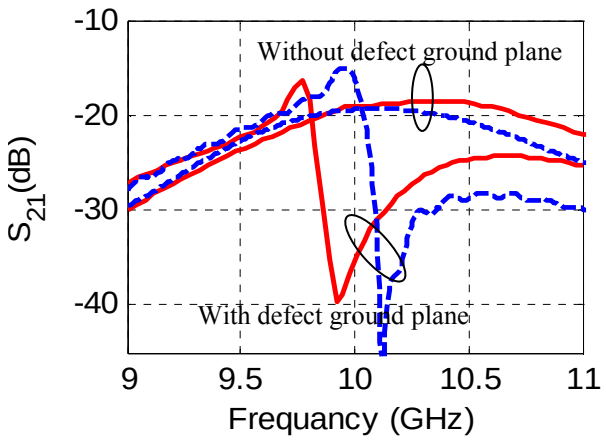

b. Two slots.

Fig. 9. The mutual coupling coefficient, S_{21}, between two identical embedded CDRAs versus frequency. With tilted defected ground plane.

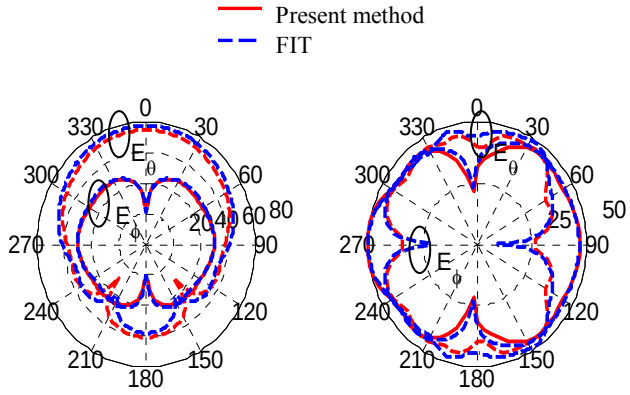

a. One slot.

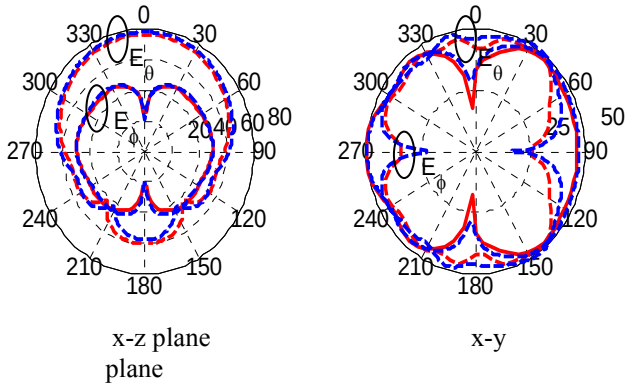

b. Two slots.

Fig. 10. The radiation pattern for two identical embedded CDRAs with tilted defected ground plane structure at 10.32 GHz.

IV. CONCLUSION

This paper presented the simulated results for the mutual coupling between two identical CDRAs embedded in a metallic hollow circular cylindrical structure in E-plane coupling and H- plane coupling. Two methods of solutions are used, the FEM and FIT. The coupling decreases faster for the H- plane coupling than for the E- plane coupling. In case 1, the surface of the cylinder is defected by using slots to decrease the mutual coupling between the two CDRAs. The S_{21} is decreased by 5.46 dB for one slot and 5.53 dB for three slots at the center frequency f=10.32 GHz. While in case 2, the cutting slot (quarter wavelength groove) is tilted and its bottom is made cylindrical with the same axis of the ground cylinder. The S_{21} is decreased by 4.07 dB for one slot and 12.14 dB for two slots at the center frequency f=10.32 GHz.

REFERENCES

[1] S. A. Long, M. W. McAllister, and L. C. Shen, "The resonant cylindrical dielectric cavity antenna," *IEEE Transactions on Antennas and Propagation*, vol. 31, no. 5, pp. 406- 412, May 1983.

[2] K. M. Luk and K. W. Leung, Dielectric resonator antenna, Hertfordshire, U.K.: Research Studies Press, 2003.

[3] S. H. Zainud- Deen, H. A. Malhat, and K. H. Awadalla, "A single feed cylindrical superquadric dielectric resonator antenna for circular polarization," *Progress In Electromagnetics* Research, PIER 85, pp. 409- 424, 2006.

[4] S. H. Zainud-Deen, H. A. Malhat, and K. H. Awadalla, "Dielectric Resonator Antenna Mounted On A Circular Cylindrical Ground Plane," Progress In Electromagnetics Research B, PIER B, vol. 19, pp. 427- 444, 2010.

[5] D. Kajfez and A. A. Kishk, "Dielectric Resonator Antenna-Possible Candidate for Adaptive Antenna Arrays," Proceedings VITEL 2002, International Symp. on Telecommunications, Next Generation Networks and Beyond, Portoroz, Slovenia, pp. 13- 14, May 2002.

[6] A. A. Kishk, A. W. Glisson, and G.P. Junker, "Study of broadband dielectric resonator antennas," Antenna Application Symposium, pp. pp. 45- 68, Sept. 1999.

[7] A. A. Kishk, Z. Xiao, A. W. Glisson, and D. Kajfez, "Numerical analysis of stacked dielectric resonator antennas excited by a coaxial probe for

wideband applications," IEEE Trans. Antennas Propagat., vol. 51, no. 8, pp. 1996- 2006, Aug. 2003.

[8] Q. Lai, G. Almpanis, C. Fumeaux, H. Benedickter, and R. Vahldieck, "Comparison of the radiation efficiency for the dielectric resonator antenna and the microstrip antenna at Ka band," *IEEE Transactions on Antennas and Propagation*, vol. 56, no. 11, pp. 3589- 592, November 2008.

[9] B. Erturk and R.G. Rojas, "Efficient Analysis of Input Impedance and Mutual Coupling of Microstrip Antennas Mounted on Large Coated Cylinders," IEEE Trans. Antennas Propagat., vol. 51, pp. 739-749, April 2003.

[10] P. Pearson and R. G. Rojas, "High-frequency approximation for mutual coupling calculations between apertures on a perfect electric conductor circular cylinder covered with a dielectric layer: Nonparaxial region," Radio Science, vol. 38, no. 4, pp. 1079- 1092, August 2003

[11] R. Chair, A. A. Kishk, and K. F. Lee, "Comparative study on the mutual coupling between different sized cylindrical dielectric resonators antennas and circular microstrip patch antennas," *IEEE Transactions on Antennas and Propagation,* vol. 53, no. 3, pp. 1011- 1019, March 2005.

[12] Emad El-Deen, S. H. Zainud-Deen, H. A. Sharshar, and M. A. Binyamin, "The effect of the ground plane shape on the characteristics of rectangular dielectric resonator antennas," *IEEE APS/URSI/AMEREM 2006 Symposium*, Albuquerque, New Mexico, USA, July 2006.

[13] S. H. Zainud-Deen, M. E. Badr, E. El-Deen, K. H. Awadalla, and H. A. Sharshar, "Microstrip antenna with corrugated ground plane surface as a sensor for landmines detection," *Progress In Electromagnetics Research B, PIER B*, vol. 2, pp. 259- 278, 2008.

[14] X. Zhou and G. W. Pan, "Application of physical spline finite element method (PSFEM) to full wave analysis of waveguide," *Progress In Electromagnetics Research, PIER 60*, pp. 19- 41, 2006.

[15] M. Clemens and T. Weiland, "Discrete electromagnetism with the finite integration technique," *Progress In Electromagnetics Research, PIER 32*, pp. 65- 87, 2001.

[16] T. Weiland, "A discretization method for the solution of Maxwell's equations for six-component fields," Electromagnetics and Communications AEÜ, vol. 31, no. 3, pp. 116-120, March 1977.

[17] M. Clemens and T. Weiland, "Discrete electromagnetism with the finite integration technique," Progress In Electromagnetics Research, PIER, vol. 32, pp. 65- 87, 2001.

[18] A. Vasylchenko, Y. Schols, W. Defaedt, and G. A. E. Vandenbosch, "Quality assessment of computational techniques and software tools for planar- antenna analysis," IEEE Antennas Propagation Magazine, vol. 51, no. 1, pp. 23- 38, Feb. 2009.

S. H. Zauind-Deen: (S'81-M'88) was born in Menouf, Egypt, on November 15, 1955. He received the B.Sc. and M.Sc. degrees from Menoufia University in 1973 and 1982, respectively, and the Ph.D. degree in Antenna Engineering from Menoufia University, Egypt in 1988.

He is currently a professor in the Department Of Electrical and Electronic Engineering in the Faculty of Electronic Engineering, Menoufia University, Egypt. His research interests at present include microtrip and leaky wave antennas, DRA, RFID, optimization techniques, FDFD and FDTD, scattering problems, and breast cancer detection

Hend A. Mahat: was born in Menouf, Egypt, on October 12, 1982. She received the B.Sc. and M.Sc. degrees from Menoufia University in 2004 and 2007, respectively. She is currently working for her Ph.D. in Antenna Engineering from Menoufia University, Egypt.

She is currently an assistance lecture in the Department Of Electrical and Electronic Engineering in the Faculty of Electronic Engineering, Menoufia University, Egypt. Her research interests at present include DRA, RFID, reflectarray, and wavelets technique.

K. H. Awadalla: was born in El-Santa – Gharbiya - Egypt, on February 1, 1943. He received the B.Sc. and M.Sc. from the Faculty of Engineering, Cairo University, Egypt, in 1694 and 1972, respectively and the Ph.D. degree from the University of Birmingham, UK, in 1978.

He is currently a Professor emeritus in the Dept. of Electrical and Electronic Engineering in the Faculty of Electronic Engineering, Menoufia University, Egypt. His research interests at present include microtrip and leaky wave antennas, DRA, RFID, and optimization techniques.

2010 INSTITUTIONAL MEMBERS

DTIC-OCP LIBRARY
8725 John J. Kingman Rd, Ste 0944
Fort Belvoir, VA 22060-6218

AUSTRALIAN DEFENCE LIBRARY
Northcott Drive
Canberra, A.C.T. 2600 Australia

BEIJING BOOK CO, INC
701 E Linden Avenue
Linden, NJ 07036-2495

BUCKNELL UNIVERSITY
69 Coleman Hall Road
Lewisburg, PA 17837

ROBERT J. BURKHOLDER
OHIO STATE UNIVERSITY
1320 Kinnear Road
Columbus, OH 43212

DARTMOUTH COLLEGE
6025 Baker/Berry Library
Hanover, NH 03755-3560

DSTO EDINBURGH
AU/33851-AP, PO Box 830470
Birmingham, AL 35283

SIMEON J. EARL – BAE SYSTEMS
W432A, Warton Aerodome
Preston, Lancs., UK PR4 1AX

ELLEDIEMME
Libri Dal Mondo
PO Box 69/Poste S. Silvestro
Rome, Italy 00187

ENGINEERING INFORMATION, INC
PO Box 543
Amsterdam, Netherlands 1000 Am

ETSE TELECOMUNICACION
Biblioteca, Campus Lagoas
Vigo, 36200 Spain

OLA FORSLUND
SAAB MICROWAVE SYSTEMS
Nettovagen 6
Jarfalla, Sweden SE-17588

GEORGIA TECH LIBRARY
225 North Avenue, NW
Atlanta, GA 30332-0001

HRL LABS, RESEARCH LIBRARY
3011 Malibu Canyon
Malibu, CA 90265

IEE INSPEC
Michael Faraday House
6 Hills Way
Stevenage, Herts UK SG1 2AY

IND CANTABRIA
PO Box 830470
Birmingham, AL 35283

INSTITUTE FOR SCIENTIFIC INFO.
Publication Processing Dept.
3501 Market St.
Philadelphia, PA 19104-3302

KUWAIT UNIVERSITY
Postfach/po box 432
Basel, Switzerland 4900

LIBRARY – DRDC OTTAWA
3701 Carling Avenue
Ottawa, Ontario, Canada K1A OZ4

LIBRARY of CONGRESS
Reg. Of Copyrights
Attn: 407 Deposits
Washington DC, 20559

LINDA HALL LIBRARY
5109 Cherry Street
Kansas City, MO 64110-2498

RAY MCKENZIE – TELESTRA
13/242 Exhibition Street
Melbourne, Vic, Australia 3000

MISSISSIPPI STATE UNIV LIBRARY
PO Box 9570
Mississippi State, MS 39762

MISSOURI S&T
400 W 14th Street
Rolla, MO 56409

MIT LINCOLN LABORATORY
Periodicals Library
244 Wood Street
Lexington, MA 02420

OSAMA MOHAMMED
FLORIDA INTERNATIONAL UNIV
10555 W Flagler Street
Miami, FL 33174

NAVAL POSTGRADUATE SCHOOL
Attn:J. Rozdal/411 Dyer Rd./ Rm 111
Monterey, CA 93943-5101

NDL KAGAKU
C/0 KWE-ACCESS
PO Box 300613 (JFK A/P)
Jamaica, NY 11430-0613

OVIEDO LIBRARY
PO BOX 830679
Birmingham, AL 35283

PENN STATE UNIVERSITY
126 Paterno Library
University Park, PA 16802-1808

DAVID J. PINION
1122 E PIKE STREET #1217
SEATTLE, WA 98122

KATHERINE SIAKAVARA-
ARISTOTLE UNIV OF
THESSALONIKI
Gymnasiou 8
Thessaloniki, Greece 55236

SWETS INFORMATION SERVICES
160 Ninth Avenue, Suite A
Runnemede, NJ 08078

TIB & UNIV. BIB. HANNOVER
DE/5100/G1/0001
Welfengarten 1B
Hannover, Germany 30167

UNIV OF CENTRAL FLORIDA
4000 Central Florida Boulevard
Orlando, FL 32816-8005

UNIVERSITY OF COLORADO
1720 Pleasant Street, 184 UCB
Boulder, CO 80309-0184

UNIVERSITY OF KANSAS –
WATSON
1425 Jayhawk Blvd 210S
Lawrence, KS 66045-7594

UNIVERSITY OF MISSISSIPPI
JD Williams Library
University, MS 38677-1848

UNIVERSITY LIBRARY/HKUST
CLEAR WATER BAY ROAD
KOWLOON, HONG KONG

UNIV POLIT CARTAGENA
Serv Btca Univ,
Paseo Alfonso XIII, 48
Cartagena, Spain 30203

THOMAS WEILAND
TU DARMSTADT
Schlossgartenstrasse 8
Darmstadt, Hessen, Germany 64289

STEVEN WEISS
US ARMY RESEARCH LAB
2800 Powder Mill Road
Adelphi, MD 20783

YOSHIHIDE YAMADA
NATIONAL DEFENSE ACADEMY
1-10-20 Hashirimizu
Yokosuka, Kanagawa,
Japan 239-8686

ACES COPYRIGHT FORM

This form is intended for original, previously unpublished manuscripts submitted to ACES periodicals and conference publications. The signed form, appropriately completed, MUST ACCOMPANY any paper in order to be published by ACES. PLEASE READ REVERSE SIDE OF THIS FORM FOR FURTHER DETAILS.

TITLE OF PAPER:

AUTHORS(S)

PUBLICATION TITLE/DATE:

RETURN FORM TO:

Dr. Atef Z. Elsherbeni
University of Mississippi
Dept. of Electrical Engineering
Anderson Hall Box 13
University, MS 38677 USA

PART A - COPYRIGHT TRANSFER FORM

(NOTE: Company or other forms may not be substituted for this form. U.S. Government employees whose work is not subject to copyright may so certify by signing Part B below. Authors whose work is subject to Crown Copyright may sign Part C overleaf).

The undersigned, desiring to publish the above paper in a publication of ACES, hereby transfer their copyrights in the above paper to The Applied Computational Electromagnetics Society (ACES). The undersigned hereby represents and warrants that the paper is original and that he/she is the author of the paper or otherwise has the power and authority to make and execute this assignment.

Returned Rights: In return for these rights, ACES hereby grants to the above authors, and the employers for whom the work was performed, royalty-free permission to:

1. Retain all proprietary rights other than copyright, such as patent rights.
2. Reuse all or portions of the above paper in other works.
3. Reproduce, or have reproduced, the above paper for the author's personal use or for internal company use provided that (a) the source and ACES copyright are indicated, (b) the copies are not used in a way that implies ACES endorsement of a product or service of an employer, and (c) the copies per se are not offered for sale.
4. Make limited distribution of all or portions of the above paper prior to publication.
5. In the case of work performed under U.S. Government contract, ACES grants the U.S. Government royalty-free permission to reproduce all or portions of the above paper, and to authorize others to do so, for U.S. Government purposes only.

ACES Obligations: In exercising its rights under copyright, ACES will make all reasonable efforts to act in the interests of the authors and employers as well as in its own interest. In particular, ACES REQUIRES that:

1. The consent of the first-named author be sought as a condition in granting re-publication permission to others.
2. The consent of the undersigned employer be obtained as a condition in granting permission to others to reuse all or portions of the paper for promotion or marketing purposes.

In the event the above paper is not accepted and published by ACES or is withdrawn by the author(s) before acceptance by ACES, this agreement becomes null and void.

AUTHORIZED SIGNATURE — TITLE (IF NOT AUTHOR)

EMPLOYER FOR WHOM WORK WAS PERFORMED — DATE FORM SIGNED

Part B - U.S. GOVERNMENT EMPLOYEE CERTIFICATION

(NOTE: if your work was performed under Government contract but you are not a Government employee, sign transfer form above and see item 5 under Returned Rights).

This certifies that all authors of the above paper are employees of the U.S. Government and performed this work as part of their employment and that the paper is therefor not subject to U.S. copyright protection.

AUTHORIZED SIGNATURE — TITLE (IF NOT AUTHOR)

NAME OF GOVERNMENT ORGANIZATION — DATE FORM SIGNED

PART C - CROWN COPYRIGHT

(NOTE: ACES recognizes and will honor Crown Copyright as it does U.S. Copyright. It is understood that, in asserting Crown Copyright, ACES in no way diminishes its rights as publisher. Sign only if *ALL* authors are subject to Crown Copyright).

This certifies that all authors of the above Paper are subject to Crown Copyright. (Appropriate documentation and instructions regarding form of Crown Copyright notice may be attached).

AUTHORIZED SIGNATURE TITLE OF SIGNEE

NAME OF GOVERNMENT BRANCH DATE FORM SIGNED

Information to Authors

ACES POLICY

ACES distributes its technical publications throughout the world, and it may be necessary to translate and abstract its publications, and articles contained therein, for inclusion in various compendiums and similar publications, etc. When an article is submitted for publication by ACES, acceptance of the article implies that ACES has the rights to do all of the things it normally does with such an article.

In connection with its publishing activities, it is the policy of ACES to own the copyrights in its technical publications, and to the contributions contained therein, in order to protect the interests of ACES, its authors and their employers, and at the same time to facilitate the appropriate re-use of this material by others.

The new United States copyright law requires that the transfer of copyrights in each contribution from the author to ACES be confirmed in writing. It is therefore necessary that you execute either Part A-Copyright Transfer Form or Part B-U.S. Government Employee Certification or Part C-Crown Copyright on this sheet and return it to the Managing Editor (or person who supplied this sheet) as promptly as possible.

CLEARANCE OF PAPERS

ACES must of necessity assume that materials presented at its meetings or submitted to its publications is properly available for general dissemination to the audiences these activities are organized to serve. It is the responsibility of the authors, not ACES, to determine whether disclosure of their material requires the prior consent of other parties and if so, to obtain it. Furthermore, ACES must assume that, if an author uses within his/her article previously published and/or copyrighted material that permission has been obtained for such use and that any required credit lines, copyright notices, etc. are duly noted.

AUTHOR/COMPANY RIGHTS

If you are employed and you prepared your paper as a part of your job, the rights to your paper initially rest with your employer. In that case, when you sign the copyright form, we assume you are authorized to do so by your employer and that your employer has consented to all of the terms and conditions of this form. If not, it should be signed by someone so authorized.

NOTE RE RETURNED RIGHTS: Just as ACES now requires a signed copyright transfer form in order to do "business as usual", it is the intent of this form to return rights to the author and employer so that they too may do "business as usual". If further clarification is required, please contact: The Managing Editor, R. W. Adler, Naval Postgraduate School, Code EC/AB, Monterey, CA, 93943, USA (408)656-2352.

Please note that, although authors are permitted to re-use all or portions of their ACES copyrighted material in other works, this does not include granting third party requests for reprinting, republishing, or other types of re-use.

JOINT AUTHORSHIP

For jointly authored papers, only one signature is required, but we assume all authors have been advised and have consented to the terms of this form.

U.S. GOVERNMENT EMPLOYEES

Authors who are U.S. Government employees are not required to sign the Copyright Transfer Form (Part A), but any co-authors outside the Government are.

Part B of the form is to be used instead of Part A only if all authors are U.S. Government employees and prepared the paper as part of their job.

NOTE RE GOVERNMENT CONTRACT WORK: Authors whose work was performed under a U.S. Government contract but who are not Government employees are required so sign Part A-Copyright Transfer Form. However, item 5 of the form returns reproduction rights to the U. S. Government when required, even though ACES copyright policy is in effect with respect to the reuse of material by the general public.

APPLIED COMPUTATIONAL ELECTROMAGNETICS SOCIETY JOURNAL
http://aces.ee.olemiss.edu

INFORMATION FOR AUTHORS

PUBLICATION CRITERIA

Each paper is required to manifest some relation to applied computational electromagnetics. **Papers may address general issues in applied computational electromagnetics, or they may focus on specific applications, techniques, codes, or computational issues.** While the following list is not exhaustive, each paper will generally relate to at least one of these areas:

1. **Code validation.** This is done using internal checks or experimental, analytical or other computational data. Measured data of potential utility to code validation efforts will also be considered for publication.

2. **Code performance analysis.** This usually involves identification of numerical accuracy or other limitations, solution convergence, numerical and physical modeling error, and parameter tradeoffs. However, it is also permissible to address issues such as ease-of-use, set-up time, run time, special outputs, or other special features.

3. **Computational studies of basic physics.** This involves using a code, algorithm, or computational technique to simulate reality in such a way that better, or new physical insight or understanding, is achieved.

4. **New computational techniques** or new applications for existing computational techniques or codes.

5. **"Tricks of the trade"** in selecting and applying codes and techniques.

6. **New codes, algorithms, code enhancement, and code fixes.** This category is self-explanatory, but includes significant changes to existing codes, such as applicability extensions, algorithm optimization, problem correction, limitation removal, or other performance improvement. **Note: Code (or algorithm) capability descriptions are not acceptable, unless they contain sufficient technical material to justify consideration.**

7. **Code input/output issues.** This normally involves innovations in input (such as input geometry standardization, automatic mesh generation, or computer-aided design) or in output (whether it be tabular, graphical, statistical, Fourier-transformed, or otherwise signal-processed). Material dealing with input/output database management, output interpretation, or other input/output issues will also be considered for publication.

8. **Computer hardware issues.** This is the category for analysis of hardware capabilities and limitations of various types of electromagnetics computational requirements. Vector and parallel computational techniques and implementation are of particular interest.

Applications of interest include, but are not limited to, antennas (and their electromagnetic environments), networks, static fields, radar cross section, inverse scattering, shielding, radiation hazards, biological effects, biomedical applications, electromagnetic pulse (EMP), electromagnetic interference (EMI), electromagnetic compatibility (EMC), power transmission, charge transport, dielectric, magnetic and nonlinear materials, microwave components, MEMS, RFID, and MMIC technologies, remote sensing and geometrical and physical optics, radar and communications systems, sensors, fiber optics, plasmas, particle accelerators, generators and motors, electromagnetic wave propagation, non-destructive evaluation, eddy currents, and inverse scattering.

Techniques of interest include but not limited to frequency-domain and time-domain techniques, integral equation and differential equation techniques, diffraction theories, physical and geometrical optics, method of moments, finite differences and finite element techniques, transmission line method, modal expansions, perturbation methods, and hybrid methods.

Where possible and appropriate, authors are required to provide statements of quantitative accuracy for measured and/or computed data. This issue is discussed in "Accuracy & Publication: Requiring, quantitative accuracy statements to accompany data," by E. K. Miller, *ACES Newsletter,* Vol. 9, No. 3, pp. 23-29, 1994, ISBN 1056-9170.

SUBMITTAL PROCEDURE

All submissions should be uploaded to ACES server through ACES web site (http://aces.ee.olemiss.edu) by using the upload button, journal section. Only pdf files are accepted for submission. The file size should not be larger than 5MB, otherwise permission from the Editor-in-Chief should be obtained first. Automated acknowledgment of the electronic submission, after the upload process is successfully completed, will be sent to the corresponding author only. It is the responsibility of the corresponding author to keep the remaining authors, if applicable, informed. Email submission is not accepted and will not be processed.

PAPER FORMAT (INITIAL SUBMISSION)

The preferred format for initial submission manuscripts is 12 point Times Roman font, single line spacing and single column format, with 1 inch for top, bottom, left, and right margins. Manuscripts should be prepared for standard 8.5x11 inch paper.

EDITORIAL REVIEW

In order to ensure an appropriate level of quality control, papers are peer reviewed. They are reviewed both for

technical correctness and for adherence to the listed guidelines regarding information content and format.

PAPER FORMAT (FINAL SUBMISSION)

Only camera-ready electronic files are accepted for publication. The term **"camera-ready" means that the material is neat, legible, reproducible, and in accordance with the final version format listed below.**

The following requirements are in effect for the final version of an ACES Journal paper:

1. The paper title should not be placed on a separate page. The title, author(s), abstract, and (space permitting) beginning of the paper itself should all be on the first page. The title, author(s), and author affiliations should be centered (center-justified) on the first page. The title should be of font size 16 and bolded, the author names should be of font size 12 and bolded, and the author affiliation should be of font size 12 (regular font, neither italic nor bolded).

2. An abstract is required. The abstract should be a brief summary of the work described in the paper. It should state the computer codes, computational techniques, and applications discussed in the paper (as applicable) and should otherwise be usable by technical abstracting and indexing services. The word "Abstract" has to be placed at the left margin of the paper, and should be bolded and italic. It also should be followed by a hyphen (—) with the main text of the abstract starting on the same line.

3. All section titles have to be centered and all the title letters should be written in caps. The section titles need to be numbered using roman numbering (I. II. ….)

4. Either British English or American English spellings may be used, provided that each word is spelled consistently throughout the paper.

5. Internal consistency of references format should be maintained. As a guideline for authors, we recommend that references be given using numerical numbering in the body of the paper (with numerical listing of all references at the end of the paper). The first letter of the authors' first name should be listed followed by a period, which in turn, followed by the authors' complete last name. Use a coma (,) to separate between the authors' names. Titles of papers or articles should be in quotation marks (" "), followed by the title of journal, which should be in italic font. The journal volume (vol.), issue number (no.), page numbering (pp.), month and year of publication should come after the journal title in the sequence listed here.

6. Internal consistency shall also be maintained for other elements of style, such as equation numbering. As a guideline for authors who have no other preference, we suggest that equation numbers be placed in parentheses at the right column margin.

7. The intent and meaning of all text must be clear. For authors who are not masters of the English language, the ACES Editorial Staff will provide assistance with grammar (subject to clarity of intent and meaning). However, this may delay the scheduled publication date.

8. Unused space should be minimized. Sections and subsections should not normally begin on a new page.

ACES reserves the right to edit any uploaded material, however, this is not generally done. It is the author(s) responsibility to provide acceptable camera-ready pdf files. Incompatible or incomplete pdf files will not be processed for publication, and authors will be requested to re-upload a revised acceptable version.

COPYRIGHTS AND RELEASES

Each primary author must sign a copyright form and obtain a release from his/her organization vesting the copyright with ACES. Copyright forms are available at ACES, web site (http://aces.ee.olemiss.edu). To shorten the review process time, the executed copyright form should be forwarded to the Editor-in-Chief immediately after the completion of the upload (electronic submission) process. Both the author and his/her organization are allowed to use the copyrighted material freely for their own private purposes.

Permission is granted to quote short passages and reproduce figures and tables from and ACES Journal issue provided the source is cited. Copies of ACES Journal articles may be made in accordance with usage permitted by Sections 107 or 108 of the U.S. Copyright Law. This consent does not extend to other kinds of copying, such as for general distribution, for advertising or promotional purposes, for creating new collective works, or for resale. The reproduction of multiple copies and the use of articles or extracts for commercial purposes require the consent of the author and specific permission from ACES. Institutional members are allowed to copy any ACES Journal issue for their internal distribution only.

PUBLICATION CHARGES

All authors are allowed for 8 printed pages per paper without charge. Mandatory page charges of $75 a page apply to all pages in excess of 8 printed pages. Authors are entitled to one, free of charge, copy of the journal issue in which their paper was published. Additional reprints are available for a nominal fee by submitting a request to the managing editor or ACES Secretary.

Authors are subject to fill out a one page over-page charge form and submit it online along with the copyright form before publication of their manuscript.

ACES Journal is abstracted in INSPEC, in Engineering Index, DTIC, Science Citation Index Expanded, the Research Alert, and to Current Contents/Engineering, Computing & Technology.